THERMAL MANAGEMENT FOR A SWITCHED RELUCTANCE MACHINE

ADVANCED THERMAL MANAGEMENT

FOR

A SWITCHED RELUCTANCE MACHINE

By **RICHARD MARLOW, P.Eng., B.Eng.Sci., M.Eng.**

A Thesis Submitted to the School of Graduate Studies

in Partial Fulfillment of the Requirements

for the Degree

Doctor of Philosophy

McMaster University DOCTOR OF PHILOSOPHY (2015) Hamilton, Ontario (Engineering)

TITLE: Advanced Thermal Management for a Switched Reluctance Machine

AUTHOR: Richard Marlow, P.Eng., B.Eng.Sci. (The University of Western Ontario), M.Eng. (McMaster University)

SUPERVISORS: Dr. A. Emadi

Dr. N. Schofield

NUMBER OF PAGES: xxiv, 216

ABSTRACT

The thermal management of electric machines is investigated with the application of techniques to a Switched Reluctance Machine and a high-speed Switched Reluctance Machine. Two novel concepts for said management of a Switched Reluctance Machine are proposed and developed: Inter-Laminate Cooling and a Continuous Toroidal Winding.

The Inter-Laminate Cooling concept is developed with application to an iron core inductor which serves as a proxy for the electric machine. The experimental results confirmed the capability of the method, expressed by the effectiveness, which defines the performance measure of the applied cooling method; a concept which itself is equally applicable to other cooling methods that may be applied to any electric machine. The effectiveness also describes the gain in allowable input power to the machine which is realized to reach the same thermal limit versus the case without Inter-Laminate Cooling. The Inter-Laminate Cooling was not applied in experimental test to a Switched Reluctance Machine due to the present economic and fabrication limitations.

The Continuous Toroidal Winding concept, originally conceived to permit the consideration of a fluid capillary core type of winding to enhance machine cooling, is developed to allow for peripheral cooling of the machine windings and end windings. The Continuous Toroidal Winding version of the Switched Reluctance Machine is investigated for both its thermal and electrical performance in the context of a machine that is equivalent electromagnetically to its conventional counterpart. The Continuous Toroidal Winding Switched Reluctance Machine was found to perform thermally as

tested, in a manner superior to that of the conventional machine where the Toroidal machine was simulated and researched at an equivalent level of operation to the conventional machine. The electrical performance of the Toroidal Switched Reluctance Machine although supportive of the simulation analysis used to develop the machine, was not fully conclusive. This may have been due to problematic iron cores used in the construction of the experimental machines.

The application of the Inter-Laminate Cooling method to a Switched Reluctance Machine is considered on an analytical basis for the special case of a High Speed Switched Reluctance Machine and found to be of net positive benefit as the machine's iron losses are dominant over its copper losses. Application of the Inter-Laminate Cooling method to a lower speed machine, whilst beneficial, is not sufficient to significantly impact the temperature of the machine's windings such that it would offset the loss of specific torque and power. As such, Inter-Laminate Cooling is only applicable where the net benefit is positive overall; in that the gain in input power realized is sufficient to overcome the loss of specific power and torque which will occur due to the increased machine volume.

The "effectiveness" and "gain" approach for the evaluation of cooling methods applied to electric machines is a concept which should be adopted to aid in the comparative understanding of the performance of myriad different cooling methods being applied to electric machines both in research and practice, of which there is only minimal understanding.

ACKNOWLEDGEMENTS

It is only fitting in the case of a work of this magnitude to acknowledge all those whose participation in varied degree from significant contribution to the work to thoughtful commentary, without which, this work might not have been possible as presented:

Mr. O. Beik,
Dr. B. Bilgin
Dr. A. Emadi
Mr. E. Fairall
Mr. S. Hurkmans
Ms. J. Lin
Dr. J. Lindstrom
Dr. M. Mittra
Mr. Z. Nie
Dr. N. Schofield
Dr. Y. Yang

With sincere apologies to anyone overlooked.

This research was undertaken, in part, thanks to funding from the Canada Excellence Research Chairs (CERC) Program and the Natural Sciences and Engineering Research Council of Canada (NSERC) Discovery Grant Program.

Finally, most special thanks to Nicole, for exceptional perseverance during rants of frustration and despair throughout the completion of this work; Mom and Dad for their generosity and understanding.

LIST OF FIGURES

LIST OF FIGURES

LIST OF FIGURES

LIST OF FIGURES

LIST OF TABLES

LIST OF TABLES

NOMENCLATURE

ACRONYMS and ABBREVIATIONS

3D – Three Dimensional

AC – Alternating Current

AWG – American Wire Gage

BLDC – Brushless Direct Current

CFD – Computational Fluid Dynamics

cm - centimeters

CSRM – Conventional Switched Reluctance Machine

CW – Continuous Winding (or Wound)

db – Decibel (Acoustic)

DC – Direct Current

DCPMSM – Direct Current Permanent Magnet Synchronous Machine

DLC – Direct Laminate Cooling

DW – Discrete Winding (or Wound)

EV – Electric Vehicle

FEA – Finite Element Analysis

FEM – Finite Element Method

GE – General Electric Co.

HEV – Hybrid Electric Vehicle

HSRM – High Speed Switched Reluctance Machine

ICE – Internal Combustion Engine

IEEE – Institute of Electrical and Electronics Engineers

IET – Institute of Engineering Technology

ID – Internal Diameter

IGBT – Isolated Gate Bi-Polar Transistor

LP – Lumped Parameter

LPTN – Lumped Parameter Thermal Network

mm – millimeters

n/a – not applicable (available)

N-m – Newton meter (torque)

n/r – not reported

NVH – Noise, Vibration and Harshness

OD – Outer Diameter

PGS – Pyrolytic Graphite Sheet

PM – Permanent Magnet

PMSM – Permanent Magnet Synchronous Machine

PWM – Pulse Width Modulation

RMS – Root Mean Square

RPM (or rpm) – Revolutions per Minute

SR – Switched Reluctance

SRG – Switched Reluctance Generator

SRM – Switched Reluctance Machine

sw - Switch

TC - Thermocouple

TGM – Thermal Graphite Material

TM – Temperature Monitor

TSRM – Toroidal Switched Reluctance Machine

VDC – Volts Direct Current

WSRM – Wye (configured winding) Switched Reluctance Machine

CERC – Canada Excellence Research Chair

ILC – Inter-Laminate Cooling

VSI – Voltage Source Inverter

SYMBOLS

3Ø - Three phase (machine)

4Ø – Four phase (machine)

A – Area (where used or specified)

A – Ampere (where used or specified)

A_s - Electrical loading

At (or A-t) – Ampere-turns

B – Flux Density

°C – Degrees Celsius

D – Bore Diameter

Dn – Diode no. "n" = 1,2,3…

E - Effectiveness

G – Gain

Hz – Hertz (frequency)

h – Convective heat transfer coefficient

h - Height i – Current

i – Peak phase current

I_{dc} – Direct current

J – Joule

kg - Kilogram

kW - Kilowatt

i – Current

i – Peak phase current

I_{dc} – Direct current

k - Thermal conductivity

k_l – Thermal conductivity of iron (steel) laminations

k_c – Thermal conductivity of thermal conductor

kg_x – Thermal conductivity of graphite in x direction

kg_y – Thermal conductivity of graphite in y direction (cross-planar)

k_e - Machine efficiency

k_d - Duty cycle

k_1, k_2 - Machine constants

k_i (or k_i) – Thermal conductivity of iron laminations

$k_{i\text{-}eff}$ ($k_{i\text{-}eff}$) – Effective thermal conductivity of iron laminations

k_p – Packing Factor

K – Kelvin degrees

K – Kilo (where used or specified)

L – Inductance (where specified)

L – Length (where specified)

m – Meters

m - Number of phases conducting at the same time

MMF – Magneto-Motive Force

N_r - Rotor speed

P_d – Power developed at shaft

q - Heat flux in watts

R – Resistance (electrical)

R – Reluctance (magnetic)

R_{cv} – Thermal Resistance of convection to air

R_n – Thermal Resistance no. "*n"* = 1,2,3…

R_{th} – Thermal Resistance

Sn – Switch no. "n" = 1,2,3…

t – Time

t_l – Laminations thickness

t_c – Thermal conductor thickness

t_g – Graphite lamination thickness

T (or *T*) – Temperature (as specified)

T_s (or T_s) – Temperature of heat sink

T_l – Iron (steel) laminations temperature

T_{ph} - Total number of turns per phase

T_∞ - Temperature at some distance from the surface

ΔT – A temperature difference

u''' – Internal heat generation

V – Voltage

V_{dc} – Volts direct current

W – Watt (thermal or electrical in the context used)

x – Distance

Δx – A distance difference

Y-Δ – Wye configuration to Delta configuration conversion

Ω – Ohm (electrical resistance)

TABLE OF CONTENTS

STATEMENT OF CONTRIBUTION

The research contained herein describes what is essentially the creation of two advances to the state of the art of thermal science and electric machine design: Inter-Laminate Cooling for Electric Machines using Pyrolytic Graphite Sheet and, A Single Continuous Toroidal Winding Switched Reluctance Machine, which, at the time of this writing have been granted United States Provisional Patent Protection Nos. 62/131,901 and 62/137,914, "Method for Cooling Electric Machines" and "Continuously Wound Toroidal Switched Reluctance Machine", respectively. For these, I claim sole responsibility.

The research has been presented at two refereed International conferences, IET Power Electronics Machines and Drives (PEMD), Manchester, UK, Apr. 2014, and IEEE Energy Conversion Conference and Exposition (ECCE), Pittsburgh, PA, Sept. 2014. Subsequent to the latter the work was accepted for one Journal publication in IEEE Transactions on Industry Applications, Jan./Feb. 2016.

The concept of thermal effectiveness has been applied elsewhere in heat transfer but not in the same context, where in this research on electric machine cooling it is applied to evaluate the performance of an applied cooling method; this is not known prior. The theory is further developed in Chapter 6 of this work.

CHAPTER 1 – INTRODUCTION

1.1 – BACKGROUND TO THE RESEARCH PROGRAM

Electric vehicles (EVs) remain range limited by the energy and power capacity of their batteries. As such, at this present moment in time any improvement which may be gained in the efficiency of the electric machine serves to improve, by even some small measure the operable range of EVs. There are many possible ways to increase the efficiency of electric machines, amongst which is active thermal management. To achieve the thermal management goal, there are a myriad of traditional bulk cooling methods. To be truly effective thermal management demands precision and control, targeted to the thermal source, with a minimum of weight and space.

The reality of the thermal limitations of mechanical equipment is well known. Electric machines (EM) are no exception, posing significant challenges to thermal management given their high power density capabilities. Historically, this has been the limitation. Advances in transportation and automotive electrification running concurrent with electrical distribution infrastructure advancements will see increasing use of the electric motor as the primary motive source for automotive applications, notwithstanding their range limitations arising from the state of present day Li-ion battery technology. Electric vehicles (EV) will have, and demand, the performance capability of a typical ICE vehicle today. As such, the characteristic curves for torque and power will bear some similarity to those of an ICE vehicle. Low end torque, i.e. at launch from a standing start will need to be at least equal to or better than the comparable ICE that it

might replace. Peak power will need to reside in the higher RPM range, ideally with a wide and relatively flat power band. These are the key elements contributing to the feel of a motor vehicle's performance, that "driveability" that the end user looks for and appreciates. Electric machines, having these characteristics, can fulfill these requirements with permanent magnet (PM) and induction machines (IM) as the top choices presently favoured in automotive design and development. The Switched Reluctance (SR) Machine not only possesses these same characteristics, but with an excellent speed ratio and favourable manufacturing economies, has been considered for automotive application however it is presently limited to special motive transport and has yet to see application in a passenger vehicle. The SR machine is limited by some fundamental problems of its operation which are: objectionable noise, vibration and harshness (NVH) characteristics, which to some extent arise from the SR machine's high level of output torque ripple. In its present state, it is unacceptable for release as a prime motive source in a passenger vehicle.

Although efficient, electric machines by their very nature are tightly packaged resulting in high temperature operation where waste heat rejection is confined to traditional methods, notably internal/external convective cooling or water jacket cooling. Unlike the ICE the EM allowable operating temperature limits are low, typically 150°C. However, when considering the automotive operating environment, external ambient temperatures available for heat rejection must consider the highest encountered, usually in the range of 50°C – 60°C. This results in a narrow thermal driving potential with which to achieve the required cooling. The cooling of electric machines in such applications will be materially important to their success.

Other than the issues of NVH and torque ripple, the SR machine is otherwise well suited to automotive applications due to its small size, permanent magnet (PM) free status, a simple and efficient design that is easy to assemble, which finds itself as a cost advantaged alternative to PM and inductance machines. It is presently used in heavy earth moving equipment drives (located at each wheel) and in small appliances, for example. The fact that it is PM free is of strategic importance as PMs suitable for use in high output machines often contain rare earth elements Neodymium (Nd) and Dysprosium (Dy) to increase the field strength of the permanent magnets or in the case of the latter the operating temperature limit. Not only are these materials expensive but are increasingly subject to geopolitical control creating uncertainty of reliable supply. PMs can also suffer from loss of magnetic strength over time especially where high temperatures are encountered or may further be compromised if subjected to a reversed flux exceeding the threshold limit. This would add a limiting factor to the output power achievable with such machines operating in the typical automotive environment. These factors have led to the revisiting of the SR machine as a technology for automotive application, notwithstanding the aforementioned undesirable characteristics of NVH and torque ripple. Solutions may exist for addressing those issues. Advanced designs have considered multiple pole (24-18) and multi-phase (3 or 4) operation along with current profiling in an attempt to address these issues. Operation at high speed (high RPM) will also serve to mitigate the torque ripple as its magnitude is diminished versus the overall torque level. It should be noted that NVH is not confined to the SR machine, but exists in the case of all other electric machines, PM, IM, although at far less objectionable levels which may be successfully isolated from the passenger compartment of a vehicle.

That said, the SRM is still subject to the same thermal limits as other EMs these being: Lamination insulation temperature and winding insulation temperature, the insulation being composed of organic materials. The SRM, unlike PM type machines, may be subject to high levels of internal heat generation from magnetic field losses in the iron core laminations when operated at high RPM levels. A brief review of the literature has revealed a dearth of cooling methods for electric machines in general; usually confined to some form of convective cooling (case fins, rotor fans) or external water/oil liquid jacket cooling as the usual approach, although in the case of compressor motors suction side refrigerant cooling has been used to cool the internals of the electric motor replacing the internal air. The latter is an integrated approach which may be considered as part of an overall system approach. Thus far, although internal liquid cooling of the rotor is known to exist, no internal cooling methods have been encountered in the literature except for one novel attempt at end winding cooling by applied oil spray. This may come as no surprise as the placement of liquid cooling via metallic conduits is not only severely challenged in terms of its packaging but also in terms of the possible losses which may be encountered by placing an added metal conduits within the proximity of alternating magnetic fields. What the literature has revealed though is that whatever the cooling method applied to the machine, in all cases some type of thermal analysis is required and used. This may take the form of a thermal FEA program as part of an electrical design software package or a lumped parameter (LP) thermal analysis of either one or two dimensions. The latter method builds a thermal resistance map of the system combined with the known or estimated losses (the heat rejection) and solves for the temperature at each node of the thermal resistance map. It was decided early on, since

the group design for the SRM was always evolving, that a simple lumped parameter thermal model would be a quick and effective method for the purpose of facilitating design development. That model was achieved and has already revealed what some of the challenges to cooling will be. These are: Air gaps, high thermal contact resistance between components, low thermal conductivity of the core, cooling is most effective when applied at the source of loss, to name a few. All of these factors contribute to driving a high temperature differential between the coolant and the internal components of the motor where traditional cooling methods are considered. The proposed research will focus on the development of alternative (internal) cooling methods applied to the high speed SRM architecture to reconcile the problem of low maximum temperature limits and coolant temperatures with the high ambient operating temperatures which are encountered in practical application, or at the very least determine the heat rejection environment and cooling method which would result in the practical application of a high-speed, high-output SRM.

1.2 – THE THERMAL PROBLEM POSED BY DESIGN OF A HIGH SPEED SRM

On or about May 2012 the CERC group began to work with a high speed SRM design intended as the basis for the development of a possible traction machine. This author's research commenced with the preliminary thermal analysis of this machine discussed in Chapter 3 section 3.3 and was the motivation for the work contained herein. Amongst the many objectives of this machine, a conventional SRM design of 12-8 pole configuration, depicted in figures 1.1 and 1.2[1] were improvement in the manufacturing of

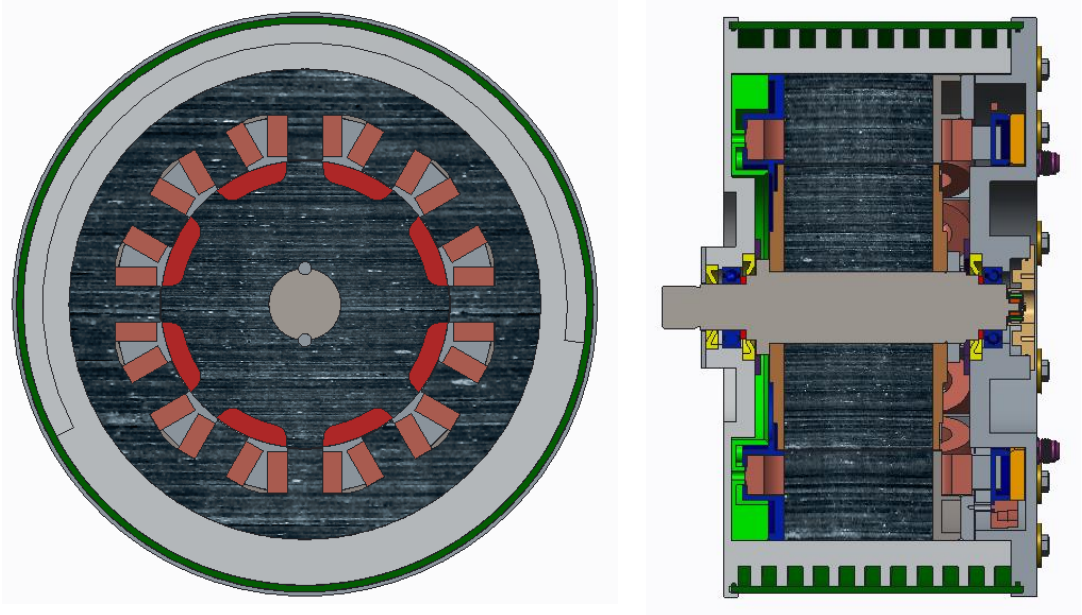

(a) HSRM cross section profile (b) HSRM full section axial profile

Figure 1.1. Proposed design for a high speed 12-8 SRM (HSRM)*

its windings and the thermal management of its coils. An SR machine for high speed will have high iron losses with respect to that of a lower speed machine, additional to the copper losses of the machine. The magnetic flux plot of figure 1.2 shows where these losses arise in the machine's iron core; predominately around the coils and the back iron surrounding each winding. As may be observed in figure 1.1(a) the windings are located well inside the machine which

* Image provided with permission from CERC author

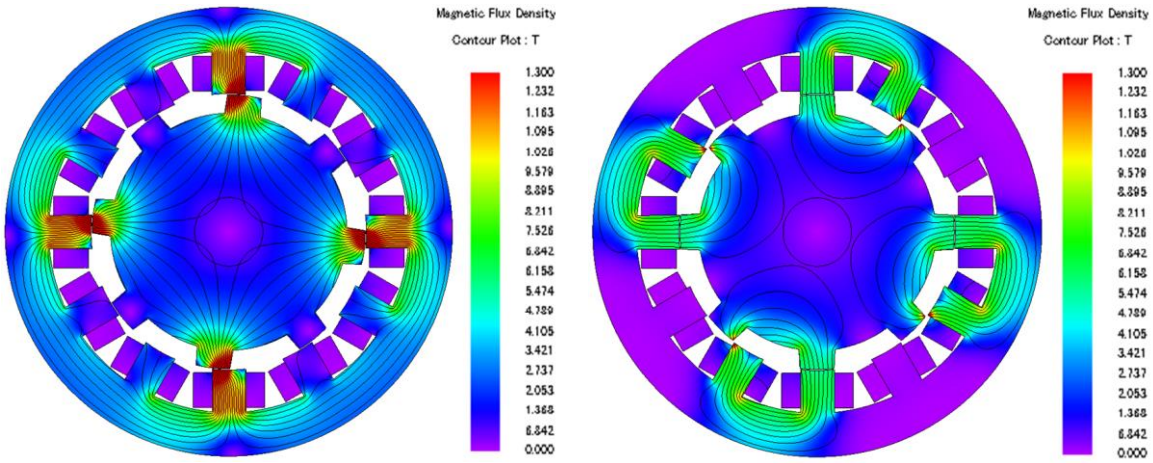

(a) Magnetic flux at commutation (b) Magnetic flux at pole alignment

Figure 1.2. Magnetic flux intensity of the high speed 12-8 SRM[†]

contributes to high operating temperatures. The overall challenge was the thermal management of the machine. Although there may be several possible design solutions to mitigate the thermal issues, this thesis examines two solutions proposed for the thermal management of such a machine: A toroidal winding configuration to improve machine cooling across the speed range, which will have as an ancillary benefit an improved packing factor for the machine windings and benefit to manufacturability and, Inter-Laminate Cooling, applied within the iron laminations, which will be of benefit at high speed operation. Each of these proposals is examined in this thesis and demonstrated experimentally, but not necessarily as part of an SRM or a high speed variant thereof. A third consideration involved the use of capillary core winding, i.e. direct winding cooling but was not pursued as part of this research.

[†] Image provided with permission from CERC author

1.3 – SUMMARY AND THESIS OUTLINE

A confluence of the events discussed has provided the motivation to undertake the research discussed herein. This begins with a comprehensive review of the literature on electric machines and their thermal management located in Chapters 2 and 3. This is followed by the research development, first, into the Inter-Laminate Cooling concept, a means to target cooling directly to the iron laminations of the core, which is proven out with the use of a simple inductor as a proxy for an electric machine, with the conceptual development, theory, analysis, application and test results confirming the approach all reported in Chapter 4. Second, the research is then progressed to the SRM itself with the development of a Toroidal SRM configuration, conceived originally as a means to facilitate the use of capillary-core windings, consisting of conceptual development and simulation analysis, much of which has been confirmed by the experimental results. This is dealt with fully in Chapter 5. The ILC method was not considered as part of the experimental SRM as this would have been cost prohibitive, so here only the simulation result and its thermal impact upon the machine has been considered. The work closes with a consideration of the thermal impact of applied ILC upon the high speed SRM design considered in Chapter 6 with overall conclusions provided by the research, and the opportunities afforded by the new TSRM topology in future research. In short, a high speed SRM could benefit from both applied ILC and the toroidal topology. Not to be lost, is the attention paid to the applied cooling effectiveness in electric machines, which is poorly, if at all, characterized in the literature as there is no universal evaluation in

place that aids the understanding of the performance of one applied cooling method to an electric machine over that of any another in a dimensionless sense.

CHAPTER 2 - THERMAL MANAGEMENT OF ELECTRIC MACHINES

2.1 – THERMAL ANALYSIS TECHNIQUES

A review of the literature on the cooling of electric machines was performed considering a variety of sources. Particular attention was paid to high speed machines, (RPM>5,000), those for automotive application such as hybrid and electric vehicles, and switched reluctance machines. Little was found with respect to switched reluctance machines. Air convective cooling is the most common approach for industrial machines and hence the most developed, and analyzed. Although many liquid cooling methods exist, there are few examples or applications of advanced methods that would deliver cooling directly to the machine internals; the most common approach being the liquid filled external cooling jacket. Thermal analysis forms a part of most papers considered on the topic. This may involve the application of lumped parameter thermal network models, finite element analysis or computational fluid dynamics to understand complex working fluid flow fields. Electric machines for all electric and hybrid electric vehicles require advanced cooling methods to meet the demands of high specific power and constraints placed upon the cooling system by the external environment, typically specified in a range from -40°C to 50°C for private and commercial automotive vehicles.

For the purpose of establishing the state of the art with regards to the thermal management of electric motors, this literature review was conducted in the field relevant to the cooling of smaller scale electric motors, as might be employed in electric vehicles. Some of the publications reviewed may be considered key papers in the field. Large utility scale motors and generators were not considered in the review since their cooling

methods, e.g. liquid sodium, mercury, heat pipes[2] etc. are not immediately relevant given their scale, complexity, environmental risk and cost.

The cooling, or more strictly the thermal management, of electric machines is a key aspect of their design, development and engineering for nearly a hundred years. From an engineering perspective the pace of development with respect to thermal management innovations has been somewhat but steady, and not particularly innovative when compared to other technology components. There are reasons. Often, a triggering event is needed to force a motivation for an advance in the technology of design. This has usually been associated with some form of rising costs for energy, materials or labour consequently demanding efficiency gains, and not so often by secondary needs such as the need for high speed or power output, quiet operation or smaller scale for packaging purposes. For example, the requirement of tight packaging space within an automotive application combined with high ambient temperatures found underhood might be thought to be the motivator to improve the cooling performance of an electric motor or generator, when in reality it is the cost of energy and improving the efficiency with respect to the consumption thereof, that is motivating factor for development. It is over the longer term that these events form a paradigm shift that drives development and advancement to the next level. Another reason for the lack of development in electric machine cooling may arise from the traditional separation of mechanical and electrical engineering disciplines. Traditionally, the design of electric machines has fallen under the domain of electrical engineering whereas issues of their cooling and mechanical losses have fallen under the domain of mechanical engineering.[3] Clearly this is evidenced by the substantial number of publications in the literature relating to electromagnetic issues versus thermal issues[4].

It has been often cited in the literature[5,6] that one must master many of the disciplines of engineering and science, mechanical, chemical, materials and others in addition to electrical to achieve a successful and thoroughly well thought out design for an electric machine, not just the electrical or electromagnetic part of the discipline. The demands of these other areas not only lie outside the competency zone of many electrical engineers but in the case of thermal management can involve phenomena which are difficult to measure or analyze, particularly for a specific design case. The problem is a complex interdisciplinary one, often far beyond the scope of a single individual. To that point, the advancement of computational aids for such extra-experiential purposes, discussed momentarily, has been of great benefit to the designer of electric machines.

Generally, one can identify two broad areas of research activity as it concerns the cooling of electric machines:

- The thermal analysis of electric machines and
- The development of the design, materials and processes to improve the cooling of electric machines, and
- Often, these areas are mixed by necessity, i.e. thermal analysis to evaluate a type of design modification, with the former often complimenting the latter.

The thermal analysis of electric machines has seen substantial growth in the literature over the past two decades with the application of Finite Element Analysis (FEA), a computational analysis afforded by high speed computers and the commercialization of software packages for this purpose. Prior to FEA developments, thermal analysis was limited to the traditional approach of lumped parameters (LP) techniques although FEA has been of benefit to lumped parameter analysis through the combined application of

FEA to certain specific components such as windings. This allows for a better understanding of the thermal behavior and temperature distribution of those components. Computational Fluid Dynamics (CFD) has also come into use for the analysis of fluid flow, within electric machines presenting capabilities to predict complex patterns of flow, the associated velocities and turbulences of both air and liquid mediums previously only estimated through empirical techniques, has ameliorated the prediction of thermal performance. The advent of numerical methods employed in commercial software packages for the specific purpose of thermal analysis has been of tremendous benefit in allowing the everyday designer of electric machines to carry out sophisticated analysis outside of their usual area of expertise, and thus to aid and improve the design process. More recently, commercial software for electric machine design has coupled electromagnetic analysis to thermal analysis further enhancing the accuracy of the final result[7]. That said, complex numerical techniques are not an absolute requirement for an effective design. The use of the simpler lumped parameter method, historically the traditional approach, can produce surprisingly accurate and quick results requiring little in the way of computational demands, although the user should have experience with the method as the specific calculations can be complex, while the thermal networks can often be simplified by executing the right decisions. Further, application of the correct boundary conditions can be challenging. The most demanding boundary conditions involve the prediction of the convective coefficients for airflow within and outside the components of an electric machine, or the same for liquid coolants where that mode is applied[8]. Although not strictly a "boundary condition" the determination of internal contact resistances between components poses a significant challenge to those modeling

thermal performance, as do the conditions of heat flux around the area of the stator coil slots. For example, the heat transfer coefficient is difficult, if not impossible, to calculate analytically for all but the simplest of geometries, are often working fluid dependent, as in the case of the viscosity and temperature of air. The same could be said of internal contact resistances, where analytic determination is impossible and values are derived entirely from empirical results, the fine adjustment of the analytic model, sometimes known as tuning, to agree with experimental measurements.

The development of design, materials and processes to effect improvements in electric machine cooling are much less dominant in the literature. Most of the literature is focused on thermal analysis, either via LP, FEA or aided by CFD. There have been several studies involving liquid cooling, usually confined to simple considerations of variations on jacket style cooling of electric machines[9,10,11]. These often though have the analysis as the main theme of the paper, rather than the design nuances of the cooling method itself, nor its practical integration into the machine. Additionally, they tend to focus on cooling of the machine exterior. There are a couple of examples of Direct Laminate Cooling (DLC) also known as Back Iron Cooling which have been studied[12,13], where again, the thermal analysis dominates the discussion. Similarly, within the scope of the papers reviewed there is no work found that discusses the improvements in materials or processes beyond those established by industry practice that would achieve improved cooling in electric machines. By way of example, the stator OD and case bore machining tolerance, surface quality and fit are of particular importance in reducing the

thermal contact resistance between the stator of an electric machine and its frame housing.

2.2 – THERMAL MANAGEMENT OF ELECTRIC MACHINES

Early electric machines were of the brushed DC type. Their commutation devices were slow and mechanically unreliable. This restricted the speed of electric machines and hence the size of said machines were comparatively large for a given power output. Thus, the size of these machines was large by necessity and, exaggerated by the practice of over-engineering given the lack of material knowledge and more sophisticated analysis methods. This would suffice in an era of abundant and cheap energy. Accordingly, cooling such machines by means of simple natural convection of air would often be all that was required. With improvements in materials and design knowledge, faster speeds became possible thus the desire to take advantage of smaller size, boost efficiency, and to economize on materials and energy. For all machines, the thermal rating is determined when operating temperatures are at the thermal limits of the materials used in the machine's construction. Those materials are usually the winding wire insulation, lamination insulation and other insulation berries (e.g. slot liners) along with the limits of permanent magnet (PM) materials if used. Table 2.1[14] shows the temperature limits for different classes of electrical insulation material. Not only is the maximum operating temperature limit of concern, but it is well established that the ageing of electrical components is substantially influenced by operating temperature. It is commonly suggested that the lifetime of an electrical insulating system is reduced by about half of the available life for every 10°C of temperature rise that they are exposed to, Bone[15].

Table 2.1. Classification of Insulation Materials and their Thermal Limits (used with permission)

Class	Max. Temp.	Description
Y		Insulation consists of material or combinations of materials such as cotton, silk and paper without impregnation.
A	105^{o}C	Insulation consists of materials such as cotton, silk, and paper when suitably impregnation or coated or when immersed in dielectric liquid as oil.
E		Insulation consists of materials or combinations of material which experience or test can be shown to be capable of operation at the class E temperature.
B	130 ^{o}C	Insulation consists of materials or combinations of materials such as mica, fibre, asbestos, etc with suitable bonding, impregnation or coating substance.
F	155 ^{o}C	Insulation consists of materials or combinations of materials such as mica, fibre, asbestos, etc with suitable bonding, impregnation or coating substance as well as other materials or combinations of material.
H	180 ^{o}C	Insulation consists of materials or combinations of materials such as mica, fibre, asbestos, etc with suitable bonding, impregnation or coating substance such as appropriate silicone resins.
C	220 ^{o}C	Insulation consists of materials or combinations of materials such as mica, porcelain, glass quartz and asbestos without or with an inorganic binder.

Thus, the point of thermal limit and the importance of thermal design was appreciated in early designs which fostered a need for reliable data, formulae and tabulations related to the calculation of thermal parameters, particularly involving the convection of air for cooling purposes. Luke[16] provides a good and instructive example on the topic of the cooling of electric machines. Although an early work, it is of high quality, continues to be referenced in modern papers, and stands in sharp contrast to some papers which

contain merely a paucity of items to be canvassed by their readers. Much of the content is devoted to issues of heat transfer involving convective cooling as it may apply in electric machines. Air convective cooling has dominated the approach, and remains to this day, one of the most common forms of thermal management for industrial electric machines. For practical purposes it is an indispensible approach where small and mid-sized motors (i.e. under 10kW) are concerned, from handheld tools to small appliances and industrial motors it remains the most often found form of cooling. There are several places of interest inside the electric machine to apply air cooling or where localized air flow is of interest:

- Commutator (if so equipped),
- rotor and stator,
- inter-slot windings, end windings, end caps, and
- external frame.

Air flow may be by natural convection or fan forced. At about the same time as Luke, Ringland[17] produced a patent which illustrates a novel approach to the air cooling of an induction motor, notably the attention given to cooling the machine's internals such as the stator and rotor lamination iron by the application of air through internal passageways, item nos. 18, 19, 23, 24, 37^a, 37^b, the circulation of which is forced by a fan and deflectors, item nos. 56, 57, 61, which have been made an integral part of the machine design and construction itself as illustrated in Figure 2.1. Such techniques are still practiced to date.

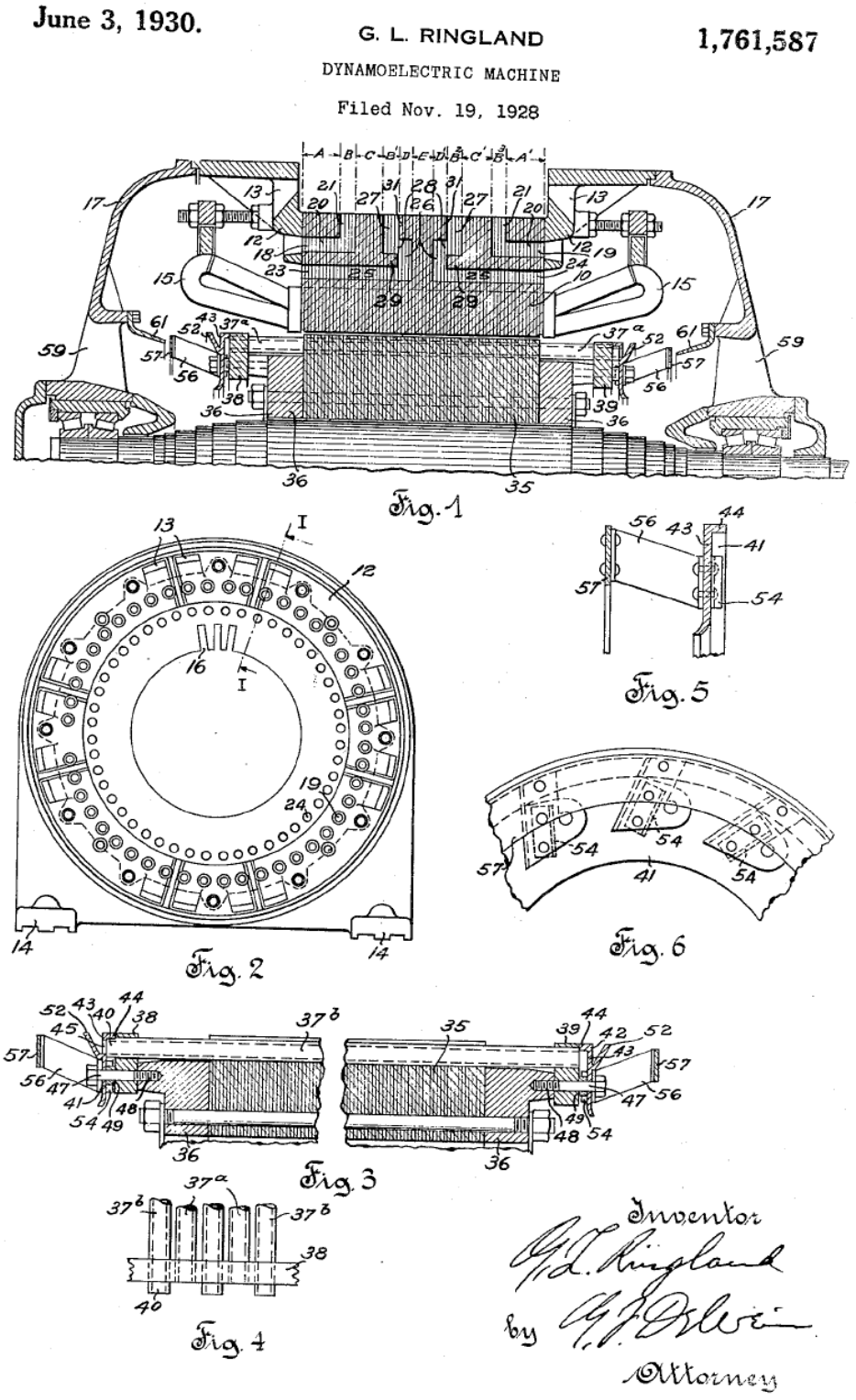

Figure 2.1. Ringland patent illustration showing various internal cooling passageways.

2.2.1 - Air Cooling Methods.

The effect of air cooling in all types of electric machines is well documented in the literature. Yoon et al.[18] reported extensively on the improvement in efficiency of an induction motor by ameliorating the cooling and other material factors. He showed clearly the reduction in motor efficiency with increasing coil winding temperature and consequently increasing coil winding losses. Experimental results were compared with theoretical calculations to support the findings. Although several improvements in air cooling method were considered, most to only marginal effect on performance, the authors make the conclusions that cooling to improve efficiency is more effective when applied directly to the coil windings and, liquid cooling is the preferred approach notwithstanding the recognized difficulties of handling liquid coolant.

One traditional approach of air cooling electric machines is the placement of the cooling fan on the rotating shaft of the machine. The difficulty with this approach is that as the machine is increasingly loaded and the rotational speed decreases, the losses increase while at the same time the performance of the cooling fan decreases, ie air flow is lost. This can quickly lead to rising temperatures and premature failure if the cooling requirement exceeds the capacity of the fan. The performance is opposed to the design. The literature has revealed that performance improvement by air cooling has been dominated by cooling techniques applied to the stator and its windings. Indeed, Pickering et al.[19] present the latter as the focus of their work in determining the heat transfer coefficient from the end winding of an induction motor. One can observe in their

findings how they are architecture dependent. There are few, if any, improvements reported for the rotor. The advent of computational fluid dynamics (CFD) has had an impact on the analysis of air flow within electric machines by way of example. Li[20] presented a detailed approach using CFD applied to the design of a centrifugal fan for a PM machine that improved the air flow through the machine, particularly about the windings, to effect improved cooling through a number of small design changes confirmed by experiment. In the analysis radiation heat transfer was ignored, a valid approach as convection would dominate and, the thermal driving potential for radiation heat transfer was small. Attention was focused on the rotor cooling where the significant axial temperature distribution of the rotor was noted on account of the low thermal conductivity of the lamination insulation, as was the high air flow velocity field over the rotor. Also noted was the limited improvement in heat transfer coefficient versus airflow increase on the rotor surface beyond a critical air flow rate. The latter finding is significant in as much as it demonstrates that which is well known with regard to convective cooling; there is a practical maximum effective limit beyond which the benefit is marginal. Kim et al.[21] present a similar approach in the application of CFD techniques to improve the air flow within a BLDC motor. Here again the authors pay careful attention to design detail to improve internal air flow characteristics around the inlet and between the windings. For example, their work illustrates the limited options to affect changes in the internal air flow of electric machines and, the importance of considering areas of flow separation and their impact on cooling performance. Flow separation, the departure of the working fluid from the surface of an object which may lead to localized flows, is a phenomenon which will seriously impact heat transfer where it occurs, i.e. it

can potentially eliminate it leading to localized areas of high temperature, commonly referred to as hot spots. Only CFD could reveal the existence of such subtleties and serves to underline the pitfalls of relying upon air cooling as a thermal management technique. Both Li and Kim tried to improve the air flow upon the coil windings, to effect their cooling. Naruta et al.[22] present a novel method of such by using a refrigerant near saturated vapour conditions to significant effect in an automotive air conditioning compressor driven via a BLDC motor. The effect is substantial due to the refrigerating capacity of the working fluid and not so much the volumetric flow rate or velocity of same as in the case when air is used as the working fluid. They note the challenges of automotive component cooling where the ambient air temperatures encountered are high by comparison to many other applications. The choice of cooling by refrigerant is logical in an automotive application due to its on-board availability and high cooling capacity.

Improvements to convective cooling of electric machines may also be realized by application of cooling techniques to the external surface of the motor. Dessouky et al.[23] present their findings for an SRM example. Here the authors alter the stator stack laminations to produce a lamination configuration which, when properly assembled, results in a periodic axial arrangement of annular exterior cooling fins as illustrated in figure 2.2. Arguably this is a further example of a direct lamination cooling technique discussed prior.

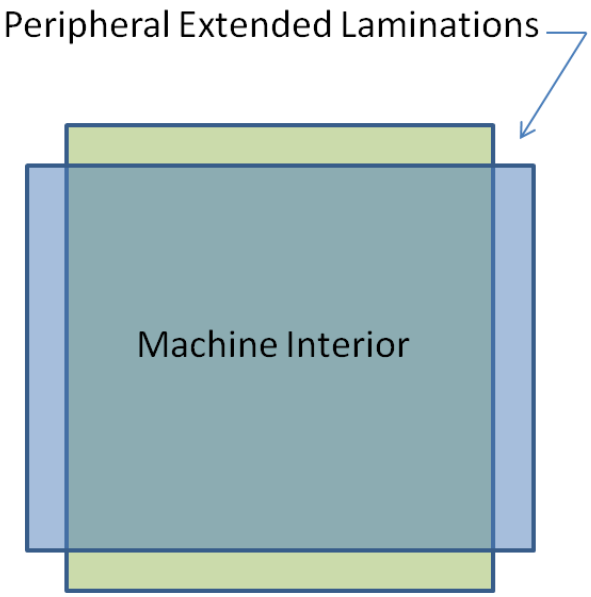

Figure 2.2. Dessouky's Extended Laminations

This method simply increases the exterior surface area to enhance convective cooling. The design modification increased the machine efficiency by 2%, or could allow an increase in its output power by about 6% for operation at the original rated temperature or, reduce the operating temperature about 10% for the same output power. Their result is significant in its simplicity and the resulting effect on cooling performance. This idea has been extended to liquid cooling, as will be discussed in section 2.2.2, and is important as it demonstrates the possibility of considering electric machine designs where the frame-stator interface can be eliminated in favour of a single piece stator with integrated cooling.

2.2.2 - Liquid Cooling Methods.

Significantly higher surface heat transfer coefficients can be achieved with liquid cooling when compared to air cooling, especially when a phase change of the working

fluid is adopted, as in the case of heat pipes. Where HEV and EV vehicles are concerned it is of particular importance and similarly challenging for several reasons. High output power densities are becoming more important. Electric machines specification requirements for EVs are now commonly found at up to 100kW of output power and further must be packaged within the confines of the automotive underhood space; that space itself is minimized for its purpose and contains within not only the electric machine but its associated power electronics, an ICE (in the case of HEV), power accessory systems and several heat exchangers, the heat discharge of which impinges upon all underhood components of which the electric machine is one. This results in high operating temperatures. Moreover, the operating window for heat rejection to the external ambient is narrow starting at around a 50°C minimum requirement for most manufacturers. Further, the electric machine operation should be sealed for best results as to the entrainment of dirt and debris that would result from air cooling internal components, something that is avoidable with sealed liquid cooling systems and would simply not be acceptable in the case of most electric machine technologies. There is generally a choice between two working fluids: a water-glycol mixture and oil, each with its own advantages and disadvantages. The latter, being non-conductive, could be said to me more user friendly in an electrical environment, particularly if the fluid is to make some contact with the winding surface, but has a very high temperature-viscosity dependence (inversely correlated) which has implications for circulation and the available heat transfer coefficient. Wenjuan et al.[24] has shown that circulation increases with increasing temperature in the case of an internally oil filled and cooled BLDC motor used for underwater purposes. Their design was a fully oil immersed machine rated at 8kW

and 3000 rpm. Although the temperature-viscosity behavior of oil as a working fluid would be favourable for the cooling of an electric machine, and their findings showed a substantial decline of viscous drag loss on the rotor at higher operating temperatures; but not expected to the degree sufficient to permit operation without substantial losses at rotational speeds of an order of magnitude higher as would be found with a high speed machine. That said, it should be noted that this approach does have the potential to provide significant rotor cooling. Huang et al.[25] has presented a more conventional approach using an oil coolant whereby the coolant is applied directly to the stator laminations. This was achieved by the creation of suitable slots in either the stator or the surrounding frame with the purpose of placing the coolant in direct lamination contact with the stator. This is as opposed to the even more conventional jacket cooler where coolant circulates within the external frame of the machine. Several slot configurations (height, width and shape) were studied, the performance of which were evaluated by a combination of CFD and thermal FEA techniques to determine the optimum slot configuration. Overall, by applying the coolant more directly to the heat generating source the authors were able to show an increase in the power density capability of the machine without undue effect on the magnetic field properties of the stator. In the case of jacket cooling, Ye et al.[26] provide a brief, but otherwise excellent study on this traditional approach, considering several different arrangements of coolant channels within an electric machine frame in an effort to determine the optimum cooling jacket channel arrangement. Again, the study is a CFD focused analysis which determined a circumferential arrangement as best for their purpose. Hsu et al.[27] have presented a similar type of approach in their patent which describes a cooling method involving

refrigerant flowed through the passageways as opposed to a water-glycol mixture. They extend the concept, allowing refrigerant to pool in the bottom of the machine (a sump) as part of the circulating pattern, to permit the liquid refrigerant to splash contact the rotor while in motion. No mention of level control was clearly given. Splash cooling has also been presented in the patent of Hernden et al.[28] where directed oil spray provides end winding cooling. They proposed an improvement upon the technique of spray cooling the machine end windings but this approach may still have potential maintenance problems.

More to direct laminate cooling (DLC) Baggu and Hess[29] applied DLC through several small circular coolant channels placed axially within the stator core itself as opposed to the surface approach of Huang et al.[30]. They have taken attention to the coolant channel placement so as not to have any effect on magnetic field performance. They completed their analysis through the application of a validated ten node LPTN model after that of Mellor et al.[31], with the appropriate cooling applied directly at the stator node. The model was solved using an electrical analogue approach with PSPICE™ software showing reduced temperatures of up to 25°C for the rotor. Advancing both this concept and that of Dessouky et al.[32], Festa et al.[33] present a most interesting arrangement of stator laminations with direct laminate cooling in a circumferential format for the purpose of cooling an electric traction machine. Essentially, they take the concept of Dessouky in a circular formation and enclose it within a traditional outer frame to then apply liquid cooling to the laminations which have been extended as cooling fins out toward the frame, thus creating internal passageways through which a liquid coolant may pass. The design, being highly integrated in function is truly avant garde. Xueli et al.[34]

present a combined cooling water and evaporative cooling method applied to a PM motor. Although their paper presents only a paucity of items to be canvassed by its reader, given the complete omission of results, other relevant information and scant conclusions, the concept presented is meritorious in its approach. Here the authors have considered the placement of periodically axially distributed slots within the full stator lamination radial dimension to include an evaporative coolant – water. The condensation of the water vapour is taken by the condenser which is placed as the traditional water jacket within the motor frame. Evaporative cooling is the most effective means to achieve high cooling densities and would be especially applicable in a high output electric motor however, their method requires the use of an inner sleeve at the stator ID to isolate the stator (contain the evaporative coolant within) from the rest of the motor. This would certainly have a detrimental effect upon performance as the magnetic field gap length is increased.

2.2.3 – Solid Cooling Methods.

Solid cooling methods involve the use of a thermally conductive material placed at some point within the machine. The material would have a thermal conductivity greatly exceeding that of any surrounding material, through which a heat flux could be effectively transmitted to some part of the periphery of the machine acting as a heat sink, which itself may be cooled by air or liquid methods previously discussed. That is the general idea, while more specifically such a material could be placed within the iron laminations themselves to aid in the conduction of heat from this region, especially where

a high speed machine was concerned. At the time this research commenced, the only article found in the literature which directly described an application of this principle was the Jarczynski[35] (GE) Patent, which has now expired. This patent clearly describes the solid cooling concept and proposes a copper sheet as the more thermally conductive material to be placed between one or more iron laminations of the stator; no mention is made of application to the machine stator. No mention is made of application to the machine's rotor. The patent makes several claims amongst which the thermally conductive material must be the same as that of the peripheral heat sink, i.e. copper to copper for instance, and must be in direct thermal contact with the heat sink. Moreover, notwithstanding the phraseology about any thermally conductive material being simply of a greater thermal conductivity than the surrounding iron laminations, the patent pointedly suggests this material be metallic, specifically copper or aluminum. It is further claimed that there exist operational machines where this method has been applied although no such examples have been found or subsequently reported on. No other reported research on this topic has been found in the peer reviewed literature. It is envisaged that the use of a metallic thermal conductor in proximity to the iron laminations would present an obvious problem with respect to the potential for the creation of electrical eddy currents within the thermal conductor, and consequently an increase in Joule loss and hence temperature thus rendering the approach of little to no value from a machine cooling perspective. The metallic conductor would have to be selected or so arranged as to minimize this feature i.e. by reducing or eliminating the electrical circuital paths. This would lead to reduction of the effectiveness of the thermally conductive material, a

possible reason for the lack of explanation of this technique to date evidenced from the lack of literature in this area.

A second patent, or rather a patent application publication by Hamer[36] (Remy Tech.), discovered near the end of the research study, follows a similar approach to that of Jarczynski, and may be related to the technique discussed herein, Chapter 4. However, the thermally conductive material is a composite whose composition is not entirely made clear in the patent description, nor the illustrations. The purpose is to enhance the cooling effect and lower the operating temperature of permanent magnet material contained within the stator of a DC machine.

2.3 – THERMAL ANALYSIS: Lumped Parameter, FEA and CFD.

The thermal analysis of electric machines can be undertaken via a lumped parameter (LP) approach where the thermal, dimensional and mass properties of a number of components of an electric machine can be aggregated or lumped into formulations of thermal resistance and thermal capacitance or complex impedance. These components often include, but are not necessarily limited to: the frame, stator, windings, rotor, shaft, bearings and machine end plates that house the bearings. Each of these thermal components is then connected into a lumped parameter thermal network (LPTN) where the mass components are modeled as thermal capacitance interconnected by thermal resistances representative of the heat flow paths. Internal losses are represented as heat rejection at certain designated nodes, and the boundary conditions are applied at other designated nodes. The boundary conditions can include such things as

convective losses from the internal components or the frame, a fixed temperature heat sink in the case of liquid cooling etc.. The boundary condition is often applied as a fixed thermal potential.

There are many approaches to the lumped parameter thermal model in the literature. These can range from a single node model as used by Crescimbini et al.[37] to over a hundred nodes as developed by Kylander[38] for the purpose of accurate and detailed representation of the heat flows within a machine. In most cases such detail is unnecessary. Different approaches are reported for the treatment of the more difficult parameters such as internal thermal contact resistance between components. Sooriyakumar et al.[39] proposes an analysis approach which is wholly dismissive of the conductive thermal resistances of the machine, concentrating on the contact resistances between components amongst others. This assumption is justified by the fact that the contact resistances are the dominant resistances in the network (typically by an order of magnitude) and are thus the greatest determinant of the resulting temperatures. This assumption simplifies the thermal network and is claimed to produce surprisingly good results; the calculated temperature results typically within 5% of the experimental test. Cezario et al.[40] simply lumps the contact resistance within the conductive resistance of a two node model and then seeks to tune the model for the result. Shoujun et al.[41] appear not to deal with the matter of contact resistance at all in their condensed eleven node model for the thermal analysis of an SRM motor-generator. Generally, the simpler the thermal model the more empirical data will be needed to solve it. Except for the most simple and idealized case, thermal contact resistance cannot be determined analytically

and at some point some empirical or usually experimental data is needed to complete the model or tune the model for the final result.

Simpler LPTN models with fewer nodes are often employed for microprocessor control applications where state variables may need to be estimated quickly by a simplified model. Duran and Fernandez[42] provide a good example of such an approach using a two node model to estimate rotor and stator temperatures. Again, such models are not analytic per se., but rather are heavily tuned for their purpose. The thing to keep in mind is that more nodes do not necessarily translate into more accuracy. The accuracy will be dependent upon what goes into the representation of the node and the representation of the thermal resistance between the nodes which is based upon the selection point of the node within the model of the actual physical system. It is possible with careful attention to node placement to produce a more accurate result than that which might be obtained through an arbitrary positioning at some location within the physical geometry of the system to be modeled. The selection of node number will depend on the purpose of the model, and the computational ability available since each node represents an equation to be solved. Nategh et al.[43] call attention to this point in their paper where they illustrate an optimized connection between a system of nodes representing a motor's coil slot winding, and a single node representing the motor's end winding. In other words they took attention to node placement to improve the results of their model.

The modern day thermal analysis of electric machines by lumped parameters has been well summarized by Mellor et al.[44]. They provide a key paper from which many others have subsequently referenced their work. Their approach to thermal analysis of

electric machines, specifically electric motors, provides a carefully detailed lumped parameter model applied to an induction motor. Their analysis considers both the radial and axial heat transfer within the machine parts which yields accurate results when compared to experimental data. Their results show that for a 75kW motor a good agreement to the order of 10% nominally, the worst results being for temperature estimates of the rotor.

Other work with LPTNs comparing results with those from FEA as has been carried out by Nategh et al.[45] (aforementioned) and Yang[46] to similar findings. Further, they have provided many detailed calculations of conductive resistances and several sources of useful correlations for the estimation of the convective boundary conditions. Contained within these papers is a sensitivity analysis which demonstrates the change in steady state temperature result versus a 20% change in heat transfer coefficient for some selected intermodal thermal resistances. The result would lead one to conclude that not all of the thermal resistances (as described in their approach) are of equal importance where the temperature result is concerned. Indeed, one could eliminate several of them and proceed to a satisfactory result. Moreover, the authors fail to consider a simple radial analysis versus the combined radial-axial analysis of their study and make comparison. Many others have recognized this. Among them, Boglietti et al.[47] completed the thermal analysis for an induction motor employing a seven node model with more than satisfactory results. They showed an agreement to within 5% of the estimated and experimental result. Specifically, they are able to demonstrate that for the typical geometry of electric motors the detailed axial calculation is not necessary, and to ignore it would only introduce an error of 2.5% or less. That is a satisfactory approach. Boglietti

further makes the point that when performing the LPTN network setup with knowledge of the individual thermal resistances, it is expedient to eliminate adjacent resistances in series or parallel where the relative differences are on the level of an order of magnitude. Mellor et al.[48] sensitivity analysis supports this conclusion. Other claimed successful thermal analysis has been carried out with low node count LPTNs. Szogyen[49] used a seven node network, several years prior to the work of Boglietti, but fails to report much in the way of temperature results, except for the temperature at one undisclosed node, although the agreement is approximately 5%. Lindstrom[50] used an eleven node network following the work of Kylander[51], being able to report some results where measurements were taken, that were in agreement by again, approximately 5%. In the case of Szogyen who performed his analysis on an induction motor, one might be tempted to draw general conclusions from the author's qualitative statement of the observations of heat flux direction from the calculated results. This would be a mistake as the heat flux within an electric machine is dependent upon the type and architecture of the machine. One cannot always say for instance, that the heat flux is from the end winding into the coil side windings through the stator slot, then to the stator. It may equally be a case of the reverse where the end windings act to cool heat being fluxed from the stator through the coil slots, to the coil side windings then to the end windings. It depends on the relative levels of the losses within the machine, as expressed at each node, the thermal conductivity of the materials forming the thermal resistances, and the geometry of the machine. Thus, there are generalizing assumptions that need to be assessed for each machine application, particularly when the machine is highly integrated within a system, for example an EV powertrain.

In recent years, with the advancements of computer hardware for greater program solution speeds, software for ease of user setup and enhanced display of results, there has been increased attention and work carried out in the area of thermal finite element analysis (FEA). At first appearance one might suspect that a thermal FEA is the ultimate answer to the problem of successfully predicting the temperature field within an electric machine. After all, the electric machine is of complex geometry, comprised of many components and materials, so obviously an advanced technique like FEA should lend itself well to the analysis. This is generally the case, except for a few complicating factors that also have to be resolved as in the case of LPTN analysis. These are:

- thermal contact resistances between internal components such as frame to stator, rotor to shaft, bearing to frame and so on,
- heat flux determination between the coil windings and the stator slot,
- the determination of convective coefficients and windage velocities and,
- the windage losses which may be important in higher speed machines.

Additionally, and perhaps most importantly, FEA of any type, be it thermal or fluid, involves a well determined geometry and extensive set up time, all known collectively as pre-processing. Where designs are not fully determined or at final completion, or boundary conditions are not well known for the geometry, FEA can be a time consuming task yielding results which may only be marginally better than that obtainable by a well thought out LPTN approach. The fact that the LPTN approach is still in use today, and is the approach used in some commercial software intended to include the thermal analysis of electric machines, speaks to this point. Either approach still requires the application of boundary conditions and, either approach, still requires the determination of some very

difficult parameters such as internal contact resistance. These simply can not be handled by a thermal FEA alone. Where the thermal FEA approach can make sense is in the solution of some of these. As mentioned earlier, Nategh et al.[52] made use of a combined approach. FEA was used to model the more difficult arrangement of the internal permanent magnet (PM) rotor and the coil side winding located within the stator slots. The latter was undertaken to develop an equivalent sub-system of LPTN explicitly for said coil side winding, and make a comparison to check results and performance of the LPTN by varying the nodes both axially and radially. They also develop a novel and original approach to considering the winding inside the slot as a number of radial elliptical layers containing therein the thermally conducting elements of the winding: copper, insulation, impregnation and contact to the stator slot as an air gap. Altogether they are able to develop a result for coil side winding temperature within the slot to within 5%, the worst being at the interior of the winding. Their result is strongly radially dependent and not strongly axially dependent, as one might expect. As mentioned previously, they optimize the connection of the end winding node to the LPTN nodal system representing the coil side winding. In the aggregate, their approach to the detailed model may not have a significant impact on the whole of thermal results for an entire electric machine, but is a capable one where details are required to predict hot spot results within the coil winding component. Compare the above approach to that of Idoughi et al.[53] where again, the FEA technique is applied to a component of the motor. The goal is to derive a representation of the coil side windings, only this time as an equivalent lumped material, the thermal performance of the lumped material being approached from the application of FEA technique to the coil winding material and impregnation material

within the slot to predict the temperature. The authors consider two different formulations of lumped winding and proceed to compare their thermal FEA results to define the best formulation. The result is the determination of an equivalent thermal conductivity vs. the copper winding material fill ratio, similar to the approach used by Kylander, and similarly in the early work of Soderberg[54]. The difference is the progression to an FEA model of the filled slot using the lumped material to predict the thermal performance of the material within the stator coil slot and then consider said material as a single node within a stator model. This stands in sharp contrast to Nategh who used thermal FEA to support the development of a LPTN of the stator coil slot material and then use this network as part of the entire motor LPTN network.

There are many other works in the area of thermal FEA. Song et. al.[55] considered a 3D FEA analysis applied to an entire induction entire motor but reported out thermal results for the stator and coil windings considering their transient dependency. Their results showed how the highest temperatures of the windings migrated over time to the end windings. Notwithstanding their use of FEA they approached the problem of the slot windings by lumping the entire winding of conductor and impregnation enveloped with insulation material, and presumably an air gap, in somewhat the same fashion originally as Kylander, and similarly from the earlier work of Soderberg cited prior. They do not elaborate on this approach but it is likely their use of commercial software precluded extending the FEA to the complexity of the windings so a lumped approach was necessary there. This would prevent any detailed result for the thermal field of the winding in the radial sense leaving only the axial result which they reported in detail.

Their treatment of the rotor to stator air gap is similarly simplifying. There, the authors resorted to a fixed thermal resistance. Cuiping et al.[56] takes these same approaches of lumping the windings, and a fixed thermal air gap between the rotor and stator when considering the analysis of a similar induction motor. Neither of these authors considers the effects of the changing thermal environment on the electromagnetic performance taking the internal losses to be constant over time. This would likely have an impact on the transient result of their analysis. Li et al.[57] approached the problem of heat transfer in the rotating air gap between rotor and stator of a high speed motor from the perspective of CFD. At higher speeds interactions in air flow between tooth slot and rotor become apparent. The flow in the air gap region transitions to turbulent at higher speeds and a circulation develops in the tooth slots. This effect is more developed for larger slots as might be encountered in an SRM. Heat transfer becomes enhanced. The result though showed only an improvement of 2°C over the simplified approach of considering the rotating air gap as smooth and the slot air as stationary. In some formulations with many stator slots the slot air would be ignored as treated by Kylander and Lindstrom. That is a satisfactory approach where induction or other high slot count motors are concerned. Srinivas and Arumugam[58] have examined the large slot effects of the SRM stator and rotor through applied CFD applied to determine the flow field within same. Traditionally, the approach would have been to simply dismiss such effects. It should be reiterated that CFD is used to determine the flow field and not the heat transfer coefficient directly, although the latter is dependent upon knowledge of the former. The heat transfer coefficients are still calculated in all the literature by means of what are now classical formulations. It is only the air velocities which are now better known and

predicted through the application of this CFD analysis. Furthermore, it is not clear that the classical formulations to determine convection coefficients can be applied to any greater effect in this fashion. Srinivas and Arumugam take this approach and then apply the result for the convective heat transfer coefficients as the boundary conditions to the thermal FEA. What is surprising is their dismissal of the motor core lamination insulation material, in their case comprising 10% of the motor length, for their analysis. In terms of the application of CFD to achieve accurate results where convective heat transfer is present, then to neglect the lamination insulation where conductive heat transfer is present is puzzling, and no sufficient justification is given for this approach. The authors then progress to consider both the transient and steady-state thermal performance of their SRM where they have fully taken into account the significant iron-core losses of the SRM into their analysis. The transient performance is notable in as much as the authors consider an applied variable load, not unlike that as might be found in an automobile drive cycle. Notwithstanding the variable loading over time, the motor temperature continues to climb in their scenario. Faiz et al.[59] present a comprehensive, although at times difficult to follow, thermal analysis of an SRM following the Mellor et al.[60] model with a fifteen node LPTN, then considering steady-state and transient operation as did Srinivas and Arumugam. In the fashion of the latter authors they make careful attention to the details of the heat transfer about the stator and rotor poles. The design of their motor is not clear as few geometric details were given, nor were any with regard to the choice of boundary conditions other than tabulated final results of all thermal resistance calculations. Of particular note was their choice to treat the stator slots as entirely of copper, thus ignoring any insulation or impregnation material. Much of the

complexity of the analysis could have been avoided as later works in the field follow the approach of a lower node count LPTN, discarding the axial heat transfer in favour of a radial model with only the end boundary conditions.

A few papers have made direct comparisons between the LPTN approach results and those obtained from the application of thermal FEA to the entire motor structure. The latter is often avoided until a stable design is known and more accurate results are required as the set-up and computational time can be significant. Fan et al.[61] makes a comparison for a 60kW PM type synchronous liquid cooled motor for automotive application. The authors use a ten node LPTN to represent their motor following the Mellor and Turner approach discussed earlier. The author's make the assumption that for their machine they can ignore the losses attributable to the heat generation within the air-gap, ie windage losses. Further, they chose to ignore the thermal effects on material properties and the heat transfer coefficient at the boundary surfaces in the case of the thermal FEM. Perhaps this was done to simplify the result or maybe thought unimportant but the latter is a significant oversight as their result will show. That result being a stator core temperature prediction of 30°C greater by the FEM vs. the LPTN method where it (convective cooling) appears, although not clearly enough in their illustrations that convective cooling was applied at several locations in the case of the LPTN model. The author's attribute the difference to possibly either the effects of anisotropic material properties or, the number of nodes selected for the LPTN. However, prior work aforementioned has already indicated the successful application of the LPTN technique with fewer nodes than ten to the effect of satisfactory results. The remaining findings for

temperatures of the coil sides, end windings and permanent magnets as predicted by FEM are greater by within 5% to 10% than that predicted by LPTN, the highest being on the permanent magnets. In other words all the LPTN predictions were running cooler. That might be expected where the convective heat transfer coefficients at the boundaries were simply ignored in the FEM work. The remaining results presented by the authors are a trivial finding of motor temperature dependence upon coolant flow rate and the not so trivial finding of motor temperature dependence upon the equivalent air gap used to represent the thermal contact resistance between the rotor and stator. The latter result, presented as a sensitivity analysis, demonstrates the importance of this effect in electrical machines, in their case resulting in a temperature rise of around 20%, or between 10°C and 20°C, for the components considered over an air gap range of .01 to .05 mm, the range fully covering that of Staton et al.[62]. A meaningful result save and except for the fact that the author's fail to disclose the value for this parameter that they selected for inclusion in their own analysis. In short, a well intentioned study, but unfortunately one containing within significant oversights.

A second work of Nategh et al.[63], one more carefully considered than the foregoing, compared the results of thermal FEA to a fifteen node LPTN for a motor rotor containing multiple layers of internal PM material. In this case the application of FEA to this part of the motor may be justified on the basis of the need for accuracy where a PM material's thermal sensitivity is concerned, specifically so as not to exceed the temperature limit that would result in their demagnetization. Here again, as in their prior work, Nategh considers the application of thermal FEA to a detailed part of the motor, same for the LPTN model, and compares their results for both the detailed analysis of the

rotor, and the analysis considering the entire motor. What is interesting is the author's consideration of both LPTN in two dimensions: axial and radial vs. one dimension only: radial where the rotor analysis is concerned to determine the magnet temperatures. Their results support the earlier claim that the LPTN approach, when undertaken with care, can perform to a level comparable to that of a thermal FEA analysis. For the case where there was no water flowing in the external water jacket, the overall two dimensional LPTN result is in agreement with that of the thermal FEA to within 0.3°C, a remarkable achievement. The radial LPTN produced an overall result to within 1°C of that of the thermal FEA, again, excellent agreement. Even better results were obtained for the case where water was flowing in the external jacket as the radial temperature difference overall for the motor is less during the application of external cooling. Results for the remaining parts of the motor, in both cases, showed a good agreement to within 2°C. What can not be revealed by the LPTN is the isotherms within the rotor, but that is not required as the PM temperatures were correctly predicted. In any event, the result is clear: A well constructed and considered LPTN can be used to support the thermal analysis of electric machines, producing accurate results, where time if of the essence.

So far we have seen that the application of thermal FEA has been used to successfully deal with the challenges of the thermal characteristics of the motor winding. Two approaches as reported in the literature have been examined. The difficulties with either approach continue to rest with the boundary conditions and thermal contact resistances of the inner components. Staton et al.[64] and Boglietti et al.[65] have provided other comprehensive works to address these issues. Much of their content was collected

from other earlier works. Here they deal with the complexity of contact thermal resistance, such as between stator and frame, being expressed as an air gap equivalent size, a common approach. There is no analytical approach, and the author's express the findings in tabular form for some common materials and motor sizes. So far, the only known way to deal with this problem that has been reported in the literature is through some kind of experimental determination and its empirical result. They deal with the coil winding in the same fashion presenting a thermal conductivity vs. a filling factor for the stator slot space, in other words as a lumped material. They do however describe a layered winding method, somewhat like that used by Nategh[66], and which has been applied in a commercial software package for the thermal analysis of electric machines. The authors provide substantial correlations for the purpose of evaluating heat transfer from internal and external machine surfaces: frame to ambient air, end cap air, air gap and bearing, for different motor configurations and power ratings. There are some difficulties with these works. For example, in the case of end cap air, so many correlations are presented that one can only conclude that there does not exist an overall governing relationship for the heat transfer in this region, probably because this area is highly nonstandard in electric machines. Further, the authors present some updated correlations in later works but fail to specify if these are improvements upon same correlations presented in earlier works. This can lead to confusion and doubt on the part of the reader as to which may be preferred in a particular analysis of an electric machine. In short, such a review may serve as a good starting point but to be sure other authors have provided methods suggesting that the application of blanket correlations should be taken with some care in the course of thermal analysis.

2.4 - CONCLUSIONS

From the literature review and discussion of same several conclusions may be drawn, amongst which are:

- The thermal management, or cooling, of electric machines has been of interest for nearly a hundred years. Although there has been much refinement and analysis of conventional methods (convective air, water jacket), there has been little progress in the development of advanced methods for electric machine cooling, particularly in the case of deep internal cooling. Nor is there a standardized method of reporting the cooling performance or efficiency across the many varieties of machines such being their size, construction, type, power density and so on. Comparisons in this regard between works are either very difficult or simply impossible.

- The cooling of electric machines has been dominated by air convective cooling, which may be adequate for small and mid size machines such as those found in appliances and commercial use but on the whole is inadequate for a high speed, high power density machine nor an automotive application. Open, shaft driven air cooling being a perfect example of a design completely opposed to the requirements.

- The liquid cooling of electric machines certainly exists where necessary, is highly effective, and when used, is often confined to an external jacket style application. There has been some work reported for the purpose of improving coolant passageway arrangements or designs that would thus improve upon thermal performance. Water, water glycol mixtures, or oil are the most commonly encountered working fluids. Oil has been used to cool the rotor directly but this approach would likely be precluded in a high speed machine.

- Advanced methods of direct laminate or back iron cooling do exist, taking one of three forms: Simple contact of coolant upon the outer stator surface, extension of the stator laminate material to enhance air convection or liquid cooling, or the placement of internal coolant passageways within the stator so as not to impact upon the electromagnetic performance of the machine. The latter method has not been reported in the literature for use in a switched reluctance machine.

- There is little reported in the literature with regard to direct cooling of the rotor by internal cooling enhancement, other than by that of simple air passageways or extension of rotor conductors to air convective cooling in the case of induction machines. Splash methods have been reported where oil and refrigerant cooling might be used, which might be employable in a high speed machine for an automotive application. One example exists of complete immersion in oil for a highly specialized application but this would be totally suitable for a high speed machine.

- Thermal analysis forms a significant part of the work where thermal management of electric machines is concerned. Of the two approaches, the classic LPTN model dominates, for its simplicity, relatively high accuracy (as compared to FEA approach) and quick computational time. FEA methods are well used, particularly in commercial software where the machine architectures are well known and rigid. The best application of the FEA method has been to solve particular areas of concern for heat transfer where complex geometry and structure exists, as in the case of the machine windings, and a precise answer is required. CFD methods have also been of use in realizing a better understanding of coolant flow fields and local velocities for the purpose of their application to calculating the localized heat transfer coefficients within electric machines.

- The ongoing development of hybrid and electric vehicles will require improved and advanced cooling methods be applied to their electric motive machines in future applications where automotive performance, underhood packaging space limitations and the environmental ambient temperature demand the employment of said methods.

CHAPTER 3 - THE SWITCHED RELUCTANCE MACHINE

3.1 – OVERVIEW

The switched reluctance machine, its principles of operation and design, are compared and summarized. For the purpose of establishing the current background as regards the switched reluctance machine (SRM), its principles of operation, design configurations, design process and existing machines, a brief literature review was conducted with benchmarking of machines in the intermediate power range, defined here as 25Kw to 100Kw range. Much of the coverage of principles of operation and design are single sourced from Krishnan[67] with the balance of material from journal publications.

3.2 - INTRODUCTION

There are, in terms of electric machines, two broad classifications: Direct Current (DC) and Alternating Current (AC). The latter includes the well known Tesla induction motor, in use for over a century, commonly found in household and industrial applications across all size ranges. Within the DC machines, three sub classifications: DC series/parallel, brushed or brushless, DC Permanent Magnet (PM), synchronous or asynchronous, and Switched Reluctance (SR). The SRM has been known for over a century but has only recently begun to see use in the higher power applications of vehicle propulsion, wind turbine generation and turbine starter-generator sets. Switched reluctance machines (SRMs) are increasingly a technology of interest for variable speed

drives which may be found in automotive and industrial process applications. It is directly related to the basic form of DC machine in that it contains the familiar field coil windings and poles, the former, usually upon the stator, however, it lacks any rotor windings, having instead a series of movable iron poles only, which may be arranged for linear or rotary operation. In this case it is known as a double salient pole machine. This

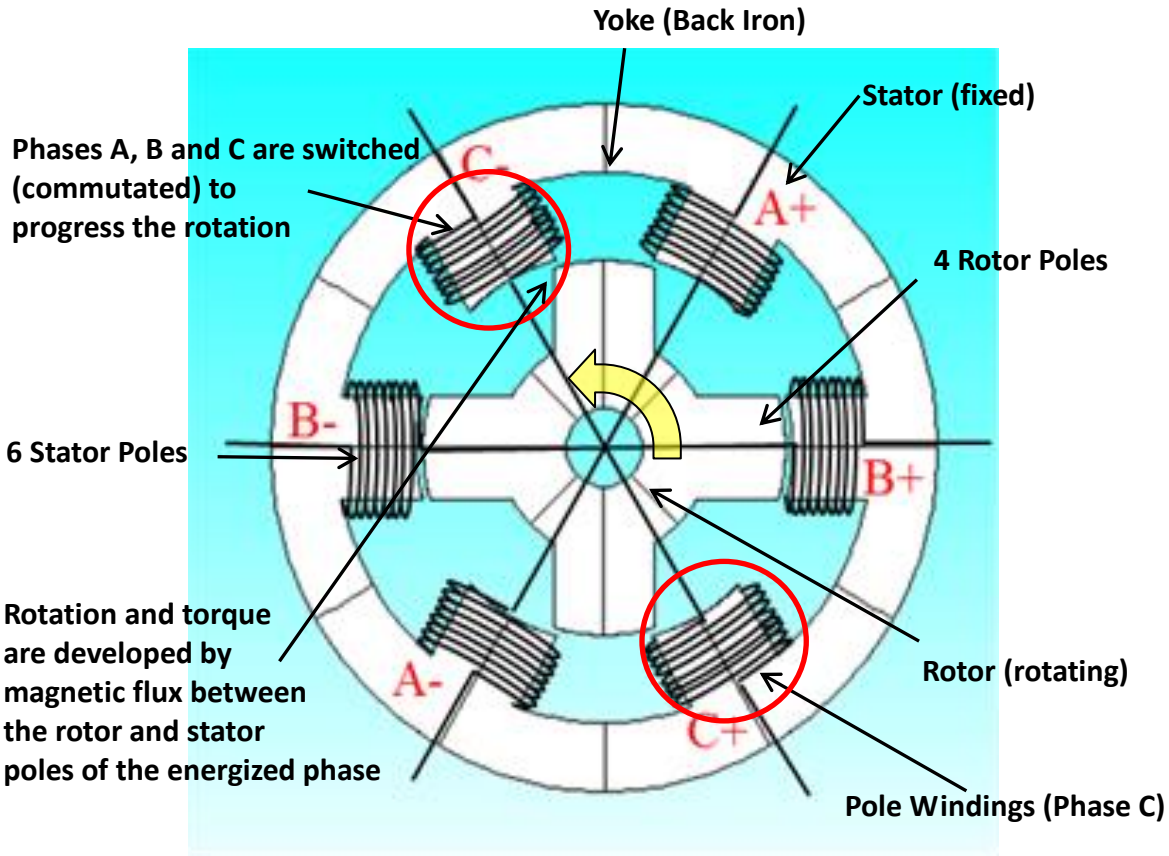

Figure 3.1. A typical 6-4 SRM Geometry showing machine parts.

simplicity in the rotor provides for high speed operation as there are no magnets, nor windings to be concerned about, at least as those items are concerned. Other issues of

high speed operation remain. Notwithstanding, it has many advantages, some of which are: Reliability of operation, inexpensive and simple construction, high efficiency and high speed. The lattermost lend themselves well to both mass production and automotive application. The downside, to be discussed briefly, is an undesirable noise, vibration and harshness (NVH) characteristic due to its architecture, the arrangement of its stator and rotor poles, and a fundamental principle of its operation being the minimization of reluctance along the magnetic circuit path providing mechanical rotation. A schematic cross section of a typical SRM may be found in figure 3.1. The principle of operation is straightforward, unlike that of the AC induction machine. That said, the SRM is a highly non-linear machine. Consider that a pole winding may be represented classically as a DC resistance (R) in series with an ideal inductance (L). The voltage developed across this circuit may be expressed as:

$$V = iR + d\psi/dt \qquad (3.1)$$

Where i represents the current; R the resistance and $d\psi/dt$ the change in magnetic field flux linkage through the pole over time. Taking ψ as the product of L and i and substituting:

$$V = iR + d(Li)/dt \qquad (3.2)$$

If the inductance was static, i.e. does not change over time, as is the case with a transformer, then 3.2 reduces to the more familiar form:

$$V = iR + i(dL/dt) \qquad (3.3)$$

But, in the case of the SRM, a component of the magnetic core flux linkage is in rotation. Accordingly, V is dependent upon both the change in current and inductance over time:

$$V = iR + i(dL/dt) + L(di/dt) \quad (3.4)$$

From the above equation the component dL/dt is directly related to the position and angular velocity (ω) of the rotor. The inductance will be at a maximum when the rotor and stator teeth are in full rotational alignment, and at a minimum when the rotor and stator teeth are in the fully unaligned position, i.e. between each other. This may be illustrated in the following graph of figure 3.2.

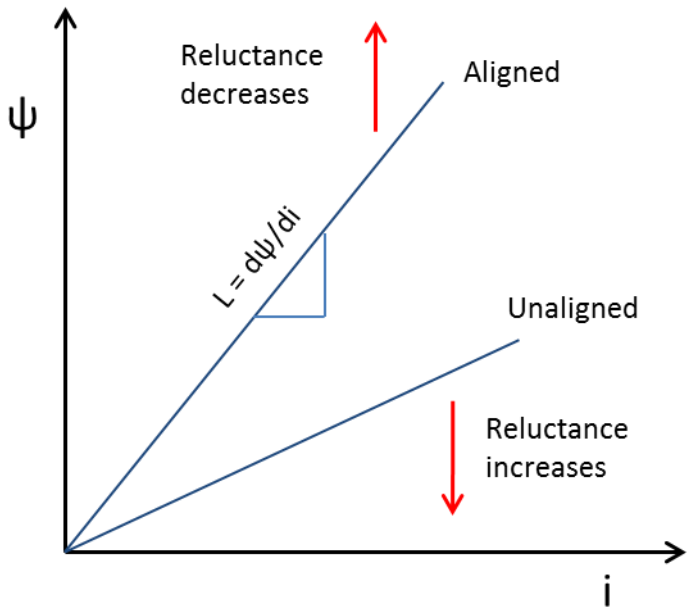

Figure 3.2. Pole flux (ψ) vs. current (i) dependency upon rotor stator tooth alignment

3a.3 – DISCUSSION

3.3.1 - Principles of SRM Operation.

Building on the foregoing, the real question is: what makes it go? Fortunately the principles of SRM operation are quite simple. A schematic cross section of a 6-4 SRM for reference in the discussion is shown in figure 3.3. Each pair of stator poles comprises a field winding which, when energized, creates a magnetic flux in the stator poles and their back iron, completed through the rotor iron circuit (rotor poles and back iron). Since the magnetic field seeks the path of least magnetic reluctance, or the lowest potential energy of the system, a torque is imposed upon the movable rotor bringing its poles into alignment with those of the stator, see figure 3.3 showing this for one field winding phase. The rotor moves from the high reluctance position to a lower reluctance position and in so doing develops a reluctance torque if prevented from doing so. Prior to complete alignment of the poles, the field winding is de-energized and the next adjacent field winding energized providing additional torque to advance the rotor poles to the next set of energized stator poles, and so on. Thus, a rotary motion of the rotor is created with the supply of available torque provided by the rotating magnetic circuit as each set of field windings is switched on-off, hence the name “switched reluctance”. Returning to figure 3.2 there are any number of possible paths to progress from the un-aligned to the aligned position. This may be accomplished by a path of either constant current or constant flux as illustrated figure 3.4. Since the latter results in the greatest potential energy change within the machine, it is the preferred method. Most machines

are driven by a constant voltage, i.e. DC supply, derived from a battery or rectified AC supply.

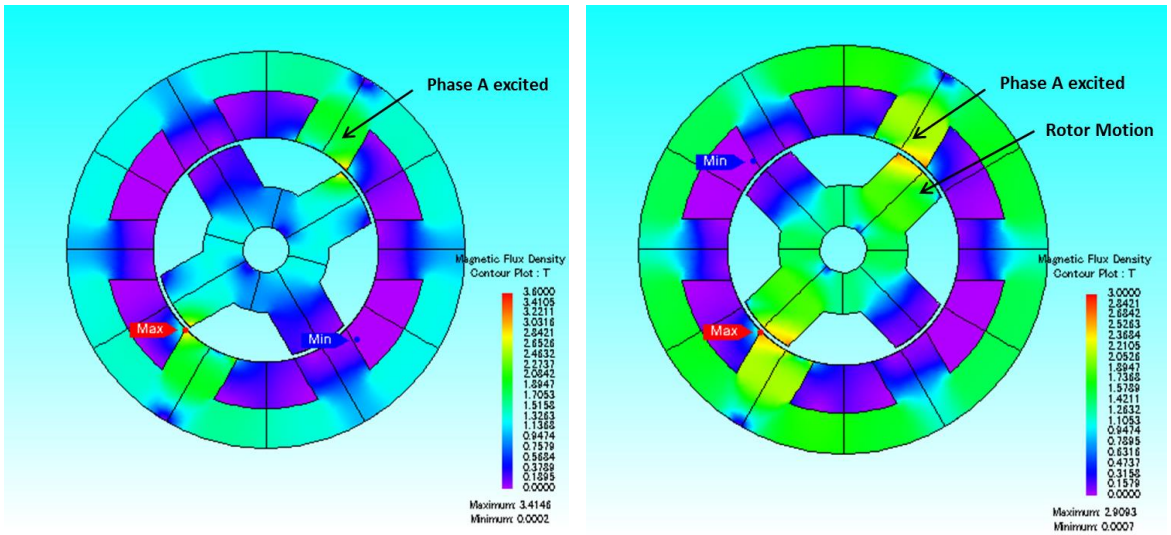

(a) SRM in High Reluctance position

(b) SRM in Low Reluctance position (prior to phase commutation)

Figure 3.3. Rotor position versus SRM state of reluctance of the magnetic flux path.

This constant voltage may then be switched and otherwise modified by means of a power electronics converter and control device to realize a constant current source supplied to the machine's windings. Alternatively, if the machine is driven by a constant voltage source which does not provide a constant current as described above, an "over-modulated supply", then the current must rise to a constant value during a short transient period while the rotor gains motion. The net result is a loss of torque from the machine.

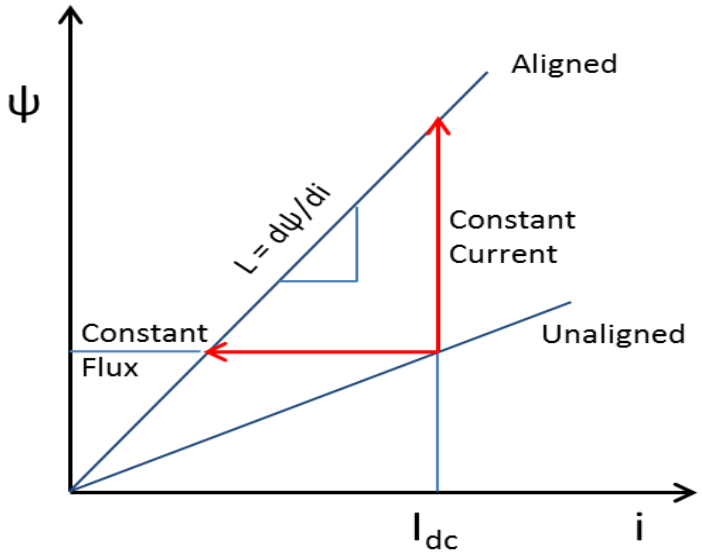

Figure 3.4. Transition to aligned position by constant current or constant flux at the pole

The conventional machine may be driven in this fashion by the asymmetric converter shown in figure 3.5 which is connected to a fixed DC supply voltage. These are the main drive elements for the switched reluctance drive system. S1 through S6 represent power electronic devices such as MOSFET or IGBT switches. D1 through D6 represent freewheeling diodes. The inductors A+A-, B+B- and C+C- represent the phase windings of the machine as depicted in figure 3.1. The status is shown for commutation state S1 and S2 closed with phase A energized. Commutation progresses next to S3 and S4 closed phase B energized, then finally to S5, S6 closed phase C energized whereupon the cycle is repeated. Again, this provides the rotary motion described foregoing. As each commutation takes place the energy stored in the phase coil is returned to the power supply by means of the freewheeling diodes which will continue to do so until they no longer remain in a forward biased state.

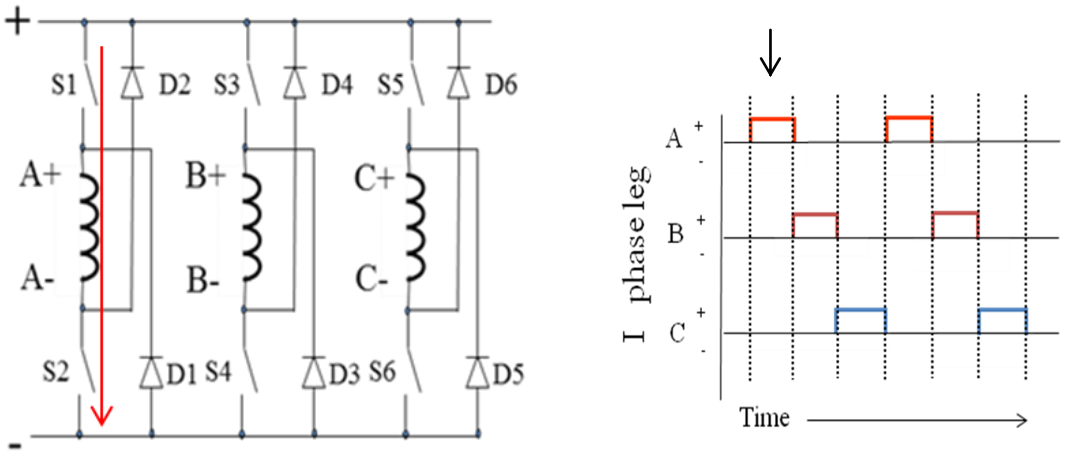

(a) Asymmetric converter (b) Timing and Phase Current (ideal)

Figure 3.5. SRM converter with phase current and timing - phase A position

This action is automatic. The commutation may progress in either direction A,B,C or C,A,B depending upon the switch control. Moreover, in actual SR operation, the timing of commutation and its dwell, i.e. the time duration of the "on" state of the switches, may be optimized to produce a maximum torque from the machine. This is a delicate process. A simple timing operation will have the commutation start at 15° (mechanical) rotor angle then progress for 30° (mechanical) of rotor rotation before next commutation.

It should be noted that the SR operation is reversible, with a small energizing field and a supplied torque input, the SRM will operate as a generator providing electric power to the field coils. This makes it particularly useful for applications where a starter generator is required, such as found in turbine engines and hybrid electric vehicles. Other advantages, this motor is capable of operating with one field winding open giving it a high reliability, again, useful in critical applications. Further, the simplicity of this design is lower cost afforded by its construction and fewer components. However, this is offset

by the need for a power control electronics device for efficient torque and speed control; high efficiencies, over 90%, are attainable with such a device. The disadvantage to this motor's architecture are torque pulsation, noise and vibration which arise from the magnetic forces acting upon the stator poles as the rotor poles are brought into alignment with them. The forces create not only torque impulses but more importantly distortion of the back iron which can lead to serious vibration in the machine when the electrical excitation frequencies reside near the natural frequencies of the mechanical structure.

3.3.2 - Design of an SRM.

The design of an SRM is related to that of a DC machine with separate field excitation. Krishnan[68] provides the following useful governing formulas:

$$P_d = k_e\, k_d\, k_1\, k_2 B A_s D^2 L N_r \qquad (3.5)$$

where: k_e is the machine efficiency, k_d is the duty cycle, k_1 k_2 are machine constants, B is the aligned flux density maximum, A_s is the electrical loading given below in (3.6), D is the bore diameter (at the air gap), L is the iron laminations length, and N_r is the rotor speed.

$$A_s = 2T_{ph} im/\pi D \qquad (3.6)$$

where: T_{ph} is the total number of turns per phase (ie per pole pair), i is the peak phase current, and m is the number of phases conducting at the same time. The latter value is "one" for a 6-4 machine and "two" for a 12-8 machine.

Thus, for a desired power output at the shaft, "P_d" at a rated speed, "N_r" and with knowledge of the machine constants, flux density of the magnetic material, electrical loading to be applied, and ratio of length to bore diameter, the L/D ratio, the bore diameter *"D"* may be determined. When combined with the electrical loading the physical parameters for the coil may be determined, ie overall winding size, no. of turns, and the wire size for the current required of the desired electrical loading to be applied. There are, of course, many other relationships which come into play but equations 3.5 and 3.6 govern the process. The design approach above starts by a determination of bore size from which all other machine dimensions follow, at the extremes frame outer diameter and length. In theory, if there is no limitation on the physical size any design is possible. However, this is not the case in practice where there will be limits to the outer physical dimensions. This then will lead to a maximum constraint on the electrical loading which can be physically placed within the confines of the motor given the number of turns of winding and the current handling capacity of the wire size. Thus, the design becomes a balance between mechanical power and electrical loading for a given space constraint. Further, the electrical loading leads to heat rejection from the coil's resistance and the iron material due to eddy current and hysteresis losses. This adds yet another constraint: a limit on the electrical loading within the space constraint and now within the thermal operating limit of the materials of the machine, given their thermal loading which is governed by the space constraint.

From this it follows that improvement in machine design as it relates to cooling and thermal management is key to achieving a high power output within the constraint of a small space as the higher electrical loading required will lead to higher levels of heat

rejection within the machine. This is true of electric machines in general which has led to any number of applied methods for their thermal management, several of which were reviewed with the literature review of said topic.

3.3.3 - SRMs in the Literature.

This section covers a benchmark review of several SRMs developed by researchers and reported in the literature. A summarization table follows. The first six motors listed in table 3.1 have been discussed with regard to their thermal management in the literature review of that section. By far the most common configuration is the 6-4 where Gallegos-Lopez et al.[74] in their study of Switched Reluctance Generators (SRGs), #11 in table 1, cited this configuration as being the best balance between efficiency and robustness of design. They observe that the core losses are proportional to the number of strokes per revolution squared, of which the 6-4 3Ø machine has 12, and the number of power devices increases with increasing poles. The number of poles however has implications for machine dynamics and consequently noise. Gallegos-Lopez et. al. considered five machine designs in their study and drew some conclusions: For a given power and fixed outer diameter, lower speed machines have a higher length to diameter ratio (L/D) which reduced specific torque and power, ie. per Kg weight, whilst conversely had higher efficiencies due to lower core and windage losses. High speed machines place a limit on the available outer diameter as a direct result of the centrifugal forces acting upon the rotor which in turn confines the available space for windings

Table 3.1. Summarization of SRM review reported from the literature.

No.	Author Journal + Date [ref.] Institution	Electrical Characteristics Motor Configuration Application	Power (kW)	Volts DC	Amps/ph Turns/ph Amp/mm²	Laminations Thickness Sat. Density	Air gap	Slot fill %	Mechanical Characteristics Torque(N-m) Peak	Power(kW) Peak	Speed(rpm) Overspeed	Bore Ø Length L/Bore	Efficiency	Cooling	Ins. Class	Weight P/W (k-W/kG)	Noise (db)	Comments
1	Srinivas K. N. et al. IEEE 2005 [58] Crescent Eng. College	6-4									3000			Air				CFD study motor for thermal analysis
2	Dessouky Y.G. et al. IEE 1998 [23] Heriot-Watt Univ.	8-6	0.104				0.25				2000	65 47.5 0.73	35.1	Air	B			Enhanced convective cooling Square form back iron
3	Shoujun S. et al. IEEE 2009 [41] Tech. Univ. of Berlin	6-4 Starter Gen	30 g	270	250 (15Krpm)				15 max m	?	27000 m 50000 g	80		Water				Turbine starter generator More/All
4	Ferreira C. A. et. al. IEEE 1995 [69] Sundstrand Aerospace	6-4 Starter Gen	30 g	270	2V49FeCo	0.15			10 ft-lb m	12.68 m	26000 m 52000 g	64		Oil 11.7l/m		7.71		Turbine starter generator Same as above
5	MacMinn S. R., Jones W.D. IEEE 1989 [70] GE Corp. R&D	6-4 Starter Gen	32 g	105	FeCo V (Permendur)				10 ft-lb m	17 hp m	26000 m 50000 g	84	80	Oil				Turbine starter generator Same as above
6	Faiz J. et. al. EM&PS 1998 [59] Univ. of Tabriz	6-5 2x salient (ie 12-10)			444	0.356					4	100 est 108/114		Air TEFC				Thermal analysis study motor
7	Qionghua Z. et. al. IEEE 2003 [71] Huazhong Univ. Sci.&Tech.	8-6 HEV	56.9	336	163 (360pk)	DW310-0.35	0.65		232 478	50.1 100	2050 4500	280	88.5	Air Natl. Conv.	H	108 1	72.5	Noise is at no load condition 2000 RPM
8	Rahman K. M. et. al. IEEE 2002 [72] General Motors Resch.	24-16 (6-4 x 4) EV		350	125 (250pk) 9 (18.5pk)	d Low Si Steel		62.5	350 700	50	900 1400?		90*	Water	H			Water jacket and internal cooling tubes *Claimed in paper taken from efficiency map Max power estimated from charts
9	Uematsu T., Wallace R.S. IEEE 1995 [73] Toyoda Auto. Loom Works	6-4 EV		312	400 (pk) 16?	Low Si. M19 20 26 gage	0.56		130	89.5	7700 10000	131.3 92 0.7	95.1 est.	Oil (end winding)		43 est. 2.1		
10	Uematsu T., Wallace R.S. "	6-4 EV		312	400 (pk) 16?	V Permendur 20 26 gage ?	0.56		165	102	7400 10000	131.3 92 0.7	96.5 est	Oil (end winding)		45 est. 2.3		
11a	Gallegos-Lopez G. et. al. SAE 2002 [74] Delphi Automotive Sys.	6-4 Generator I HEV	300 g	600	580 (1000pk) 5 13.3	AISI 4340 1.2 Tesla	0.4	35		820 g	100000	76 200 2.6	41 est.			22.6		Design Study
11b	" "	6-4 Generator II HEV	300 g	600	510 (900pk) 7 16.5	AISI 4130 1.2 Tesla	0.4	35		530 g	60000	76 250 3.3	64 est.			27.9		Design Study
11c	" "	6-4 Generator III HEV	300 g	600	465 (800pk) 8 17.1	AISI M-15 1.4 Tesla	0.4	35		366 g	30000	76 370 4.9	92 est.			40		Design Study
11d	" "	6-4 Generator IV HEV	300 g	600	417 (700pk) 10 5.8	AISI M-15 1.4 Tesla	0.4	35		367 g	30000	136.8 165 1.2	92 est.			61.2		Design Study
11e	" "	6-4 Generator V HEV	100 g	600	200 (345pk) 14 13.1	AISI 4340 1.2 Tesla	0.4	35		319 g	100000	76 76 1	36 est.			9.1		Design Study
12	Mueller M. A. IEEE 2005 [75] Univ. of Edinburgh	12-16 Generator Low speed wind turb.	20 g		36.8 (full load) 130				1723 (full load)		115	650 350 0.54	87.8					Current 36.8A is time averaged. 85A peak.
13	Sun T., et al. IEEE 2007 [76] Hanyang University	6-4 Segmented Rotor Toroidal Winding		100	16 (comment) 120		0.3		5 (chart) 5.4 (chart)	1	2000	71.6 97 1.35	80 (chart)					SSRM - Segmented SRM Amps at rated speed from chart
14	Lee J. Y. et. al. IEEE 2005 [77], [92] Changwon National University	6-4 Toroidal	1.259	55	22.9		0.3		4.86	1 2.6 (100V in)	2000	71.6 97 1.35	80.75					Conventional Rotor Toroidal SRM
15	Fairall, E. Unpublished Thesis McMaster University (CERC)	12-8	200		123 21		0.8	55		175 350	22000	221.6		Water				Water jacket with end winding cooling

69 70 71 72 73 74 75 76 77

resulting in higher current densities, and consequently losses which has implications for cooling. Reduced turns per pole are favourable by increasing rated speed. Increasing machine length has rotordynamic implications for lubrication and vibration which will place a practical limit on these. If achieving higher speeds requires higher strength lamination material, this may come with reduced magnetic properties and consequently lower efficiency. All of the aforementioned conclusions are supported by equations (3.5) and (3.6) and, in fact, could be drawn from said equations without performing an extensive study. The final design direction suggested would be to design a machine as large in outer diameter as the space and strength of laminate material selected allows given the operating speed required, for efficiency, cost and cooling, although this will come with a sacrifice to specific power and torque. The final design realized will be dependent upon which parameters the designer values most such as, weight, cost, torque, speed, efficiency, NVH for example, and will be application specific.

In the case of automotive applications, where a high value is placed on optimizing all the aforementioned parameters Rahman et al.[72], machine #8 in table 3.1, have performed a high efficiency SRM design intended for vehicle propulsion with special attention to torque and NVH issues which, to date, have challenged SRM design for use in passenger vehicles. Notwithstanding the latter, they have noted improved results and high power density for the SRM when compared to the induction motor. In EV applications, low weight is paramount, so consequently, high torque, high power densities and high efficiency are required. They achieve these through the use of low silicon lamination steel having a high saturation flux density *"B"*, the impact of which on developed power can be observed by referring back to equation (3.5). It is not as

effective a method as increasing the outer diameter which is precluded by the need for high power and torque densities. Torque overload at low speeds was achieved by increasing the electrical loading and consequently liquid cooling of the coil windings by cooling tubes was required, the details of which were not disclosed. To address the NVH issues, Rahman et. al. selected a 24-16 pole configuration, which would place it completely at odds in terms of cost and efficiency, but is effective at circumferential distribution of the magnetic force loading between the rotor and stator by distributing the force over eight contact points as opposed to the two points of the 6-4 configuration. This helps control stator distortion to reduce the level of noise but the authors still found noise levels unacceptable notwithstanding the use of current profiling to control it at low speeds and excitation of natural vibration modes at higher speeds remained a problem. Moreover the 24-16 configuration intended to reduce noise, provided little room for phase advancing of the winding current which was found to limit power at higher operating speeds.

Standing in contrast to the foregoing is the work of Qionghua et al.[71]. They investigated the use of a 50kW (100kW peak) 4Ø 8-6 SRM of similar speed, machine #7 table 3a.1, and claim this configuration for the expressed purpose of reducing acoustic noise. Like Rahman et al., they selected a low silicon steel lamination to improve torque density and efficiency. They further improved efficiency, increasing electrical loading by increasing the slot fill factor by making use of a non-standard slot profile. Although they have reported noise data at 72.5db, it is a meaningless figure being for the no load case. Unfortunately, Rahman et al. does not provide many design details, not even peak power, so further comparisons here are not possible. However, Uematsu and Wallace[73],

machines #9 and #10 table 3.1, have provided design details of a 100kW 6-4 SRM for vehicle propulsion. They observe the relationship of increasing specific torque and power with smaller machine diameter running concurrent with the higher current density of increased electrical loading and its consequent requirement of direct cooling. They note the specific relationship of the former parameters and to that of the L/D ratio. With regard to the latter, they state the importance of a low stack ratio as this reduces winding inductance resulting in a nearly constant motor power. Their results would support the findings of Gallegos-Lopez et al. discussed earlier and again, are in agreement with the governing equations (3.5) and (3.6). Although any reference to noise considerations is entirely missing from their work, they provide a good summarization of their comparative work between their SRM and other electric machines in tables available in their published paper. Their SRM has provided the best specific peak power and torque ratings in comparison to the other machines cited of similar speed and power ratings.

3.3.4 – The Toroidal SRM.

Although many authors have published in the field of SRMs, these machines generally employ a concentrated wound pole as illustrated in figure 3.1, showing a typical 6-4 configuration. The machine drive topology is usually via an asymmetric converter suitable for the 6-4 SRM as in Figure 3.5(a) with switch timing shown in Figure 3.5(b). Previous publications, Sun[76], and Lee[77], have reported benefits in the torque and efficiency of a form of toroidal switched reluctance machine (TSRM) configured with six discrete 3-phase wye windings (DW) referred to here as the "WSRM", and compared to a CSRM. However, these publications are not specific in

terms of the actual comparison criteria, nor do they reveal full machine details which results in their being somewhat ambiguous.

In prior work, Lee et. al. described a 6-4 TSRM having discrete coils situated around the machine stator back iron. The six discrete coils are connected in delta with two phases active during switching. Further they described a similar TSRM (DW) with the discrete coils connected in a wye configuration with two phases active during switching. Either configuration may utilize a voltage source inverter (VSI) drive. The characteristics of the WSRM in terms of current, torque, efficiency and power, are compared in detail to the CSRM. However, the comparison results as presented were made on the basis of equalized rated output power, but made under different conditions of voltage and current which may result in inconsistencies in the conclusions drawn from the results. For example, inconsistencies in ampere-turns yield inconsistent pole flux and field saturation, similarly winding loss analysis yield inconsistent efficiency comparisons. The TSRM configuration shows promise for vehicle motive power applications where the drive system power band is wide and nearly flat, hence the interest in this topology. The work of Lee et al. was understood to be motivated by an SRM configuration that could operate in a conventional 3 phase industrial drive.

3.4 – CONCLUSIONS TO SECTIONS 3.1 THROUGH 3.3

From this review, several conclusions may be drawn regarding SRMs and their design:

- SRM machines are of simple design and construction with accordingly low cost. Their operating principle is simple and robust. They present favourable specific power and torque ratios when compared to other machines of comparable power and speed level.

- Several design parameters, inclusive of but not limited to: poles configuration, size, power, speed, efficiency, electrical loading, winding size and current are in direct conflict with one another as to their optimum value. For example: What is best for efficiency, like a larger machine outer diameter, may result in poor specific power and torque ratios, whereas a smaller diameter combined with higher electrical loadings can present cooling difficulties; A 6-4 machine may have a higher operating efficiency but be prone to unacceptable noise levels which can only be mitigated through design variations that would compromise its efficiency.

- Most mid power SRMs of the size range considered and of a compact design for vehicle propulsion will require some form of applied direct cooling, usually liquid cooling. Methods of electric machine cooling were discussed in the literature review of that topic.

- Effective SRM design, like that of any other machine, is best achieved with a clear understanding of the application and evaluation of the critical parameters for said application. Only with that can priorities be established and a design

progress in an effort to optimize the remaining parameters to produce a satisfactory result.

- The toroidal SRM design as described herein, the “WSRM”, shows comparable efficiencies to that of its conventional counterpart, the “CSRM”, and may show promise for vehicle motive power given its reported torque characteristics.

- The benchmark study failed to provide any clear direction with regard to design optimization nor best practices.

3.5 – INTRODUCTION TO THE THERMAL ANALYSIS OF A HIGH SPEED SRM

Chapter 3, sections 5 and 6, is comprised of an early work which explored the thermal analysis of a high speed SRM under development in the Canada Excellence Research Chair Program for Hyprid and Electric Vehicle Powertrain. It was an early motivator for the present research program of this author. This work resulted in the development of a lumped parameter thermal network from which the thermal analysis of the SRM machine, and subsequent toroidal SRM developed in Chapter 5 could evolve.

As described in Chapter 2, the evaluation of thermal performance may take the form of a thermal FEA program as part of an electrical design software package or a lumped parameter (LP) thermal analysis of either one or two dimensions. The latter method builds a thermal resistance map of the system combined with the known or estimated losses (the heat rejection) and solves for the temperature at each node of the thermal resistance map. It was decided early on, since the group design for the SRM was always evolving, that a simple lumped parameter thermal model would be a quick and effective method for the purpose of facilitating design development, although it will not consider detailed layered winding temperatures unless extended specifically to do so. That model was achieved and has already revealed what some of the challenges to cooling will be. These are but not limited to: Air gaps, high thermal contact resistance between components, low thermal conductivity of the core, cooling is most effective when applied at the source of loss. All of these factors contribute to driving a higher temperature differential between the coolant and the internal components of an electric machine where traditional cooling methods are considered.

This approach started by repeating the work of Lindstrom[78], who applied the LP approach to a 50KW PMSM electric motor, to build confidence with the method, the calculations, and to reveal any problems with the approach. Although the LP method is simple enough to understand, the calculations are detailed, complex and rely upon many assumptions. This was followed by applying the LP method to the aforementioned high speed SRM then being developed. That quickly identified internal cooling as a requirement for such a machine and the difficulties to be encountered in both the modeling of the heat transfer and the practical application of the cooling techniques. These are: Thermal contact resistance modeling and determination, convective heat transfer coefficient determination, and the extent of cooling to be applied and to which internal locations.

3.6 - LPTN MODEL FOR SRM THERMAL ANALYSIS

3.6.1 – Introduction.

Since the calculations involved in setting up a LPTN model can be highly detailed, if not so difficult, it was decided to set up the LPTN model construction first, as stated, by repeating and verifying the work of Lindstrom[36] with the construction of an 8 node LPTN for a 48 pole DCPMSM. The reader is referred to the publication for illustrations, specific dimensions and materials details. Although not without error, Lindstrom's work in this regard is the most complete to be found in the literature with diagrams, dimensions and formula developments which are described well enough as to permit an attempt to repeat it – it is an instructional work. As such, this would accomplish several things:

- An LPTN model which could be checked against known results
- Serve to identify problems with the calculations and assumptions.
- Provide a template network that we might have confidence in, suitable enough for conversion to the SRM architecture as these machines are similar in their construction.

At the time of this development, an SRM identified as #15 in the literature review of same, chapter 3 section 3.3.3, prior to the development of this author's own SRM, was employed as a vehicle for the direct application of a LPTN to an SRM architecture, from which variations could be studied. The studies included a sensitivity analysis to understand the effect on temperature arising from variations in thermal resistance, either from uncertainty in the calculations arising from errors in the assumptions, or from the placement of direct cooling upon certain nodes within the model, or by the elimination of certain cooling paths within the model. This developed a clear cause and effect understanding with respect to the heat flow path within the machine, applied cooling and the result of errors in the calculation of thermal resistances.

3.6.2 – The development of the Lindstrom LPTN.

The heat flux paths within an electric machine are complex three dimensional flows. Given the high thermal conductivity of the iron material and length of the machine, the temperature is assumed level in the axial direction except for the boundaries at each end to be discussed further on. This reduces the heat flux to a two dimensional flow in the radial and circumferential directions. In the case of the latter, again, the

temperature is assumed level except for the boundaries between the teeth and coils, which reduces the problem to a one dimensional flow in a more or less radial direction between the elements of the machine: Frame, stator yoke (back iron), stator teeth, coil sides, air gap, rotor teeth, rotor yoke, shaft, bearings, end frame. The governing equation for the heat flux is the three dimensional conduction equation reduced to the familiar one dimension form in steady state, Fourier's equation:

$$q = -kAdT/dx \qquad (3.7)$$

where q is the heat flux in watts, k is the thermal conductivity in W/mK, A is the area in m^2 through which the flux passes in the normal direction and dT/dx is the temperature gradient in K/m between two points. The equation may be rewritten:

$$q = - dT/(dx/kA) \qquad (3.8)$$

The numerator dT is now the driving potential ΔT, and the denominator (dx/kA), ie. $\Delta x/kA$ may be regarded as a resistance term, Rth in units K/W. This forms the well known electrical analogue for thermal resistance, heat flow and thermal potential to electrical resistance, current (coulombs/second) and electrical potential (volts). A similar argument may be made for transient analysis and the development of a thermal capacitance but that is not considered here at this time. The convective boundary conditions at each end of the rotor, stator, end windings and end shield may be described by Newton's law of cooling:

$$q = hA(T- T_{\infty}) \qquad (3.9)$$

where *h* is the convective heat transfer coefficient to be determined from standard relationships as may be reported from various sources in the literature for air, A is the surface area, T is the temperature of the surface and T_∞ is the temperature at some distance from the surface.

The above was applied to the geometry of the Lindstrom motor. This allows for the linking of conduction paths within the radial, and some circumferential direction in the case of coil sides, direction of the machine. At the boundaries convection to the internal air, end shields and end windings is dealt with by adding the appropriate branch thermal resistance into the thermal network. The fully developed network is shown in figure 3.6. The results for the calculations of thermal resistance – R_{th}, based upon the Lindstrom motor geometry are tabulated in table 3.2.

Table 3.2. Comparison of thermal resistances calculations with Lindstrom's calculations.

R thermal calculated vs. reported by Lindstrom			
Thermal R_{th} Resistance	Calculated K/W	Reported K/W	Error (%) %
R_1	0.0002	0.0002	3.5
R_2	0.0066	0.0064	2.7
R_3	0.0083	0.0085	-2.2
R_4	0.0272	0.0056	386.2
R_5	0.0742	0.0747	-0.61
R_6	0.5259	0.4350	20.9
R_7	2.9515	1.5489	90.6
R_8	1.2891	0.2242	474.0
R_9	0.1935	0.1811	6.8
R_{10}	1.1059	2.8640	-61.4
R_{11}	0.0000	0.3119	-100

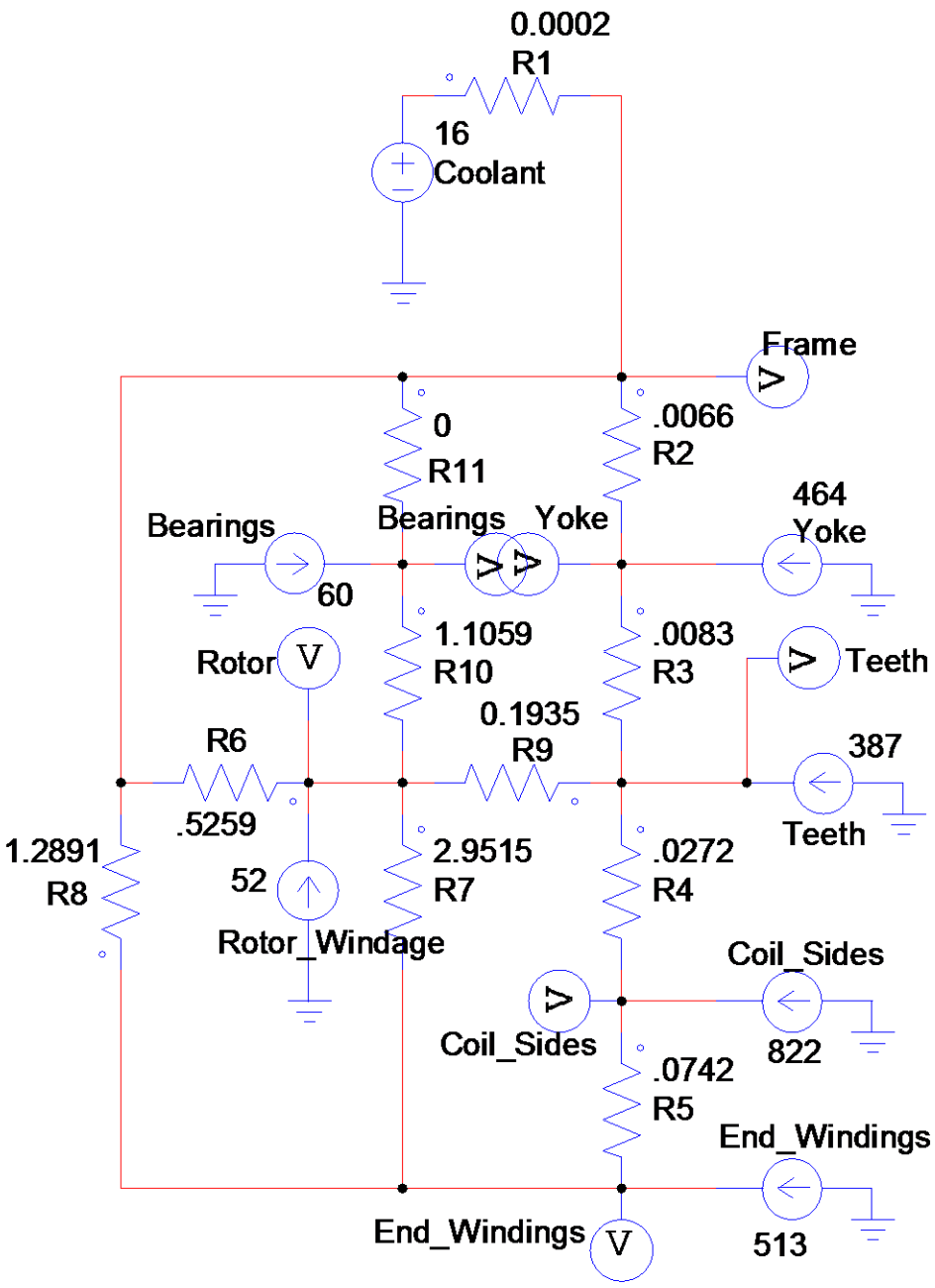

Figure 3.6. The Lindstrom LPTN model for a DCPMSM shown with calculated resistances from table 3b.1 without thermal capacitance (i.e. steady state solution)

Examining the table 3.2, several large discrepancies are observed, namely R_4 – conductive between coil sides and teeth, R_7 – convective between windings and rotor, R_8

– convective between frame and end windings, R_{10} – Rotor to bearings and R_{11} bearings to frame. The lattermost two errors were later determined to be of little significance to the resultant temperature calculations so were not investigated. The R_7 and R_8 are related to formulae for determining convective heat transfer, which were later discovered to be published with errors in Lindstrom's work; they were sourced from Kylander[79]. The errors were corrected but without the individual values of thermal resistance before the Lindstrom Y-Δ transform of R1, R2 and R3 to obtain R_6, R_7 and R_8, there was no means to further troubleshoot the source of the discrepancies. Furthermore, Lindstrom does not provide some sufficient geometrical data to do so. In any event, R_4 poses the greatest sensitivity in the temperature analysis as it is located directly in the main heat transfer path from coil end windings to frame. The calculation of R_4 is based upon an algorithm developed by Soderberg[36] for the heat transfer between coil sides and teeth in larger generators. It is dependent upon the overall effective air gap between the coil sides and teeth, something which is not possible to determine in actual practice but may only be estimated. It is believed, but not known, that Lindstrom may have made an error in the calculation as adjustment of the air gap by one order of magnitude provides the correct figure for thermal resistance.

The LPTN was set up in a power electronics simulator "PSIM" for a solution to the temperature values at the indicated nodes under steady state conditions, ie no thermal capacitance values were considered nor included in the network. The results of the temperature simulation for the Lindstrom motor using the calculated, Lindstrom and adjusted values of thermal resistance for R_4, R_7 and R_8 to Lindstrom' values are reported in table 3.3. Note the thermal input in watts at each nodal point.

Table 3.3. Simulated temperature results using the calculated thermal resistances R_1 through R_{11} compared to Lindstrom's results with Lindstrom's thermal resistances.

PMSM steady state results @ 50kW, 6000 rpm and 16°C					Adjustment	Thermal
	Node point temperatures °C					
Node	Calculated	Lindstrom Reported	Lindstrom Measured	Adjusted R_4=.0056	R_4=.0056 R_7=1.5489 R_8=.2242	Input W (%) 2298 total
Frame	17	17	n/r	17	17	n/a
Yoke	30	29	n/r	30	29	464
Stator Teeth	46	42	n/r	47	44	387
Coil Sides	81	47	51	54	50	822
End	113	68	72	88	70	513
Magnets	42	39	n/r	41	39	22 (1)
Bearings	18	27	n/r	18	18	60 (3)
Coolant	16	16	16	16	16	n/a
Windage	n/a	n/a	n/a	n/a	n/a	30 (1)

The end winding and coil side temperatures are most strongly influenced by the thermal resistance R_4 which is comprised mainly of the thermal contact resistance between the coil sides and teeth, and the thermal resistance of the winding impregnation material. Of the two it is most sensitive to the contact resistance which is governed by the effective air gap between the teeth and coil sides. As discussed, this last parameter is difficult, if not practically impossible, to determine by any means of direct measurement. The usual approach to deal with it is to tune that input to the model against a known experimental result of temperature dependent upon it. In this case the "tuning" was performed by using Lindstrom's reported value for R_4 which resulted in an immediate reduction in the calculated temperature for the coil sides and end windings of 27°C and 25°C respectively. This brought the coil side calculated temperature to within 3°C of Lindstrom's measured result although the end winding temperature remained 16°C above the measured value. As noted earlier, the majority (58%) of the thermal input occurs in

the end windings and the coil sides, so it is not unexpected that the temperature results will be sensitive to the thermal resistance at that point of input. Since the end windings are dependent upon both conductive and convective heat transfer an adjustment to R_7 and Rth8 were performed as these governed heat transfer from the end windings to both the rotor and frame through the air. With this adjustment calculated temperatures for both coil sides and end windings were brought to within 1°C and 2°C of the measured values reported by Lindstrom respectively. Again, 22 % of the total thermal input occurs at this node so it is expected that the temperature result there will be sensitive to the local thermal resistance encountered. At this point the calculations of the LPTN were progressed to the SRM architecture. It is clear from these results that the temperatures obtained are most sensitive to those thermal resistances residing in the main heat flux path, in this case directly between the end windings and the motor frame. Unfortunately, it is not clear from Lindstrom's work where the difference between calculated and reported values resides as there were several parameters required for the calculations not disclosed. Fortunately, the sensitivity of the temperature results to those thermal resistances not directly in the heat flux path is significantly less than otherwise. Further, it is not necessary to have precise temperature predictions when one is interested in studying the effect of applied points of cooling at different nodal locations, as say in the case of direct cooling of the stator back iron or coil sides as has been reported in the literature previously cited.

3.6.3 - The development of the high speed SRM LPTN.

The transformation to an SRM LPTN from that of the DCPMSM LPTN is readily accomplished through straight forward geometry and dimensional changes. The major adjustments are to the stator tooth profile, a significant reduction in the number of said teeth, and the removal of the permanent magnets from the rotor profile and the addition of an end shield to the frame; something not considered/discussed in the Lindstrom analysis. Accordingly, the thermal resistances R_9 and R_{10} were updated to relocate the rotor node to the central portion of the rotor whereas in the case of the Lindstrom motor it was located on the permanent magnets. The resulting thermal resistances used in the SRM are shown in table 3.4. The LPTN developed for the SRM is shown in figure 3.7 with the thermal resistances and input to each node (in watts) shown on that schematic. The "rotor" node and "teeth" node included windage losses of 2500 watts split evenly and applied at these points.

Table 3.4. Thermal resistance calculations for the high speed SRM

Thermal resistance calculations for SRM		
Thermal	Calculated	Node
R1	0.0002	Cooling water to
R2	0.0124	Frame to yoke
R3	0.0166	Yoke to teeth
R4	0.0091	Teeth to coil sides
R5	0.0211	End winding to coil
R6	0.0391	Rotor to frame
R7	0.1898	Rotor to end
R8	0.1139	Frame to end
R9	0.4021	Rotor to teeth
R10	1.2923	Rotor to bearings
R11	0.0490	Bearings to end
R12	0.0325	End shield to frame

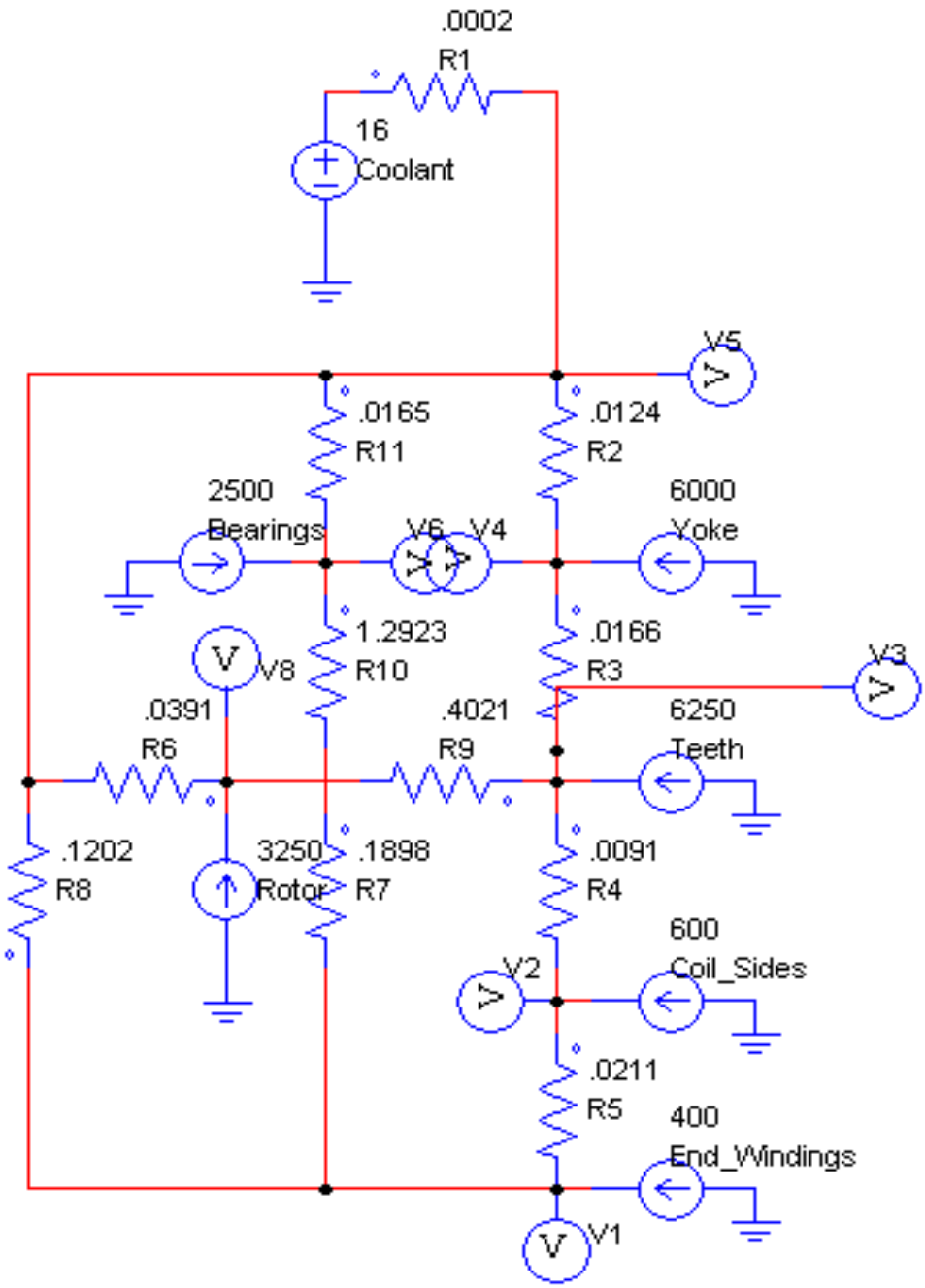

Figure 3.7. LPTN model in PSIM for SRM thermal resistances, thermal inputs in watts

Here, it should be noted, the significant difference in distribution of thermal input between the PMSM and the SRM, the latter having significantly higher core losses and consequently higher thermal input to the stator and rotor yoke nodes as compared to those

of the windings. As will be seen, this will contribute to the sensitivity of the results to the thermal resistance in that part of the machine as well as the direction of heat flux out of the machine.

There were several iterations to the design of the high speed SRM and the aforementioned figure shows the initial starting design LPTN which was in essence nothing more than a raw application of the Lindstrom motor LPTN parameters and material properties with changes in geometry applied to the SRM architecture and changes to thermal input as required for the SRM. The results for predicted temperature and adjustments to thermal resistance and bearing thermal output are shown below in table 3.5. The shortcomings of this approach are soon evident.

Table 3.5. Simulated temperature results for the subject SRM.

SRM steady state results @ 200kW, 22000 rpm and 16°C cooling water						
	Thermal input W (%)		Temperature °C		Adjustment (with end shields)	
Node	Initial	65Wbrg.	Calculated	Adjustment R_2=.008	$R_{11}+R_{12}$=.081	w/65W brg.
Frame	n/a	n/a	20	20	20	20
Yoke	6000 (32)	6000 (36)	158	91	159	158
Stator Teeth	6250 (33)	6250 (38)	244	187	245	244
Coil Sides	600 (3)	600 (4)	236	184	237	236
End Windings	400 (2)	400 (2)	206	164	206	205
Rotor Surface	3250 (17)	3250 (20)	161	151	165	160
Bearings	2500 (13)	65 (<1)	61	61	219	33
Cooling Water	n/a	n/a	16	16	16	16

The temperatures calculated based upon the "initial" thermal input show most residing above the thermal design target of 150°C for the insulation material. Given the high core losses (iron losses) it was decided to investigate the effect of thermal contact resistance to the frame (ie between stator yoke and frame). Lindstrom chose to take this as approximately equal to the material resistance between the nodes. Staton et al.[80] reported an interfacial conductance range of 4000-40000 W/m²/°C for iron-aluminum, which would imply a contact resistance for iron-aluminum at 0.0019 K/W based upon the size of this machine at an effective interface gap of .006mm with moderate pressure and usual finish. As such gaps found in electric machines average 0.037mm as reported by Staton et al.. It is expected that the actual thermal contact resistance will be greater than 0.0019 K/W for a practical machine. The sensitivity of temperature to this effect was studied by removing the thermal contact resistance from R_2 and performing the calculation. That would show the best result attainable under the ideal condition of no yoke to frame thermal contact resistance. Depending upon the node, temperatures are reduced by 40 to 60 °C as would be expected but still reside above the 150 °C thermal limit. The next adjustments were made to the R_{11} with the addition of end shields to the thermal path of the motor, something which Lindstrom does not describe in the geometry but the presence of which is considered in the convective calculations. R_{11} was thus divided by adding an R_{12} which describes the thermal resistance from an end shield node to the circumferential frame node. Further, the initial condition of 2500W bearing thermal input was corrected to 65W. Considering both of these adjustments and the original contact resistance the predicted temperatures returned to their original result except the bearing temperature was reduced. It was readily concluded that to be successful some form of

applied internal cooling would be required for this machine as even the complete elimination of thermal contact resistance to the frame would not be sufficient to reach the intended thermal target of 150 °C, nor was there an effective cooling path for the rotor by conduction through the shaft, bearings and end shields, nor by convection.

3.6.4 - Transient response of the high speed SRM LPTN model**.**

There were no suitable transient results available from the Lindstrom model, and none were obtainable, as there were no thermal input data given for each node, so no validation was possible with that approach. As such, a transient response was obtained for the SRM LTPN model. The SRM LPTN transient model is shown in figure 3.8, with thermal capacitance elements (J/K) added to the network of figure 3.3 at thermal input nodes. The end shield adjustment and 65W bearing are used, ref. table 3.5.

Table 3.6. Transient results for the high speed SRM.

Transient results @200kW, 22000 rpm, 16°C coolant. Time step 0.01s, run time 2400s.			
Node	Maximum Temp. °C	Time to 150°C seconds	Time to .99Tmx. seconds
Frame	19.3	n/a	959
Yoke	159	846	1344
Stator Teeth	247	265	1387
Coil Sides	240	304	1307
End Windings	212	392	1375
Rotor Surface	155	1491	1930
Bearings	34	n/a	992
Coolant	16	n/a	n/a

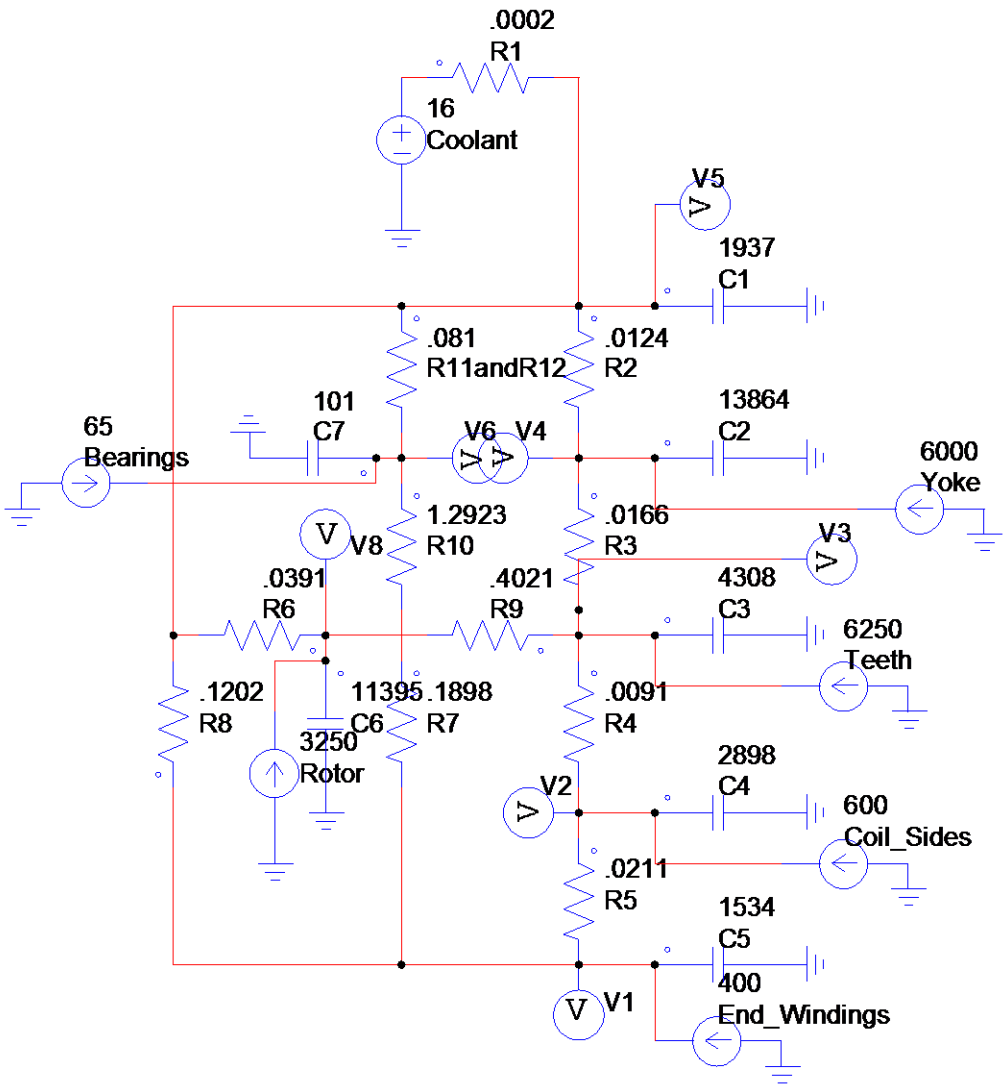

Figure 3.8. LPTN model in PSIM for SRM transient analysis, thermal resistances and thermal inputs in watts, capacitance in J/K

The results of the transient thermal analysis are shown in table 3.6 and figure 3.9. First, a discrepancy must be noted between the maximum temperatures obtained through transient analysis vs. those obtained from the steady state analysis as indicated in the last column of table 3.5. The error is on the order of 3%. This is perhaps due to the small error introduced with each time step, here 0.01s, over a long time run totaling 2400

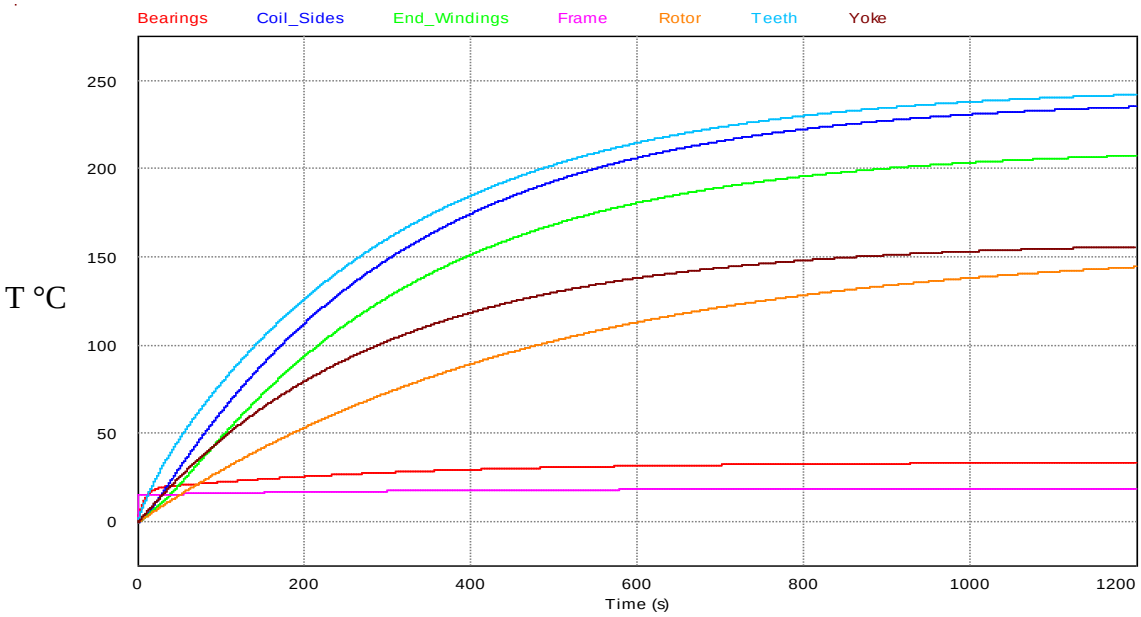

Figure 3.9. LPTN model solution in PSIM showing SRM transient thermal results

seconds of simulation. Accordingly, the steady state results for maximum temperature should be regarded as correct. The result does confirm the direction of heat flow from stator teeth to end windings and indicates the stator teeth are at first risk of exceeding the 150°C thermal limit for this SRM at 265 seconds, or about 4 minutes.

3.6.5 - SRM thermal management with various internal cooling approaches.

From this point direct internal cooling of the high speed SRM was investigated. Cooling in the form of a fixed heat sink temperature as considered before, was applied to the internal locations stator yoke, end windings and coil sides both individually and in combination. The effective thermal resistance at the point of application was held constant in all cases at the same value considered for the prior studies. This was

reasonable as the observed effect was more important than the actual temperature result. The results are presented in table 3.7.

Table 3.7. Simulation results with various applied internal cooling schemes at location

SRM steady state results @ 200kW, 22000 rpm and 16°C cooling water, and applied internal cooling							
Node	Rotor R_n Adjustment R_9=.7377 R_{10}=.912	Ceramic Bearing Model R_{11}=0	+ Coil Side Cooling R=.0091	+ End Winding Cooling R=.0091	+ Stator Yoke Cooling R=.0091	Stator Yoke Cooling Only	Stator + Coil Side Cooling
Frame	19	19	19	19	19	65	55
Yoke	159	159	106	128	**82**	**19**	19
Stator Teeth	245	246	123	175	180	134	80
Coil Sides	237	238	**75**	144	178	139	**56**
End Windings	206	206	78	**59**	160	139	**71**
Rotor Central	156	**163**	136	137	153	182	162
Bearings	35	**222**	195	196	212	242	221
Cooling Water	16	16	16	16	16	16	16

New for this study, thermal resistances R_9 and R_{10} were updated to relocate the rotor node to the central portion of the rotor whereas in the case of the Lindstrom motor it was located on the permanent magnets. In addition, the model proceeds with a ceramic bearing instead of a metallic model. The ceramic bearing behaves as a thermal insulator effectively cutting off the thermal conduction path between the shaft and end-shields return to the motor frame. This is clearly evident from the rise in temperature of both the bearings and the rotor. Ceramic bearings have a thermal limit greater than 150 °C. There is little or no predicted effect upon the stator side cooling as this heat flux path remains unaffected. The next three cases add coil side, end winding and stator yoke cooling individually. Except for the last two cases frame cooling, as before, is included. The

results show, somewhat as expected, that the minimum temperature resides at the point of cooling application with the most effective method being coil side cooling. In the latter two cases, direct stator yoke cooling only, while effective at reducing stator, coil side and end winding temperatures significantly, places the source of cooling further away from the rotor and its temperature is observed to rise accordingly. The effectiveness of stator yoke cooling results in part from the elimination of contact resistance between the frame and stator material. Adding coil side cooling to that approach returns the rotor temperature to that of the frame cooling only case but remains high compared to the other internal temperatures. The applied cooling at the coil sides in close proximity to the rotor though is effective at reducing rotor temperature. The effect could be further enhanced with the consideration of enhanced turbulent cooling effects applied to the tooth gap of the stator and rotor.

3.7 – CONCLUSIONS TO SECTIONS 3.5 AND 3.6

Although it is unlikely the predicted temperatures from these studies are precise, some of the reasons for which have been discussed, some conclusions may be drawn from this work:

- To achieve temperature prediction with certainty the thermal contact resistance between components where it exists, especially in critical heat flux paths, is required to be known with some precision otherwise the model will require tuning against some known result.

- The convective effects at the boundary, while not unimportant, do not reside in the main heat flux path and are, accordingly, secondary to affecting the predicted temperature result.

- In the case of the high speed SRM as studied, direct internal cooling is required to bring the operating temperature of this machine to within acceptable operating limits. Direct internal cooling circumvents certain internal thermal contact resistance within the heat flux path.

- The effectiveness of internal cooling is highly dependent upon where it is applied within the machine and may be said to be superior to conventional cooling applied at the machine's frame as cooling applied directly to the stator yoke of this machine was able to reduce the predicted temperature by over 100 °C in the case of the stator, and by a similar level for the coil sides.

- In the case of the high speed SRM as studied, even with direct applied internal cooling, rotor cooling will remain challenging, requiring unconventional approaches to effect significant temperature reduction. The use of ceramic bearings may not be possible as this eliminates a useful heat flux path for the rotor thermal input.

CHAPTER 4 – INTER-LAMINATE COOLING FOR ELECTRIC MACHINES

4.1 - INTRODUCTION

The traditional approach of air and liquid cooling methods, often applied to the periphery of a machine are well known and utilized. In the case of electric machines (EM) for motor vehicles, such as hybrid electric vehicles (HEV) and all electric vehicles (EV) the demands for more power from smaller package envelopes conflicts directly with the thermal limit of EMs, which is usually governed by the temperature limits of the winding conductor and/or lamination insulation, and in the case of permanent magnet machines, the magnetic material.

As previously discussed, the main heat sources are the machine's windings via copper (I^2R) losses and the soft magnetic iron core losses (eddy current and hysteresis). For machines that are primarily cooled on the stator periphery the main heat flux path is from the copper winding through the slot insulation to the stator teeth, yoke and then out towards the frame at the peripheral outer diameter where it is transferred to the environment by either means of natural or forced air convection, or alternatively a liquid jacket cooling method. This work introduces the approach of Inter-Laminate Cooling (ILC) to transfer heat directly from inside the iron core of the machine to the peripheral diameter and thus to reduce the stator temperature or, conversely, allow for a higher operating power level by means of improved loss dissipation. The use of Pyrolytic-Graphite-Sheet (PGS) as a transfer medium is proposed, analyzed, and examined experimentally as one potential means to achieve this goal.

Electric machine (EM) cooling presents several challenges in HEVs and EVs. There is an ongoing requirement for EMs with higher output power to improve performance and efficiency. Higher output power, and consequently thermal losses, within the same package space leads to higher operating temperatures. Tighter packaging spaces arise from the presence of supporting equipment such as power electronics, batteries, multiple cooling system heat exchangers, plus the need to reduce overall vehicle weight and size. The thermal limits of typical organic-polymer insulators coating the wire and iron laminations limit the output of EMs which directly conflicts with the above requirements. A further constraint factor is that high vehicle ambient operating temperatures and the low thermal limit of the EM that results in a narrow window of thermal potential with which to reject the internally generated thermal losses.

Although there are many approaches in practice, as stated prior, EM cooling has been dominated traditionally by air and liquid (usually oil or water) methods. Often the cooling is applied peripheral to the source of heat generation, i.e. external jackets in the case of liquid cooling, or forced air circulation , either over the EM casing, or by pulling air through the interior of the machine. But, the heat generation is deeply internal to the EM originating from the winding losses and iron losses within the stator and rotor. More recently, Direct Laminate Cooling (DLC) confined to the outer iron lamination edges or small internal passageways within the iron laminations has been proposed and researched Baggu & Hess[81], Huang et al.[82], Festa et al.[83]. This helps to move the applied cooling, the working fluid, to a point somewhat further inside the machine. Inter-Laminate Cooling (ILC) is proposed here to move the applied cooling point to a deep interior location within the iron laminations themselves. To date there is no reported Inter-

Laminate nor solid thermal conductor approach in the literature although a patent on the approach is known from Jarczynski[84]. The literature also reveals a poor characterization of cooling method effectiveness where only temperatures are typically reported, with little regard to the significance of the cooling method or enhancement achieved.

4.1.1 – The ILC Concept.

The Inter-laminate cooling method uses a thermal conductor of high thermal conductivity and minimal thickness (relative to the surrounding iron laminate), placed in-between the machine laminations commonly found in motors or transformers. This is illustrated in Figure 4.1. Only one reference to this concept has been found in the literature and this was the aforementioned Jarczynski patent. Management of eddy current loss within the copper sheet and their consequent disturbance of the machine magnetics notwithstanding, the Jarczynski patent has within certain claim to a number of facts or suggestions, some of which will be demonstrated as true for the performance of the concept, where some others are not.

What is newly proposed and novel for this research is the use of a non-metallic polymer thermal conductor having high thermal conductivity with respect to its surrounding material, electrical lamination steel, i.e. the soft magnetic iron laminations. To investigate the concept of inter-laminate cooling within an electric machine an analytic study was undertaken to model the effect within an electrical transformer architecture, more specifically as an inductor. The analysis was subsequently validated

via a laboratory test facility and apparatus designed specifically to show proof of the concept.

4.1.2 – Overview, Losses in Electric Machines.

All electric machines will exhibit copper and iron losses to some degree, the composition of which varies depending upon the machine's design and operating conditions. In the case of a High speed Switched Reluctance Machine (HSRM), like any other high speed, and hence high frequency electric machine, the losses are expected to be dominated by the iron losses, as opposed to the copper losses. This makes the application of an inter-laminate cooling (ILC) method particularly useful. ILC may be conveniently studied by utilizing a simple inductor as illustrated below in Figure 4.3, intended to replicate the coil and magnetic circuit of an EM.

4.2 – INTER LAMINATE COOLING

4.2.1 – Concept.

The ILC method introduces a thermally conducting material having a thermal conductivity much greater than the surrounding iron, in-between the laminations of the EM or in this case the SRM. Ideally, this material would be both a good electrical insulator and a superior thermal conductor with respect to the surrounding iron. Thermal Graphite Material (TGM), more specifically known as Pyrolytic Graphite Sheet (PGS), is available as a commercial product from manufacturers such as Panasonic Corporation[85] for example. The 0.1mm PGS from Panasonic Corp. has both good electrical insulating

and thermal conductivity properties as detailed in Figure 4.2 which shows a schematic of the material structure along with a tabulation of its physical properties.

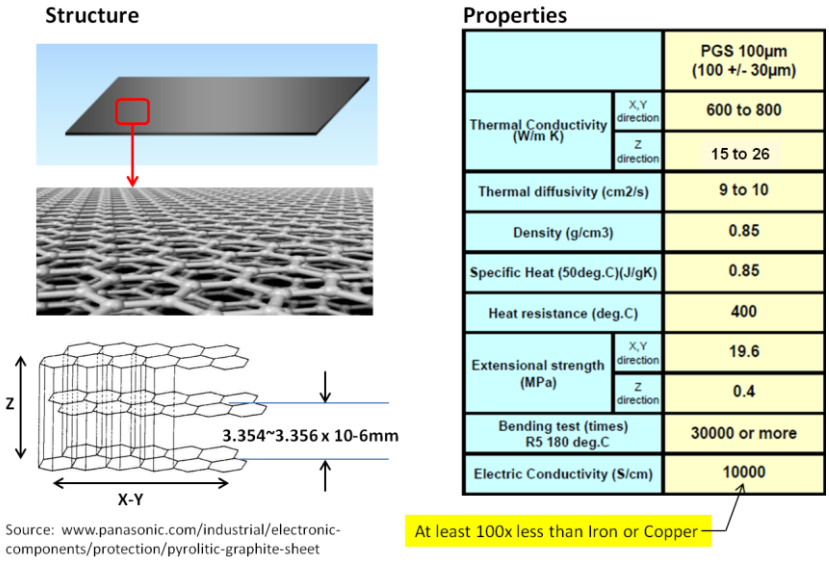

Figure 4.2. Physical structure and properties of Pyrolytic Graphite Sheet (PGS) provided by Panasonic Inc.[84]

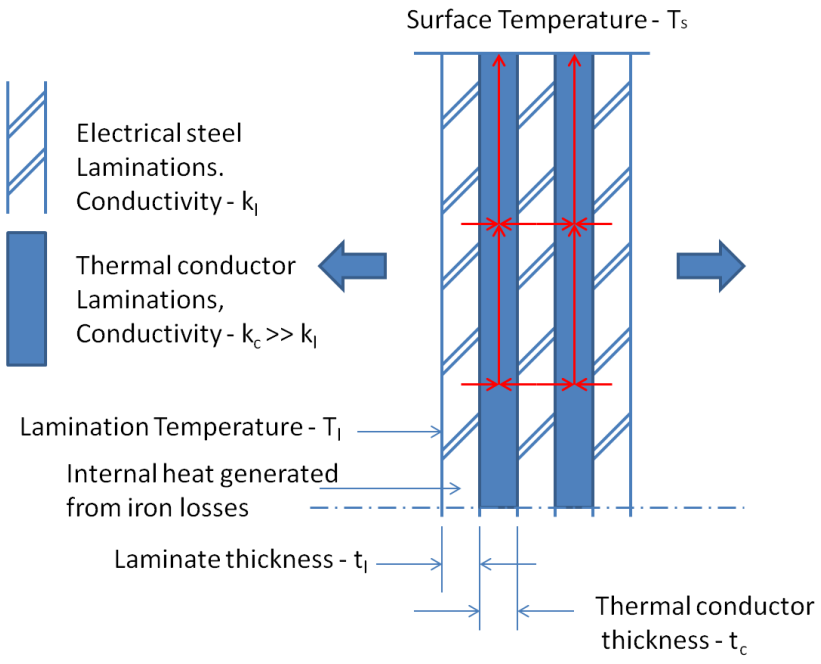

Figure 4.1. Inter-laminate cooling concept.

When placed between the iron laminations of an electric machine the high thermal conductivity of PGS serves to conduct heat away from the iron toward the peripheral surface temperature.

4.2.1 – Analytical Model.

For the purpose of studying the phenomenon in an electric machine it is convenient to use a transformer model to serve as a proxy for the electric machine environment, as illustrated in Figure 4.3.

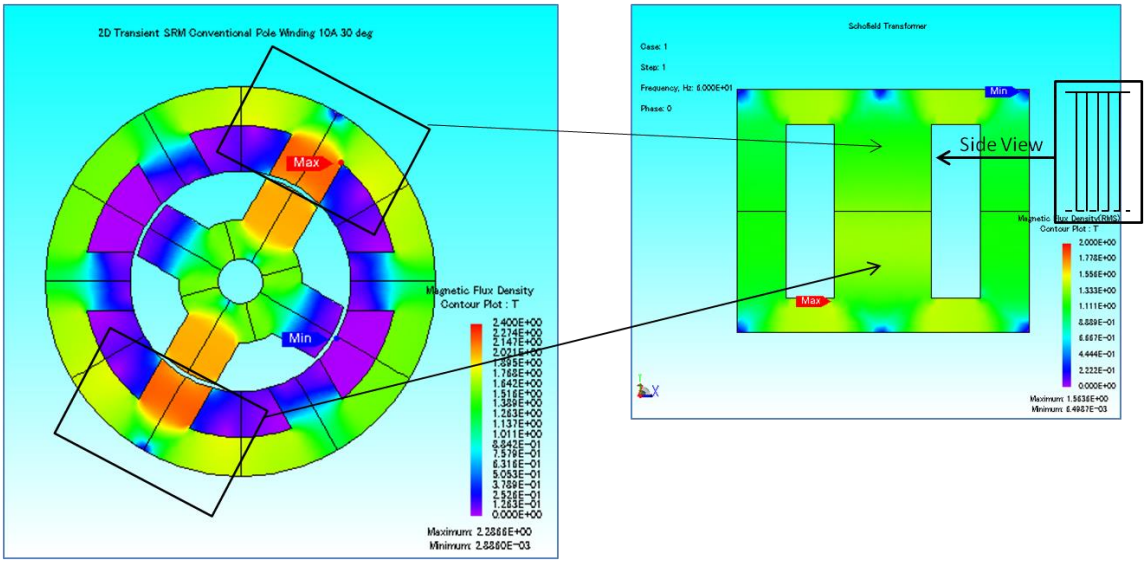

Figure 4.3. Transformer proxy for an electric machine (SRM shown)

This simplifies the prototyping and test facility requirements while maintaining the main heat transfer mechanisms present in an electric machine. The transformer closely replicates the magnetic field flux induced by a single pole winding within the iron core of an SRM. The structure holds the same symmetry as found in the SRM where the machine's air gap may be thought of as existing at the centerline of the transformer. Here, ideally due to symmetry, the heat flux resulting from the iron losses is of equal

magnitude, but in opposite directions at either side of the transformer's centerline location. For this analysis, the ILC application can be modeled as a parallel half sheet of iron laminate and a half sheet of thermal conductor, in this case the Pyrolytic Graphite Sheet (PGS), having a fixed height-to-thickness ratio and of infinite depth, as detailed in Figure 4.4a.

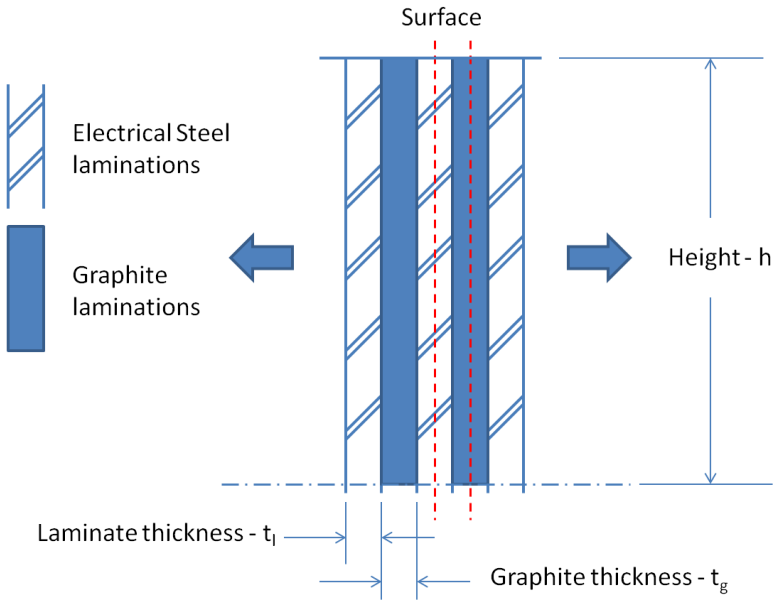

Figure 4.4a. Half sheet each of Steel and Graphite Laminations

To take advantage of symmetry, the assembly is considered perfectly insulated (zero heat flux in or out) on all sides except for the top side which is fixed at a predetermined temperature, i.e. a perfect heat sink, detailed in Figure 4.4b. This would be considered as the ideal condition but, as it will turn out, is actually closely representative of the experimental situation. The material space is then discretized into the customary nodes forming a small lumped parameter thermal network (LPTN), which is, strictly speaking, a finite difference network in this case, as illustrated in Figures 4.4c. and 4.4d.

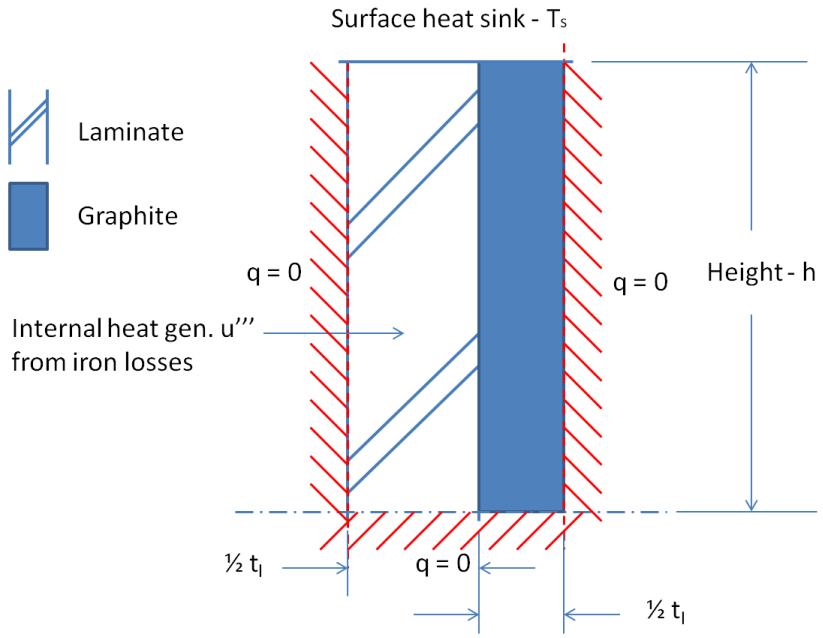

Figure 4.4b. Half sheet of Steel and Graphite Lamination and associated boundary conditions

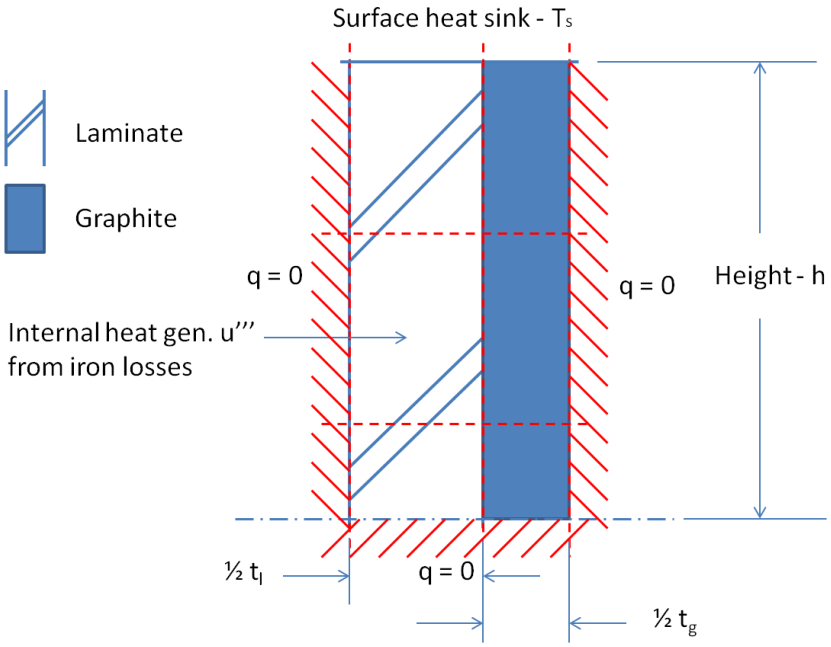

Figure 4.4c. Discretization of the Space into Elements

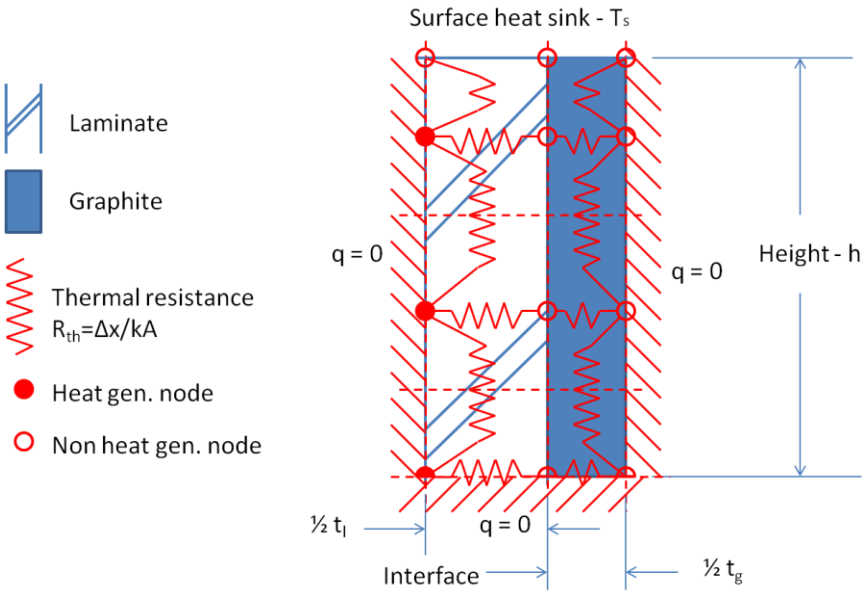

Figure 4.4d. Finite difference components of LPTN model

The resulting material temperature at the centerline is solved according to the governing one dimensional equation for heat conduction:

$$q = -kA(\Delta T/\Delta x) \qquad (4.1)$$

where q is the heat flux, k the thermal conductivity of the material, A the cross sectional area through which q occurs, $\Delta T/\Delta x$ the thermal gradient. Equation (1) may be rearranged thus:

$$q = -\Delta T/(\Delta x/kA) \qquad (4.2)$$

where the term ΔT is the thermal driving potential difference between any two nodes and the term group $(\Delta x/kA)$ represents the thermal resistance R_{th} between any two nodes. The heat flux q occurs as a thermal input to the iron laminate nodes as illustrated on Figure 4.4d. The aforementioned is similar to that discussed in Chapter 3b section 3b.3.2 except that that the network is extended within the same material to several nodes. This results

in the more familiar "finite difference" network of thermal analysis as described in Holman[86].

Alternatively, although with much greater difficulty, the heat transfer problem as discussed above has an analytic solution when the problem is formulated from the first principles of Leplace's equation for multi-dimensional heat flux and Fourier's Law for steady state heat conduction, then solving the heat transfer equations in two dimensions. This results in two coupled second order differential equations which both describe the heat flux along the x-y plane and the x, cross plane, direction. The heat flux between the two materials in the aforementioned direction constitutes a boundary condition between the two materials, which may be represented by a differential equation. The first two equations are coupled at this boundary by the equation.

4.2.2 – Solution Procedure.

The analytic solution to the thermal network of equation 4.2 which results from reducing the generalized three dimensional heat conduction equation to one dimension and applying a discretization scheme as depicted in Figure 4.4d is a straight forward matter of linear algebra. An analytic solution to the temperature field starting with the generalized three dimensional heat conduction equation as described above in section 4.2.1 is rather difficult and tedious. For the purposes of the ILC discussion and the results, the numerical solutions derived from the electrical analogue network PSIM^{TM} [87] solver of the LPTN model are therefore used throughout. As discussed in chapter 2 of the literature review, the use of such solvers is routine practice in electric machine thermal simulation. The small thermal network based upon the illustration of figure 4.4d.

is now shown in Figure 4.5 as implemented in the PSIM solver showing temperature results for t_l/t_g=1 with 1W input at each node of the iron laminate. Thermal resistance is stated in K/W, temperature in °C.

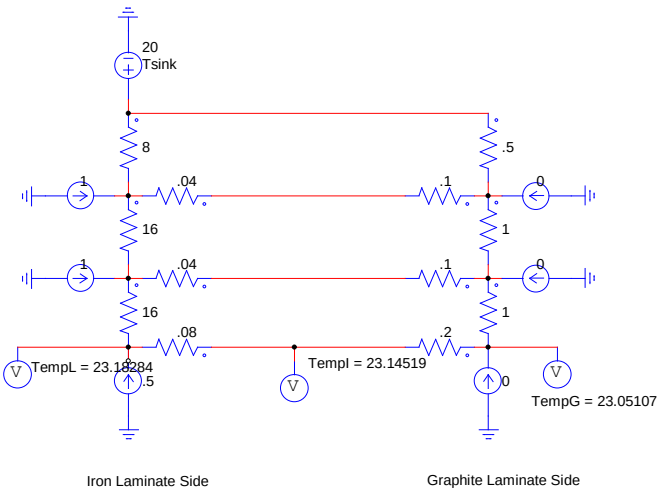

Figure 4.5. 5 node LPTN representation of ILC in PSIM.

The small thermal network, although sufficient for a solution to the problem (as will be demonstrated later) is perhaps too crude for detailed analysis. Hence, it was expanded to a total network of 42 nodes as illustrated in Figure 4.6, representing an increase in the discretization level by a factor of 4x in the planar direction and 2x in the cross planar direction, which is better suited to the length to thickness aspect ratio h:t_l being considered. Further, this network incorporates the important concept of thermal contact resistance arising from the physical interface between the iron laminations and the graphite sheet, which is governed predominately by the pressure between the two surfaces. This has been researched by the manufacturer, Panasonic, for their particular product and is disclosed in their product literature as referenced. Their claimed value for thermal contact resistance is: 0.7°C-cm²/W at 0.5Kg/cm² contact pressure.

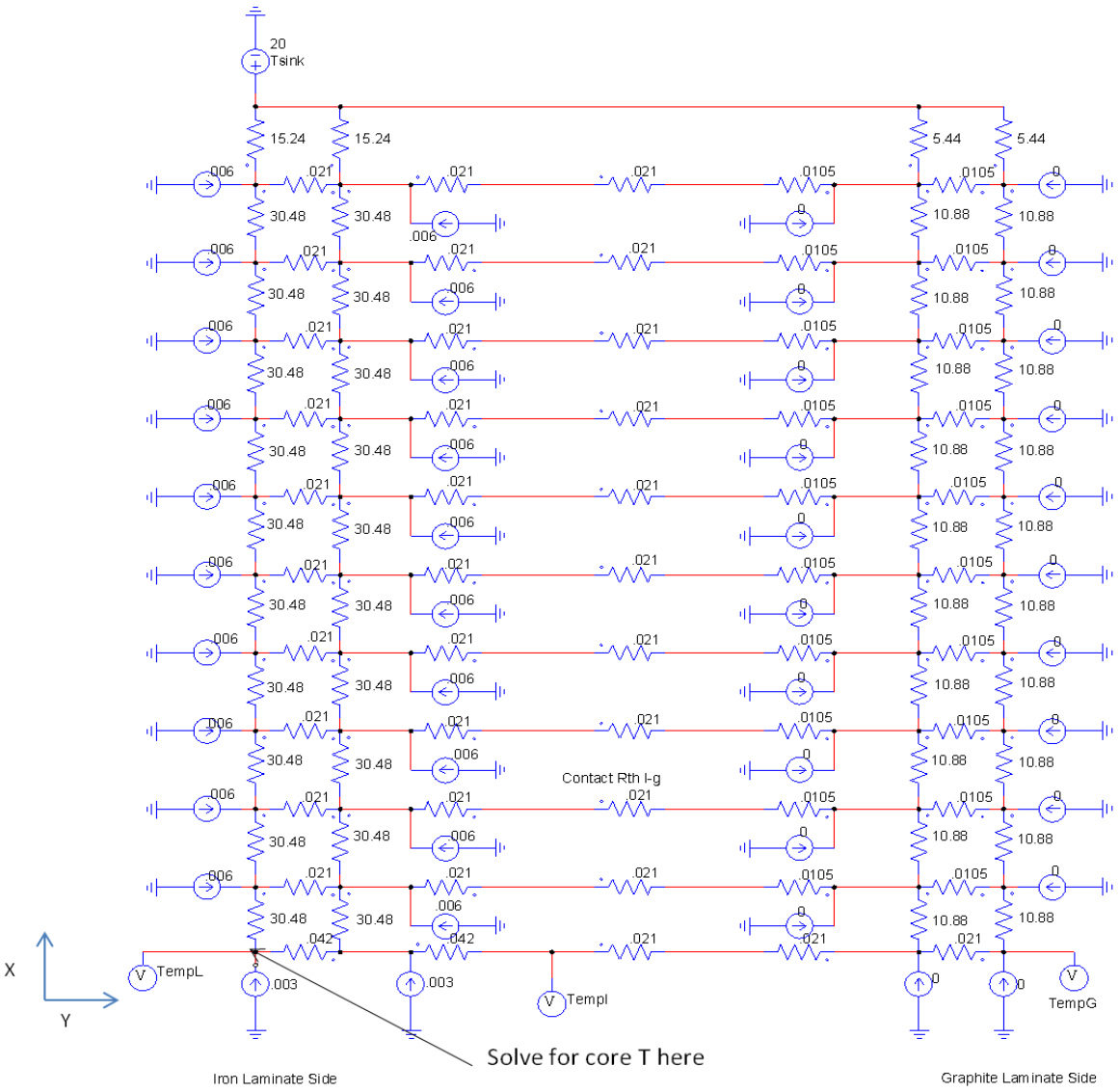

Figure 4.6. 42 node LPTN model for the ILC analysis as implemented in PSIM.

This value translates into 0.0875 °C/W for the model. The model physical dimensions, material properties and dimensionless parameters are shown in Table 4.1. It should be noted that the physical properties of graphite in the form of PGS, particularly its thermal conductivity, are highly anisotropic, as can be seen by the respective values in the x and y directions, kg_x and kg_y, respectively and are based upon the thickness of the

sheet, i.e. 100µm, 10µm or other available sizes. The properties were taken from the Panasonic data sheet for Pyrolytic Graphite Sheet (PGS) as detailed further in Appendix A. A unit value of 1, representing 1 Watt was selected for the thermal input at the iron laminate nodes. Since there are only 2.5 nodes in the first network (a result of the model symmetry) the total thermal input to the iron laminate was therefore 2.5 watts. There are no consequences to this selection as will be discussed shortly. The heat sink temperature was set at 20°C.

Table 4.1. Physical dimensions and material properties for the ILC LPTN model.

Material dimensions and properties:	**Value**	**Unit**
Height of ½ section: h	25	mm
Length of section: l (depth into page)	25	mm
Iron lamination thickness: t_l	1	mm
Graphite lamination thickness: t_g	1	mm
Thermal conductivity Iron: k_l	50	W/mK
Thermal conductivity Graphite: kg_x	800	W/mK
Thermal conductivity Graphite: kg_y	20	W/mK
Model properties:		
Nodes in x direction	2.5	
Nodes in y direction in each material	1	
Dimensionless parameters:		
Ratio: t_l/t_g	1	
Ratio: h/t_l	25	
Ratio: kg_x/k_l	16	
Ratio: kg_y/k_l	0.4	

An important concept, originally developed for heat exchangers, but evident from the temperature results, is that of the "Effectiveness"[88] of the Inter-Laminate Cooling method as it is applied to the system at hand, in this case between the iron laminations. With the ILC a reduction in the maximum temperature of the iron at the centerline node is expected, which can be shown to be the maximum temperature location for the iron lamination where indicated in figure 4.6 as "Solve for core T here". The Effectiveness

(E) is defined here in this research as the temperature difference between the maximum material temperature at $t_l/t_g = \infty$ (no ILC present) and the material temperature at some t_l/t_g (ILC present), divided by the temperature difference between the maximum material temperature at $t_l/t_g = \infty$ and the heat sink temperature T_s.

$$E = (Tmax_{@\infty} - T_{@tl/tg})/(Tmax_{@\infty} - T_s) \qquad (3)$$

4.2.3 - Simulation Results.

Simulation results for maximum material temperature calculated via the five node model of Figure 4.5, data Table 4.1 are shown below in Table 4.2 below for the thermal input of 1 Watt (the unit value of 1), and ratios of iron laminate thickness to graphite laminate thickness described.

Table 4.2. Simulation results from the five node model of figure 4.5, table 4.1.

Sink Temperature set to 20°C			Maximum Temperatures °C			
No.	Ratio t_l/t_g	Log_{10} t_l/t_g	Laminate	Interface	Graphite	Effectiveness
1	0.1	-1	21.35	21.31	21.31	0.9740
2	1	0	23.18	23.15	23.05	0.9388
3	10	1	40.02	40.00	39.99	0.6150
4	100	2	64.83	64.82	64.82	0.1379
5	1000	3	71.18	71.18	71.18	0.0158
6	∞	∞	72.00	72.00	72.00	0.0000

Result No. 6 is the case of the iron laminate structure without the presence of any graphite material as would be found in a conventional electric machine or transformer. No effects for iron laminate insulation were considered as these would be minimal due to the very low thermal resistance of such material as compared to that of thermal graphite, ie around 1W/mK to 1000W/mK typical of Lindstrom[89]. The defined "Effectiveness"

figure represents the cooling effectiveness for that particular ratio of t_l/t_g, a dimensionless parameter. It is the temperature difference between the maximum material temperature at $t_l/t_g = \infty$ and the material temperature at some t_l/t_g, divided by the temperature difference between the maximum material temperature at $t_l/t_g = \infty$ and the heat sink temperature. Plotting on a logarithmic scale reveals the graph of Figure 4.7. The cooling effectiveness is expected to approach a value of unity (1.0) when the graphite dominates and approach a value of zero (0) when the graphite is thin and the laminate dominates. In the latter case, where t_l/t_g approaches infinity, the maximum material temperature of the graphite approaches the value 72°C and consequently the cooling effectiveness falls to zero. In the former, where t_l/t_g approaches zero, the maximum material temperature of the graphite approaches the value of the sink temperature, or 20°C in this case, and consequently the cooling effectiveness rises to 1.0. This would be expected in the physical sense, hence the result is reasonable.

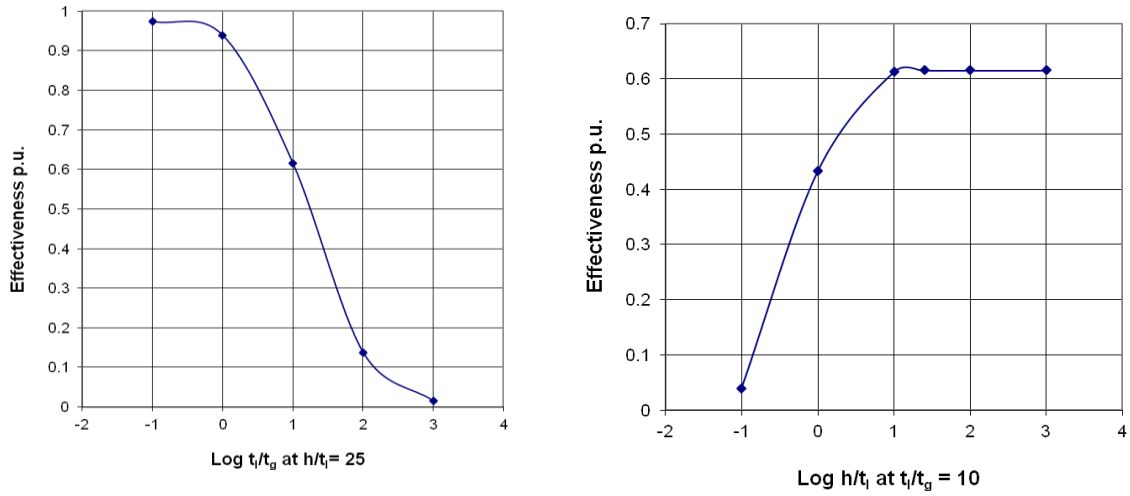

(a) Versus thickness ratio t_l/t_g at fixed h/t_l (b) Versus the aspect ratio h/t_l at fixed t_l/t_g
Figure 4.7. Cooling effectiveness versus thickness ratios and aspect ratio

The core losses were then adjusted based on the iron core size of the experimental transformer, details of which are given in the Appendix B, and a total core loss of 10W or 22.7W/kg. The result, again from the 5 node model, which translates to an input of 0.0037W at each node is displayed Table 4.3. Changes in the effectiveness are noted,

Table 4.3. Simulation results from the five node model of Figure 4.7, 10W core loss

Sink Temperature set to 20°C			Maximum Temperatures °C			
No.	Ratio tl/tg	Log_{10} tl/tg	Laminate	Interface	Graphite	Effectiveness
1	0.1	-1	20.02	20.02	20.02	0.991
2	1	0	20.16	20.16	20.16	0.931
3	5	0.69	20.61	20.61	20.61	0.738
4	10	1	20.97	20.97	20.97	0.584
5	100	2	22.04	22.04	22.04	0.124
6	1000	3	22.30	22.30	22.30	0.013
7	∞	∞	22.33	22.33	22.33	0.000

which may be the consequence of so few nodes applied over a rather large aspect ratio of 35:1 for the iron laminations to be discussed shortly. Taking item No. 3 of Table 4.3, where the t_l/t_g ratio = 5, a sensitivity analysis to input power was performed with the 5 node model the results of which are shown in Table 4.4. This t_l/t_g ratio equal to 5 was selected for further study as it is coincident with the combination of materials, iron laminations and PGS thickness that are commercially available.

Table 4.4. Sensitivity analysis with respect to core losses for the 5 node model of Figure 4.5

Sink Temperature set to 20°C			Maximum Temperatures °C			
Loss W/kg	Ratio t_l/t_g	Log_{10} t_l/t_g	Laminate	Interface	Graphite	Effectiveness
22.7	5	0.69	20.61	20.61	20.61	0.7382
	∞	∞	22.33	22.33	22.33	
75.7	5	0.69	21.99	21.99	21.99	0.7371
	∞	∞	27.57	27.57	27.57	
174.1	5	0.69	24.60	24.60	24.60	0.7367
	∞	∞	37.47	37.47	37.47	

It is clear from the result of Table 4.4 that the calculated effectiveness is invariant to the 2nd decimal place, or less than 0.2% over the range of core losses considered, short of an order of magnitude. Hence, the model was then progressed to a total of 42 nodes and a subsequent sensitivity analysis performed and compared to the results with that of the 5 node model as detailed in Table 4.5.

Table 4.5. Sensitivity analysis with respect to nodes, at fixed core loss 75.7 W/kg

Sink Temperature set to 20°C			Maximum Temperatures °C			
Node Count	Ratio	Log_{10}	Laminate	Ratio	Laminate	Effectiveness
5	5	0.69	21.99	∞	27.57	0.7371
21	5	0.69	21.86	∞	27.07	0.7368
42	5	0.69	21.86	∞	27.07	0.7368

Again, the calculated effectiveness is changed by only 0.04%. This finding was used as the basis for concluding that, for the purpose of the analysis here, a 42 node model would be sufficient to demonstrate the expected effectiveness and hence thermal performance of the ILC method. That performance would be governed not only by the thermal conductivity of the inter-laminate material relative to the laminations, but the physical parameters as well, the most important being the relative thickness of the iron-laminations to the inter-laminate material. To that extent, what could be studied and applied in practice, would be limited to the inter-laminate graphite, in this case PGS supplied by Panasonic, that what was readily available commercially. In short, the 5 and 42 node model not only served to simulate performance of the ILC method, but to also guide the design of the experimental apparatus which would be used to validate the concept.

4.2.4 – Design of the experimental test facility.

The effectiveness as a function of the ratio of t_l/t_g at a fixed h/t_l aspect ratio of 25, has been shown in Figure 4.7. The practical availability of graphite material in the form of pyrolitic graphite sheet (PGS) will determine the result in application. For electric machine or transformer applications where individual iron laminations thickness will typically range from 0.3mm to 1.0mm typically and given that PGS is readily available in a thickness of 0.1mm the effectiveness of the ILC will range from 61% to 80% in the best case scenario. If PGS were to be interspersed between several iron laminations, as opposed to between each lamination, then a consequently lower cooling effectiveness will be realized.

For the experimental transformer fixture available the iron laminations were 0.5mm thick and the range of PGS thickness readily available being 10µm to 100µm with thermal conductivities in the x-y plane of 1950 W/mK to 700W/mK respectively (Appendix C), thus a candidate sheet thickness was selected for further study. The cross plane thermal conductivity ranges from 10W/mK to 20W/mK and was not considered in the decision process as its impact upon the thermal resistance of the network is minimal given the thin nature of the sheets compared to the iron laminations. When examining the range of thickness options it was readily observed that the product of each available material thickness and its thermal conductivity lay in a range from 0.07 W/K at 100µm thickness down to 0.0195 W/K at 10µm thick. A 100µm thickness having a thermal conductivity of 700W/mK was selected as the suitable size to work with in further simulation study and the experimental verification. There were other practical considerations for this choice to be discussed shortly. With the combination of iron

lamination thickness of 0.5mm and 0.1mm (100μm) PGS thickness, the ratio $t_l/t_g = 5$, and $\log_{10}$ ratio $t_l/t_g = 0.69$, the expected effectiveness E, in the most ideal sense, would be 0.737 as evidenced from the preceding tabulated results and graph of Figure 4.7.

The value E=0.737 would, as stated, represent the best expected performance given the material properties and physical parameters employed. However, the model and calculations so far are ideal in the sense that there is neither consideration of thermal contact resistance between the iron laminations and the PGS laminations, nor between the laminations and the heat sink which is held at temperature T_s. Any contact resistance will serve to degrade the effectiveness of the ILC method from the stated ideal value. Accordingly, this impact had to be understood before the experimental apparatus design could be concluded and constructed.

Panasonic provides some guidance with respect to contact resistance of PGS to other materials, as provided in Appendix A. Using their stated values for the highest contact resistance of PGS to finished aluminum (as none was given for iron) an estimate was made on the impact to effectiveness by examining a range of thermal contact resistances around these values and beyond. The thermal contact resistance was introduced into the model between the iron-laminations and PGS as a pure resistance element whose value was taken as a multiple of the cross planar (z-plane) thermal resistance of the PGS. The effectiveness degradation was determined at several multiples, the result of which is shown Figure 4.8a for $t_l/t_g = 5$, along with the net effectiveness resulting from the degradation. A value of zero implies no degradation and no impact upon effectiveness, whereas a value of 1.0 implies full degradation of performance leading to an effectiveness of zero.

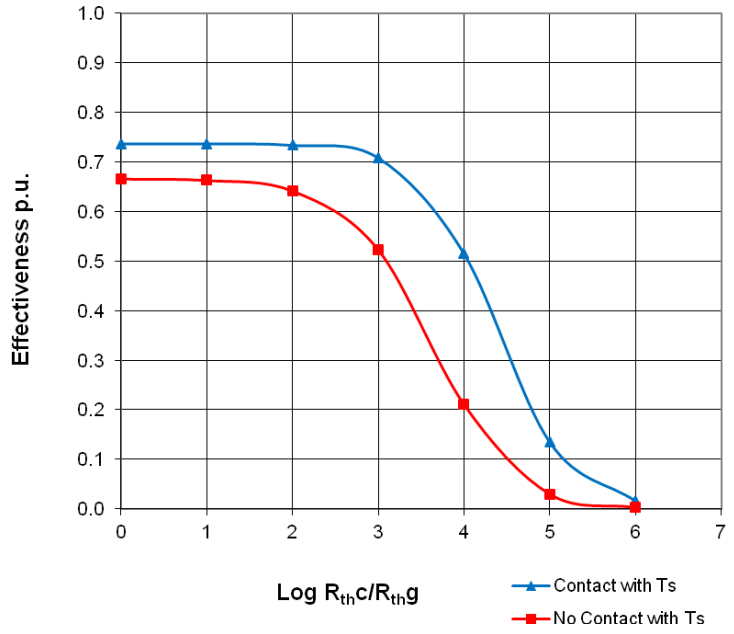

(a) Degradation of cooling effectiveness with contact resistance to the heat sink and contact resistance between iron laminations and PGS.

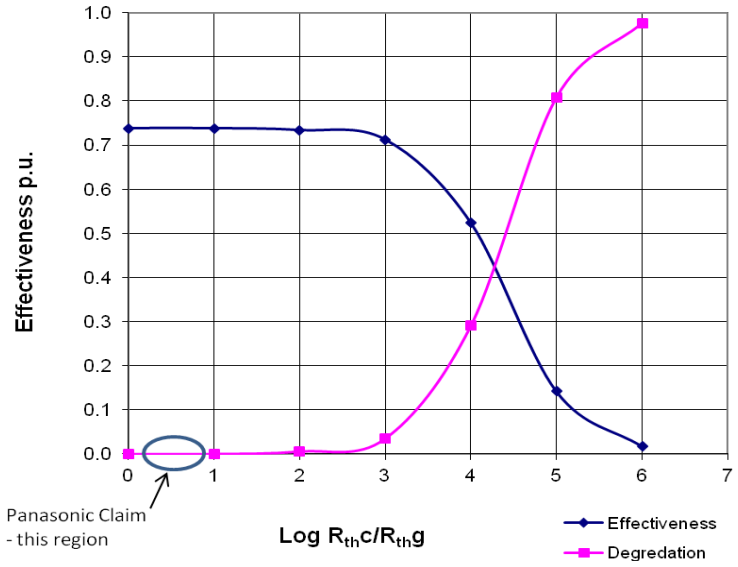

(b) Cooling effectiveness and degradation vs. contact resistance between iron laminations and PGS.

Figure 4.8 Degradation of cooling effectiveness

Further considered was the contact resistance between the PGS and the heat sink. There are, of course, no stated values for such resistance in the literature. Since the PGS sheets are thin and not rigid, compared to the neighbouring sheets of iron-laminations, they would be expected to exhibit little if any contact pressure against the heat sink, which could, in effect, pose a substantial barrier to thermal transport in this area. Given that, the simulation was carried out with the assumption that there would be no contact between the edges of the PGS sheet at the heat sink or, in other words, the thermal resistance would be infinite in the worst case. The result upon the cooling effectiveness of this scenario where $t_l/t_g = 5$ is shown in Figure 4.8b. The best case value for E is reduced from 0.737 to 0.667 or only 7%. This is quite a remarkable and encouraging observation, since it demonstrates is that even without any direct contact of the inter-laminate cooling material to the heat sink, the ILC is, nonetheless, an effective means for heat transfer from the internal region of the electric machine (or transformer in the experimental case) to the heat sink, since any heat flux will, at the point of reaching the end of the sheet, return to the heat sink via the neighbouring iron lamination material.

Another consideration was the effect of the aspect ratio upon the calculated effectiveness E. Several aspect ratios were studied ranging from $h/t_l = 10$ to 200 over the full range of t_l/t_g as shown Figure 4.9. It is clearly evident that over the range studied the effectiveness of the cooling method is not limited by the aspect ratio and is rather invariant to it.

What does this mean in a practical operating sense? In short, the ILC method, like any other applied cooling method, will serve to either lower the operating temperature at some point of interest, in this case the iron core temperature under study

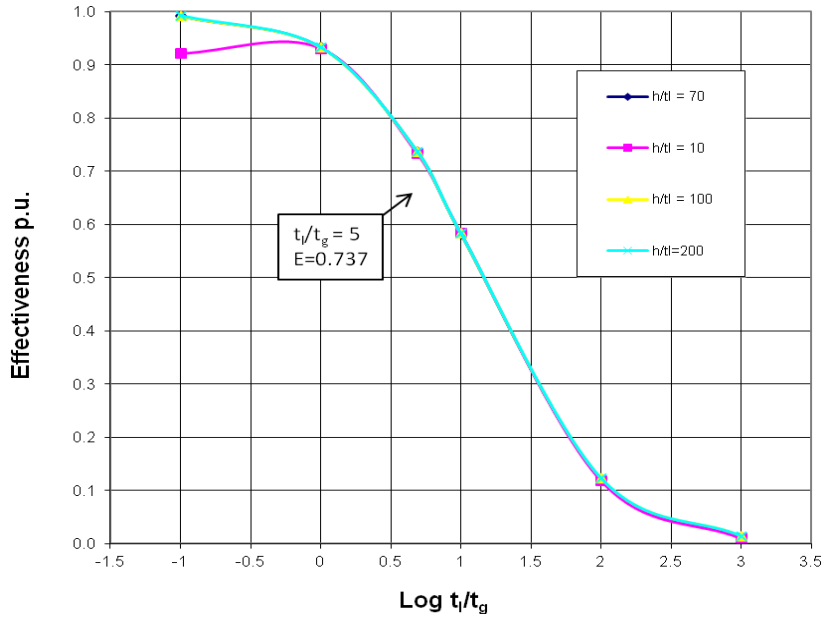

Figure 4.9. Cooling effectiveness versus aspect ratio

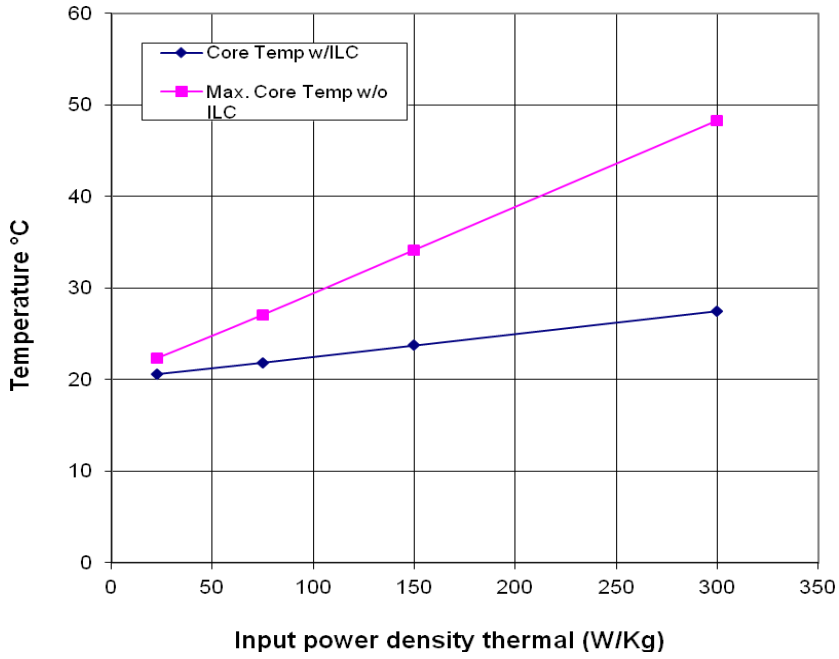

Figure 4.10. Allowable gain in operating input using ILC with PGS

or, it will serve to permit a greater thermal input for any allowable temperature limit of the material as illustrated Figure 4.10. Here, the study considers ideal conditions for E = 0.737 and $t_l/t_g = 5$. The "Max. Core Temp." represents the maximum temperature realized for a given thermal input without applied ILC, i.e. no PGS and the "Core Temp" is that realized with ILC, i.e. including PGS. It is observed that the same temperature of 27°C is reached at a power input that is 4x greater than that where no ILC is present. The gain, "G", in allowable heat dissipation is governed by the relationship:

$$\text{Gain in heat dissipation, } G = 1/(1-E) \qquad (4)$$

4.2.5 - Conclusions from the Simulation Study and the Test Facility Design.

A number of important conclusions were drawn from the results discussed. The cooling effectiveness, E, is wholly dependent upon the thermal conductivity of the material and its thickness and, equally, by association, the product of those two properties. The effectiveness is independent of the heat generation within the iron lamination material and the aspect ratio of its height to its thickness. E constitutes a dimensionless parameter in terms of temperatures, changing here only with the thickness ratio of the iron and PGS laminations. The gain, G, in allowable heat generation for a given temperature limit is raised by the value 1/(1-E).

4.3 EXPERIMENTAL TEST FACILITY

4.3.1 – Test Inductor Construction.

As discussed in the introduction, an inductor, would be the logical approach with which to study the ILC method in the applied physical sense. A readily available transformer build kit was selected for convenience having the physical dimensions in the same order as those of the simulation study, as detailed in Appendix B. The inductor was wound as a single coil where each turn was formed from multi-strand copper wire connected in parallel. The inductor was fitted with a modified lamination at its center point width that allowed a thermocouple probe to be inserted to the center of the iron core. Each lamination stack end surface was fitted with a heat sink that was maintained at a constant temperature by a recirculating water bath chiller capable of absorbing 500W of thermal energy while maintaining a temperature of 20°C, the heat sink temperature fixed for the duration of the test, and regulated to within 0.1°C – more than sufficient for the purpose of the tests. Initially, two inductors were constructed, one with inter-laminate PGS, the other without, but having instead a paper of equal thickness to the PGS as a substitute; this was the control inductor. This method was adopted based upon some early observations in trial construction that the inductor's inductance, and hence the current draw, was slightly affected by the spacing of the iron-laminations. The presence of any inter-laminate PGS material forces a small space between the iron laminations which affects the leakage paths in the iron thus lowering the coil inductance. This feature would require adjustment of the input voltage to maintain the same coil current conditions between samples. This was a concern as it would be based on the assumption

that the heat flux was predominately vertical, towards the heat sinks, as opposed to axial, which had already been shown to be insignificant in the literature where electric machines were concerned. In any event, a third inductor, the "no-material" inductor was constructed without paper, to evaluate and verify this assumption and problem solution. See experimental set-up Figure 4.11.

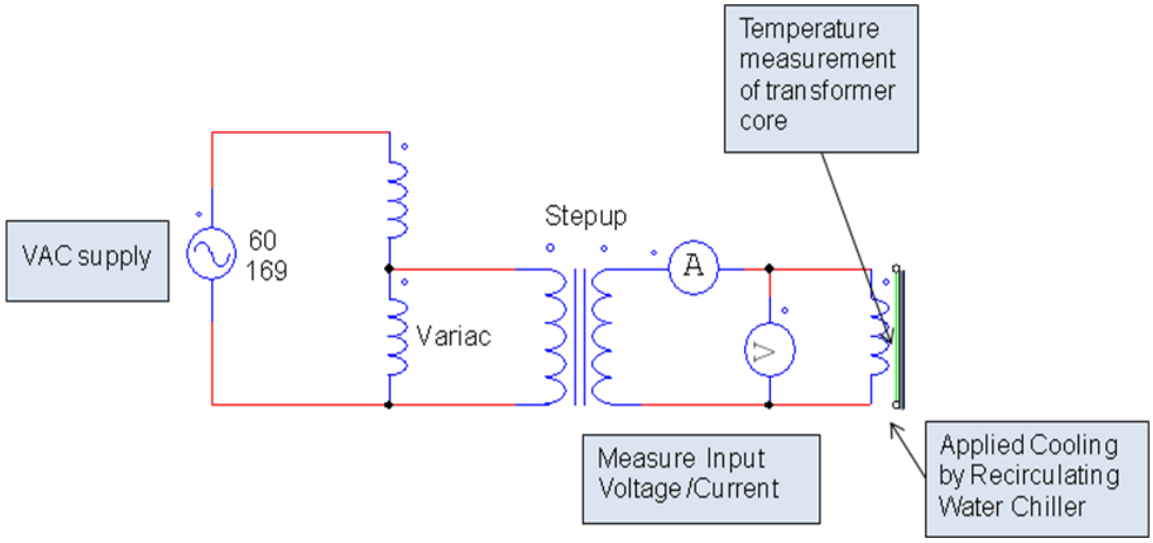

Figure 4.11. Schematic of experimental test procedure for the ILC inductor.

As stated, a transformer build kit was used for the test inductor construction. The iron laminations of the E-I style, M-19 material and 0.5" thickness were already available and predetermined from the kit. The inductors would then need to be supplied with a wound coil, coil former and coil insulation, the inter-laminate material (PGS and paper or none) and last but not least of which the thermocouple for temperature measurement. Altogether 37 such laminations of each material were fabricated for the purpose of the experiment. The coil winding was designed based upon a target of 120VA capacity to result in a 1A current at 120VAC with a wire size that would be sufficient to handle the coil current and provide the maximum number of ampere-turns that could be realized

within the space provided. Although the target number of turns was determined at 500, only 405 turns of 4 strand #27 copper wire were possible within the actual winding space after construction. The coil winding method is shown in Figures 4.12(a)-(c). The coil former was constructed light gauge corrugated cardboard (2 mm or .079") impregnated with polyurethane varnish and wound over a wooden mandrel, Figure 4.12(b). This was powered by a manual hand drill with the winding tension governed by hand, Figure 4.12(c).

4.12(a) Multi-Strand coil winding set-up

4.12(b) Coil winding machine – hand driven

4.12(c) Coil winding in progress

4.12(d) Coil former with partial winding

Figures 4.12(a), 4.12(b), 4.12(c) and 4.12(d)

Hand winding is not the most desirable method of construction as the winding space is seldom efficiently packed to the maximum available which would be achieved via a more precise automated procedure hence only 405 turns were realized instead of the desired 500 turns. Further, hand winding produces an uneven tension within the strands with some being stretched more than others, which may affect their resistance. To compensate, the three coils wound for the inductor builds were matched for their resistance by adjusting the end lead lengths to bring the DC resistance to within 10 milliohm, or 0.5%, 2.653 ohm and 2.656 ohm. Notwithstanding, an error in the winding count remains possible but its effect upon the result would be minimal as the core flux is near saturation and a few turns error out of a total of 407, even if the response were linear, would only be on the order of 1%, which applied over a temperature difference of less than 10°C would result in an error in the result due to winding error which would be on the order of 0.1°C, which is less than the tolerance of the thermocouple at 0.3°C and well under the digital instrument readout of 1°C. In other words a substantial error in the winding count would be required to affect the outcome of the result in a measureable way, i.e. greater than the tolerance of the thermocouple.

The most difficult task was the manufacture of the inter-laminate PGS material. Several methods were considered and two, stamping and cutting (by sharp knife), were tried. The latter proved to be the most successful (but time consuming) at producing an accurate cut with the least damage, although a few pieces were torn in the learning curve of the process. Accuracy would be essential as there would be gaps between the E and I iron lamination sections where they joined, as illustrated Figure 4.14(a), so any such gaps were to be minimized by employing an accurate cutting and alignment method, although

the arrangement of the inter-laminate sheets was such that there would always be an unbroken thermal path from the laminations to the heat sinks. The cutting of PGS sheets is shown Figure 4.13(b) where an iron lamination was used as a template for the process. The PGS was cut with an excess of material to be trimmed later in the construction, as shown in Figure 4.13(c). The cutting of the paper laminations for the control inductor was performed in an identical fashion. The partial core construction with paper laminations is shown figure 4.13(a)

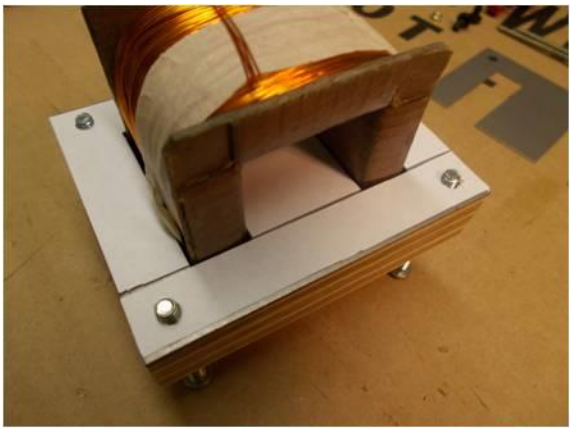

4.13(a) Transformer paper inter-

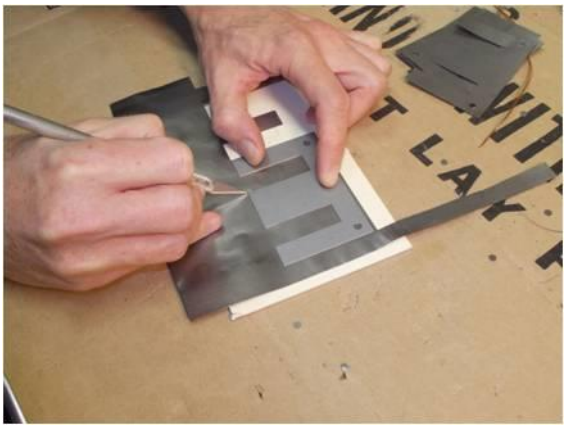

4.13 (b) Cutting PGS inter-laminations

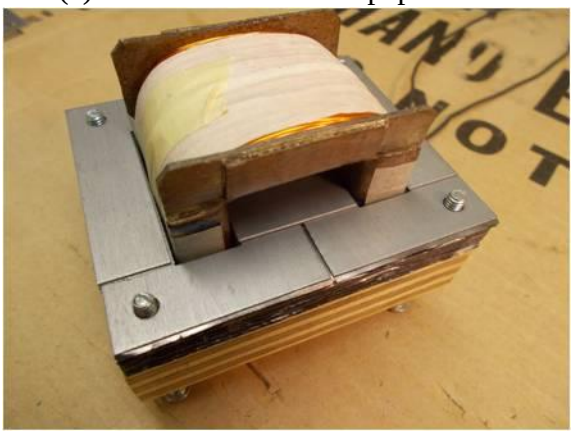

4.13(c) ILC transformer thermocouple slot

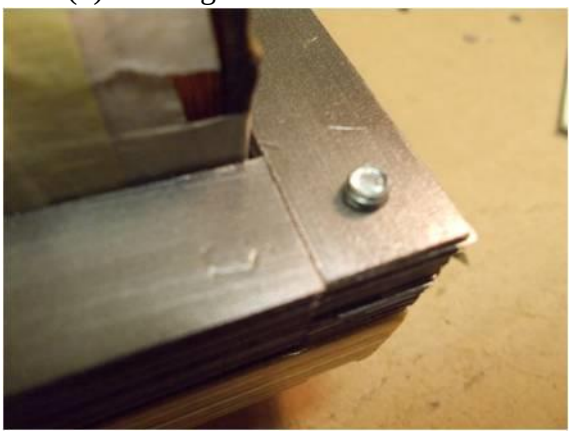

4.13(d) ILC PGS fit at E-I laminations

Figures 4.13(a), 4.13(b) and 4.13(c)

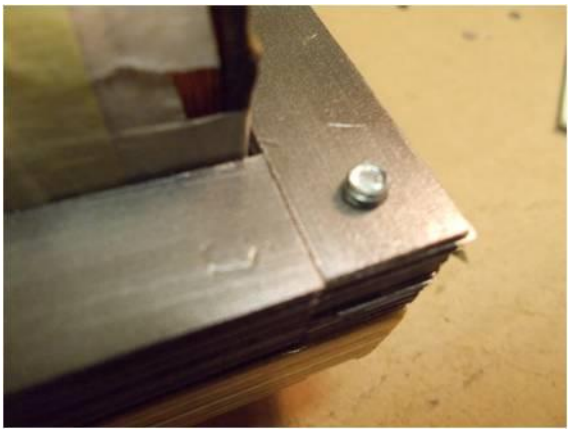

4.14(a) ILC PGS fit at E-I laminations

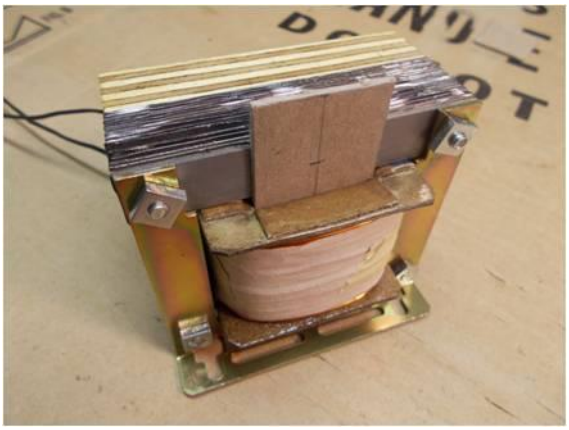

4.14(b) Inductor test assembly

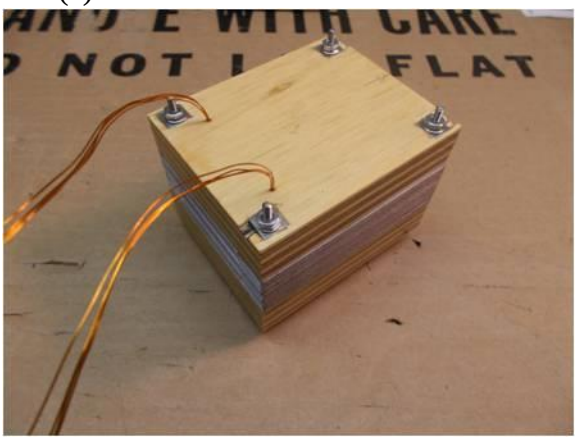

4.14(c) Completed ILC inductor assy.

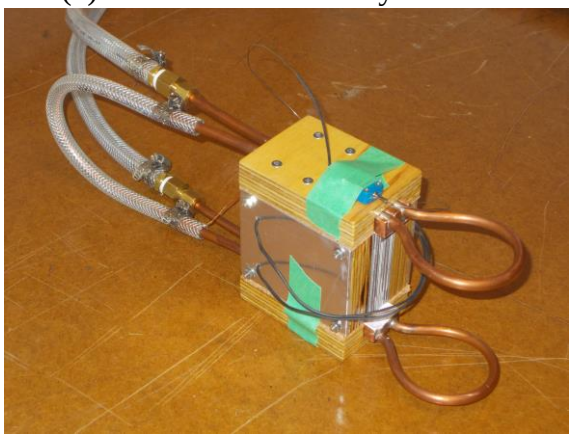

4.14(d) Final inductor assy. with heat sinks

Figures 4.14(a), 4.14(b), 4.14(c) and 4.14(d)

The assembly of the pieces would need to be carefully controlled. The transformer build kit as delivered was not well suited to the task. A jig was developed to maintain a close alignment between the iron laminations and the PGS as the assembly progressed. This consisted of a wooden block fashioned from common ¾" plywood such that the wound coil former when completed would sit with one internal edge of the opening in a position level to that of the inside block surface. A pocket was fashioned in the block to accept the wound coil former. Four machine screws were selected with a

size to provide a close fit to the laminations' mounting holes, and fixtured within the block at each corner shown such that they could be advanced as the laminations were laid into place during construction as shown in Figures 4.13(a) and 4.13(c) and 4.13(d). Each transformer was fitted with 37 laminations, and the required inter-laminations, the mid-point one being cut to permit the acceptance of a stainless steel thermocouple probe which was inserted after construction of the transformer assembly but prior to affixing the heat sinks into position, Figure 4.13(c). Both the materials of the coil former and the jig, corrugated cardboard and plywood respectively, were selected for their ease of construction and their insulating capabilities so as to not only prevent heat loss but also to limit the amount of heat transfer into the iron core from the coil. Any remaining space between the coil former and the lamination stack was taken up with a shim, Figure 4.14(b), to maintain pressure against the lamination stack, sufficient to provide a positive contact without being so excessive as to neither deform the coil former nor crush its corrugated cardboard construction thus defeating its insulating quality.

Once completed, the assembly screws were withdrawn one at a time and a smaller insulated machine screw was inserted in its place to hold the assembly together once bolted, but not too tightly so as to permit a final alignment. At this point the laminations were aligned to permit proper contact with the long edge surfaces that would be in contact with the heat sinks. This was necessary as improper contact could lead to significant error in the results due to excessive thermal resistance at the interface of these two surfaces. Figure 4.14(c) shows the final inductor assembly. The final alignment was carried out with the aid of precision machined steel blocks with the entire assembly firmly clamped in a vise to provide sufficient force to meet alignment and ensure contact

of the internal E and I iron core sections. Once the final alignment was completed the assembly bolts could be firmly tightened.

Once assembled, aligned and tightened, the transformer block of Figure 4.14(c) was fitted with a heat sink along each long end, as shown Figure 4.14(d). The heat sinks were constructed of solid copper with a contact surface milled to within .0005" and mirror polished with rouge. The coolant feed was arranged through a U shaped .25" copper tube fully soldered into position in slots within the sink block. From there, suitable hardware was supplied to connect the recirculating chiller bath which served as the coolant supply for the experiment.

4.3.2 – Complete Test Facility.

With the fully completed assemblies, each inductor was connected in turn to the electrical supply which consisted of a 120V-240V step-up transformer coupled to a 120V Variac 60Hz. A voltage meter and current meter were inserted to monitor the inductor voltage and current inputs. The inductor heat sinks were supplied with coolant from the polystat^{TM} recirculating water bath chiller, which could be configured to supply coolant in a full range of temperatures from -10°C to 90°C at a heat transfer capability of up to 500W – more than sufficient capability for the range of tests performed. The full inductor test facility is shown in Figure 4.15.

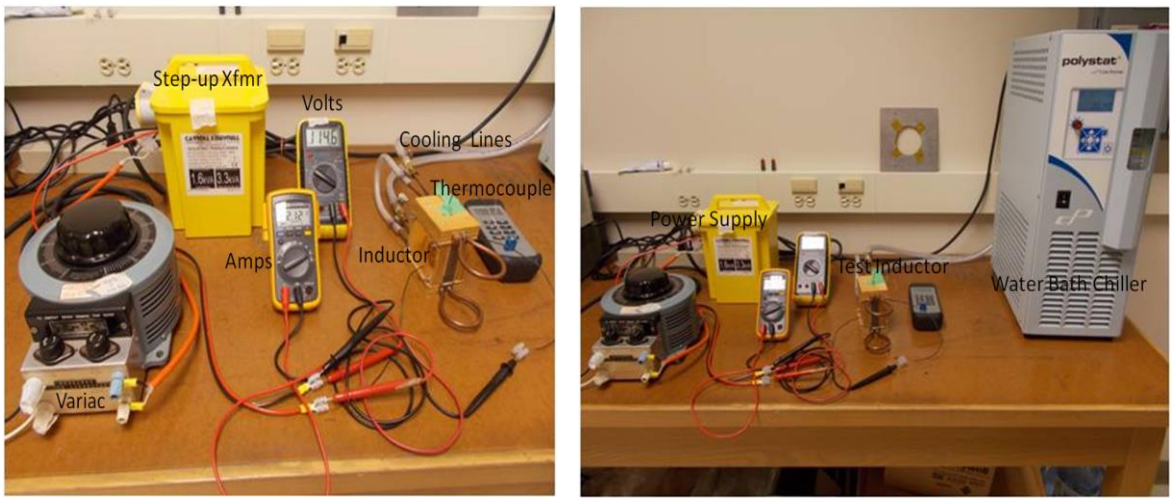

Figure 4.15. Inductor test facility showing power supply, inductor assembly, thermocouple display and recirculating water bath.

4.3.3 - Temperature Monitoring and Data Collection.

The recording of temperature data was performed manually by simple reading of the thermocouple (TC) output every few seconds initially during the transient response then every few minutes as the temperature at the core began to stabilize and reach equilibrium. The available TC monitor, a Ken-May KM340 digital TM, is a digital device with resolution to 1°F, was suitable only for a type K thermocouple. However, a type T thermocouple had to be chosen since this was the only device available in the size range required, i.e. less than the 0.5mm thickness of the iron lamination. Accordingly, the TC monitor was re-calibrated for the purpose by a two point calibration employing the ice-water and boiling-water bath method. Intermediate points were established by direct comparison method employing a stable warm water bath. This resulted in a calibration correction curve for the type T thermocouple as utilized in the type K TC monitor. Temperature readings were then taken directly from the monitor and adjusted

by means of this curve to provide the correct type T reading. The calibration correction curve is provided in Appendix C. All temperature readings from the TC device were taken directly in degrees Fahrenheit then converted to degrees Celsius for reporting purposes.

4.3.4 - Experimental Procedure.

The control inductor was tested first, connected to the power supply described in the section 4.3.2. The recirculating bath chiller was set to provide a steady coolant temperature of 20°C (68°F) to the heat sinks which were set up to flow coolant in a series configuration, so as to guarantee the same coolant flowrate in both heat sinks. The temperature rise across the coolant was less than 0.5°C (1°F) based upon the capacity of the chiller and the maximum flowrate of the coolant water. Each inductor test was started from room temperature where the coolant had been applied for some time such that the core temperature was nominally at a steady 20°C (68°F). The inductor current was then applied instantaneously at values of 2.0A, 2.5A, 3.0A and 3.5A to the coil, with the resultant voltage of 115V, 119V, 123V, 127V, respectively. The coil currents and voltages were matched for each of the inductor cores showing the equivalence of the electromagnetic circuits. The core temperature was taken directly from the inserted thermocouple and noted, initially every few seconds then, every few minutes, as the internal temperature climbed towards the equilibrium value. The temperature readings were terminated when the value did not change over a twenty minute period. Often, the thermocouple temperature indicated was not steady between two integer values, and was noted as such to be later interpreted as a half value; a shortcoming of using a digital

device. This same procedure was repeated for the other two inductors, i.e. the ILC PGS inductor and the no-material inductor.

Each of the inductors, except the no-material inductor were tested with a 3.0A input to the coil with the cooling water temperature increased to 80°C (176°F) in steps of 20°C (36°F); an additional 3 trials for each. This was done to examine the sensitivity of the experiment with respect to the absolute temperature, of which there should ideally be none.

4.4 – EXPERIMENTAL RESULTS

The measured temperature data, once compiled, was corrected using the calibration curve for the type T thermocouple as discussed previously, and plotted as a series of temperature-time curves shown in Figures 4.16(a) though 4.16(d) for each inductor and current setting. The data shown for the 3.0A coil current condition is also shown with the tolerance range of the thermocouple temperature as indicated by the dashed lines above and below the nominal readings. This was to demonstrate, for one condition at the least, the significant difference in the temperature readings between the ILC and non-ILC inductors, as described shown to be greater than that of the tolerance of the thermocouple. From this data the value of E was thus calculated at the stable temperature, or equilibrium, condition. The no-material inductor test was performed at a coil current of 2.0A and 3.0A and was used to verify the non-ILC inductor which had included the paper laminations in place of the graphite laminations.

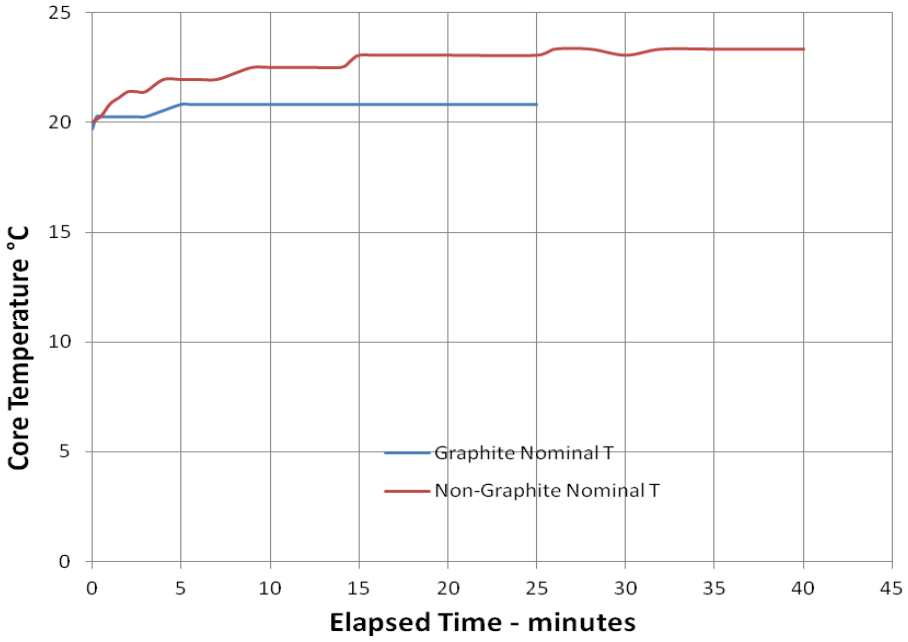

(a) 2.0A Coil Current

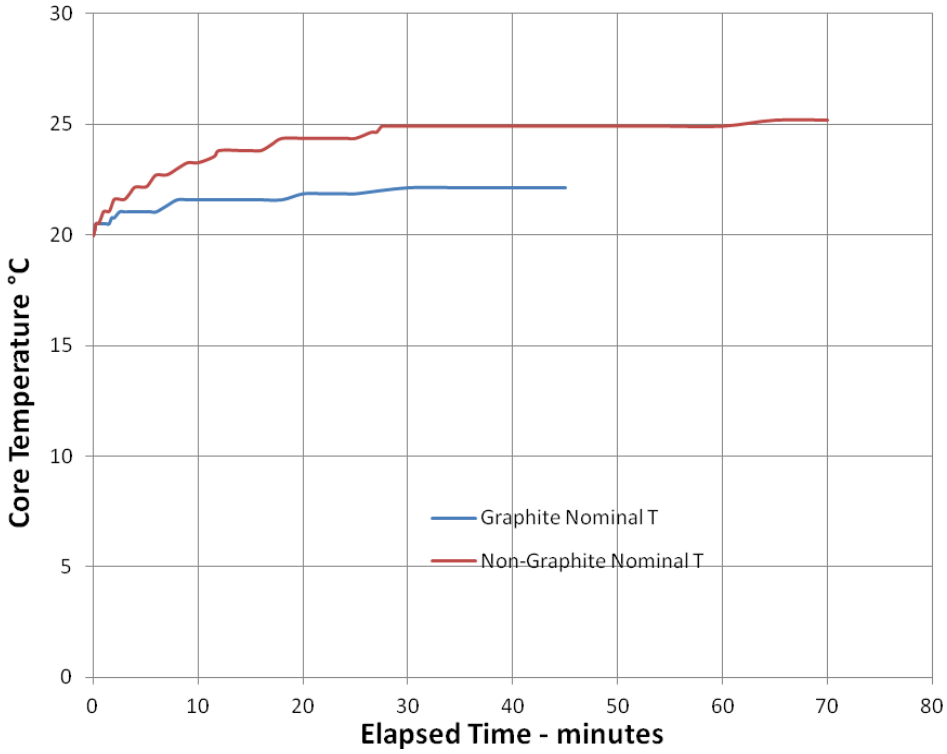

(b) 2.5A Coil Current

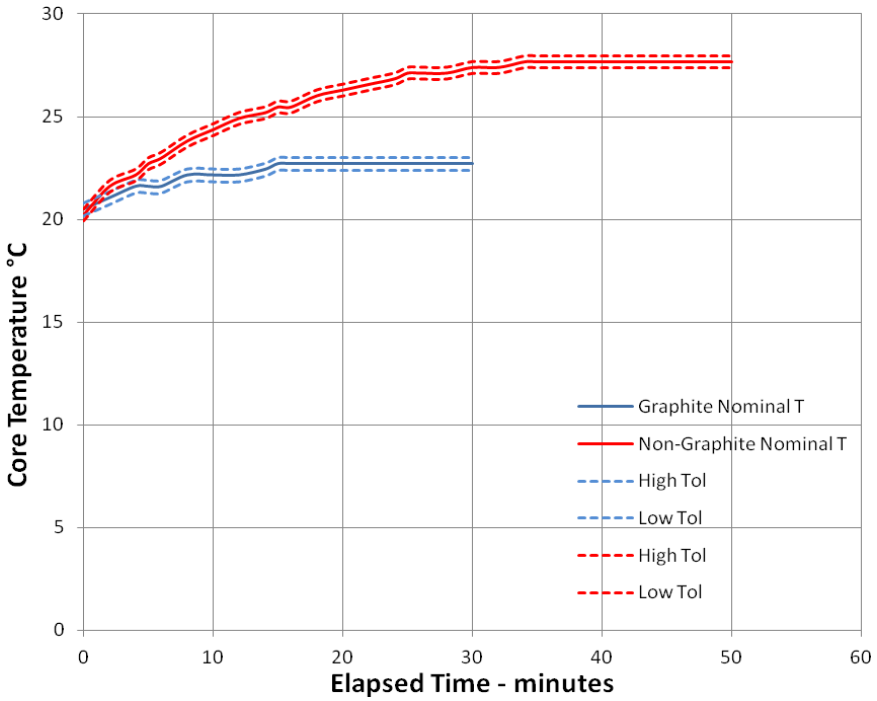

(c) 3.0A Coil Current

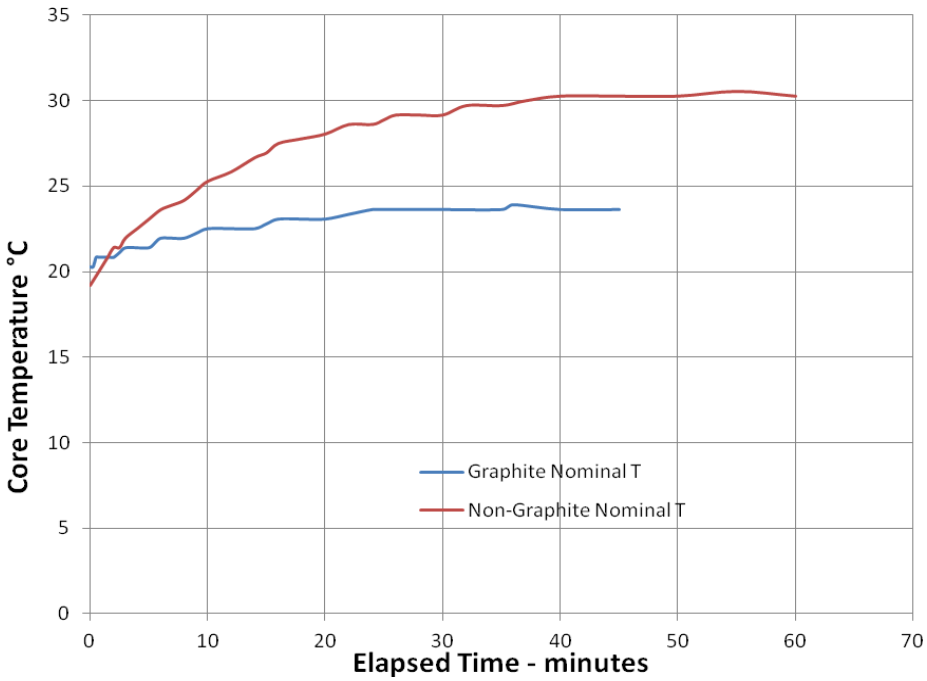

(d) 3.5A Coil Current

Figures 4.16(a), 4.16(b), 4.16(c) and 4.16(d). Inductor Core Temperature Response versus Time at Applied Coil Currents

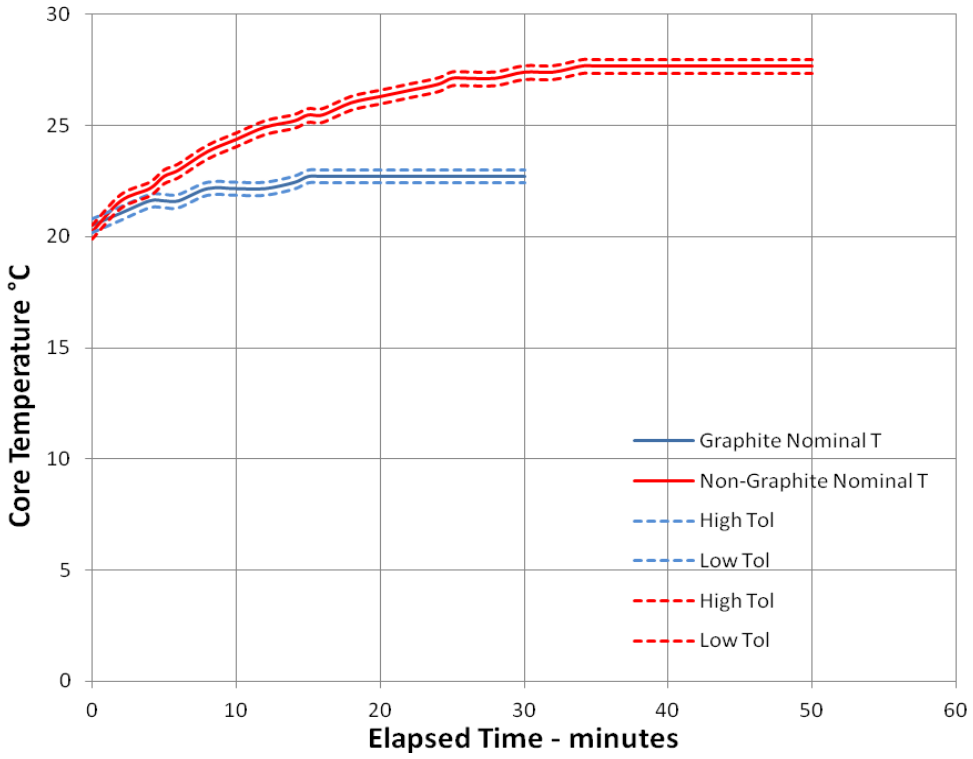

(a) 20°C Cooling Water

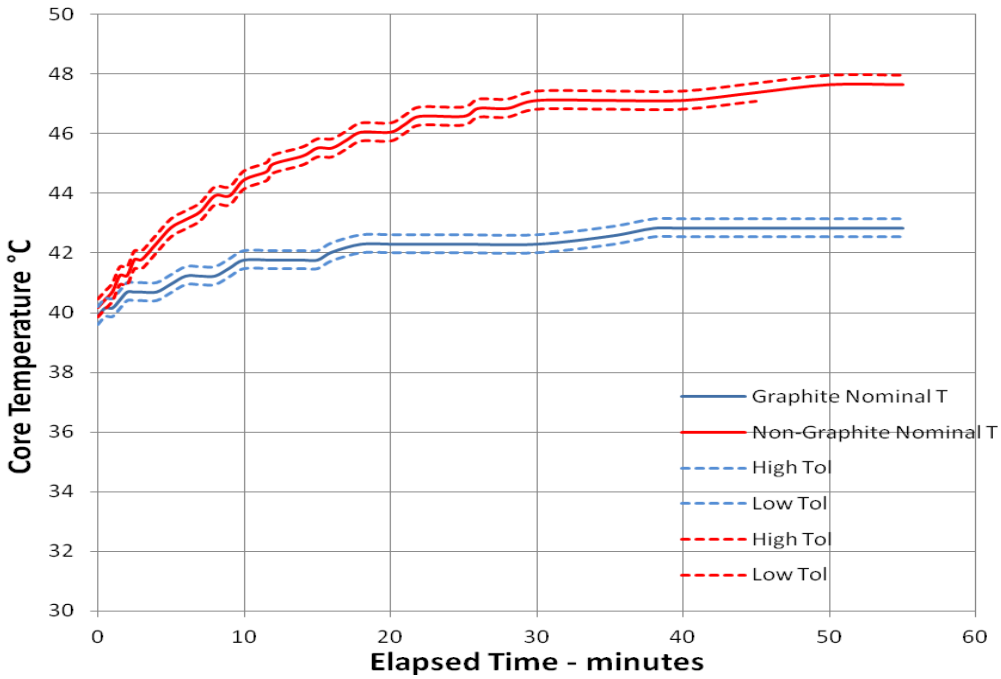

(b) 40°C Cooling Water

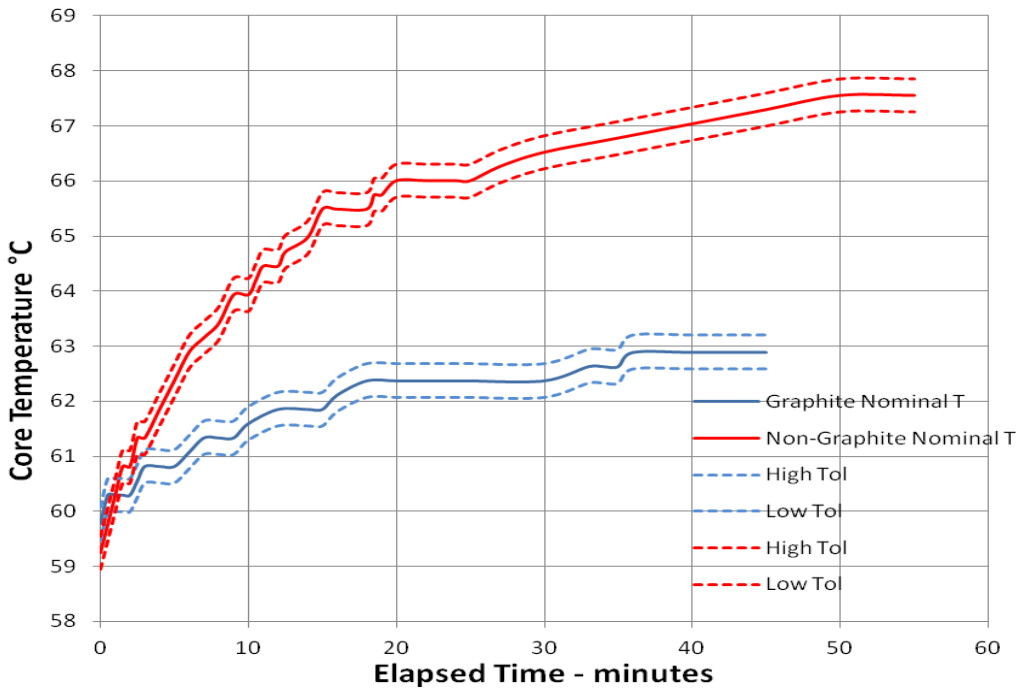

(c) 60°C Cooling Water

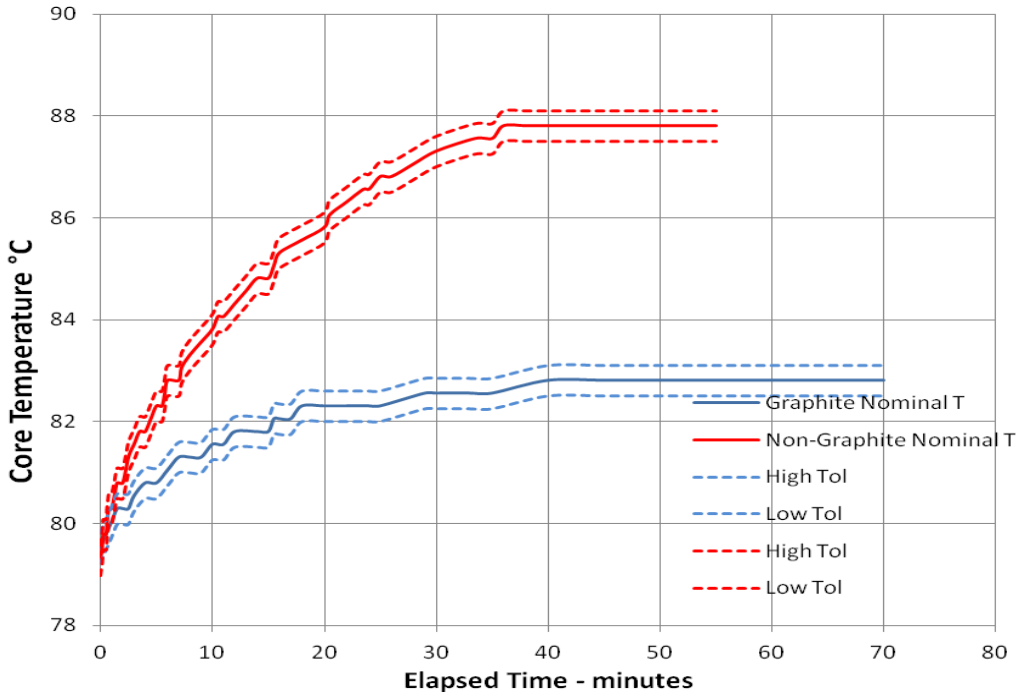

(d) 80°C Cooling Water

Figures 4.17(a), 4.17(b), 4.17(c) and 4.17(d). Inductor Core Temperature versus Time at 3.0A Coil Current at Different Cooling Water Temperatures

The no-material inductor under test conditions of 20°C coolant water, 2.0A and 3.0A coil current as stated, reached a maximum core temperature of 23.8°C versus 23.3°C and a temperature of 28.8°C versus 27.7°C, respectively. These are nominal values. The additional temperature may be attributable to a slightly higher input voltage, about 1V required to drive the same current which was observed during the trial construction. Further the temperature differences lie within the tolerance and uncertainty of the thermocouple display. In any event, the no-material inductor was not an indicator of axial heat transfer that would either support or refute the use of paper laminations in the control transformer. Moreover, it was shown in table 4.4 that the effectiveness of the method was invariant to the thermal input which would hold true whether that input was internally generated within the material or transferred across the boundary as would be the case with axial heat transfer.

The calculated values for E are shown in Table 4.6 below as are those for the second group of trials, figures 4.17(a) through (d) where the coolant water temperature was adjusted in 20°C steps from 20°C to 80°C, carried out at a fixed coil current of 3.0A.

Table 4.6. Calculated Effectiveness versus Coil Current and Coolant Temperature

Coolant Temp.→ Coil Current ↓	20°C	40°C	60°C	80°C
2.0A	0.75			
2.5A	0.58			
3.0A	0.67	0.64	0.62	0.62
3.5A	0.65			
Nominal	0.66			

From this collection of data the nominal calculated value of E was determined as being 0.67, which given the physical characteristics had an expected ideal value of 0.74.

This then constitutes agreement to within 10% of the expected ideal value. If however, the degraded performance is considered as discussed in section 4.2.3, then the calculated E from the experimental data is in complete agreement with that of the theory at 0.67. From the second group of trials where the coolant temperature was varied, it was determined that E further degraded by 10% over the temperature range considered, with increasing temperature of the inductor core. This result was not expected.

Finally, to close, the result as displayed in figure 4.18 with all results overlaid clearly demonstrates the gain, G, in the allowable input current, and consequently power, to the coil as the temperature condition of 23.5°C is realized with at an input current of 3.5A with ILC vs. an input current of 2.0A without ILC. Since power goes as the square of the input current, assumed to be apportioned equally as losses in either case, and the impedance of both coils is matched, the ratio of the ILC allowable power is 3.06 times that of the non-ILC allowable power, for the same temperature limit. This then is in agreement with the relationship G=1/(1-E) which would yield a result of G = 3 based upon the nominal E of 0.67.

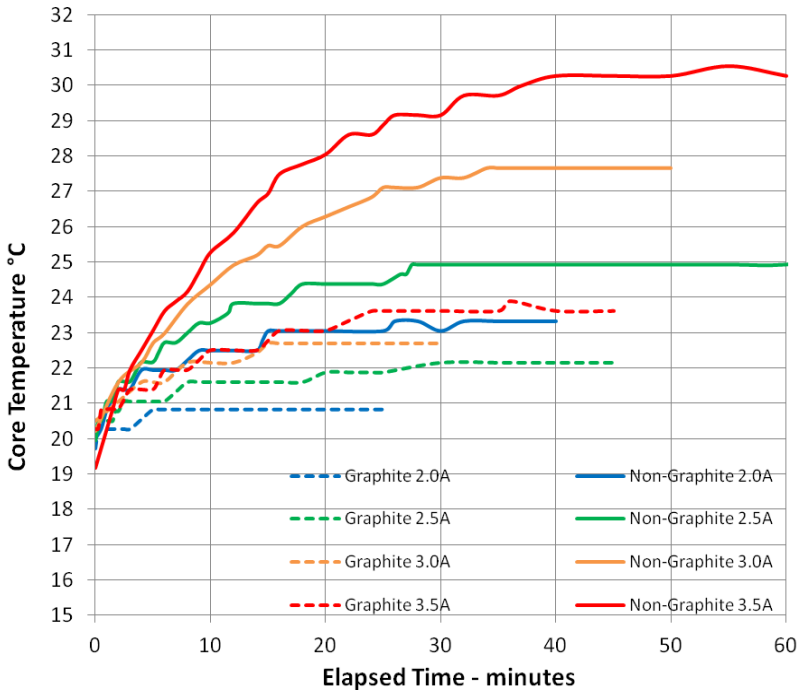

(a) All Results Inductor Core Temperature versus Elapsed Time

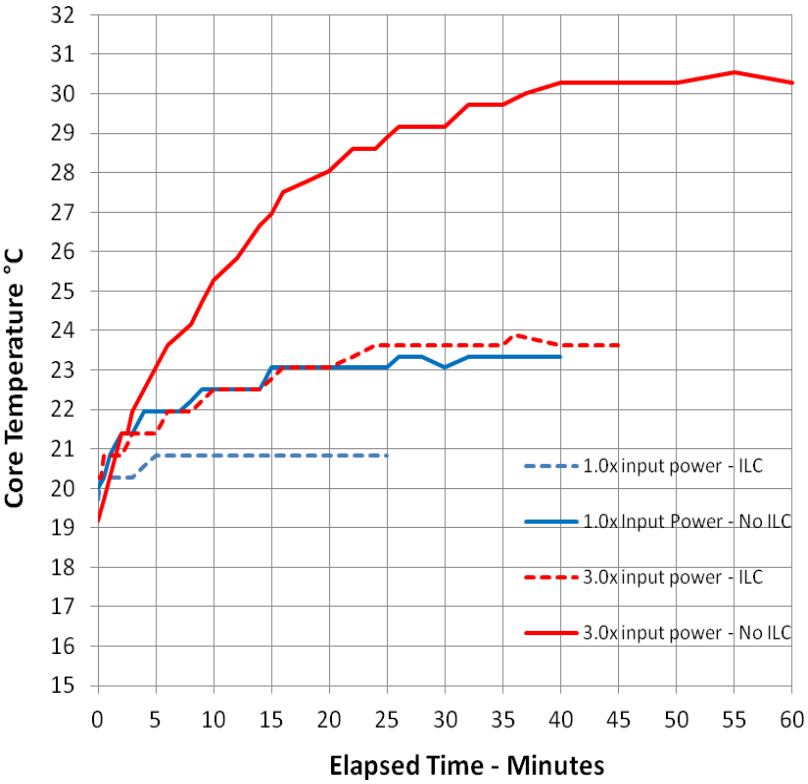

(b) Results Expressed as a Multiple of Input Power

Figure 4.18(a) and 4.18(b). Gain in allowable power with ILC PGS vs. no ILC

4.5 - CONCLUSIONS

Considering for the moment that the value of E at 2.0A coil current was determined as 0.75, which was greater than the expected ideal value 0.74, when this value is disregarded from the set, the nominal value of E resulting is 0.63, about a 15% error from the expected value. It is clear from the temperature data, and the resulting value of E determined from that data, that the experimental result has confirmed the theory; that E would be invariant to temperature and input power to the coil except as limited by the experimental methodology. The input power to the coil was shown to be increased for the same temperature limit where ILC with PGS was employed; the gain G in allowable input power was shown to result from E as expected in the relationship described section 4.4.3. Further, the degradation in the expected value of E from that of the ideal value, is most likely attributable to the poor contact between the terminating ends of the thin PGS inter-laminations with that of the copper heat sink as the value of E was in agreement with the simulation result of this condition which considered no contact would exist at all. There may be degraded performance due to poor inter-lamination thermal contact resistance. However, the lamination stack was tightly assembled, and any such further degradation as a result would have resulted in an effectiveness value less than that arising from poor contact to the heat sinks, although, strictly speaking there is no way at the present to make this determination with certainty.

We are surprised by the degradation in effectiveness due to the temperature of the coolant and consequently the overall transformer temperature. This may be attributable to heat loss where the temperature of the transformer assembly under test is significantly

greater than that of the ambient otherwise, the cause it not known. Accordingly, this may be an area for future research investigation.

CHAPTER 5 - A CONTINUOUS TOROIDAL WINDING SRM OPERATING WITH A 6 OR 12 SWITCH DC CONVERTER

5.1 - OVERVIEW

The subject material of this chapter is based upon two peer reviewed conference papers presented to IET Power Electronics Machines and Drives (PEMD) conference, April 2014, and IEEE Energy Conversion Conference and Exposition (ECCE), September 2014. A new toroidally wound switched reluctance machine (TSRM) with a single continuous multi-tapped winding (CW) is developed. This machine may be driven by a 6 switch asymmetric converter which supplies uni-polar coil currents, or a 12 switch voltage source converter that supplies bi-polar coil currents. The TSRM magnetic design and power electronic control is described, and its performance is compared to a conventional switched reluctance motor (CSRM) and, to a previously reported toroidal format switched reluctance machine that utilizes 6 discrete winding (DW) coils in a 3-phase wye connection (WSRM) driven by a voltage source inverter (VSI). A fixed 6-4 CSRM magnetic circuit design is selected for comparative analysis of the three machine topologies by static and dynamic finite element simulation.

5.2 – INTRODUCTION

Switched reluctance machines (SRMs) are increasingly a technology of interest for variable speed drives which may be found in automotive and industrial process applications. Although many authors have published in the field of SRMs, these machines generally employ a concentrated wound pole as illustrated in figure 5.1(a),

showing a typical 6-4 configuration. The machine drive topology is usually via an asymmetric converter suitable for the 6-4 SRM as in figure 5.1(b) with switch timing shown in figure 5.1(c).

Previous publications have reported benefits in the torque and efficiency of a form of toroidal switched reluctance machine (TSRM) configured with six discrete 3-phase wye windings (DW) referred to here as the "WSRM", and compared to a CSRM, see Sun et al.[90] and Lee et al.[91]. However, these publications are not specific in terms of the actual comparison criteria, nor do they reveal full machine details, which may result in their being somewhat ambiguous.

The subject TSRM of this paper, not previously reported in the literature, with a single continuous multi-tapped winding, is shown in figure 5.2(a). A continuous winding is defined here as one which is uninterrupted mechanically or electrically which may be constructed of individual windings joined in series to form said continuous winding. The TSRM machine may be driven by either a 6 switch asymmetric converter supplying uni-polar coil currents as shown in figure 5.2(b) and figure 5.2(c) respectively, or by a 12 switch voltage source converter that supplies bi-polar coil currents as shown in figure 5.3(a) and figure 5.3(b) respectively. The latter may also be readily configured to operate in a 6 switch mode, to be discussed further. At present, a full converter analysis is outside the scope of this paper and will be covered in a separate work.

In prior work, Lee et. al.[92] described a 6-4 TSRM having discrete coils situated around the machine stator back iron. The six discrete coils are connected in delta with two phases active during switching. Further they described a similar TSRM (DW) with

the discrete coils connected in a wye configuration with two phases active during switching. Either configuration may utilize a VSI drive. The characteristics of the WSRM in terms of current, torque, efficiency and power, are compared in detail to the CSRM by Lee et al.[93]. However, comparison results presented in Lee et al.[94] were made on the basis of equalized rated output power, but made under different conditions of voltage and current which may result in inconsistencies in the conclusions drawn from the results. For example, inconsistencies in ampere-turns yield inconsistent pole flux and field saturation, similarly winding loss analysis yield inconsistent efficiency comparisons. The TSRM configuration shows promise for vehicle motive power applications where the drive system power band is wide and nearly flat, hence the interest in this topology. The work of Lee et al.[95] was understood to be motivated by an SRM configuration that could operate in a conventional 3 phase industrial drive. What is sought here is a replication of the CSRM by the TSRM topology for alternative purposes.

Thermal performance is an important consideration in the design of electric machines, and the switched reluctance machine is no exception. The current motivation for the subject continuously wound toroidal winding topology has its origin in electric machine cooling enhancement. As might be evident from figure 5.2(a), the proposed TSRM design will place the majority part of the machine windings in the peripheral space formerly occupied by the machine frame or casing. This significant benefit, from a thermal performance standpoint, is one of providing either direct exposure of the winding to a cooling fluid, such as forced or natural convective air, or ready access to the winding in which to place a circulating liquid coolant conduit. The ability to enhance cooling in this manner will have a direct impact on the machine thermal rating and consequently its

specific power and torque available from a pre-defined space requirement. Simply put, improved cooling means more power from smaller package requirements.

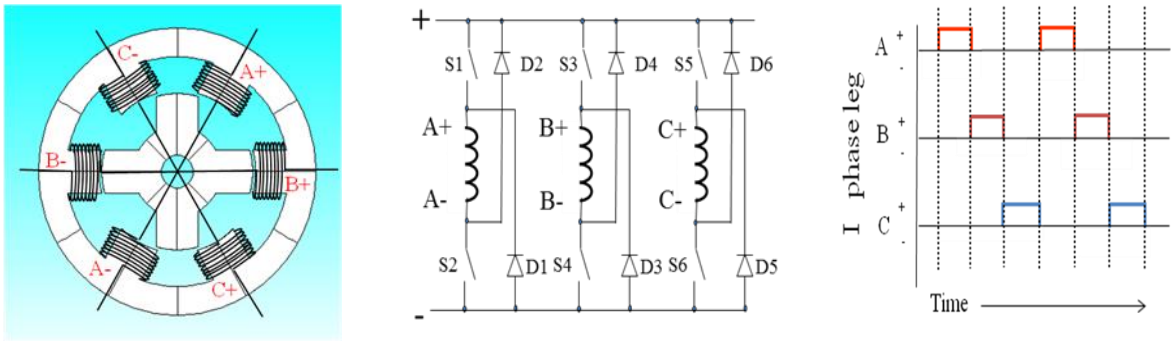

(a) Conventional SRM (b) Asymmetric power (c) Timing, phase currents

Figure 5.1. Conventional SRM

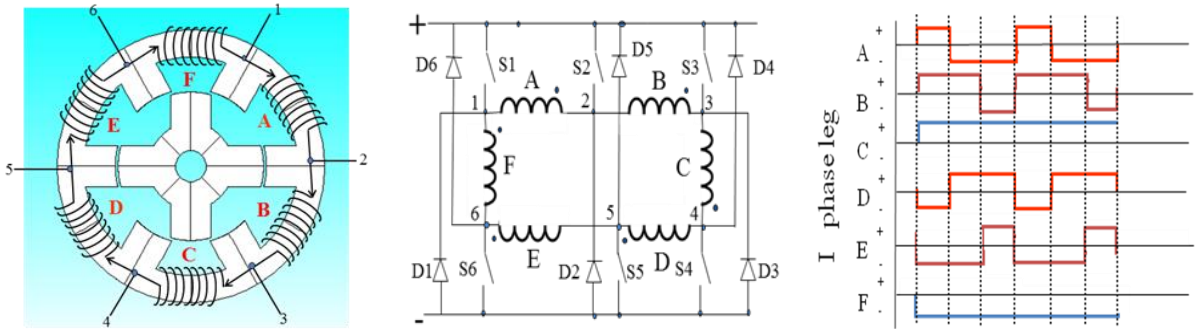

(a) Continuous Winding (b) A 6-switch converter (c) Timing, phase currents

Figure 5.2. TSRM (CW)

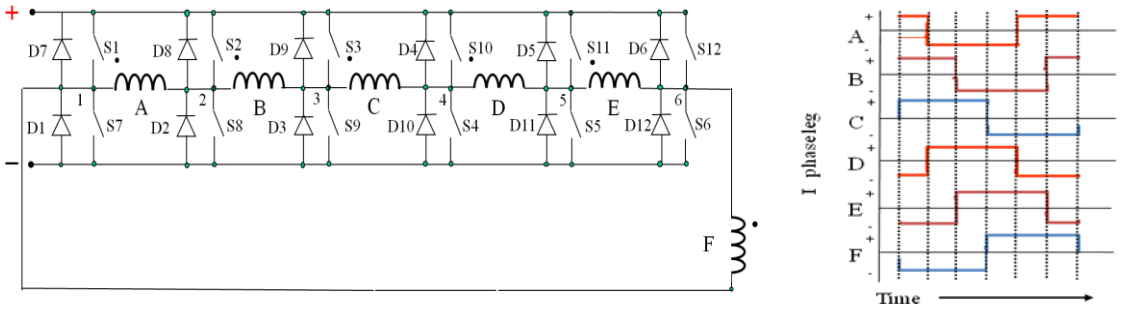

(a) A 12-switch power electronic converter configuration (b) Timing, phase currents

Figure 5.3. TSRM (CW) 12-switch converter

5.3 – MACHINE DESIGN

5.3.1 - Electromagnetic Equivalence.

The comparison of electric machine performance has hereto, in the literature, been dominated by the examination of such items as their input and output power, efficiency and other factors like weight or specific power and torque, with the passing of meritorious judgment thereupon. While such measures are not invalid, it is often not clear, with the various combinations of machine physical details, winding details, and electrical drive schemes, as to whether or not a true machine to machine comparison is being made.

The analysis approach here is to employ the same physical machine structure as that of the CSRM, with 250 turns per coil (500 per full phase winding), and then to design the TSRM winding so as to produce the same electromagnetic flux magnitude at the wound pole of the TSRM as per the CSRM under ideal circumstances (i.e. assuming no leakage flux). The equivalent winding for the TSRM in terms of the number of turns, current, and physical packing factor, that will result in the same magnetic flux in the TSRM stator poles, had the TSRM been wound as a CSRM is determined accordingly. This then is known as TSRM (333) which describes 333 turns per each coil slot of A through F of figure 5.2(a). For the alternative winding topologies, drive system equivalence is maintained by specifying the same total input DC voltage and current to the machine, winding copper loss and physical packing factor available within the coil slots. The analysis for comparison of the ideal CSRM vs. the TSRM structure is

illustrated in figure 5.4, and developed with the CSRM represented by the LHS and TSRM the RHS:

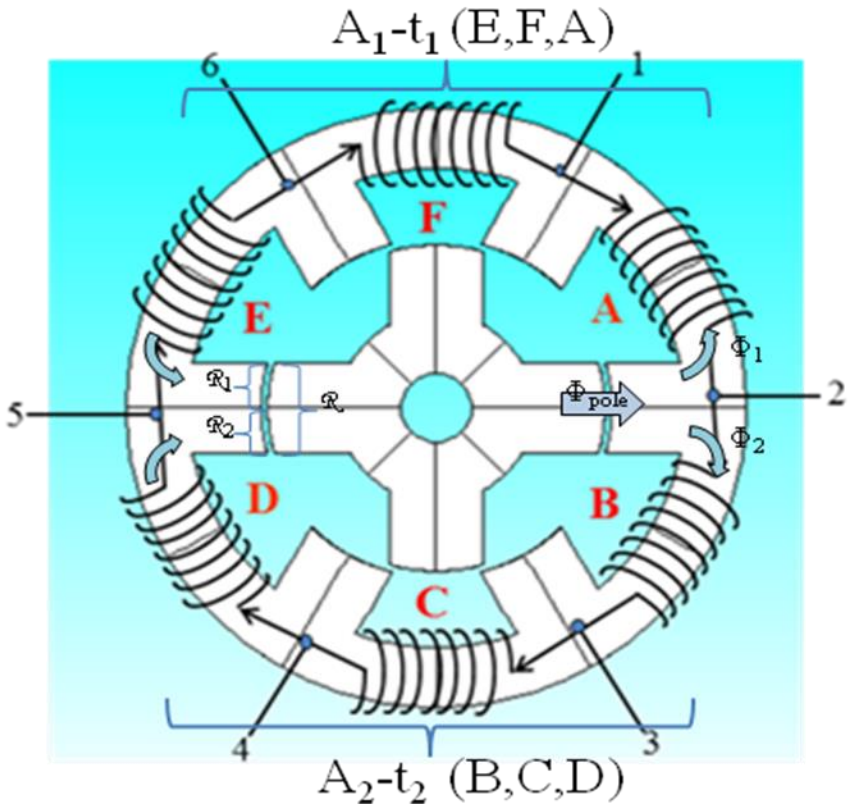

Figure 5.4. Electromagnetic Equivalence

By equations (1) through (4) we have:

$$\Phi pole = \Phi 1 + \Phi 2 \qquad (1)$$

$$MMF/R = MMF1/R1 + MMF2/R2 \qquad (2)$$

where Φ is the magnetic flux and R the reluctance of the air- gap at alignment, Φpole the CSRM flux per pole, Φ1 and Φ2 are the flux path of each TSRM winding branch, for example coils ABC and DEF respectively of figure 5.2(a). Recognizing that MMF =

Ampere-turns (A-t) and R1 and R2 are defined as each being 2xR then substituting into (2) yields:

$$At/R = A1t1/2R + A2t2/2R \qquad (3)$$

Dividing the total current between branches 1 and 2, such that A1 and A2 are equal and each ½A, and recognizing t1 and t2 are each 2t, substituting into (3) and solving yields:

$$At/R = At/2R + At/2R \qquad (4)$$

Therefore, the number of turns of each winding branch of the TSRM is 2x that of a CSRM phase winding. That said, with the same wire diameter, the packing factor will be reduced for each slot. When the winding losses are considered, it can be shown that the total losses are equal to that of the CSRM pole winding. Following this approach, each TSRM toroidal winding coil requires 333 turns versus the original 250 turns for each pole of the benchmark CSRM, or 1000 turns per branch, where each machine is supplied with the same total current and hence copper losses. Since the maximum allowable turn count in each slot is 500, this results in a lower packing factor of $k_p = 0.203$ for the TSRM than that of the CSRM where $k_p = 0.305$.

Notwithstanding the approach noted above, the winding was extended to fill the slot whilst maintaining the same copper loss, known here as TSRM (407) describing 407 turns per coil. This will increase the Ampere-turns count beyond that for the ideal CSRM equivalence and comes as an added benefit of relocating winding to the outer diameter of the machine. Each machine variant is considered with both 6 and 12 switch converter operation and the simulation results detailed figure 5.5 and figure 5.6.

The previously reported WSRM design, also referred to as Lee's machine, presents a problem with the approach taken here as it regards electromagnetic equivalence. Although of toroidal topology, and a uni-polar flux set equivalent to that of a CSRM having 500 turns per coil, notwithstanding Lee et al.[63] do not explicitly call out a value for said winding, with a 3-phase VSI shown in figure 5.3(b) as the drive, there is no fully equivalent magnetic circuit to that of a CSRM having the same pole flux as the WSRM is a short flux path machine. Moreover, with the drive topology shown there is no physical combination of coil winding arrangement that will replicate the long flux path magnetic field of the 6-4 CSRM. Nonetheless it is considered in this analysis given its toroidal topology and the possibility of being able to create the same flux intensity at the stator pole.

5.3.2 – Machine Physical Dimensions and Coil Winding Specifications

Table 5.2 presents the benchmark CSRM's physical dimensions and characteristics from which all studies, results and conclusions were derived, the "benchmark" being a commercial machine[96]. Table 5.1 presents the coil winding data derived from the procedure outlined in the foregoing section 5.3.1 and subsequently used in each machine analysis.

Table 5.1. Coil Winding Specifications.

Motor	**Winding Turns**		**Slot k_p**	**DC Resistance (Ω)**
	Per Slot	***Per Phase***		
CSRM	500	500	0.305	13.75/ph.
TSRM i	333	1000	0.203	9.2/slot
TSRM ii	407	1221	0.305	9.2/slot
WSRM	500	1000	0.305	13.75/slot

Table 5.2. CSRM Physical Dimensions and Characteristics.

Parameter	
Type	***Value and Units***
Number of poles	Stator: 6 Rotor: 4
Stator outer diameter	83.0mm
Bore diameter	47.0mm
Stator back iron height	8.3mm
Stack length	50.5mm
Air gap length	0.9mm
Stator pole arc	30°
Rotor pole arc	31°
Turns per phase slot	500 (250 per pole)
Wire size	0.36mm 27AWG
Slot packing factor k_p	0.305
Commutation	-15°unaligned, 30°dwell
Rated power	300W at 300V_{dc}
Rated speed	3000RPM

5.3.3 – Analysis Procedure

Both static and dynamic machine simulation analyses were undertaken utilizing JMAG[97] v11.0 software. These were each completed independently of the other with a transient fixed mesh for the former and a dynamic sliding mesh for the latter. In the dynamic analysis, a stabilized full rotor revolution was selected for the results. A fixed 1mm mesh element size for the entire model, air-gap excepted, with the dynamic having 1800 divisions, 600 steps for the time duration of one revolution, the time divisions thereof being adjusted accordingly was used in the analysis. This permitted a reasonable balance between an accurate analysis and computational time.

Static simulations were performed at levels of a total current supplied to the machine of 20A, 10A, 7.5A, 5A and 2.5A for the CSRM and TSRM. The WSRM static analysis considered total current supplied to the machine of 10A, 7.5A, 5A, 2.5A and

1.25A, values which permitted the equal pole flux at the aligned condition considering the series winding arrangement provided by the inverter topology. The 10A results for all machines are reported.

All dynamic simulations assumed an over-modulated 300V DC source power converter with no attempt made to examine performance with a modulated supply. The commutation start time was set to the un-aligned rotor position (-15° as per figures 5.1(a), 5.2(a) and 5.3(a)), with a rotor dwell angle of 30° which was used for all comparisons.

5.4 – SIMULATION RESULTS

5.4.1 – Static Analysis.

The static analysis results presented here in figure 5.5, evaluated on the basis of rotor torque verses rotor angle, demonstrate that a continuously wound TSRM configuration is capable of delivering greater torque per unit active volume than its electromagnetically equivalent CSRM or WSRM. This is primarily afforded through utilizing the peripheral outer diameter for winding space as stated earlier. The simulated static torque of the CSRM reported here, upon which this analysis was based, when compared to the static test results from measured data reported by Desai[98] was within 10% agreement. The electromagnetic equivalence which formed the basis of the analysis is shown in figures 5.6(a) and 5.6(b) respectively.

In the case of TSRM (333), representing the ideal winding derived from electromagnetic equivalence having ignored any leakage flux loss, the static peak torque was reduced by 23% compared to the CSRM. With the TSRM winding extended to a

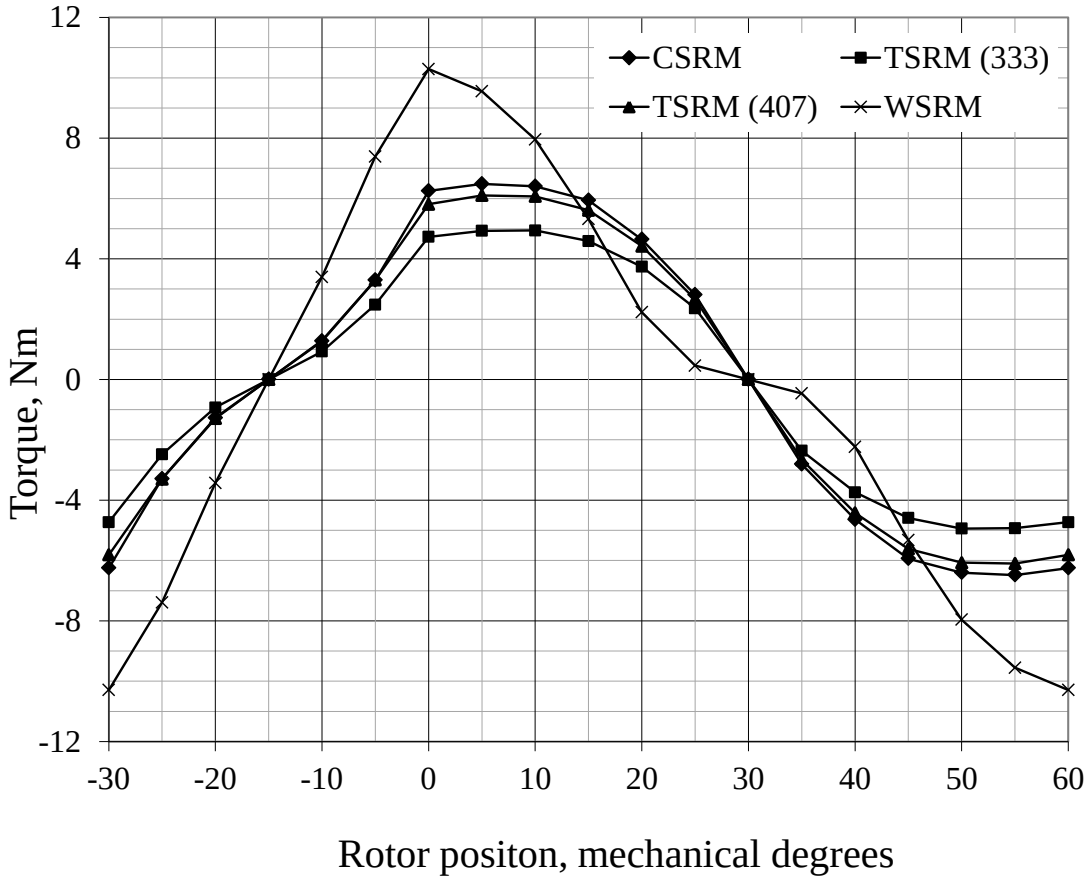

Figure 5.5. SRM Static torque verse rotor angle

fully packed 407 turns per slot, i.e. TSRM (407), but electrically equivalent loss condition, static torque increased by 20% compared to the ideal TSRM (333), but remained 8% below that of the CSRM.

Since the WSRM has the slot packing factor which was already fully utilized at 500 turns no such enhancement was possible. Note that for this machine, at equivalent uni-pole flux to the CSRM, the total current (10A) is equal to that of either the CSRM or TSRM.

Moreover, electromagnetic equivalence was lost as evidenced by the torque-angle response when the rotor position is greater than 0 degrees due to opposing torques from the second pole, as the WSRM is a short flux path machine. This may be observed from figure 5.6(c).

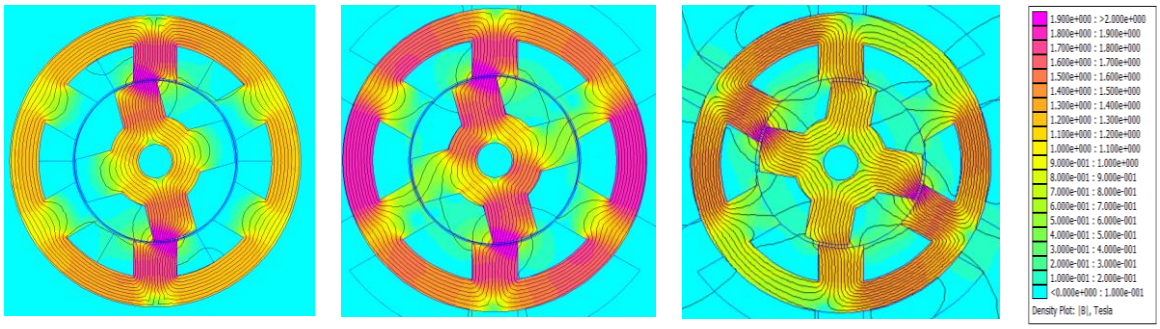

(a) CSRM (b) TSRM (c) WSRM Scale

Figure 5.6. Magnetic flux distribution and direction

5.4.2 – Static Pole Flux.

The equalization of pole flux between the different machine topologies formed the original basis for comparison. Accordingly, the result for said flux at the pole alignment condition is reported table 5.3 and the nominal value shows agreement within 5% across the machine topologies. Deviations from the ideal flux comparison developed above in section 5.3.1 may be attributed to the following: The short flux path WSRM exhibits a slightly higher flux than the long path CSRM. Slightly lower flux of TSRM (333) is due to leakage around the individual slot windings, whereas the TSRM (407) compensates with additional winding to realize nearly equitable flux at aligned position while maintaining the same winding DC resistance. In short, an Ampere-turn benefit is realized for the TSRM (407), although this has an effect upon the dynamic result due to the increased inductance resulting from the higher turns count as evidenced in table 5.4.

Table 5.3. Pole Flux at Alignment.

Motor	**Pole Flux (Tesla)**	
	Range	***Nominal***
CSRM	1.96-2.02	1.99
TSRM i (333)	1.90-1.95	1.93
TSRM ii (407)	1.95-2.0	1.98
WSRM	2.0-2.05	2.03

5.4.3 – Static Inductance.

It is a straightforward matter to calculate the machine self inductance at the poles, as if it were a conventional machine, from the magnetic flux and current changes at each rotor angle. This calculation at both aligned and un-aligned rotor positions, in the saturated (7.5A) and linear (unsaturated, 2.5A) regions, is summarized in table 5.4.

Table 5.4. Calculated Inductances (microhenries)

Motor	**Aligned Rotor**		**Un-Aligned Rotor**	
	Linear	***Saturated***	***Linear***	***Saturated***
CSRM	219	20	31	32
TSRM (333)	213	20	29	24
TSRM (407)	261	16	34	24
WSRM	176	53	39	52

The resulting calculated inductances will further serve to confirm the equivalence of the CSRM and TSRM (333) machines. The TSRM (407) would be expected to show a higher inductance in the linear region due to its higher coil winding turns count, whereas recall the TSRM (333) was derived from ideal conditions and consequently shows a lower result. Since the machine's dynamic operation takes place predominately on or about the un-aligned rotor position the inherently lower inductance of the saturated region of the TSRM will be of benefit in the dynamic operation. The lower self inductance at

alignment of the WSRM is in agreement with findings reported by Lee et al.[99] as the WSRM is a short flux path machine.

5.4.4 – Dynamic Analysis.

The dynamic analysis considered the average torque realized from each machine and power converter across an RPM range from 250 to 3000 as shown in figure 5.7. The CSRM reference was simulated as operated with the 6 switch asymmetric converter shown in figure 5.1(b).

Examining the average torque outputs from the conditions simulated, it is clear that neither TSRM (333) nor TSRM (407) achieved the output torque of the CSRM across the RPM range considered when operated with the 6 switch converter. However, the 12 switch converter option affords improved performance over this range, with said improvement being RPM dependent. The average torque increased at 1000RPM, by 9% and 19% for the TSRM (333) and TSRM (407) respectively. Further, at very low RPM conditions the results begin to converge to the static condition notwithstanding which converter is utilized.

At speeds greater than 1000RPM the 12 switch converter has the advantage and, for practical purposes, above 1250 RPM, results in the TSRM achieving similar output

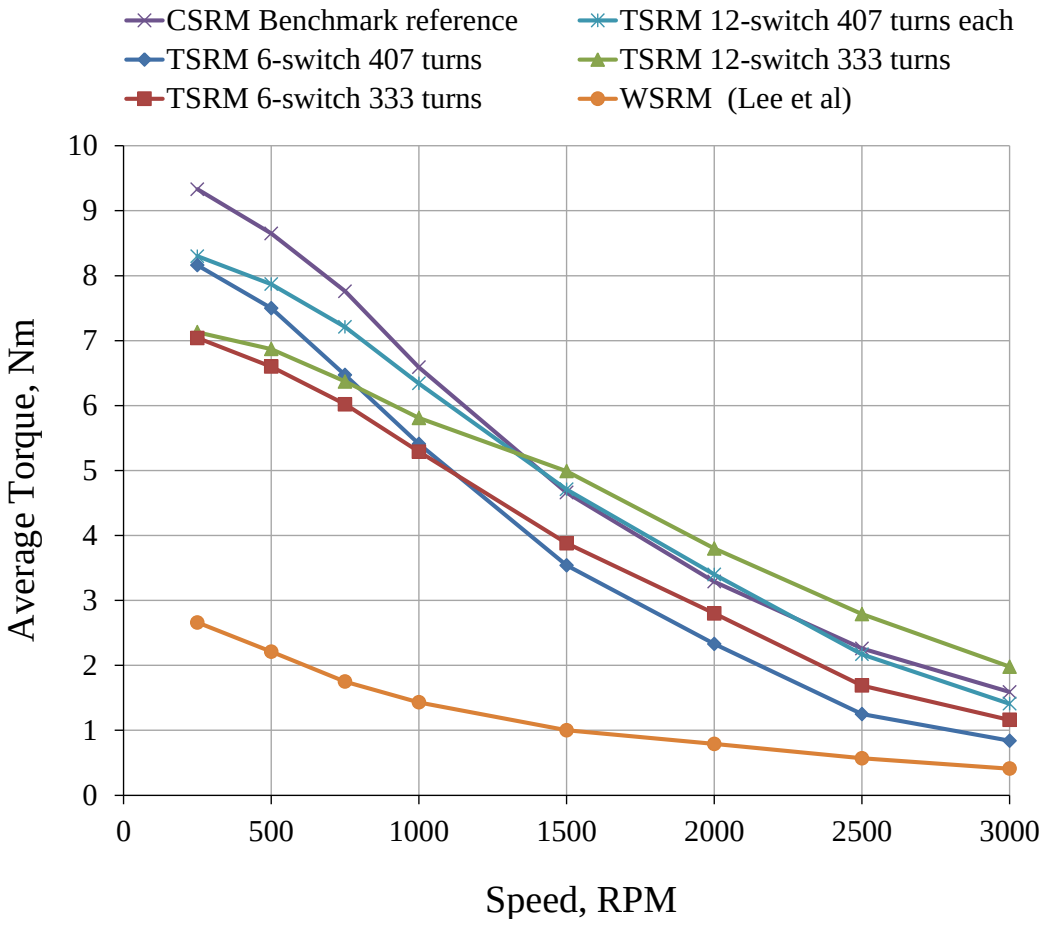

Figure 5.7. Average torque versus RPM for each machine

torque to the CSRM. Improved results were attained with the TSRM (333) version versus the TSRM (407) winding version given the reduced coil inductance. The WSRM with full bridge inverter was unable to achieve comparable results, although the torque-RPM profile was found to be similar to that reported by Lee et al.[100].

It should be noted that Lee et al. conducted their comparison utilizing a current approximately 2x that of their CSRM, whereas for a comparison based upon electromagnetic equivalence, as per the case here, the required current would be only one

half that of the CSRM which was evidenced in the static analysis. The difference in dynamic performance is obvious.

The machine efficiencies, exclusive of any consideration of the converter, were calculated and are reported in table 5.5, and are inclusive of iron losses notwithstanding that in absolute terms these are of low magnitude where these speeds are concerned. Notably, said losses at 3000 RPM are 3% and 1% in the case of the TSRM (407) when operated on the 6 switch and 12 switch converter, respectively. This is reflective of the latter's lower switching frequency of the phase currents, and its bipolar operation leading to a lower switching frequency of the magnetic flux in the back iron core location, the material of which comprises approximately one third of the machine's iron mass. Either 6 or 12 switch operation permitted the TSRM (407) to achieve a higher efficiency vs. the CSRM. The difference is an improvement of about 8% over the latter. The deterioration in efficiency below 3000 RPM for all machines considered is reflective of the high turns count and copper loss of the original machine design winding resistance, where higher phase currents are encountered at such speeds. Although converter and system efficiencies are not dealt with in this paper, it should be noted that, considering the present over-modulated (non-PWM) supply, the switching losses are negligible, the IGBT switch losses are comparable, and any difference in converter loss between the CSRM and TSRM versions is dominated by the diode conduction losses which are reduced compared to the CSRM as less inductance is being switched during each commutation event. Moreover, as alluded to above, the 12sw converter operates at ½ the switching frequency of its 6sw counterpart resulting in less power dissipation in smaller devices, albeit twice the count.

Table 5.5. Calculated Efficiencies (per unit).

Motor	**Rotational Speed (RPM)**		
	1000	***2000***	***3000***
CSRM	0.23	0.49	0.61
TSRM i 6sw	0.17	0.29	0.43
TSRM i 12sw	0.16	0.34	0.39
TSRM ii 6sw	0.23	0.39	0.64
TSRM ii 12sw	0.20	0.43	0.66
WSRM	0.25	0.39	0.48

The resulting current waveforms illustrated in figures 5.8(a) through 5.8(c) and those of the rotor torque in figures 5.9(a) through 5.9(c) will serve to support those illustrated in figures 5.1(c), 5.2(c) and 5.3(c) as they embody the basic form of their ideal counterparts. The current profile depicted in figure 5.8(b) illustrates the limitations of the 6 switch converter operation that results in a lower average torque due to a full current reversal during every third commutation period. Although 12 switch operation allows for more torque output, it comes at the expense of higher phase current and copper loss, and accordingly, a lower efficiency when operating at non-peak power conditions.

5.4.5 – Dynamic Inductance.

Beyond the static analysis of inductance, an important consideration is the dynamic effect of the toroidal winding arrangement. In operation, during commutation of the TSRM (333) or TSRM (407) considered here, two windings, each of a lower turns count, 333 or 407, vs. that of the conventional SRM at 500 turns per phase, are switched simultaneously. The division of the windings results in a lower time constant (LR) for the circuit vs. that of the conventional SRM. Accordingly, this should manifest itself as

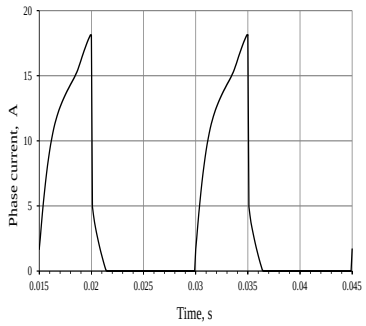

(a) CSRM Current

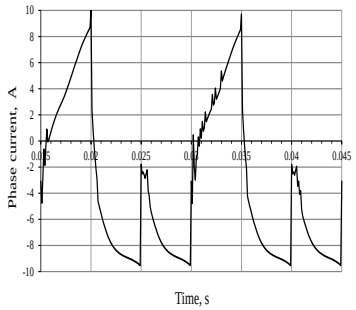

(b) TSRM Current 6sw Converter

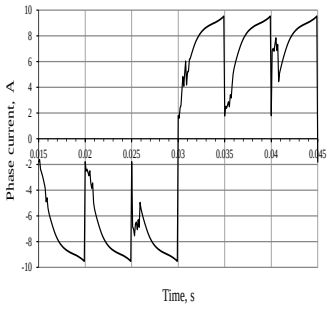

(c) TSRM Current 12sw Converter

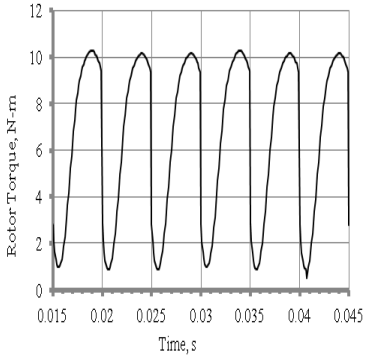

(a) CSRM Torque

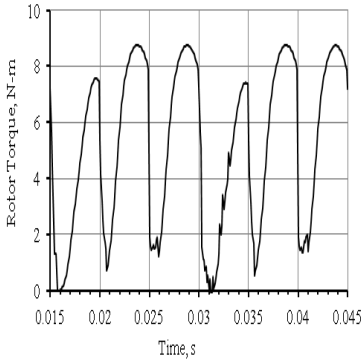

(b) TSRM Torque 6sw Converter

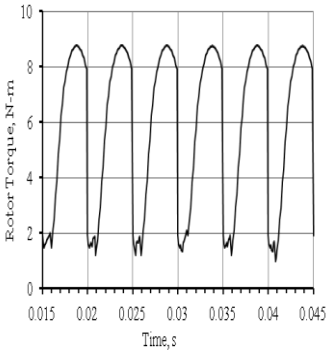

(c) TSRM Torque 12sw Converter

Figure 5.8 and 5.9. Current and Torque Waveforms at 1000RPM from Simulation

increased torque output at higher speeds. This is evidenced during the 12 switch operation of TSRM (333) at speeds exceeding 1250 RPM, although not evidenced upon closer examination of the current waveforms, of figures 5.29 and 5.30.

5.4.6 – Conclusions of the Simulation Results.

The static analysis results presented demonstrate that a TSRM (CW) configuration is capable of delivering nearly the torque per unit active volume as its electromagnetically equivalent CSRM. This is primarily afforded through utilizing the peripheral outer diameter for winding space. The winding schemes are confirmed by the results for pole flux which were shown nearly equal, except for small losses with multiple windings for the TSRM topology, and flux path length difference of the WSRM.

However, the dynamic results show that, in practice, higher turns are required at low speed, RPM < 1250, whereas for the 12 switch converter it is of benefit at speeds where RPM >1250 in this case, along with the ideal turns count TSRM (333). The former, TSRM (407), was capable of approximately replicating the CSRM torque-speed profile. The 12 switch operation, where used, has resulted in an absolute torque output improvement and an efficiency improvement of the TSRM over the CSRM due to its lower switching frequencies of both the phase current and resulting back iron magnetic flux. In absolute terms of torque output the lower inductance of the TSRM (333) winding can be of benefit at higher speeds in 12 switch operation although its efficiency is compromised by its lower turns count, i.e. higher phase current. The WSRM as presented is not an equivalent to a CSRM and, underscores the point that static analysis and magnetic considerations should accompany any conclusions drawn from dynamic machine analysis.

Beyond the basis of electromagnetic equivalence, which served here to establish the TSRM design, it is clear that both the machine topology and converter design must be considered in a final evaluation of a practical machine encompassing all measurables including overall machine efficiency.

5.5 – THERMAL PERFORMANCE

5.5.1 - The development of the SRM LPTN.

The development of the LPTN analysis for as applied to an SRM was discussed in Chapter 3b. The thermal resistances for the LPTN have been updated to reflect the new machine parameters reported in tables 5.1 and 5.2, being shown in table 5.6.

Table 5.6. Thermal resistance calculations for an SRM

Thermal resistance calculations for CSRM LPTN		
Thermal	Calculated	Node
R1	0.0002 K/W	Cooling water to frame
R2	0.0287	Frame to yoke
R3	0.0448	Yoke to teeth
R4	0.5712	Teeth to coil sides
R5	0.2794	End winding to coil sides
R6	26.0	Rotor to frame
R7	9.7	Rotor to end windings
R8	14.1	Frame to end windings
R9	10.1	Rotor to teeth
R10	11.8	Rotor to bearings
R11	0.646	Bearings to end shield
R12	0.059	End shield to frame

The LPTN developed for the CSRM upon which the subject TSRM has been based is shown in figure 5.10. The thermal resistances and input to each node (in watts) are shown on that schematic as before. Since this is not a high speed machine as described in Chapter 3b, the “rotor” node and “teeth” node windage losses have been removed as they may be ignored where the RPM is a full order of magnitude less, i.e. under 3000 RPM. Here, it should be noted, the significant difference in distribution of thermal input between the high speed CSRM and the one considered here, with the former having significantly higher core losses and consequently higher thermal input to

the stator and rotor yoke nodes as compared to those of the windings; by comparison the copper losses dominate in the CSRM being considered.

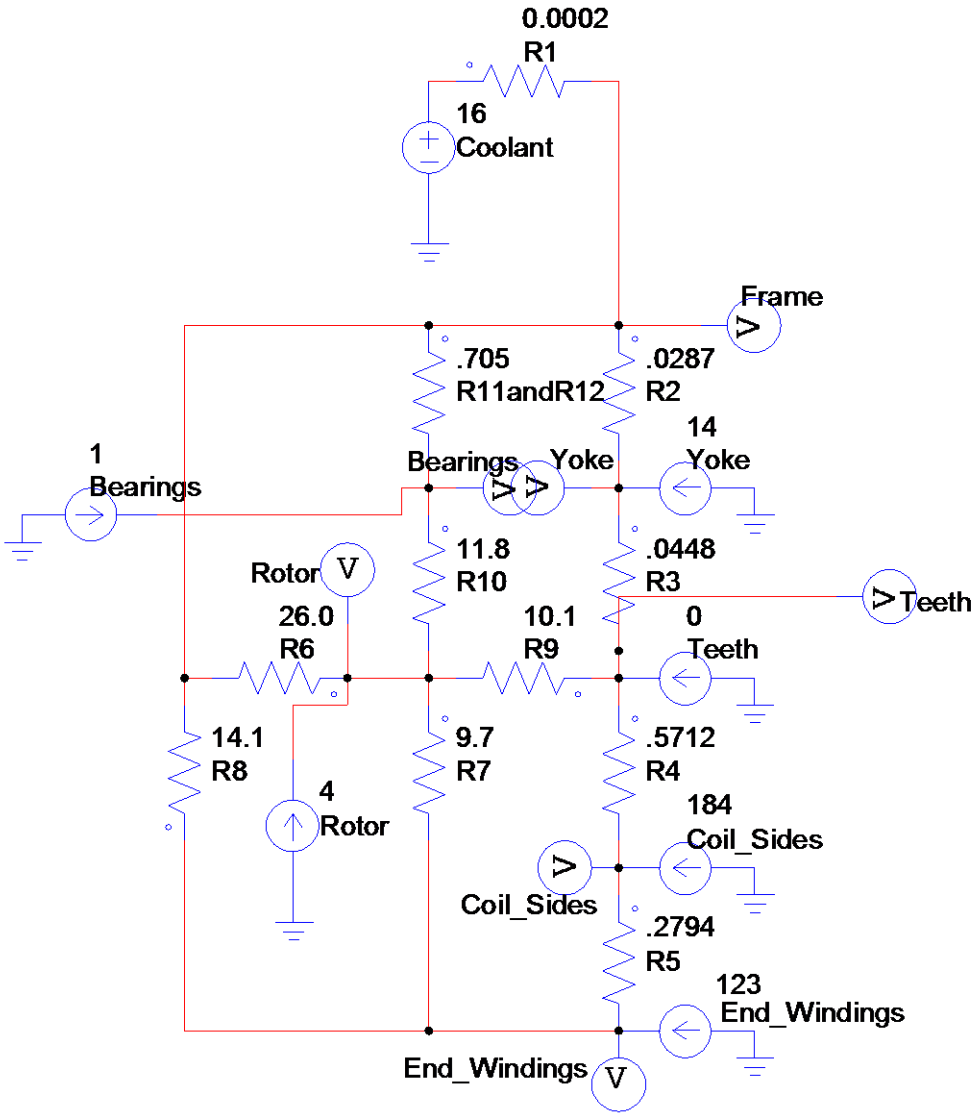

Figure 5.10. LPTN model in PSIM for SRM thermal resistances, thermal inputs in watts

As before, there were several iterations to the design of this SRM and the aforementioned figure shows final design LPTN which was derived from the resulting equivalent TSRM and CSRM with the material properties and boundary conditions for convective heat transfer derived from the Lindstrom work applied to this analysis. The

results for predicted temperature and adjustments to thermal resistance and bearing thermal output are shown below in table 5.7.

Table 5.7. Simulated temperature results for the subject CSRM.

CSRM steady state results @ 500W, 3000 rpm and 16°C cooling water					
	Thermal input W (%)		Temperature °C	Adjustment	Adjustment (with end shields)
Node	Initial	%	Calculated	R_2=.0097	R_{11}+R_{12}=.705
Frame	n/a	n/a	16	16	20
Yoke	14	4	25	19	25
Stator Teeth	0	0	38	32	38
Coil Sides	184	56	197	192	197
End Windings	123	38	224	219	224
Rotor	4	1	102	99	102
Bearings	1	<1	21	21	22
Cooling Water	n/a	n/a	16	16	16

The temperatures calculated based upon the "initial" thermal input show the end windings and coil sides residing above the former thermal design target of 150°C for the insulation material class. The thermal limit for the experimental version used in the research test here was 200°C, although no tests would be conducted near that level. Given the open frame construction the frame thermal contact resistance was not investigated here.

5.5.2 - Transient response of the CSRM LPTN model.

As with the high speed machine considered in Chapter 3b, transient results were obtained for this CSRM LPTN model. The CSRM LPTN transient model is shown below in figure 5.11, with thermal capacitance (units J/K) added to the network of figure 5.10 at thermal input nodes. The end shield adj. and 1W bearing are used, ref. table 5.6.

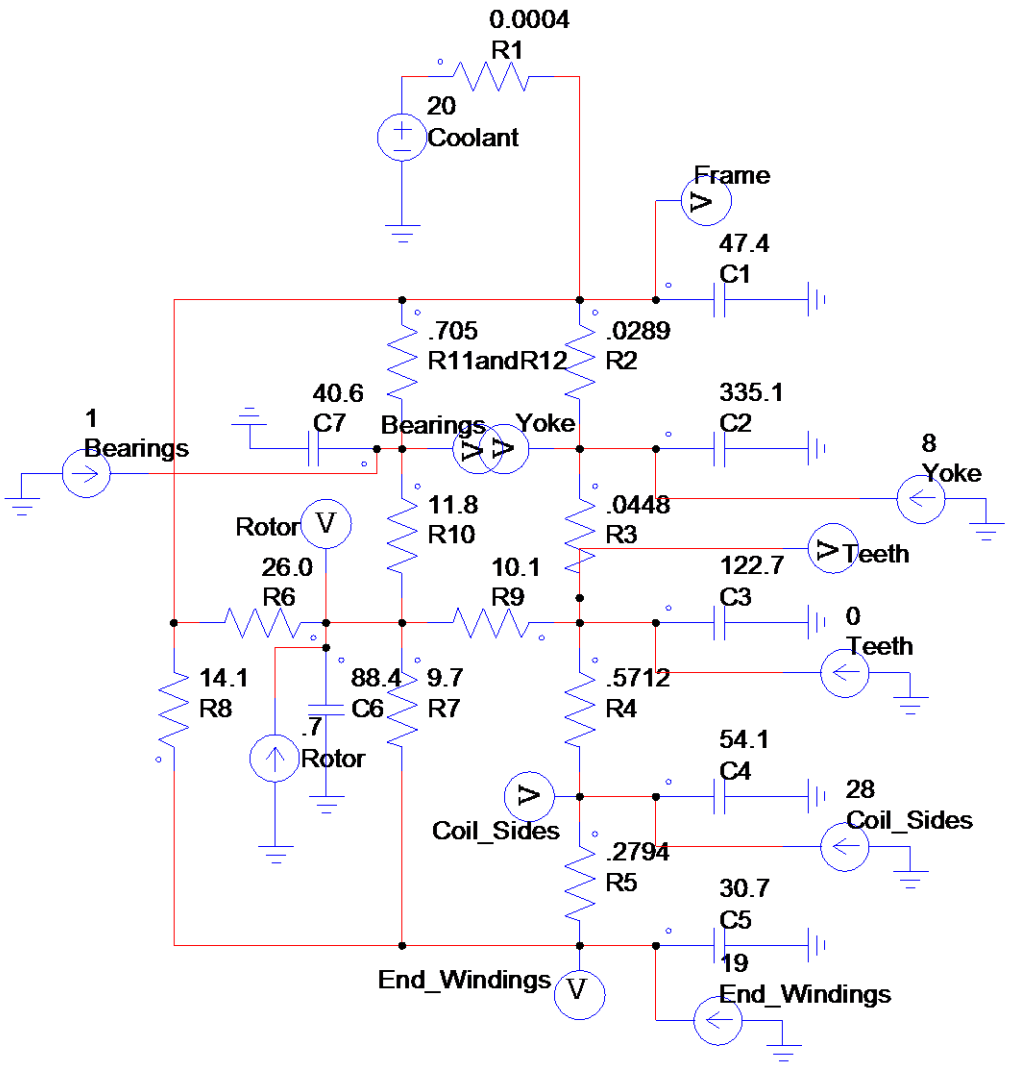

Figure 5.11. LPTN model in PSIM for CSRM transient analysis, thermal resistances K/W, thermal inputs in Watts, and capacitance in J/K

The results of the transient thermal analysis are shown in table 5.8 and figure 5.12. In this analysis no discrepancy was noted between the maximum temperatures obtained through transient analysis vs. those obtained from the steady state analysis as indicated in the last column of table 5.7. This is perhaps due to the lower thermal inputs and the shorter running time of the transient analysis, approximately half that of the prior analysis of Chapter 3b.3.4. Where this machine is concerned the result does confirm the

direction of heat flow from end windings to stator teeth and indicates the end windings are at first risk of exceeding the 150°C thermal limit for this CSRM at 64 seconds, or about 1 minute.

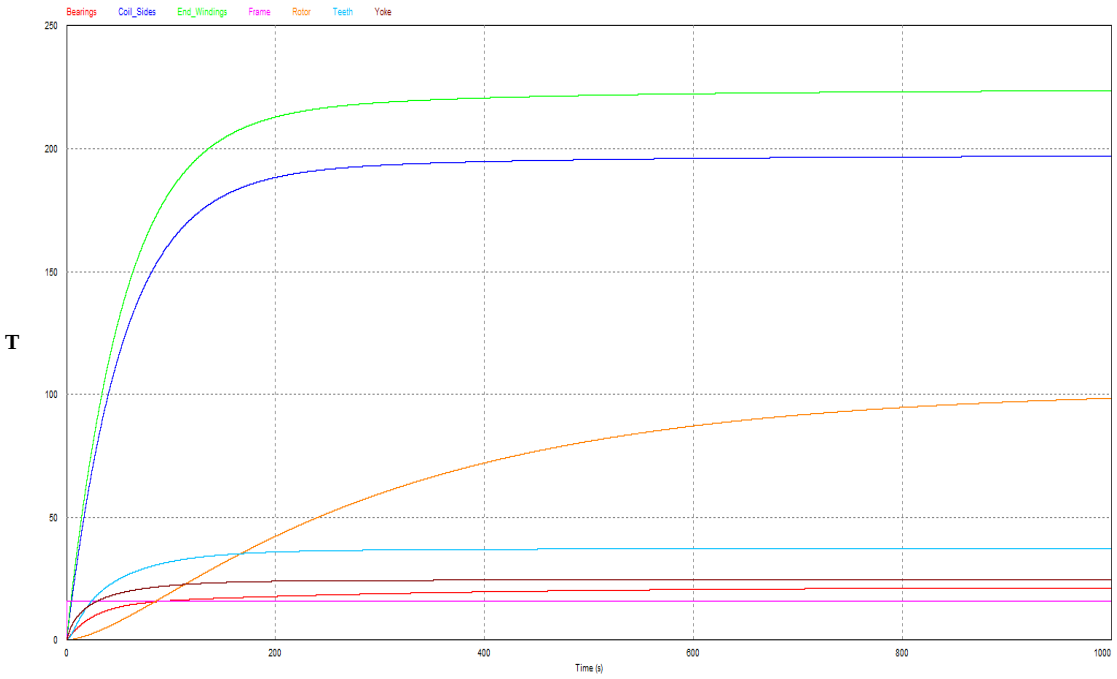

Figure 5.12. LPTN model solution in PSIM showing SRM transient thermal results

Table 5.8. Transient results for the subject SRM

Transient results @500W, 3000 rpm, 16°C coolant. Time step 0.01s, run time 1200s.			
Node	Maximum Temp. °C	Time to 150°C seconds	Time to .99Tmax. seconds
Frame	16	n/a	<1
Yoke	25	n/a	368
Stator Teeth	38	n/a	460
Coil Sides	197	82	1040
End Windings	224	64	480
Rotor	102	n/a	1322
Bearings	21	n/a	645
Coolant	16	n/a	n/a

5.5.3 – Thermal Performance Continued, the IEEE paper.

The networks applicable to the CSRM and TSRM here are illustrated in figures 5.13 and 5.14 where the air convective coefficient for thermal resistance to the environment is shown, along with the thermal inputs totaling 55W and 52W respectively for each machine operating at 3000RPM producing 79W mechanical shaft power. For the CSRM the dominant heat flux path is from the end windings to the frame as evidenced by the low thermal resistance of said path compared to that of other possible heat transmission paths in the machine. The foregoing thermal network is solved with the usual electrical analog and the resulting temperatures shown in table 5.9 where both liquid cooling and air natural convection cooling were considered in the analysis, whereas until now we have considered only liquid cooling. The LPTN for the continuously wound TSRM with the increased winding count operating on the 12 switch converter, ie 407 12sw., is illustrated on the same basis in figure 5.14. One additional node is added ("Upper Coil Sides") as the toroidal winding has been split into upper and lower portions, i.e. internal and external or peripheral portions. In the case of an open frame machine, this quickly leads to a heat flux path "R4c" directly to the coolant, in this case air natural convection. It may also result in a heat flux path return to the yoke through "R4b". It should also be noted, the difference in thermal input due to iron loss. In the case of the TSRM operating with the 12sw converter rotor and teeth (poles) iron loss is increased. However, this is more than offset by a reduction in iron loss at the yoke. Without digressing too deeply into the magnetics, the bi-polar operation of the 12 switch converter results in a lower hysteresis loss in the yoke as the flux reversals occur at half the frequency of the conventional machine.

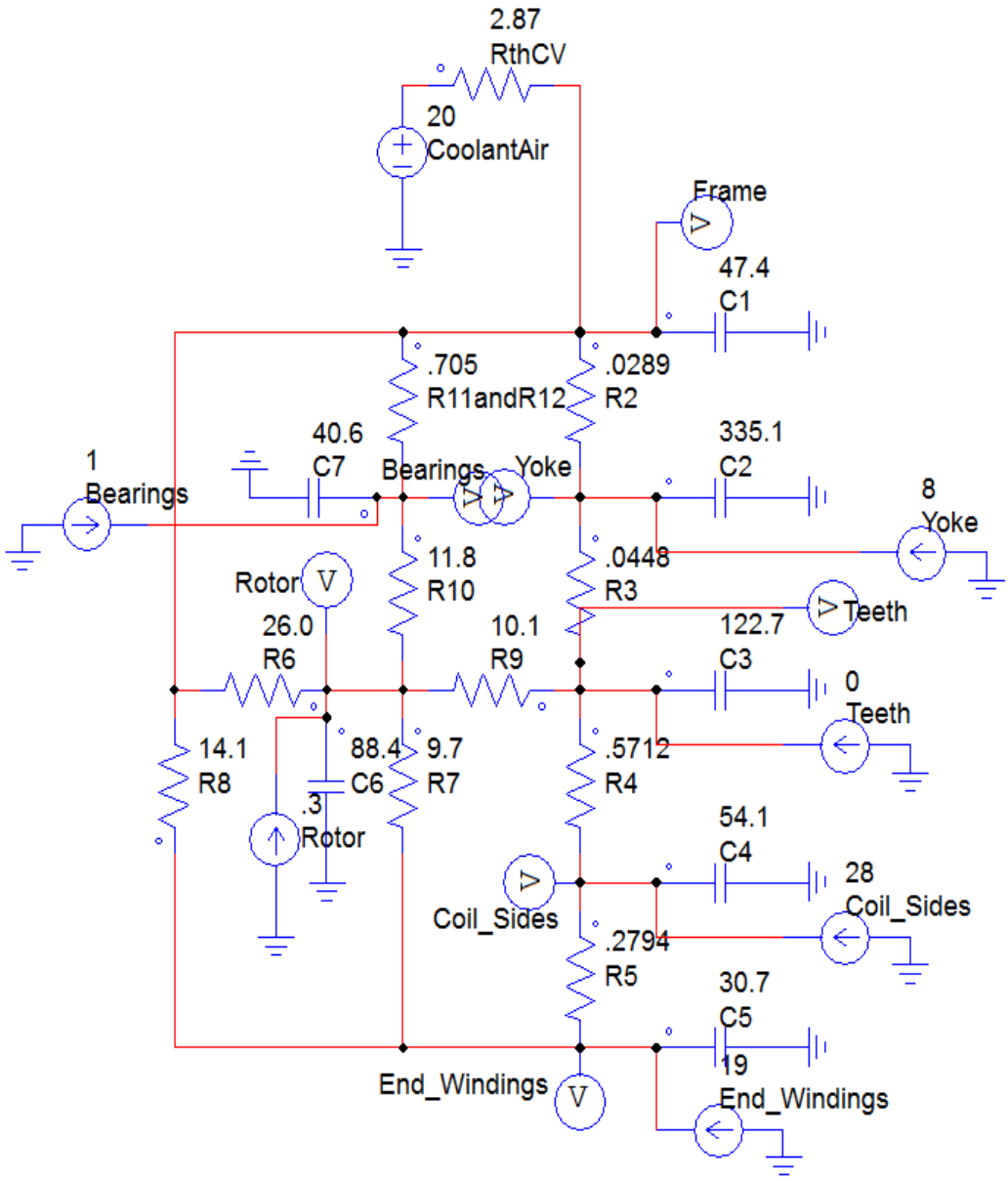

Figure 5.13. CSRM Lumped Parameter Thermal Network

Of course, this means hysteresis losses are now present at the teeth but, since the majority of the rotor iron mass resides in the yoke there is a net reduction in iron loss for the stator. Overall, the iron loss difference under the operating conditions considered was about 3%.

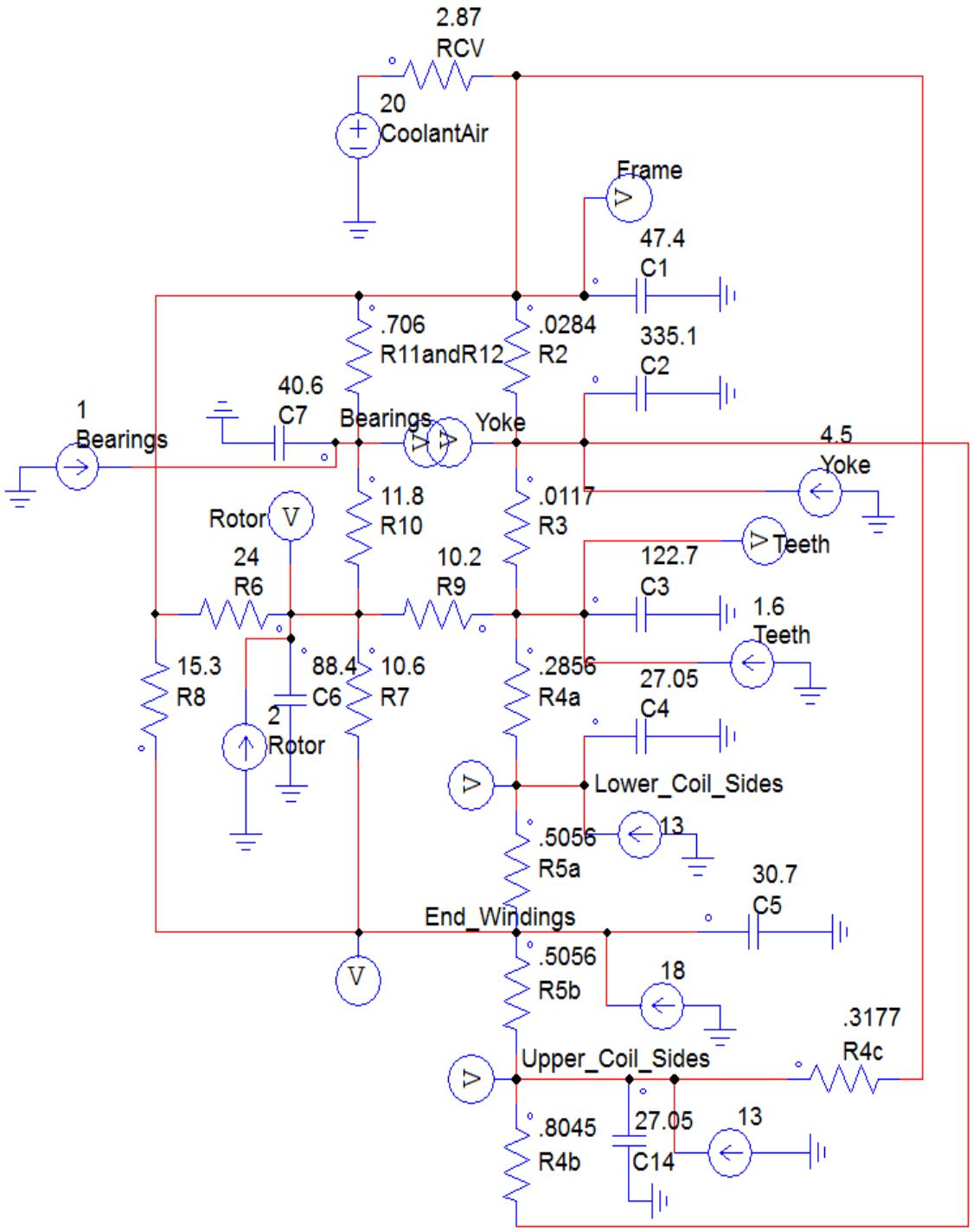

Figure 5.14. TSRM Lumped Parameter Thermal Network

This will become more pronounced at higher RPMs and, moreover, the iron losses will eventually dominate over the copper losses at some significantly higher speed. As to

the copper losses, these were somewhat less for the TSRM as previously discussed in section 5.3.1.

Table 5.9. Calculated Temperatures (°C) at 3000RPM, 79W Gross Mechanical Power

Motor	**Machine and Cooling Configuration**					
	CSRM		***TSRM(407)***		***TSRM(407)****	
Component	***Water***	***Air Nat.***	***Water***	***Air Nat.***	***Water***	***Air Nat.***
Bearings	21	173	21	163	21	170
Coil Sides-upper	48	N/A	26	168	26	175
Coil Sides-lower	48	199	27	169	27	177
End Winding	52	203	31	173	31	180
Teeth	24	175	21	163	21	170
Rotor	34	183	30	171	31	178
Frame	20	172	20	162	20	169
Yoke (Back Iron)	21	173	21	163	21	170

Note: *normalized thermal input compared to CSRM, 55W

Both machines were compared initially operating at equal gross mechanical power, i.e. inclusive of all rotary losses, of 79W which represented said power available at 3000RPM. Accordingly, the thermal performance as illustrated by the various component temperatures will reflect not only the topology difference, but also the improved efficiency of the TSRM over that of the CSRM. Nonetheless, when taken together the result is a 16% reduction in temperature rise over a 20°C ambient, at the end windings, being the maximum calculated for each machine. Notwithstanding the foregoing, if the thermal input to the TSRM is normalized with the CSRM at 55W total the resulting rise over ambient is still lower for all components although the maximum reduction in temperature rise is now only 11%. Unfortunately, it is not possible with the analysis to make a comparison on an "all other things being equal" basis as the losses are not distributed in exactly the same fashion between the two topologies.

5.5.4 – Conclusions from the TSRM Thermal Analysis.

- The continuously wound TSRM as presented here with increased winding count has been shown to provide approximately equivalent static and dynamic performance characteristics when compared to the CSRM on the basis of electromagnetic equivalence. This is supported by the static torque, magnetic flux and inductance characteristics being considered. When taken as a complete system with the machine drive, this is supported by either improved torque capability or system efficiency under operating conditions considered here in this analysis.

- Moreover, the thermal analysis has demonstrated the advantage of the toroidal topology insofar as thermal management is concerned where either lower machine operating temperatures are permitted or, equal temperature targets may be realized at increased input and output power to the CSRM.

- Accordingly, the TSRM (CW) topology shows promise for future applications especially where enhanced cooling requirements are present owing to its peripherally exposed winding arrangement.

5.6 – TSRM DESIGN VARIANTS

We have arrived at the point in the research where other machine variants may be considered. So far, we have examined the TSRM on the basis of a fixed CSRM physical size and properties, in particular, the stator and rotor dimensions. This had formed the basis of the original argument for equivalence between the two machines. It remains so,

however, it precludes some realities of the TSRM architecture which have been hitherto ignored.

First, is the obvious reduced winding occupancy of the slot where said slot is occupied by only 333 turns, the ideal case from the aforementioned electromagnetic equivalence discussed in section 5.3.1.

Second, is the improvement in winding efficiency, or packing factor, where the winding is toroidal. Unlike the concentrated pole winding which is usually wound over a form and placed into position over the pole requiring a non-reentrant section, or at the least additional slot space to permit rearrangement of the winding once inserted, the toroidal winding is capable of filling the entire slot space. Accordingly, a higher packing factor may be realized.

Heretofore in the analysis, this was not considered. The 333 turns were taken without regard to the foregoing, resulting in a lower packing factor being applied (k_p =.203) than would otherwise be the case in actual manufacture. If the original packing factor were used, then only about 2/3 of the slot area would be occupied, notwithstanding any further improvement to be realized by the improved slot space utilization of the toroidal winding itself. The reduced slot area occupied will permit either one or two approaches in design variant. Enlarge the bore diameter of the machine or, reduce the outer diameter of the stator while maintaining the original bore diameter. The former has the advantage of improved torque and adds little to the overall outer diameter of the machine where the outer portion of the toroidal winding is permitted to occupy that portion of the machine's frame that would have enclosed the CSRM stator outer diameter, figure 5.15.

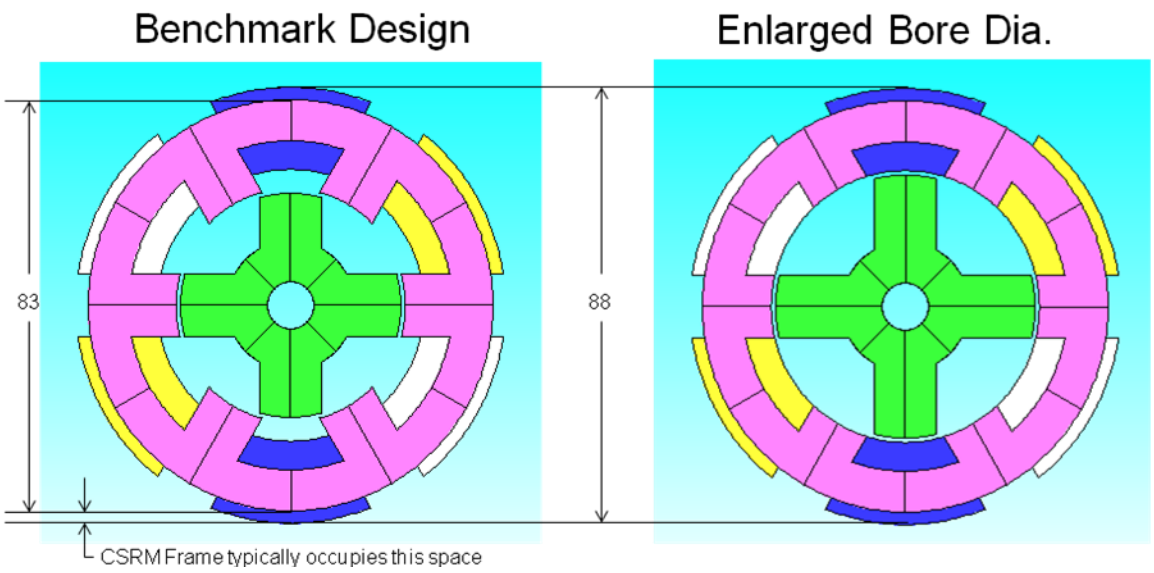

Figure 5.15. OD of Benchmark vs. Enlarged Bore Diameter with filled slot winding

The latter will permit the entire TSRM to be enclosed within nearly that of the CSRM stator outer diameter, albeit with a corresponding loss of torque, but when applied to the reduced volume, a nearly equal torque and power density. See figure 5.16. As to the 407 turns per slot winding variant, this increased copper content may be taken up

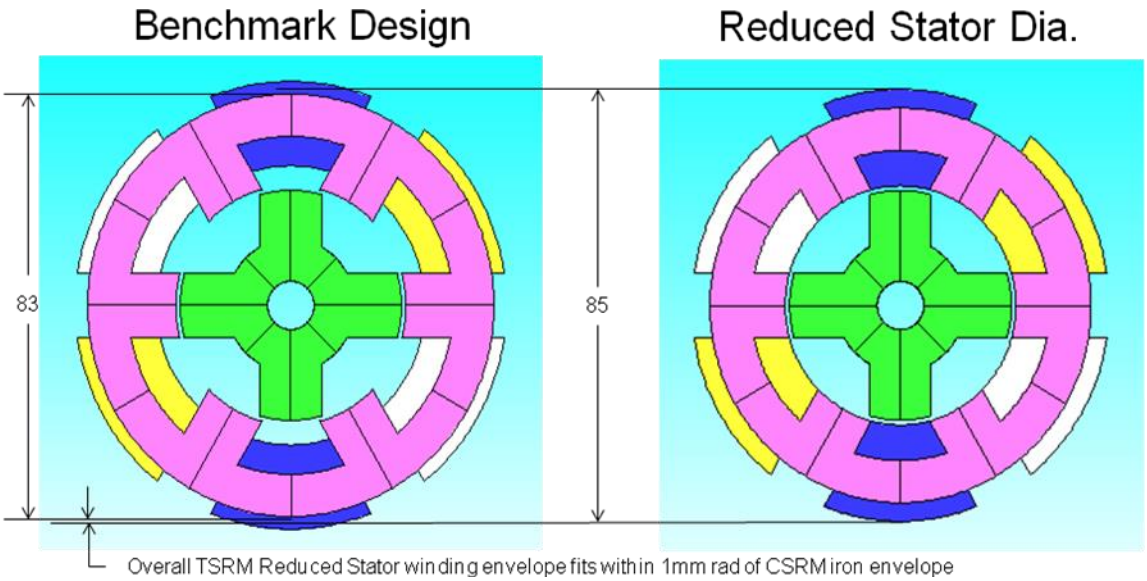

Figure 5.16. OD of Benchmark vs. Reduced Stator Outer Diameter with filled slot

entirely by the improved winding efficiency of the toroidal topology. The packing factor realized here k_p = 0.65, which is possible in manufacture. It is a relatively straight forward matter to manage the packing of the winding to achieve a tight form. No slot space is wasted due to non re-entrant sections.

The dynamic performance results may be found in figs. 5.17 and 5.18. For the enlarged bore diameter variant the improvement in torque capability is obvious and permits even the TSRM with a six switch converter to achieve nearly the torque result and profile of the CSRM. That said, the TSRM (407) version matches plus the performance of the CSRM while at higher speeds, the TSRM (333) exceeds it by a wide margin.

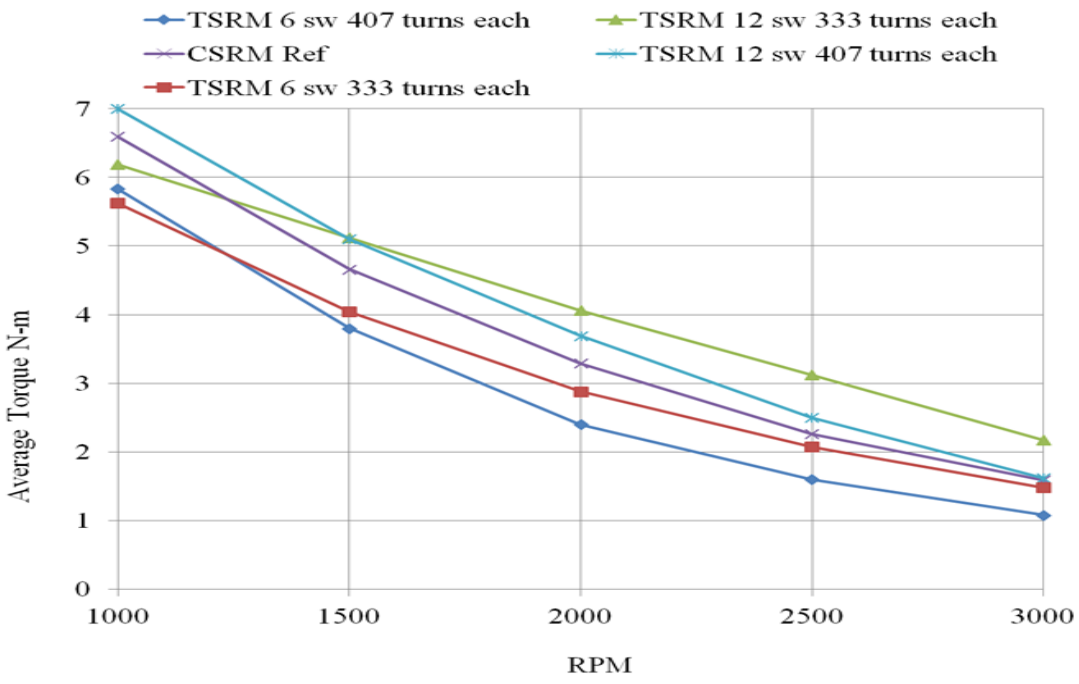

Figure 5.17. Average Torque vs. RPM for each machine with enlarged bore TSRM

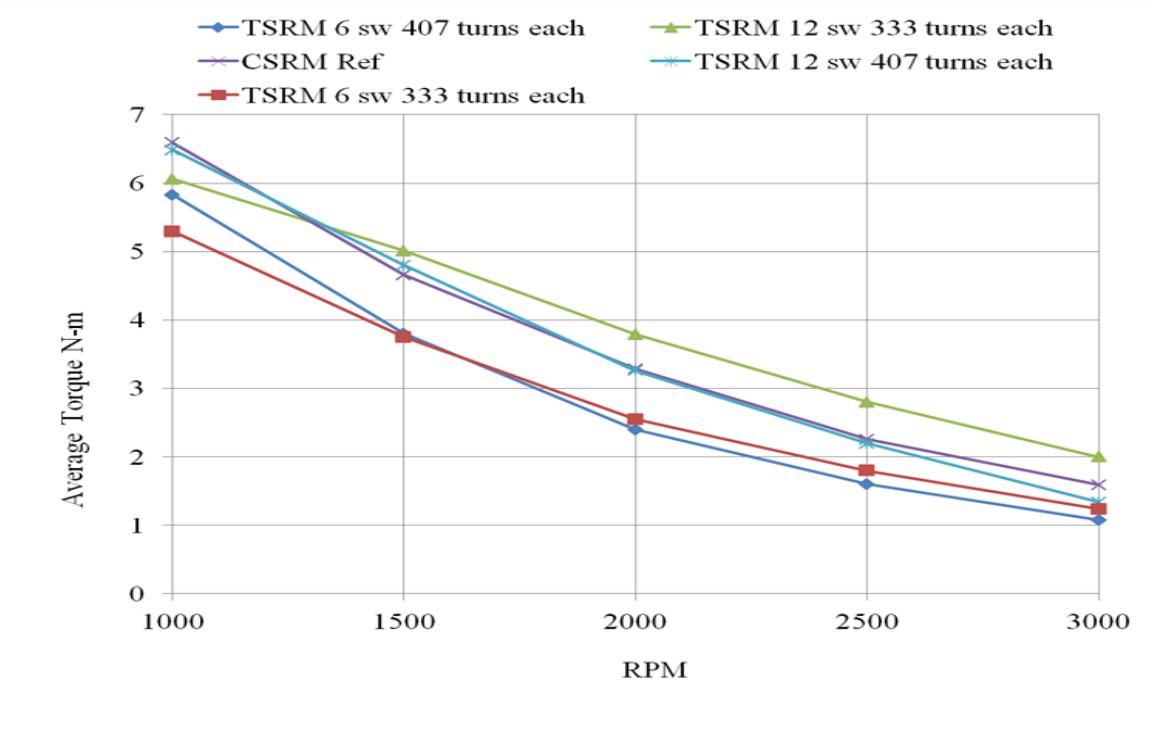

Figure 5.18. Average Torque vs. RPM for each machine with reduced OD TSRM

The reduced stator diameter version resulted in an expected reduction in dynamic torque however, the TSRM (407) with a 12 switch converter provided a nearly identical match to the torque profile. Again the TSRM (333) with same exceeded it by a wide margin at higher speeds.

While these results may be somewhat expected, their examination in the context of machine efficiency, torque and power density are warranted. These are available in tables 5.10 and 5.11. For power density, since all machines were of the same stator length with similar construction, the power density is expressed on a per unit area basis, ie W/cm^2.

In terms of specific power all machines, showed improvement. In the case of efficiencies, most machines showed an improved result, with some reduced at the higher speeds, but only minimally.

Table 5.10. Comparison of calculated efficiencies vs. RPM for each machine variant

Motor + converter	Enlarged Bore Diameter - RPM			Reduced Stator Diameter - RPM		
	1000	2000	3000	1000	2000	3000
CSRM (ref.)	0.23	0.49	0.61	0.23	0.49	0.61
TSRM i 6sw	0.18	0.35	0.55	0.18	0.34	0.52
TSRM i	0.16	0.35	0.48	0.16	0.36	0.44
TSRM ii 6sw	0.23	0.41	0.63	0.23	0.40	0.64
TSRM ii	0.22	0.42	0.63	0.21	0.41	0.61

Table 5.11. Comparison of calculated specific power (W/cm²) vs. RPM for each machine variant

Motor + converter	Enlarged Bore Diameter - RPM			Reduced Stator Diameter - RPM		
	1000	2000	3000	1000	2000	3000
CSRM (ref.)	12.75	12.59	9.24	12.75	12.59	9.24
TSRM i 6sw	10.89	11.14	8.59	9.72	9.37	6.82
TSRM i	11.98	15.71	12.59	11.12	13.93	11.01
TSRM ii 6sw	11.28	9.28	6.27	9.71	7.47	4.63
TSRM ii	13.55	14.29	9.39	11.91	11.98	7.39

Overall, the enlarged bore TSRM (407) operated with a 12 switch converter proved to be the best match to the CSRM, which improved torque and specific power without sacrificing efficiency. The reduced stator TSRM whilst showing torque and density improvement, was found compromised with respect to efficiency when compared to the benchmark machine. The best design point in terms of torque density for a reduced stator TSRM 12 switch converter operated machine would lie somewhere between 333 and 407 turns per slot, however its efficiency would be less than that of the benchmark and/or CSRM.

In conclusion, the results speak to the fundamental nature of the bore diameter in the DC machine power equation. Accordingly, the research should be progressed with the enlarged bore diameter machine. This would not only provide for a simplified frame support structure as those parts would remain common, only a single enlarged rotor would need to be provided for the purpose of data acquisition.

5.7 – TSRM MACHINE CONSTRUCTION

As stated earlier, the machine was based upon a commercial design, with some of the hardware for a pre-prototype machine (mule) build already being available: stator iron core, rotor assembly (with shaft and bearings), and end plates. This permitted the ready construction of the "mule" machine which would be used for the development of the converter drive, controller, and a few initial tests of the entire dynamometer bench set-up. The construction of the mule itself would serve as a learning exercise for the prototype machines prior to their construction, particularly the approach taken with TSRM winding, electrical insulation, and stator retention.

The mule build required only the rewinding of the stator and fashioning a suitable frame case which, with the end plates, would serve to hold the entire apparatus together whilst properly align the stator core bore diameter with that of the rotor. The motor design running airgap of 0.9mm was ample to permit routine machining tolerances for this purpose. The frame case was designed such that it would serve to maintain the proper distance between the end plates, alignment of the end plates, retain and align the rotor by both axial and circumferential compression, respectively.

There would be two prototype builds: the subject TSRM and a CSRM upon which the TSRM design was based, where the stator and rotor iron were both known, unlike that of the mule where they were not. This required the procurement of said iron cores and further required the construction of a new motor shaft and assembly.

5.7.1 – Stator Winding.

The winding of toroidal machines is not unknown, and in the case of transformers is common practice carried out with the aid of automated winding equipment dedicated to the purpose. That said, it is still a somewhat arduous task to complete on a prototype machine. Unlike a conventional machine, pre-winding of the pole windings is precluded unless a segmented iron stator is employed with said windings then welded post construction. In the study here a completed, welded stator was used so the machine winding would have to be carried out by passing the winding wire (on its spool) through the bore repeatedly until complete. With a bore diameter of only 45mm it would be necessary to decant the wire for winding on a separate winding bobbin suitable for the purpose, ie. of a total outer diameter of less than 45mm when wound that would permit an easy pass through of the bobbin through the stator core, ideally without damage to the wire. As such, each bobbin was constructed of a 1¼" (1 17/64", 32mm) outer diameter x 3" length wooden dowel fitted to a drive shaft such that it could be affixed to the hand winder which was employed in chapter 3 for winding the transformer coils, figures 5.19(a) and 5.19(b). The wound diameter of 37mm was sufficient to allow for pass through with the stator poles suitably covered with a felt guard to prevent any damage to the wire as the winding bobbin was passed through, figures 5.19(c) and 5.19(d). The first layer was wound to secure the insulation paper in place, described in section 5.7.2. , see figure 5.20(a). The width of the winding was limited to about 25mm at the base. Since the outer diameter of the winding is greater than the inner diameter of the winding (inside the slot) it was decided to control the outer portion of the winding by maintaining it as close wound as possible and permit the inner winding to occupy the space as necessary.

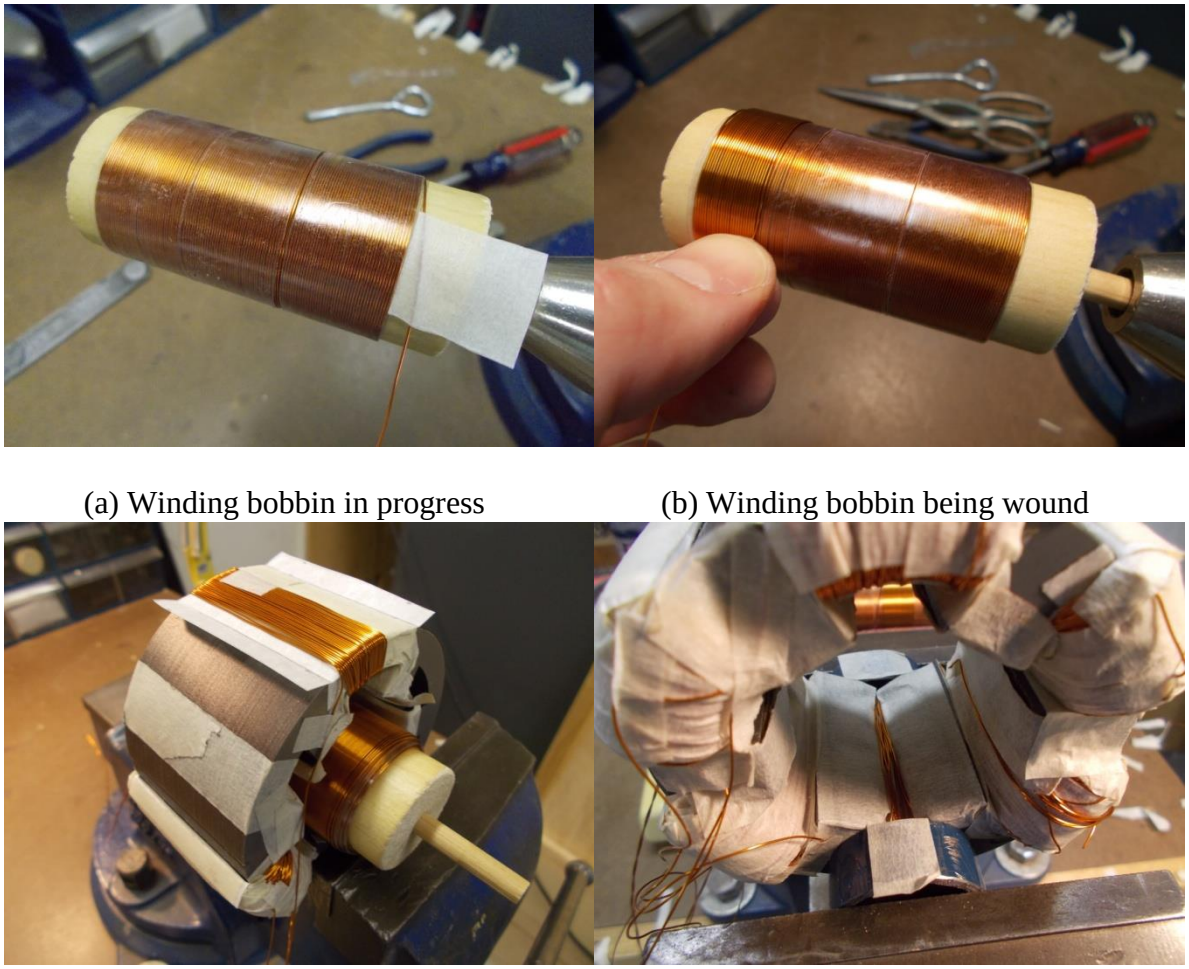

(a) Winding bobbin in progress (b) Winding bobbin being wound

(c) Bobbin passed through machine bore (d) Bore showing protective coating

Figure 5.19. Winding bobbin construction and winding process

To minimize any error in the turns count each winding layer was covered with a masking tape, shown in figure 5.20(d), allowed for an easy counting of the winding turns for each layer as they were completed otherwise it would be impossible to visually verify the turns count with copper on copper layering. Accordingly, there is confidence that this part of the process was carried out to a high level of precision. This could later be verified by comparing the wound resistance of each section, approximately 7.7Ω/slot winding.

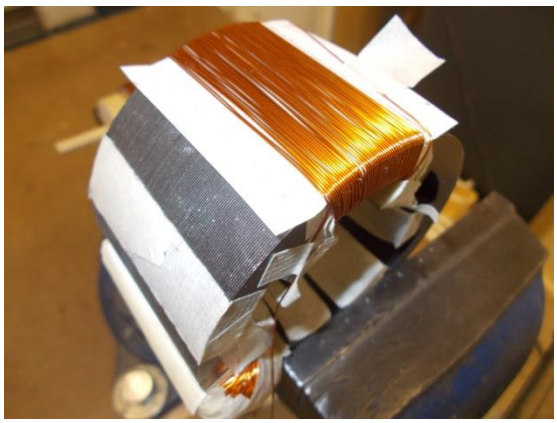

(a) First winding layer

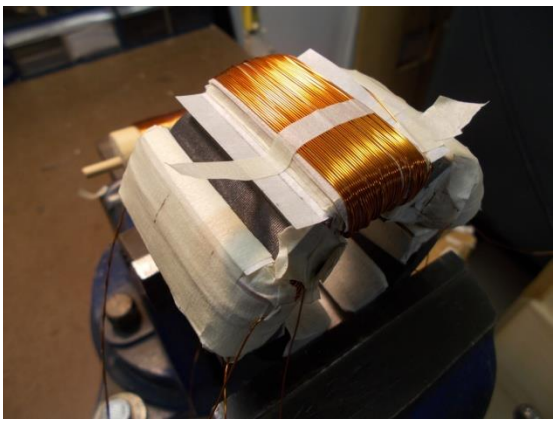

(b) Multiple winding layers

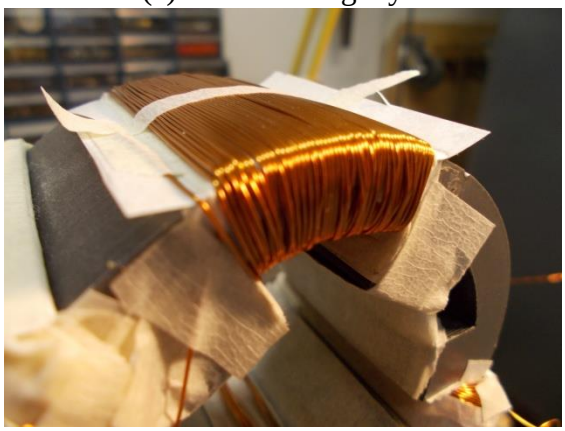

(c) End winding arrangement

(d) Winding overlay for turns counting

(e) Finished slot winding

(f) Instrumented with thermistors

Figure 5.20. Various stages of motor winding slot under construction

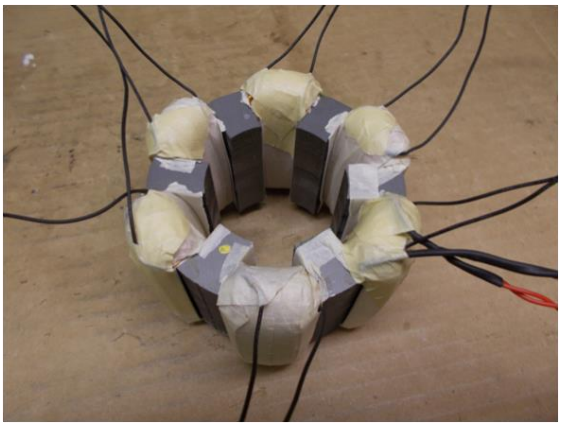

(a) Wound stator complete

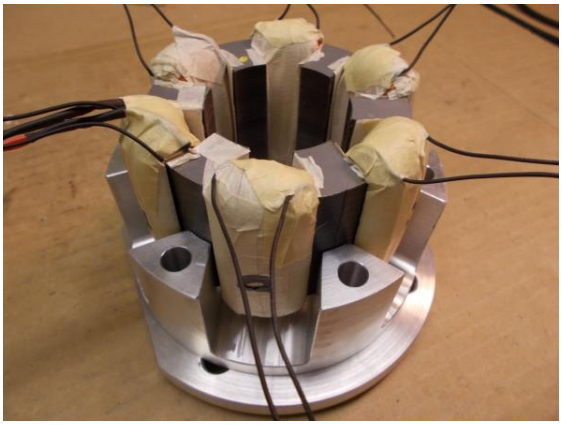

(b) Stator inserted into first half housing

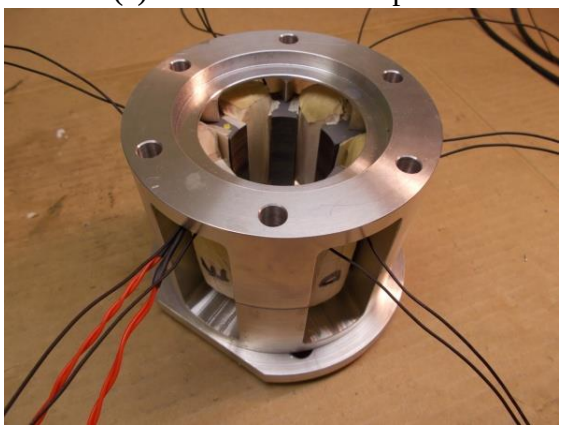

(c) Fully assembled with second half

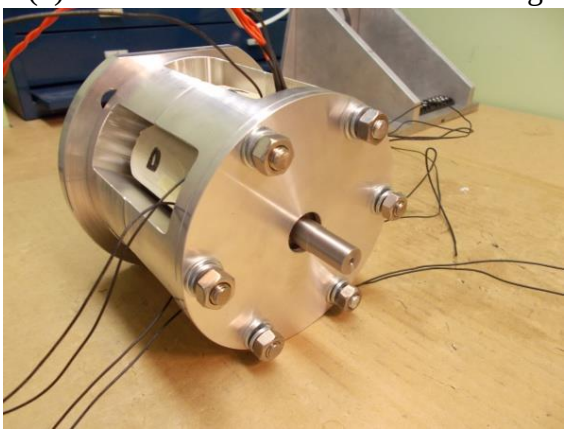

(d) Complete motor assembly with shaft

Figure 5.21. Stages of TSRM assembly

As the winding processes continued to multiple levels, figure 5.20(b), it was necessary to manage the end winding profile, figure 5.20(c), to permit the same perimeter coverage width, which would help reduce the number of winding layers. This was overlooked during the winding of the mule and, consequently, it had over 50% more winding layers on the outer level, 14 vs. 9 for the prototype. The "management" of the end windings is accomplished by careful positioning of the wire, as it is passed though the interior slot, so as to develop an inward tension on it and thus prevent its slipping off the end of the built up winding layers. Accordingly, there is much cross-over of the end windings, however, when properly executed it allows for a reduced layer count and an

even winding form, see figure 5.20(c). This process could be managed with an automated winding machine.

It was noted that the completed winding's available slot space remaining was far greater than the total available within the slot; the packing factor realized was greater than that expected for the slot, which was based originally upon the winding of the conventional pole wound machine. This observation supported the further development of the machine design where the machine variants were concerned, aforementioned section 5.6, although these variants were not constructed for test in this research program.

As the winding of the sections progressed fixturing of the stator would become a problem. To complete the winding of each section the stator, one side was initially affixed in a bench vise for the purpose such that it allowed the winding bobbin to pass through. Once a few windings were completed the available surface area for fixturing was reduced as any possible surface space with which to clamp the stator was no longer available. To complete the last two windings, a retention sleeve was designed and fabricated from ordinary steel tubing to contain the ends of the wound coils as the stator was fixed in the bench vise, refer to figure 5.19(d). With that the stator winding could be completed with the stator held firmly in position at all times during the winding process.

Prior to completion of the last winding, two 5KΩ thermistors were inserted into the corner of the winding slot adjacent to a tooth, one at the center of the rotor, the other at the end near the end winding location. This position was selected as attempting to place a thermistor in the end winding itself without disturbing its form or, the end winding leads being in the way of the winding operation and possibly being damaged,

would be difficult. As such, for the mule build, these two locations were selected with some advance knowledge from simulation that these would be the highest temperature locations within the machine aside from the rotor which, given its complexity, would not be instrumented. Once all windings were complete, the paper extensions were taped into position and the entire winding wrapped with several layers of tape. The winding leads were cut, bared for connection, then insulated with heat shrink tubing. A completed stator winding is shown in figure 5.21(a).

5.7.2 – Stator Insulation.

Prior to winding an electrical insulation paper of thickness .005" (0.127mm) was cut and placed into position inside each slot, and held in position by 3M™ two sided tape, which was sufficient for said purpose until the winding itself retained the slot paper. The stator outer diameter was insulated in a similar fashion with pieces of insulation paper cut to size 20mm wider than the winding width such that the excess ends could be wrapped around the completed winding and taped firm. The stator ends were insulated with the same paper except these were cut to the profile of the stator using a lamination as a template, similar to the procedure of Chapter 4.3.1, figure 4.13(b) then fixed into position with ordinary LePage's™ contact cement. The cut lengths of the paper used for the stator slots and outer diameter was approximately 2mm longer than the stator core length and projected beyond each insulated end when in position. This permitted the wrapping of said projection over that of the end paper insulation as the first slot winding was completed. This was intended to prevent possible contact of the winding with the stator iron at the slot edge locations which would most surely occur were the paper insulation pieces cut to the stator length only.

5.7.3 – Machine Assembly.

With the stator winding, motor case and end frames complete, the final assembly was a straight forward matter. The motor head plate was fitted with six ¼ x 20 through bolts, the first half of the motor case, and placed upon the bench, figure 5.21(b). The stator was then placed into the first half of the motor case with the second half placed over top of it, figure 5.21(c). Each of the winding leads was positioned as required for later connection in series. The shaft with rotor iron and bearings was then placed into the machine with the bearing seated in the head plate pocket. The end plate was then placed upon the second half of the motor case to seat the bearing into its pocket then bolted until snug, figure 5.21(d). The final torque of the through bolts was applied in a six point star fashion, opposite side to opposite side (as when tightening the lug nuts of an automobile) so as to apply an axial and radial compression to the stator core evenly as the gap between the two halves of the assembled motor case was closed. This comprised the completed motor assembly which would then be affixed to the machine dynamometer test bed.

5.7.4 - Prototype Construction.

As it stands presently, the mule construction was able to provide guidance for a successful prototype construction. In the case of the prototype, as discussed, a set of iron rotor laminations would be required, along with a new shaft with a means to retain said rotor. The axial end play of the shaft with bearings was stacked and set to .040” within the bearing pockets. It is customary in commercial practice to press fit the rotor to the stator shaft. In prototype, it was elected to use a slot and key retention to prevent relative

rotation while the axial position was secured by means of a locknut and lockwasher mechanism. The use of a locknut device required that the shaft diameter at that end of the motor be reduced for assembly, which, in turn, forced a reduction in the size of the bearing at that location from a 10mm bore to a 7mm bore with a corresponding width increase to 9mm; a series 637 miniature bearing. Since the loading and speeds of these prototypes are relatively low this would not present any problem in purpose or operation.

Further, it is customary in commercial practice to fill the rotor slots (the voids between the rotor poles) with a material sufficient to maintain the cylindrical shape of a complete rotor otherwise the rotor poles would, in effect, act as paddle wheels creating circulation losses within the machine, notwithstanding the rotational drag. Although it has been presented in the literature, Srinivas and Arumugam [101], Li et al.[102], that there may be a benefit to extended poles over that of a smooth bore variety, such was not the focus of this work and, accordingly, a smooth surface for the rotor was employed. To fill the rotor slots an elastomeric polymer of hardened polyurethane was cast into position and retained to the rotor iron by an adhesive. This process was contracted to a commercial supplier.

The stator and rotor iron laminations both of M19 electrical steel, 0.5mm thickness (24ga.) was supplied by an outside supplier, Polaris™, in accordance with the specifications of table 5.1. The winding of the former was undertaken in the same fashion as described in the aforementioned mule construction.

5.8 – CSRM MACHINE CONSTRUCTION

The CSRM was constructed from the same set of stator and rotor iron core physical dimensions as that of the TSRM of section 5.7, as was the case with the simulations described in section 5.4. Except for the requirement of a different frame casing for the CSRM versus the TSRM given its external winding arrangement, all other parts were commonized, this included the machine rotor. This was so as to readily facilitate swaps on the test bench and minimize prototype costs.

5.8.1 – Stator winding.

Since the CSRM is comprised of individual pole windings these would have to be fabricated individually then placed into position around each pole within the available slot space – arguably a more challenging task than winding directly about the back iron of the core as in the TSRM.

A special coil winder was constructed for the task and illustrated figures 5.22(a) and 5.22(b). The coil is wound in the slot provided for the purpose. The form at the base of the slot (which replicates a stator tooth) is approximately the size of a stator tooth. In this case it is approximately 1mm (.05”) greater in width and 5mm (.2”) greater in length than the stator tooth, while being shorter in height. The sides of the tooth form are inclined with a draft angle of about 2° permitting the wound coil to be easily released from the form. In any event, the coil must not be tightly wound as to permit its ready flexibility upon insertion into the slot around the stator tooth. Each coil was wound with 250 turns of #27 AWG size wire and taped loosely when removed from the form, figure 5.22(c). Each completed winding was then stretched into shape, fashioned into a tall

(a) CSRM Coil winder

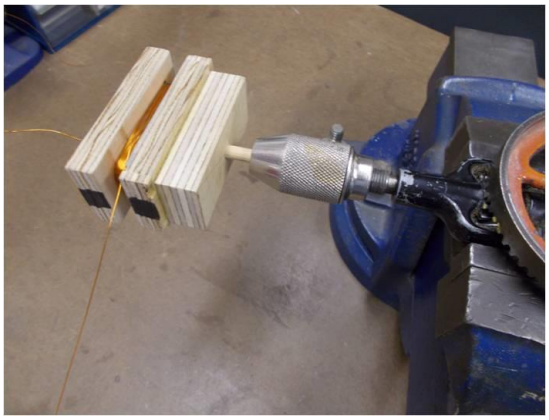

(b) CSRM Coil winding in progress

(c) Completed CSRM winging

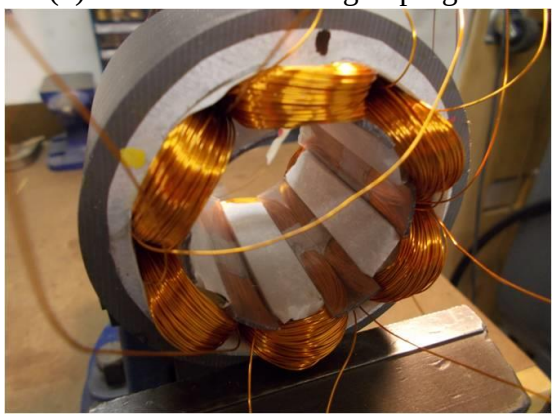

(d) Installed windings and slot keepers

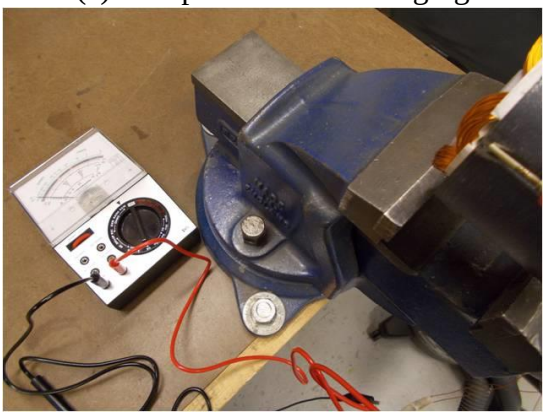

(e) Checking for shorts to laminations

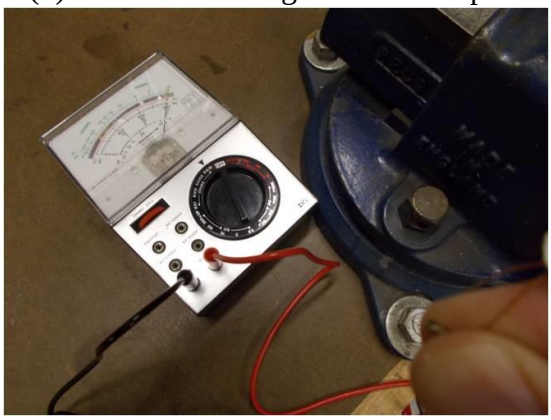

(f) Checking for winding opens

Figure 5.22 – CSRM Construction

profile, then placed over the insulated stator tooth, then stuffed into the slot such that the coil height was below that of the tooth height. Both the leads were all positioned to one end with the coil polarity assigned later. The next coil was inserted in the same fashion.

Once a slot was full then a slot keeper was inserted to hold both windings firmly in position within the slot. The keeper was fashioned from clear ABS thin wall (1mm) 2" diameter piping to a length of approximately 55mm and a width of 12mm. The last winding would prove extremely difficult to insert, such that the winder form was modified to a larger size providing what was essentially a loose fit to allow the last winding to be inserted where all the other windings were in position. With all the windings and keepers in position, figure 5.22(d), the wires were bared for the continuity and short testing, figures 5.22(e) and 5.22(f). This is an essential step for both machines, but more so for the CSRM as there is a risk with the process of stretching windings over poles that the insulation could either become compromised leading to a short or allowing a conductor to be nicked by part of the tooth. The latter occurred during the construction of the CSRM prototype, so it is always best to check. For instrumentation purposes, a single winding was fitted with an end winding 5KΩ thermistor sensor same as the TSRM construction.

5.8.2 – Stator insulation.

Again, as with the TSRM construction, the stator would require full insulation between the windings and the iron core. The same electrical insulation paper was used for the slot lining as described in 5.7.2. Pieces were first fashioned for the ends of the stator by cutting from a stator lamination used as a template, in the fashion described in chapter 4, section 4.3.1 for cutting the graphite sheet and paper laminations. These were then affixed to the stator ends using contact cement. The slot liners were cut to the nearly same size and fashion as described in section 5.7.2 for the TSRM – the only difference being 5mm longer providing a larger over-hang at each end of the slot. The corner edges

were then cut and folded over the ends of the stator teeth then held in position with masking tape. Thus, each stator tooth was completely insulated on all sides. The only difficulty to be overcome was to successfully insert the coil over the insulated tooth and into the slot without disturbing the paper insulation nor nicking the wire with the sharp edge of the stator tooth (esp. at the corners) when inserting the winding – much easier said than done. To solve that problem a paper insulation cap was fashioned and placed over the tooth, and taped into position along its sides. Not only would this help protect the winding upon insertion but it would also make said insertion a far easier task. The only drawback was in having to remove the paper cap as it would have otherwise interfered with the rotor motion. The cap was removed by trimming each along its length with an Xacto^{TM} knife, at the location of the slot keeper The completed winding is shown figure 5.22(d).

5.8.3 – Machine Assembly.

Before the final assembly into the case the leads were insulated with PVC heat shrink tubing of the appropriate size and color coded for identification of coil polarity and phase; red, black, yellow for phases and white band for polarity. See figures 5.23(a) and 5.23(c). Either winding lead may be identified as positive or negative, but must be consistent for all windings. The stator was then inserted into the lower case half (without the provision for wiring access) leads up first. As the case to stator fit was somewhat tight the case was warmed to permit easy assembly – this helps prevent jamming and possibly having to remove or pull the core backwards which may risk damaging the lamination welds, figure 5.23(b). The top case half was then lowered over the part assembly and the leads placed through the slots provided, figure 5.23(d). This sub

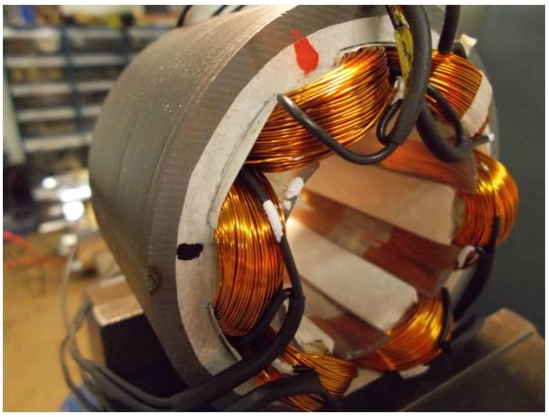

(a) Lead insulation and Identification

(b) Expanding the case for improved fit

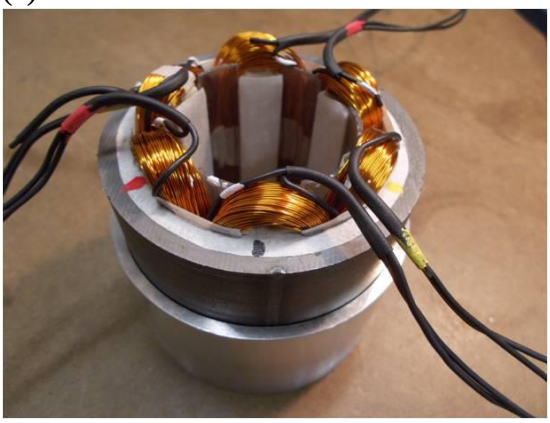

(c) Assembled into first half casing

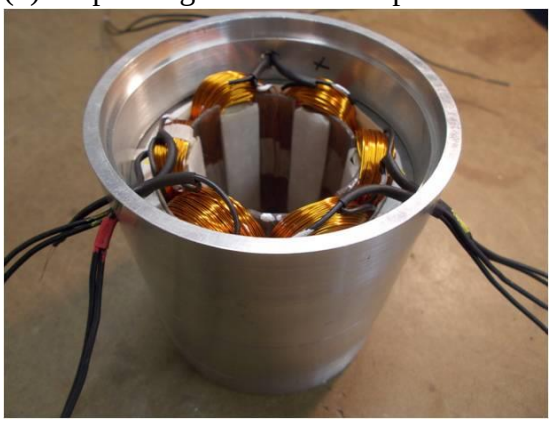

(d) Assembled into second half case

Figure 5.23. Assembly of the CSRM motor winding and casings.

assembly was then placed into the head plate, the rotor assembly inserted, then the end plate fixed into position and the completed assembly bolted together.

5.9 – EXPERIMENTAL TEST SET-UP AND PROCEDURE

The machine tests were performed on a motor-generator-dynamometer test stand fabricated for the purpose. The generator, a calibrated Sensor Technology "SEW Eurodrive" type CMD93L/TorqueSense, multi pole 3 phase DC Permanent Magnet Synchronous Machine (PMSM) capable of providing up to 52N-m load at 4000RPM was fitted to the subject test TSRM or CSRM. See figure 5.24 (c) and (d). A load cell for the

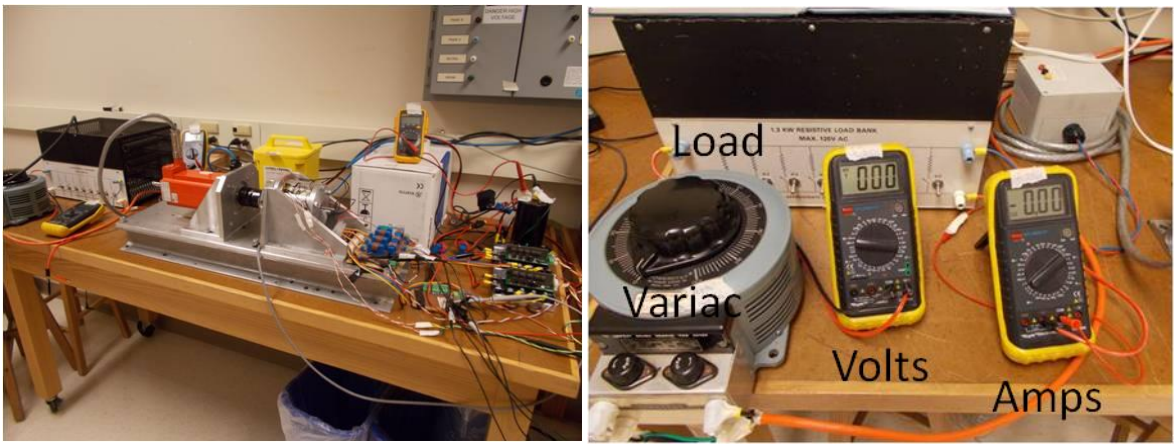

(a) Motor dynamometer test bench (b) Dyno generator volt and current meas.

(c) Dyno. Generator and optical timing (d) TSRM test machine

Figure 5.24. Motor Dynamometer Test Bench set-up

purpose of torque measurement was contained within said DCPMSM which provided a direct readout of torque load via a TorqueSense Sensor Technology electronic signal processor and display type E302. This signal was processed to the data acquisition oscilloscope shown at the right of figure 5.24 (d) for computing the average torque value. Each of the SRM under test was fitted with a photo-diode (opto-electric) shutter wheel to provide the necessary commutation signal to the power electronics converter/drive controller. See figure 5.24 (c) and (d) right hand and left hand sides, respectively. The controller, an Arduino board model no. DUE R3, open source electronics prototype

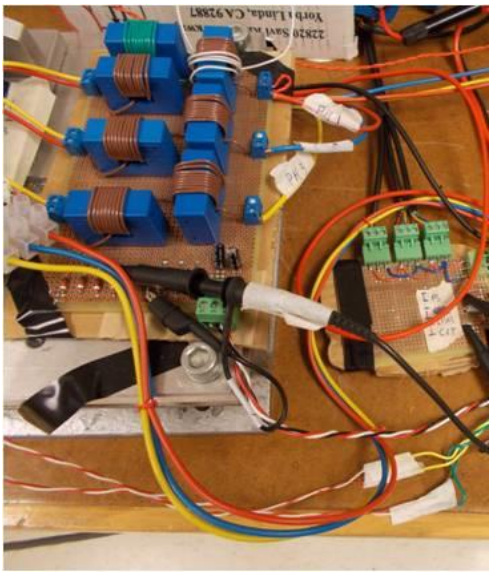

(a) Coil and phase current transducer board with test points

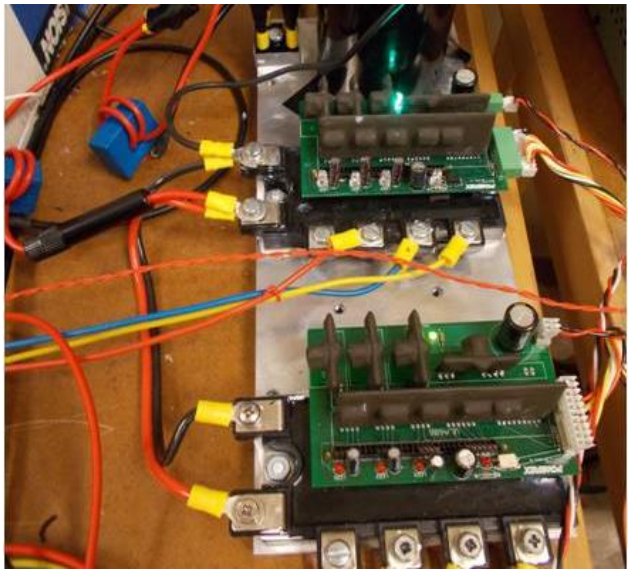

(b) 12 Switch DC Converter Assembly

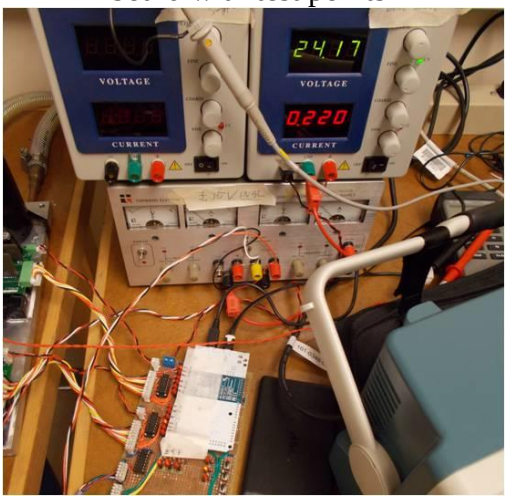

(c) Arduino board and power supply

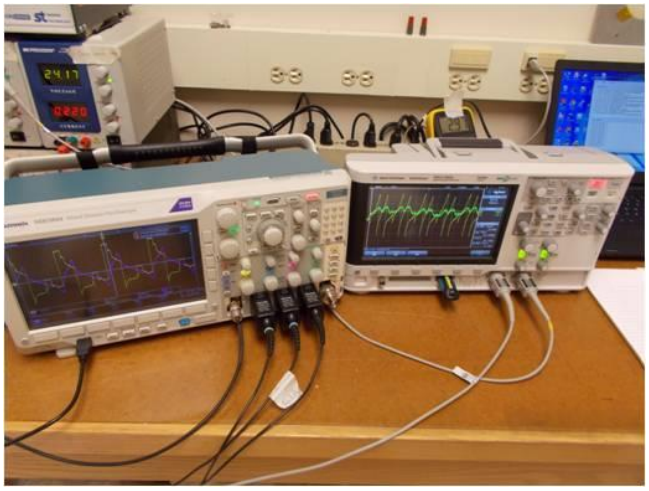

(d) Oscilloscope data acquisition

Figure 5.25. Converter Motor Drive, Arduino Controller and Data Acquisition

platform shown figure 5.25(c), was programmed for the commutation sequence necessary to activate the power electronics switching devices as required for each commutation scheme outlined section 5.2. Commutation was provided by the DC converter shown figure 5.25(b) capable of either 12 switch or 6 switch operation selectable from the circuit board. As stated section 5.7 the test set-up and commissioning was performed with the mule TSRM operated at lower voltages until such confidence was developed in the

apparatus to permit a regime of full operational tests. The machine RPM was abe to be determined directly from the opto-coupler and oscilloscope input by simple calculation from the commutation period.

5.10 – EXPERIMENTAL RESULTS

The performance of the subject machines has been evaluated electrically, mechanically and thermally. Each will be considered and discussed separately. Generally, the test results have confirmed that which was expected from the simulation results for the TSRM versus the CSRM performance with torque output as the criteria. However, the absolute predicted values of torque and calculated efficiencies from JMAG simulation were not supported by the experimental result; all predicted values for machine torque from simulation were significantly higher than those realized from the tests, by a factor of approximately four times. Further, the indicated machine efficiencies from the tests (electrical power in versus shaft power out) were significantly lower than those predicted in simulation. This however, does not limit the comparison of the TSRM to the CSRM as the differences are systemic and carry through to each machine with both having used the same power converter and iron laminations (of same manufacture). In the case of the thermal performance, the TSRM demonstrated itself to be a "cool performer" when compared to its CSRM counterpart operating under similar conditions. Again, the absolute operating temperatures predicted by the LPTN simulation model were not realized but, once tuned with experimental data, the model was able to show an agreeable result.

5.10.1 – Machine mechanical and electrical performance.

The TSRM tests were performed first. The TSRM was evaluated at two winding levels, 407 turns per slot and 333 turns per slot as aforementioned in section 5.3.1, 5.3.2, 5.4.1 and 5.4.2. Two voltage supply, VDC input levels were considered, 150V and 300V. This was necessary to best demonstrate the performance of the machine as several of the load and speed combinations simulated were precluded from the actual test due to the thermal limits of the winding insulation. Some tests were run for only a few seconds, enough time to acquire all the necessary data. Although the said insulation was capable to 200°C, the machine was equipped with a thermal cut-out set to a 150°C limit so as to provide reasonable protection for the windings; the testing was conservative as there was no desire to risk a damaged winding given the extensive rebuild time involved.

With the TSRM tests complete the machine was removed and replaced with the CSRM or more accurately, the rotor shaft and bearing assembly was removed from the TSRM, placed into the CSRM frame assembly, the bolts tightened and the final wiring completed. The same set of tests was performed at the same input voltage settings described above, measuring the machine torque across the permitted speed range. The same 150°C thermal limit was imposed. The torque-speed results are shown in figures 5.25 and 5.26. The machines are referred to in the legend as “TSRM turns-switch mode-volts” or “CSRM turns-switch mode-volts”. The sub designation “ii” in the case of the CSRM indicates this was the second winding version of the machine. During the course of the thermal tests the first CSRM was damaged from a slot keeper thermal incident and had to be rewound. The average torque produced by the second machine was markedly greater than that of the first so these results are the ones shown. The machine operation at

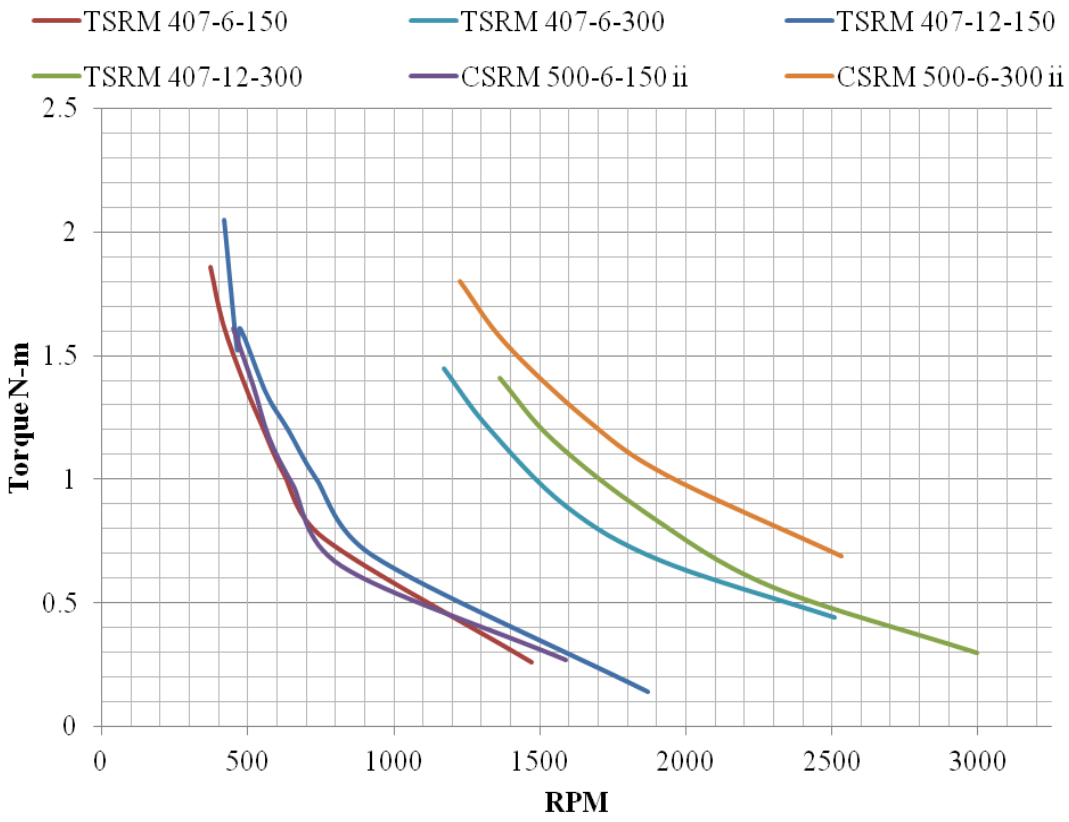

Figure 5.26. Average Torque vs. RPM for TSRM (407) and CSRM (500)

150 VDC has shown to be nearly identical for both machines, with the TSRM 12 switch mode operation producing an improved average torque on the order of 0.1 N-m across the speed range considered. The same 12 switch mode operation shows an improvement in average torque at the 300 VDC input level, of about 0.2 N-m declining to 0 nearing the 3000 RPM limit. Improved 12 switch mode operation over 6 switch mode operation is consistent with the simulation findings. At the higher RPM range, the TSRM (407) average torque performance at 300 VDC was not able to match that of the CSRM as predicted from the simulation results. However, when examining the results for the TSRM (333) winding version the average torque in 12 switch mode operation at 300

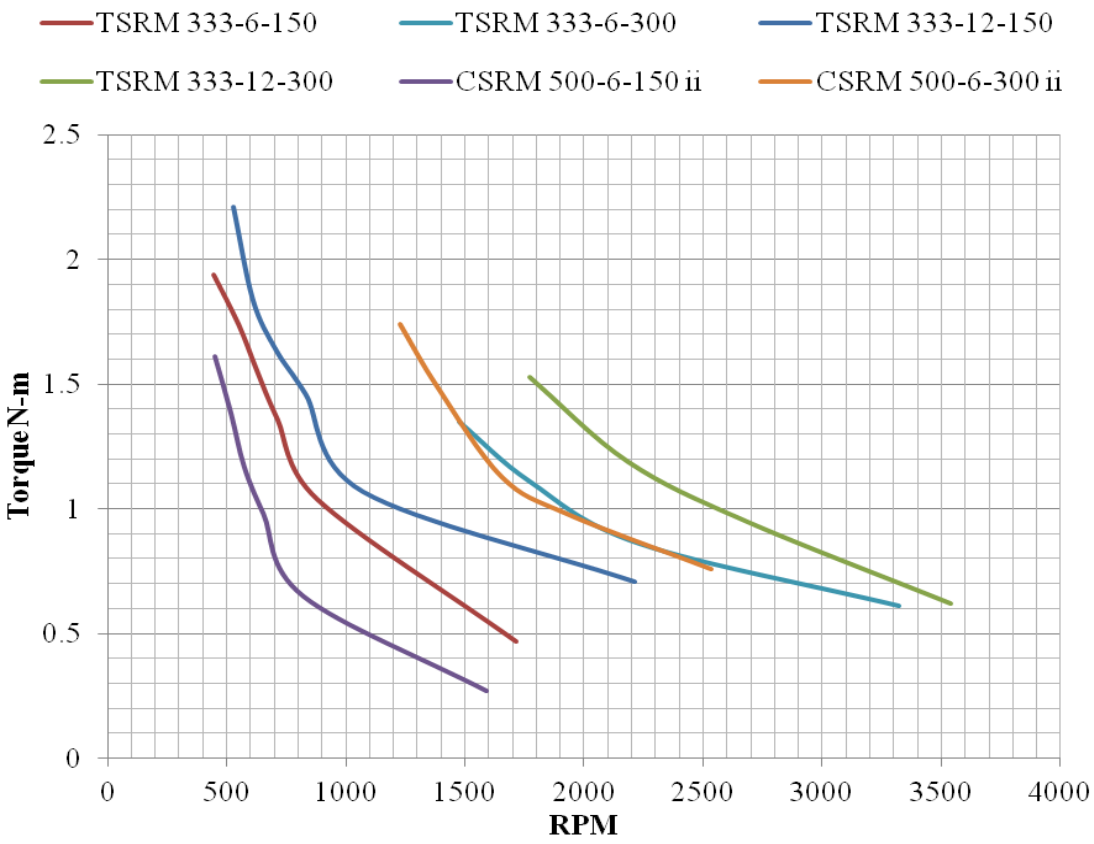

Figure 5.27. Average Torque vs. RPM for TSRM (407) and CSRM (500)

VDC was found to be greater than that of the CSRM by a wide margin, from 0.5 to 0.3 N-m over the speed range of comparison 1800 RPM to 2500 RPM, respectively. This represents an average torque improvement of 50% at best, down to 30%. This margin of improvement diminishes above 2500 RPM. This too appears to be consistent with the simulation results. What did surprise was the 6 switch mode operation of the TSRM (333) which had been estimated to produce a lower average torque than the CSRM. Here however, the TSRM (333) in 6 switch mode closely matched the CSRM's average torque over the speed range from 1500 to 2500 RPM, whereas the simulation result indicated otherwise. This led to the development of the 407 turns per slot winding but the thinking behind that has not been proven out in the experimental results as the simulation

indicated that TSRM (407) performance in 12 switch mode would at least match or exceed that of the CSRM.

Returning to examine 150 VDC operation for the TSRM (333), the average torque was seen to be greater than that of the CSRM at the same voltage, a significant improvement over the TSRM (407) winding version, so this is consistent with the last result but not with the simulation result.

During the testing, as stated, it was not possible to test at all points which were originally simulated due to loading limitations. The dynamometer loading was not a "dial in" but rather an incremental loading with only certain operating points being available as permitted by the load resistance bank used to absorb the generated power. As such, for a truer comparison of the torque and current waveforms to the simulation results, it was necessary to simulate the operating points encountered during the testing. The figures 5.27(a) through 5.27(d) shows the torque and current comparison for the TSRM (407) at the 300 VDC operating point under 12 switch mode operation at 1325 RPM. Disregard the first cycle transient of the simulation result, figures 5.27(a) and 5.27(c). As discussed, the absolute values of the torque measurement do not compare with those of the simulation as there are significant losses within the machine, additional to the copper losses, which may be attributed to the iron lamination's material fabrication and/or assembly quality. Notwithstanding, there are two features to note: The superimposition of a lower frequency on the torque waveform, which is estimated to come from a mechanical coupling (shaft and universal joint) to the dynamometer generator set and, the torque ripple of approximately 50% value which is significantly less than the 75% predicted by simulation analysis. As to the current waveforms, the

experimental result captures more accurately the inductive effect with the representation of the change in coil current after a commutation event that would change the current direction in said coil. The measured RMS current value of 4.13 amps compares to a simulation value of 4.9 amps, or agreement within 20%.

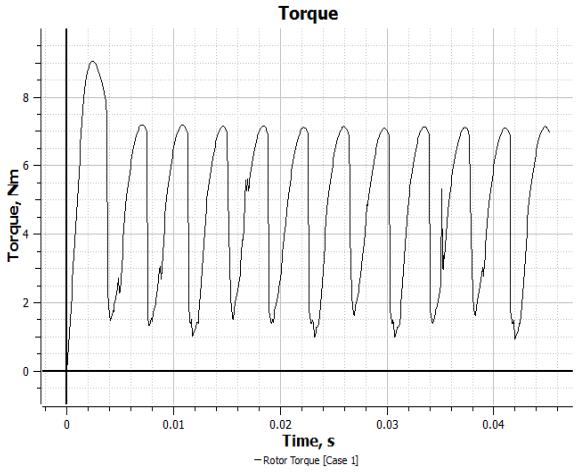

(a) Simulated torque waveform

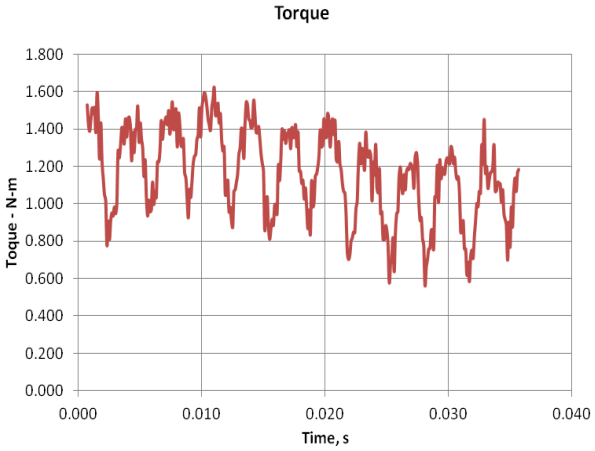

(b) Observed torque waveform

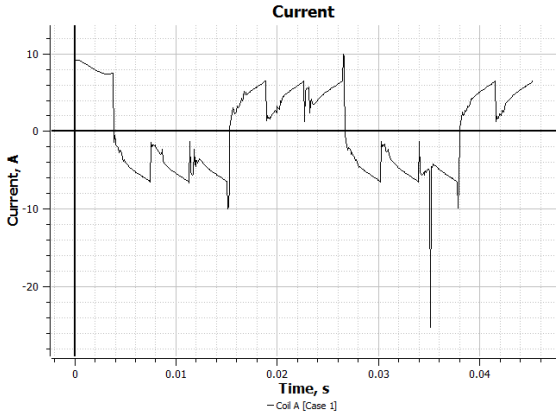

(c) Simulated current waveform

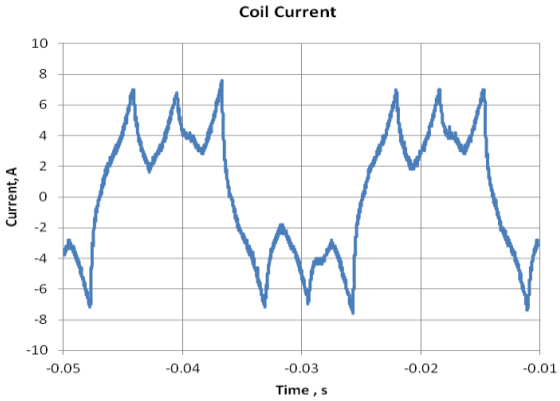

(d) Observed current waveform

Figure 5.28. TSRM (407) Waveforms at 12 switch operation, 1325 RPM, 300VDC

The same comparison under similar conditions but at 3000 RPM shows similar results, see figure 5.28. At this RPM level the similarities are less clear but the current waveform shows the same period and commutation features although these are more difficult to recognize. What's going on here? The observed current waveform, upon closer

examination represents an exaggerated form of the simulation result. As to the torque waveform, again the periodicity is identical, although as before the magnitude does not agree with those of the simulation for the reasons stated. The torque ripple here is nearly 100% as per the simulation result. It should be noted that the applied dynamometer electrical loading was zero (open circuit), with only the generator's mechanical rotational resistance serving as a load. The superimposed sinusoidal waveform observed prior, remains, indicating that this feature clearly emanates from the mechanical coupling between the TSRM and the load generator.

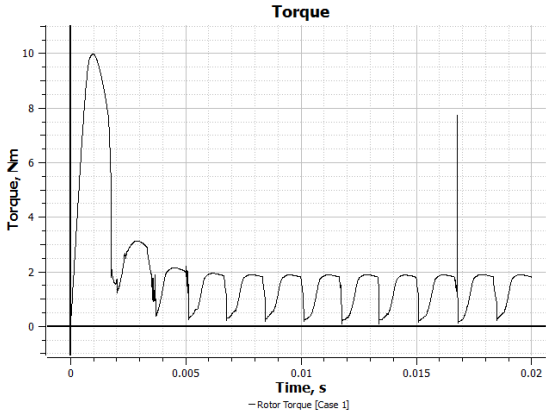

(a) Simulated torque waveform

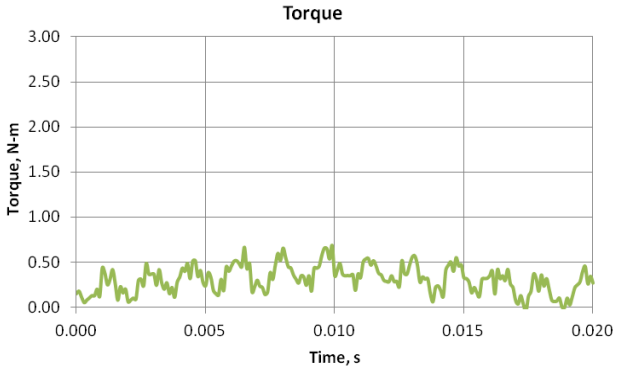

(b) Observed torque waveform

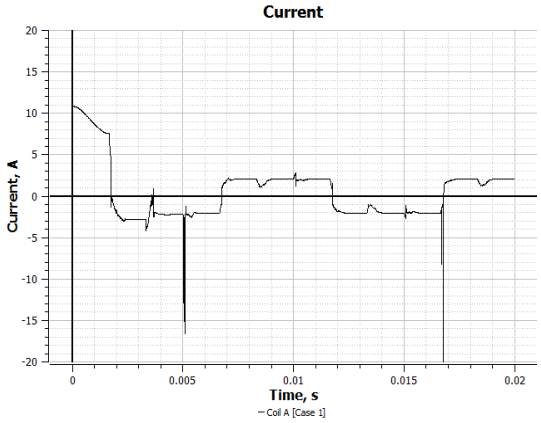

(c) Simulated current waveform

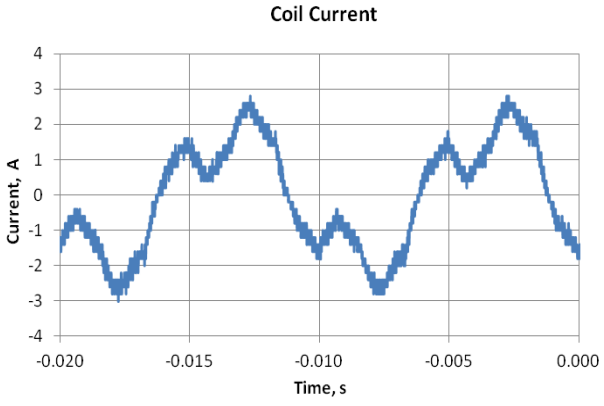

(d) Observed current waveform

Figure 5.29. TSRM (407) Waveforms at 12 switch operation, 3000 RPM, 300VDC

The test result from the CSRM may also be compared to that of the simulation result where as above the latter was performed specified at or near to the test conditions of RPM, in this case at 2500RPM with no applied load to the generator; the 3000RPM condition was not attainable. At such conditions the resulting torque is revealing more of the system dynamics as before than any torque ripple, although it is certainly present in the waveform. The observed current waveform is markedly dissimilar from that of the simulation, bearing a closer resemblance to that of figure 5.8(a) showing the simulation result for a lower 1000RPM. The effect on coil current of the machine's winding inductance is clearly visible in the observed result. See figure 5.29.

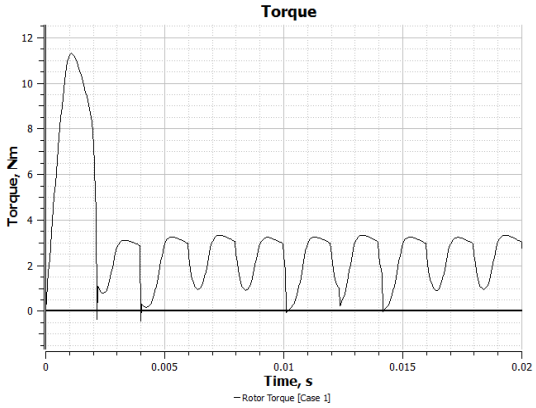

(a) Simulated torque waveform

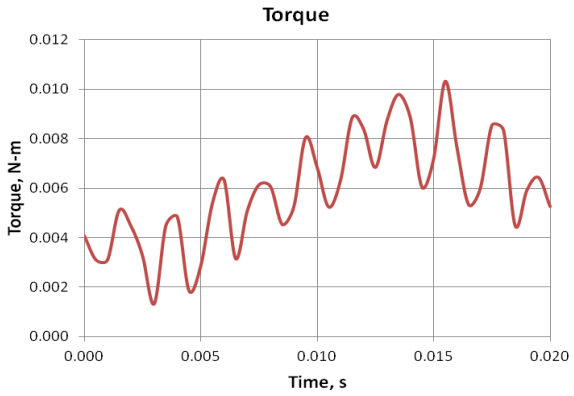

(b) Observed torque waveform

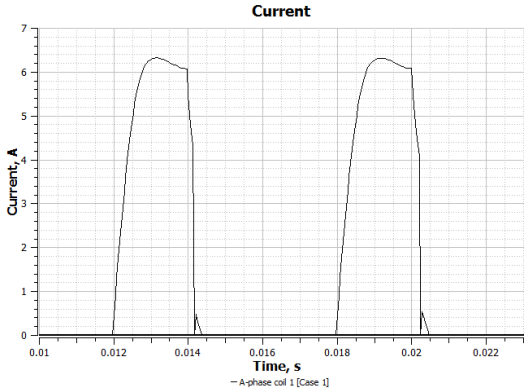

(c) Simulated current waveform

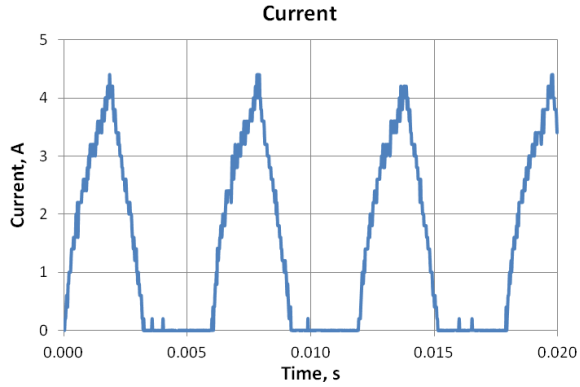

(d) Observed current waveform

Figure 5.30. CSRM (500) Waveforms at 6 switch operation, 2500 RPM, 300VDC

5.10.2 – Thermal Performance.

The thermal performance of the TSRM was central to its development. The thermal performance of this machine was evaluated first by selecting an operating point that would permit its continued operation, i.e. to reach steady state temperature. Accordingly the machine was operated at 100 VDC input at 1 Amp (rms) for several hours test duration until such time as the temperature change at the end windings and coil sides was less than 2°C per hour. At these conditions, the machine operated at 1350 RPM without applied load or any forced air cooling assistance, in natural convection. The steady state temperature of the TSRM reached 123.7°C on the end windings and 98.9°C on the coil side temperatures. This difference, where the end winding temperature was greater than the coil side temperature was consistent with the thermal simulation result of table 5.9, notwithstanding that prediction was for operation at 300 VDC and 3000 RPM it was expected that the same pattern of relative component temperatures would hold true.

With the measured results it was a straightforward matter to return to the thermal simulation LPTN model of figure 5.14 and tune the model in an effort to improve the predictive performance. The thermal resistances were updated to reflect the prototype machine build where contact resistance between components is higher, the windings are not impregnated with polymer, and the machine RPM was lower (affecting internal convective heat transfer). With that, the convective thermal resistance, R_{cv}, was the only thermal resistance adjusted to tune the model. This was selected as the overall temperature of all the machine components is dominated by the convective heat transfer coefficient, that R_{cv} is, in some cases, several orders of magnituede greater than other

thermal resistances which lie in the main heat transfer path, i.e. directly from end windings to frame; it is the dominant resistance in said path. The convective thermal resistance was reduced substantially, by about a factor of $1/10^{th}$ from 2.87 K/W to 0.25 K/W, to reflect a much higher overall convective heat transfer coefficient of the open frame design and, indirectly, some heat transfer to the mounting frame of the dynamometer brake, something not considered in the theoretical analysis. The adjustment was executed manually by trial and error until the closest match to the experimental result for the end winding temperature was obtained. See table 5.12.

Table 5.12. Calculated Temperatures (°C) at 1350RPM

Motor	**Machine and Cooling Configuration**			
	CSRM		***TSRM(407)****	
Component	***Untuned***	***Tuned***	***Untuned***	***Tuned***
Bearings	257	N/A	207	51
Coil Sides-upper	N/A	N/A	276	119
Coil Sides-lower	295	N/A	279	123
End Winding	301	N/A	281	125
Teeth	259	N/A	210	52
Rotor	302	N/A	256	139
Frame	253	N/A	203	45
Yoke (Back Iron)	256	N/A	208	51

*TSRM equalized copper loss to that of CSRM (as fig. 5.14)

It was not possible to match both experimental temperature results for both the end winding and coil side temperatures as the latter point referred to in the model is actually calculated at the centre of the winding whereas experimentally it was evaluated at a point on the edge of the winding next to the tooth; the thermistor was situated in an area between the tooth and coil side nodes in an area of contact resistance. Accordingly, its temperature should reside between the two thermal model predictions of 123°C and 52°C for the coil sides and the end windings, respectively. At 98.9°C, it does, being closer to

the coil side temperature than the tooth temperature. Indeed, it was mounted on the inboard side (closer to the coil) of the insulating paper and masking tape in construction, so it comes as no surprise that its closer to the coil side temperature than the tooth temperature.

The thermal performance of the TSRM would then have to be compared to that of the CSRM under the same operating conditions, that being where the thermal input was approximately the same as that of the TSRM which have led to the above described results. Accordingly, the losses of the TSRM in the thermal analysis complied above in table 5.12 were effectively equalized to that of the CSRM as in table 5.9 of section 5.5.3. Where it was expected that the thermal input at 1350 RPM would be dominated by the copper losses, a target input current to the CSRM was calculated, at which to set the control variac (current) for the thermal test. This was achieved at an input voltage of 101VDC supply to the CSRM with a current of 1.13 Amps (rms); this condition would provide for the same level of copper loss in the CSRM, and thus the same total heat rejection from this source. No attempt at adjustment was made for any differences in the iron loss of the CSRM versus the TSRM as these are inherent in the different electromagnetic switching operation of the machines, and as such can't be reconciled. The CSRM under test in this fashion was operated until either steady state operating temperature was achieved or the operating temperature under transient conditions exceeded that of the steady state temperature realized from the TSRM test noted above. The test was discontinued when the end winding temperature reached 139.9°C in transient response after 2 minutes, with a corresponding coil side temperature of 43.7°C.

The TSRM steady state temperature was surpassed after only 90 seconds of operation at this condition.

Tuning the CSRM model would be another matter as it was not possible to reach a steady state temperature during the test. Accordingly, no such model tuning could take place on that basis. The thermal model time prediction to reach the transient temperature of the end winding at the point of the test discontinuation was approx. 9 minutes, a significant disagreement with the experimental experience of 2 minutes. This would suggest a convective thermal resistance, R_{cv} that was either substantially higher than that used, 2.87 K/W, or significantly higher internal thermal contact resistance, or greater losses internal to the machine than provided for. Tuning the model to the transient time result by adjustment of R_{cv} (increasing) would have little effect on the transient result and lead to erroneously large steady state temperature estimates. This would suggest the possibility of an error in the calculated thermal capacitance of the winding component; the mass could be lighter. In any event, it may be fairly concluded that the steady state operating temperature of the CSRM is indeed higher than that of the TSRM in the both the experimental findings and the analysis, by a wide margin.

5.11 – CONCLUSION

The development of a toroidal switched reluctance machine was stated earlier as being motivated by electric machine cooling enhancement, in this case that of an SRM. That was the original purpose of this research undertaking. To that point, the thermal results obtained, both predicted from the LPTN simulation model and derived from the experimental, support the earlier claim that the toroidal topology for the SRM would

provide a means for enhanced cooling primarily due to the fact that part of its windings are exposed to the peripheral environment. That has been clearly borne out, particularly with the experimental result confirming that for the same input losses to the core, dominated by copper losses, the temperature rise of the CSRM exceeded that of the TSRM maximum temperature observed. That would seem obvious at some level, but not so obvious is the development of an equivalent toroidally wound machine to replicate the equivalent performance of the conventional machine as part of realizing the thermal performance improvement.

Notwithstanding the foregoing, the mechanical and electrical performance of the toroidal topology is another matter altogether. Again, the early research sought to find a toroidal winding which would represent the equivalent of the conventional winding, and was based upon the concept of electromagnetic equivalence. That is to say, the topology would be transparent in so far as the electromagnetic circuit was concerned. And, with that the performance of the TSRM would thus be comparable to that of the CSRM. In simulation however, it was determined that a magnetic flux leakage would reduce the former's torque performance, and so, with additional slot winding space afforded by the toroidal topology, it would be possible to adjust for this by adding additional winding turns whilst maintaining the same copper losses (more turns, larger diameter) which would compensate for flux leakage. With these two versions of the machine were considered, one with 333 turns per slot, the other 407. The simulations showed that under dynamic conditions the 407 turns version of the TSRM operated in the 12 switch mode would replicate the CSRM. However, with the experimental result, it would appear that in fact, the "ideal" 333 turns winding TSRM has achieved the performance based

upon average torque that is at the least equal to, or better than the CSRM considered. The improved performance of 12 switch mode operation, over that of 6 switch mode operation was predicted in simulation and confirmed with the experimental result. The improved high speed performance with the 333 turns winding TSRM versus that of the 407 turns winding TSRM was also confirmed with the experimental result. This result is realized as effectively the inductance under commutation in a TSRM is divided such that the change in current during commutation events is taking place simultaneously within two separate windings, whereas in the case of the CSRM this must occur in one larger winding only. Recall from figure 5.3(b), in the ideal sense, that in the TSRM only two of the machine's six windings experience a coil current direction change and the coil current is half the value of that of the CSRM.

In closing, the thermal performance of the TSRM winding topology as a means to improve the thermal management of an SRM has been proven out although there is admittedly considerable work going forward with regard to the electrical performance of the machine and its true equivalent to that of the CSRM. The results, although not ideal, as if they were fully supportive of the simulation results, particularly considering the discrepancy in absolute torque, and efficiency realized, are, nonetheless encouraging.

CHAPTER 6 – SUMMARY CONCLUSIONS FROM THE RESEARCH AND FUTURE WORK

6.1 - INTER-LAMINATE COOLING APPLIED TO THE SRM

6.1.1 – Introduction

The application of inter-laminate cooling (ILC) was brought together with the switched reluctance motor's thermal performance in simulation, its principles of operation compared and summarized. ILC provided a substantial improvement in the thermal performance where the high speed SRM was concerned. While an improvement in thermal performance is evidenced in any SRM, the high speed machine makes practical use of the increased effective thermal conductance of the iron laminations with ILC as, in high speed operation, this is where the dominant the iron losses are located.

The use of the transformer structure to serve as a proxy for the electric machine was well described in chapter 4. The research was limited to the use of this device as presently, the construction of an ILC high speed SRM is precluded due to considerations of cost and processing of the Pyrolytic Graphite Sheet (PGS). I would reiterate that the principle is not limited in application to the SRM but may be of benefit in any electric machine or device employing iron laminations structure. In the case of the latter, hand cutting of PGS as described in the foregoing chapter 4.3.1 would prove nearly impossible with the SRM lamination's profile. The proper alignment of the SRM lamination used as a template to cut the sheet material could not be guaranteed during the cutting process. Moreover, there is presently no means to create the weldment for the stator or rotor assembly having laminations with PGS material contained therein, whereas the

transformer assembly was facilitated by the presence of through-bolt holes. No such mechanism was available for the SRM and the development of such was outside the scope of the present research. Moreover again, the design of a high speed SRM to demonstrate the benefit was outside the scope of the present research and a machine build is not required to prove out the performance of the concept in similarly constructed machines. That said, what must be recognized in machine performance is the loss of space consumed by the ILC material. This will affect the specific power and torque of the machine as the axial length will be increased by the presence of the ILC material, however minimal in thickness. This may be reconciled by increasing the input power to the ILC machine to equalize the specific power and torque, however the mechanical output power and thermal inputs would be greater resulting in higher temperatures than would otherwise be realized. These two conditions with such an adjustment may not be reconciled other than to determine the machine with the higher input power, same specific power and torque, has an operating temperature not greater than the machine without the use of ILC. If so, the net benefit would be positive overall.

Accordingly, it was decided to limit the treatment of the ILC method applied to the SRM as a simulation study only. This is not only justified by the foregoing, but further by the knowledge that the thermal conductivity of the iron containing PGS has been well established and confirmed by experimental means as described in chapter 4.

6.1.2 – Thermal Conductivity of Iron Laminations with ILC.

The concept of “Gain” in input power was presented in chapter 4, sections 4.3.3 and 4.4.5. This concept may also be extended to the gain in thermal conductivity of the

iron laminations with the presence of PGS as the inter-laminate material. It is a straight forward matter to calculate and show that the effective, or overall, thermal conductivity of the iron laminations are increased by an amount equal to that of the gain, where recall G = 1/(1-E). This was confirmed in simulation by determining the thermal conductivity of the iron lamination material that would be required to produce the same core temperature that would result with ILC using PGS in place. It is no coincidence then that the thermal conductivity of the iron required $k_{i\text{-}eff}$, is a multiple equal to the gain, greater than that of the iron without ILC, k_i. In other words:

$$k_{i\text{-}eff}/k_i = G \quad (1)$$

With this, the adjustment in iron thermal conductivity was made to the thermal resistance calculation for the LPTN thermal model, which was then solved with thermal input from the SRM.

6.1.3 – High speed SRM.

As stated in the foregoing, the benefit of ILC is best observed with a high speed machine. In the case of the SRM this does not evidence itself until the iron losses begin to exceed the copper losses; the former increasing with RPM where the latter are declining. However, the subject machine, the TSRM (333), TSRM (407), or its CSRM version, in simulated operation at 300VDC would not show such a condition where the iron losses exceeded the copper losses as magnetic saturation could not be maintained much above 3000RPM, beyond which iron losses would remain flat. Accordingly, thermal simulation with ILC was performed with the CSRM version of these machines

operated at 3000RPM, 300VDC. Consequently, we returned to the high speed SRM of chapter 3 with which to perform the thermal simulation. We then used the Effectiveness "E" concept developed in chapter 4 to characterize the benefit in cooling performance as a result of ILC applied to each machine.

6.1.4 – Thermal Simulation.

The thermal simulation was performed following the same technique as outlined in Chapters 3b section 3b.2.3 through 5 and conducted as a steady-state temperature solution. The same construction was assumed for both machines although differences in size and speed will affect the values of the convective coefficients used. This is not a major factor as the main heat flux path in either case is from the end windings to the frame. The thermal conductivity of the iron was adjusted by the aforementioned gain, with E determined from the transformer experimental results from chapter 4, section 4.4.5. With E=0.67, the resulting gain of 3 was applied to the thermal conductivity of the iron k_i = 38 W/mK resulting in an effective thermal conductivity, $k_{i\text{-}eff}$ = 114 W/mK. This value would be applied to calculating the iron laminations' thermal resistance used in the LPTN representing each machine. Understand, in so doing, it is assumed that the same degree of thermal contact resistance existing in the experimental transformer, between the iron laminations and the heat sink, can be replicated, more or less, in the machine build. This is not an unreasonable assumption in as much as a mechanical shrink fit is possible in the latter whereas the experimental transformer was limited as to contact force between the heat sink and laminations; the fastening method in that case employed wood screws.

Recall that to compensate, great care was taken in the construction and assembly by way of precision machined heat sinks and setting blocks for the laminations assembly.

6.1.5 – Simulation Results and Discussion.

6.1.5.1 – Thermal inputs to the LPTN model.

The following loss inputs were determined and used in the simulation, table 6.1. The cooling was modeled as water jacket cooling applied to the machine's frame acting as the heat sink.

Table 6.1. Total Copper and Iron Losses input to the LPTN model

Machine Type	RPM at rated VDC			
	3,000		20,000	
	Copper	Iron	Copper	Iron
HSRM	n/a	n/a	1000W	15500W
CSRM (figure 5.10)	307W	18W	n/a	n/a

6.1.5.2 – Thermal results from the LPTN model.

From the thermal simulation for the conditions of 6.3.1 the results are detailed tables 6.2(a) and 6.2(b) below, which are shown for the major machine components of the CSRM and HSRM. The corresponding cooling effectiveness, E, is calculated for each location in accordance with the equation 3, presented chapter 4 section 4.3.2. Where a component is not directly subject to applied cooling, i.e. every component except the stator yoke and teeth which comprise the whole of the stator iron, the effectiveness value calculated represents the cooling effectiveness which results at that component location as a result of the ILC method being applied to the stator iron. It is a net effectiveness.

Table 6.2(a). Calculated Temperatures (°C) and effectiveness values "E" at stated conditions of Table 1. and LPTN model for the CSRM.

Machine	**Machine and Cooling Configuration**		
	CSRM sILC	***CSRM cILC***	
Component	***Temp***	***Temp***	***E***
Coolant	20.0	20.0	n/a
Bearings	25.6	25.1	0.089
Coil Sides	221	187.8	0.074
End Winding	228	215	0.063
Teeth	41.1	27.3	0.66
Rotor	106	97.6	0.101
Frame	20.1	20.1	n/a
Yoke (Back Iron)	28.7	23.0	0.66

Table 6.2(b). Calculated Temperatures (°C) and effectiveness values "E" at stated conditions of Table 1. and LPTN model for the HSRM.

Machine	**Machine and Cooling Configuration**		
	HSRM sILC	***HSRM cILC***	
Component	***Temp***	***Temp***	***E***
Coolant	16	16	n/a
Bearings	35.0	34.1	0.056
Coil Sides	237	113	0.57
End Winding	206	108	0.52
Teeth	245	110	0.60
Rotor	156	135	0.15
Frame	19.0	20	n/a
Yoke (Back Iron)	159	73.7	0.61

It is postulated that, generally, the net effectiveness at a component level may be expressed as:

$$E(n) = E_1 \times E_2 \times E_3 \times \ldots E_{n-1} \times E_n \qquad (2a)$$

or the form,

$$E(n) = \prod_{1}^{n} E_n \qquad (2b)$$

where E_n represents the component level removed from the heat sink. The cooling method applied to the heat sink itself, E_0, is taken to have an effectiveness of unity (1) so therefore is redundant. All other values of E are less than 1 as would be expected from the results described in chapter 4. E_1 represents the effectiveness of the applied cooling method to the stator iron, which would be in contact with the heat sink, as was the transformer iron in the subject of chapter 4. Each subsequent neighbouring component, beyond the stator iron, will see the cooling effectiveness of the applied method reduced by a factor. This factor may be calculated from the above equation. For example,

$$E(2) = E_1 \times E_2 \quad (3a)$$

$$E_2 = E(2)/E_1 \quad (3b)$$

where E_2 represents the effectiveness of the applied ILC method to the stator as seen upon the winding component (2). This will be demonstrated further on.

6.1.5.3 – Discussion.

Examining the tables 6.2(a) and 6.2(b) it is clear that the maximum effectiveness of the ILC cooling method is experienced at the stator iron of both machines. However, where the copper loss dominates over the iron loss as in the CSRM the results of table 6.2(a) show that the ILC method is largely ineffective in reducing the temperatures of the coil sides and end winding components of the machine, the components of highest temperature. This might be expected given that the interface between the coil sides and stator represent an impediment to heat transfer such that reducing the latter's temperature has only a marginal effect on the temperature of that component where said component is

not the major source of heat generated within the machine. In other words, the stator acts as the sink for the coil windings, so a small reduction in its temperature has little effect on the temperature of the coil windings whose temperature is much higher. The change in stator temperature at the teeth was 13°C, the change in coil side and end winding temperature was also 13°C, but from a level of over 200°C this change is of minor significance. Further, where the copper loss is the major heat loss of the machine, there will be convective heat transfer at the end windings to the interior air and end shields of the machine. This additional heat flux path would remain little changed by the addition of ILC material to the stator.

The value of "E" at the stator is also of interest. Calculated here at 0.66 it is close to the theoretical value of 0.67 as determined in chapter 4, where it was assumed to be degraded from its maximum theoretical value of 0.737 by imperfect contact of the ILC material to the heat sink, in this case the machine frame. The degradation here from 0.67 to 0.66 is arising from the thermal contact resistance present between the frame and the stator, as built into the LPTN model. Otherwise E would have a value of 0.67. We see again the independence of E with respect to the level of internal heat flux as these levels in the CSRM are different than that of the transformer model or experiment.

The high speed machine, having an entirely different heat generation pattern, the losses being dominated by the stator iron, yielded a significantly improved result as to the reduction of end winding and coil side temperatures. Here, a reduction in the stator iron temperature, where the heat generated is significant, has led to a drop in the coil side and end winding temperatures of a greater magnitude than that of the HSRM. This is evidenced not only by the temperatures themselves but also by the effectiveness result of

the applied ILC method, 0.52 and 0.57 versus 0.063 and 0.074, respectively for end windings and coil sides components. Since the stator iron is now the dominant source of heat generation, the cooling method is applied to a component at a much higher temperature than before, as in the CSRM prior, the resulting change in stator iron temperature, while of the same relative magnitude as before, having a greater absolute temperature change, can produce a greater effect upon the end winding and coil sides temperatures. The change in stator temperature at the teeth was 135°C, the change in coil side and end winding temperature was 123°C and 98°C respectively where the component temperatures without ILC were 237°C and 245°C respectively. This represents a magnitude of temperature change difference of about 9.4x and 7.5x respectively over that of the CSRM. The difference from that of the CSRM is reflective of some difference in the machine sizes and convective cooling within the machine.

It is also worth noting the change in temperature of the HSRM rotor. Here again, this is greater in absolute terms than that of the CSRM largely due to the change in winding temperature and stator tooth temperature as these are a heat transfer path across the air gap for this machine. This is also true for the CSRM but again, the rotor is not a high heat loss component of the machine, whereas in the HSRM it is, as is the stator, so it can benefit from a temperature reduction of that component along with that of the end windings and coil sides as a result.

Finally, we return to the neighbouring component effectiveness aforementioned section 6.1.2. Returning to the example and following equation 3b, the effectiveness E_2 for each machine may be readily calculated from the simulation data of tables 6.2(a) and 6.2(b). In the case of the coil sides these values amount to 0.11 and 0.95 respectively for

the CSRM and HSRM. What the value of E_2 speaks to is the ability of the applied cooling method to make a change upon the neighbouring component, in this case the coil sides. We determined from the result that this was not possible to any significance in the case of the CSRM whereas in the case of the HSRM the resultant change in temperature of the coil sides was greater by a factor of about 9.4x versus the CSRM. That, coincidentally is nearly the difference in magnitude between E_2 of the two machines. 0.95/0.11 being equal to 8.6x, not exact agreement with 9.4x but within 10%, suggests that these items are related and indicative of the value of E_2 as a guide to evaluating the performance of an applied cooling method, as is the value of E_1 as discussed in chapter 4. It is possible that the deviation of the multiples lies within the differences of the machines themselves.

6.1.6 – Conclusions on ILC applied to the SRM.

The study of the effect of the applied ILC method upon the CSRM and the high speed SRM as a means of thermal management of these machines has yielded the following conclusions:

- The method is of greatest benefit in a machine where the iron losses dominate over the copper losses, where the application of said method is to the component of greatest loss. This was expected.
- Adjacent components will see a benefit from the applied ILC method, but this is most effective where the ILC is applied to the high heat loss component. If the adjacent component, as in the case of the CSRM, is the high heat loss component,

then the effect will be far less pronounced. This was evidenced from the differences in the values of "E" determined for each component.

- The effectiveness as described by "E_1" is a useful characterization of the performance of the applied cooling method to the electric machine, something which is sadly lacking in the literature, as discussed in chapter 2. The concept is not limited to the ILC method applied to the machines discussed here, but rather may be applied to any cooling method being considered for an electric machine.
- The concept of the overall effectiveness of an applied cooling method upon a neighbouring component, "E(2)", within the machine, as expressed by "E_2" as discussed, may prove useful in characterizing the performance of applied cooling methods. Unfortunately, E_2 appears to be machine dependent so this may not be as useful when considering machines of different type, with different loss patterns. In any event, the result is supportive of the theory which should be the subject of some future work to bring it to a firm conclusion.

6.2 – SUMMARY CONCLUSIONS TO THE ENTIRE WORK

6.2.1 – Inter-Laminate Cooling

The Inter Laminate Cooling or ILC concept was developed and proven out by the experimental results as evidenced through the effectiveness measure which was developed as part of the analytical evaluation of the ILC approach. The effectiveness was calculated for the first level component, i.e. the heat generating component. The expected effectiveness of the method, E=0.67, based upon the physical characteristics and

dimensions of the system, along with the consideration of the thermal contact resistance between the surfaces was realized with an experimental result of E=0.66. This is sufficient to confirm the application of the concept. Great care was taken in the construction of the experimental inductors to minimize any difference between the control and the test device with careful matching of the components, use of the same measuring instruments and supporting equipment in each trial run. The data was presented with a consideration of the thermocouple error and it was clear that the difference in measured temperatures was several times greater than the thermocouple tolerance. Minor errors in construction, particularly the coil winding count, were considered upon the impact to the final result, where it was concluded that an error on the order of 1% would lie well within the measurement tolerance of the thermocouple and would not register.

It was also observed that the effectiveness was directly related to, and considered as, the gain which would occur in the capability to handle increased levels of input power that would result in the same operating temperature were ILC not applied. With the presence of the ILC graphite material (PGS) the power density of the machine will be reduced with the increased volume of the stator. In the case here the 100 micron material thickness of the graphite represented a 20% increase in stator volume. However, this may be improved with the use of thinner PGS material. When considering the gain realized by the application of ILC the loss of power density, here 17% or a factor of 0.83, is more than overcome by a gain factor of 3 where such gain is occurring at the first level. However, at the second level, E(2), as would occur when evaluating the effectiveness of the ILC upon the machine winding, the effectiveness was substantially reduced, by a

factor of 10 and approximately 1.2 for the CSRM and HSRM respectively, considered in the analysis. The corresponding gain was 1.06 for the CSRM and 2.22 for the HSRM. The ILC method would be able to overcome the loss of power density due to its presence where a second level, E(2), effectiveness is concerned when considering a high speed SRM but may not be able to overcome said loss when utilized within the core of a low speed SRM. The stator would see cooling but the effect upon the windings would be limited to the extent that the loss of power density could not be more than made up by the improvement in cooling afforded by the ILC method when considering the winding component. In short, this approach, while clearly of benefit, will not apply equally to all machines.

6.2.2 – The Toroidal Switched Reluctance Machine

The TSRM developed in Chapter 5, while not delivering the expected output in terms of torque at RPM and machine efficiency, was clearly able to demonstrate the improvement in machine cooling when the CSRM and TSRM machines were compared on a one to one basis under equivalent thermal input conditions to the windings. The improvement in machine cooling capability was the original motivation for considering the toroidal winding architecture. Accordingly, an optimized machine design was not considered for this work and thus remains part of the future work to be carried on with these machines. An optimized design should consider both the thermal and electromagnetic aspects of the machine and, as such, constitutes a global optimization problem. The cooling improvement was made on the basis of the “electromagnetic equivalence”, i.e. the TSRM being the magnetically equivalent machine to the CSRM

such that electrically the machines would appear to be transparent, a black box. The experimental data that was obtained was able to support the analytical solution save and except for the magnitude of the machine torque and machine efficiencies could not match that of the simulation analysis by a wide margin. This was attributed to either of iron loss not considered in the simulation analysis or excessive iron loss present in both prototype CSRM and TSRM machines. In any event, this was concluded to be a systemic loss, as when ignored, the performance comparisons machine to machine were upheld by the experimental result – we saw the trends that we expected to see in the results. The requirement for the higher turns count, 407 versus the ideal 333, was not supported conclusively, but the improved dynamic result at higher speeds when the 333 turns count winding is used was, as was the improved bipolar 12 switch operation versus the unipolar 6 switch operation. The machines were remarkably similar in performance at operating voltages lower than the 300V considered in the simulation analysis. There was also the improvement in the winding packing factor realized with the toroidal winding arrangement which would permit changes to the internal construction which could also be used to improve the specific torque and power density as observed in the analysis of Chapter 5, section 5.6. The winding form was also observed to be much tighter to the core, something permitted by toroidal winding, and would serve to improve the compactness of the end windings, which, to a small extent, would offset part of the increased outer diameter of the machine, conserving its volume.

As to the application of the ILC method to the SRM or a TSRM, this was found to be of benefit in the case of certain machines, particularly the HSRM variety. However, presently, the cost of material and its fabrication suitable to electric machine application

precludes achieving the higher cooling efficiencies which it may bring. With time improvements in manufacturing processes to reduce cost may see this approach as reality.

6.3 – OUTCOME OF THE RESEARCH

This research has resulted in the following:

- Two US Provisional Patents, the first for the the ILC method using PGS applied to electric machines, the second, for the Single Continuous Winding TSRM.

- Two international conference papers, the first at IET PEMD, Manchester, UK, 2014, the second, IEEE ECCE, Pittsburgh, PA, 2014. The latter has further been accepted for journal publication IEEE Trans. Industry Applications, Jan. 2016.

- The development of the effectiveness concept applied to the cooling of electric machines in an effort to evaluate the performance of the applied cooling method. Such evaluation was lacking in the literature consulted.

APPENDIX A

A.1 – PANASONIC PYROLYTIC GRAPHITE SHEET PROPERTIES AND AVAILABILITY

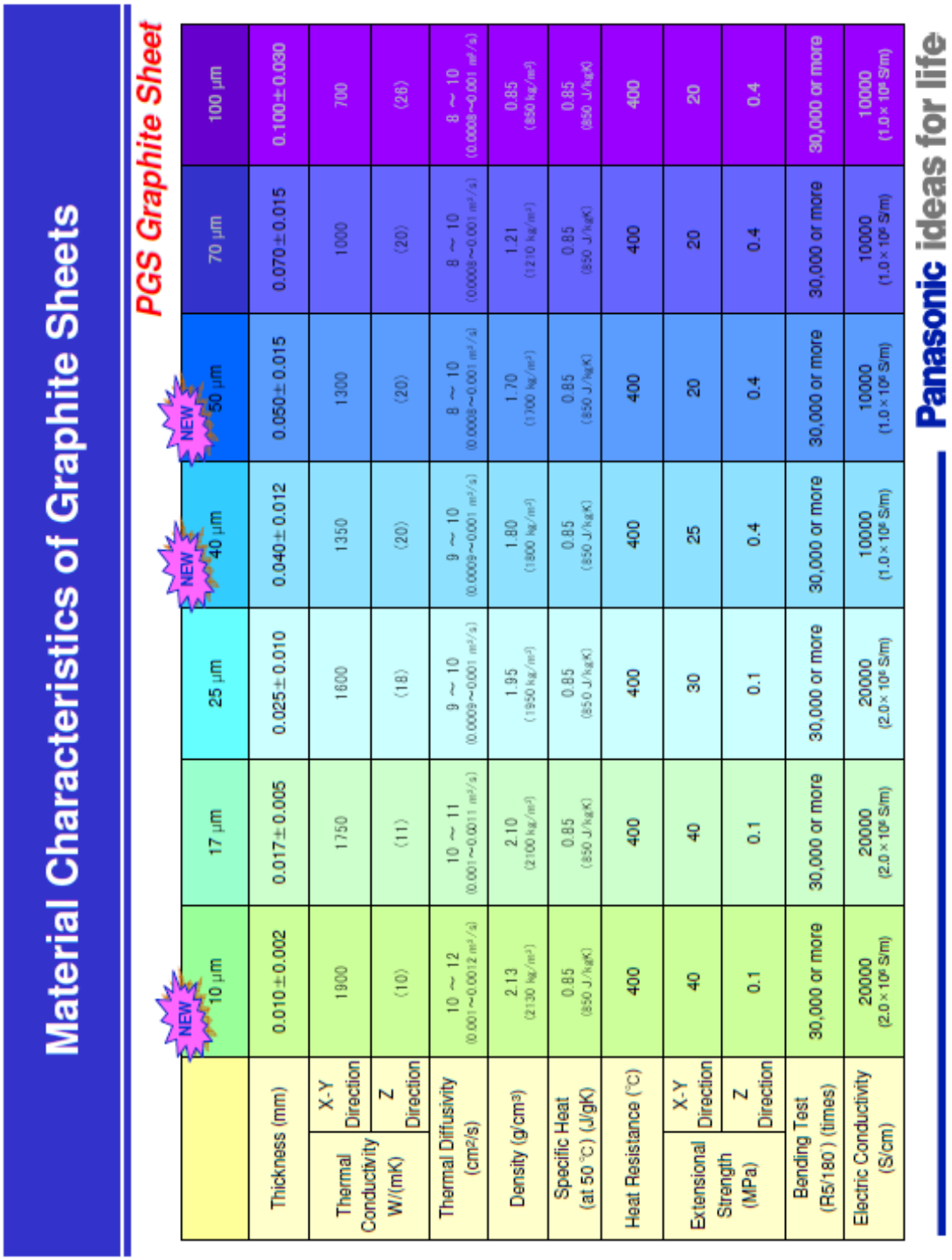

Material Characteristics of Graphite Sheets

PGS Graphite Sheet

		10 µm (NEW)	17 µm	25 µm	40 µm (NEW)	50 µm (NEW)	70 µm	100 µm
Thickness (mm)		0.010±0.002	0.017±0.005	0.025±0.010	0.040±0.012	0.050±0.015	0.070±0.015	0.100±0.030
Thermal Conductivity W/(mK)	X-Y Direction	1900	1750	1600	1350	1300	1000	700
	Z Direction	(10)	(11)	(18)	(20)	(20)	(20)	(26)
Thermal Diffusivity (cm²/s)		10 ~ 12 (0.001~0.0012 m²/s)	10 ~ 11 (0.001~0.0011 m²/s)	9 ~ 10 (0.0009~0.001 m²/s)	9 ~ 10 (0.0009~0.001 m²/s)	8 ~ 10 (0.0008~0.001 m²/s)	8 ~ 10 (0.0008~0.001 m²/s)	8 ~ 10 (0.0008~0.001 m²/s)
Density (g/cm³)		2.13 (2130 kg/m³)	2.10 (2100 kg/m³)	1.95 (1950 kg/m³)	1.80 (1800 kg/m³)	1.70 (1700 kg/m³)	1.21 (1210 kg/m³)	0.85 (850 kg/m³)
Specific Heat (at 50 °C) (J/gK)		0.85 (850 J/kgK)	0.85 (850 J/kgK)	0.85 (850 J/kgK)	0.85 (850 J/kgK)	0.85 (850 J/kgK)	0.85 (850 J/kgK)	0.85 (850 J/kgK)
Heat Resistance (°C)		400	400	400	400	400	400	400
Extensional Strength (MPa)	X-Y Direction	40	40	30	25	20	20	20
	Z Direction	0.1	0.1	0.1	0.4	0.4	0.4	0.4
Bending Test (R5/180°) (times)		30,000 or more	30,000 or more	30,000 or more	30,000 or more	30,000 or more	30,000 or more	30,000 or more
Electric Conductivity (S/cm)		20000 (2.0×10⁴ S/m)	20000 (2.0×10⁴ S/m)	20000 (2.0×10⁴ S/m)	10000 (1.0×10⁴ S/m)	10000 (1.0×10⁴ S/m)	10000 (1.0×10⁴ S/m)	10000 (1.0×10⁴ S/m)

Panasonic ideas for life

Material Characteristics of Pyrolytic Graphite Sheet (PGS) from Panasonic Corp.

APPENDIX A

A.2 – PYROLYTIC GRAPHITE SHEET INTERFACIAL CONTACT RESISTANCE

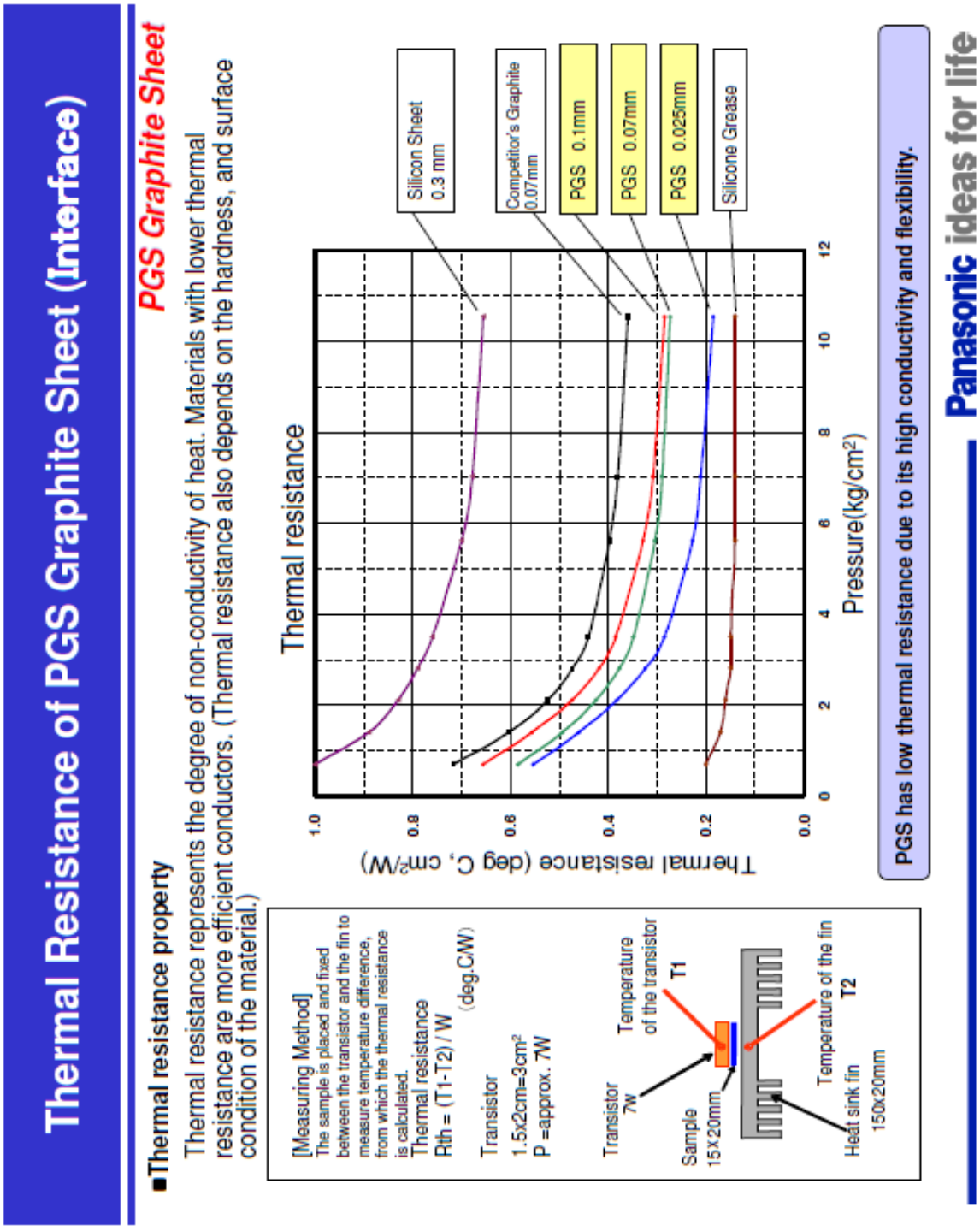

Thermal Contact Resistance of PGS versus Interfacial Contact Pressure

APPENDIX B

B.1 – EXPERIMENTAL TRANSFORMER (INDUCTOR) LAMINATIONS SIZE DETAIL

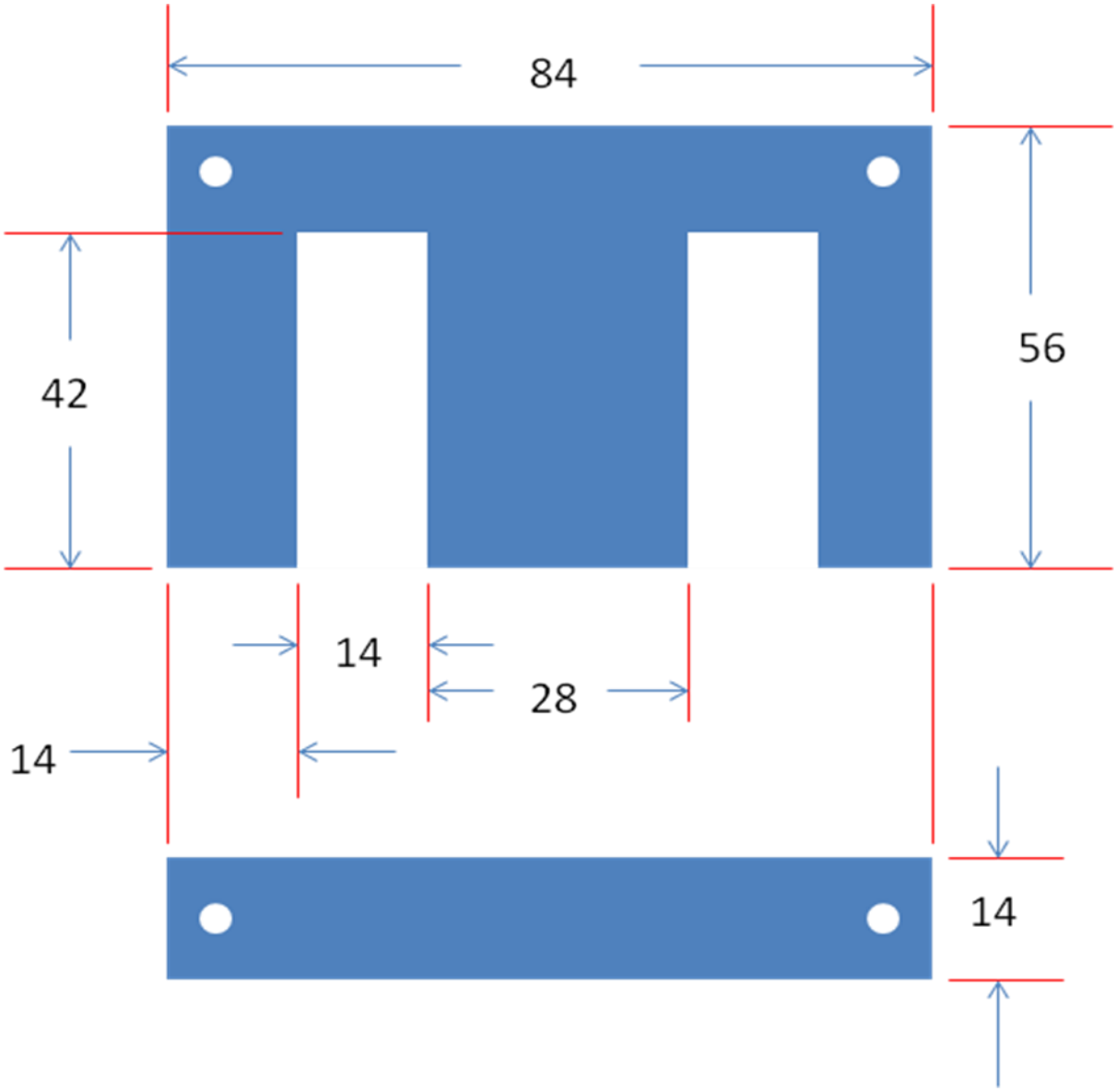

Laminations thickness approx. 0.5mm

APPENDIX C

C.1 – KEN MAY THERMOCOUPLE CALIBRATION CURVE FOR TYPE T THERMOCOUPLE USED

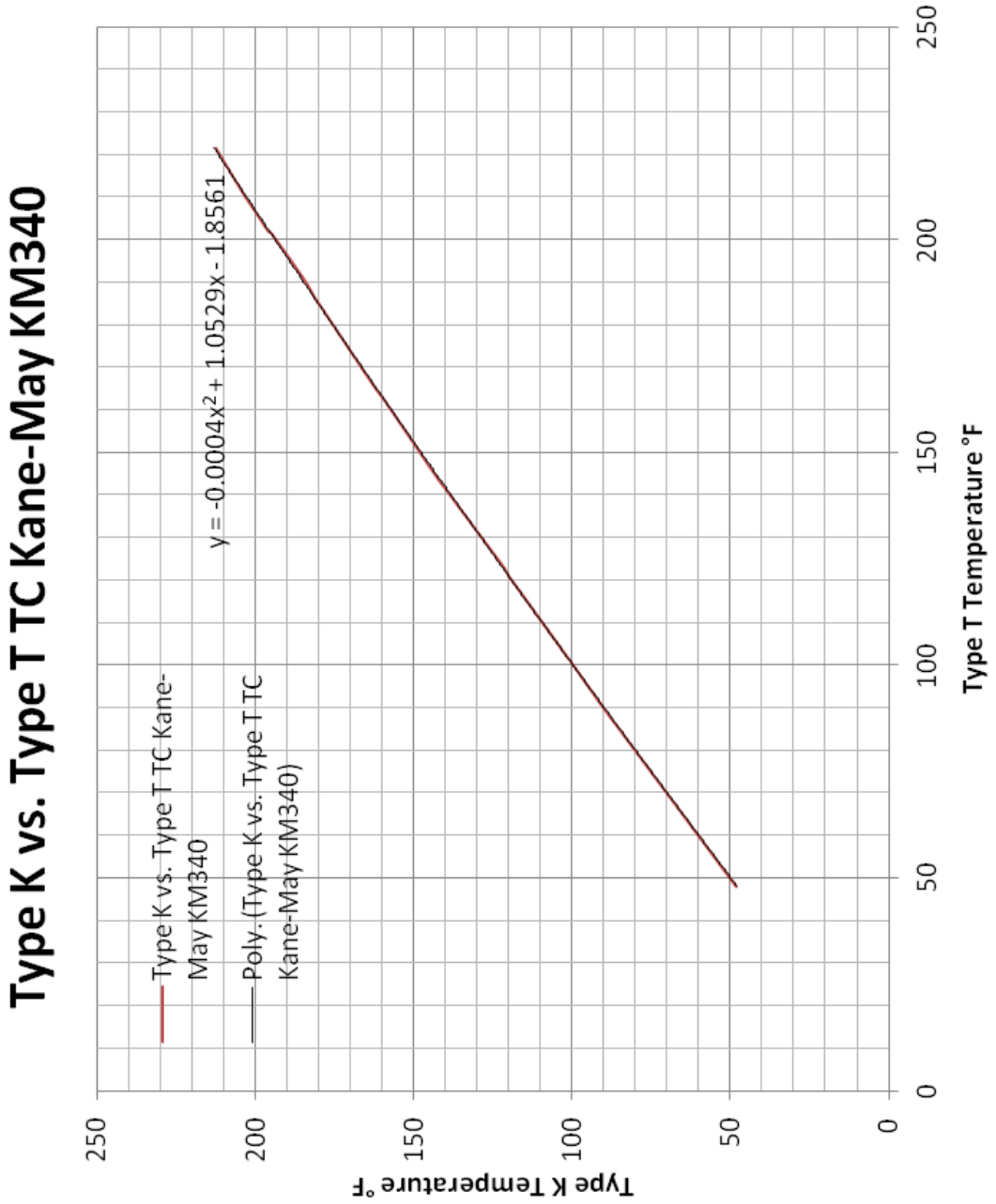

APPENDIX C

C.2 – KEN MAY THERMOCOUPLE CALIBRATION CURVE FOR TYPE T THERMOCOUPLE USED

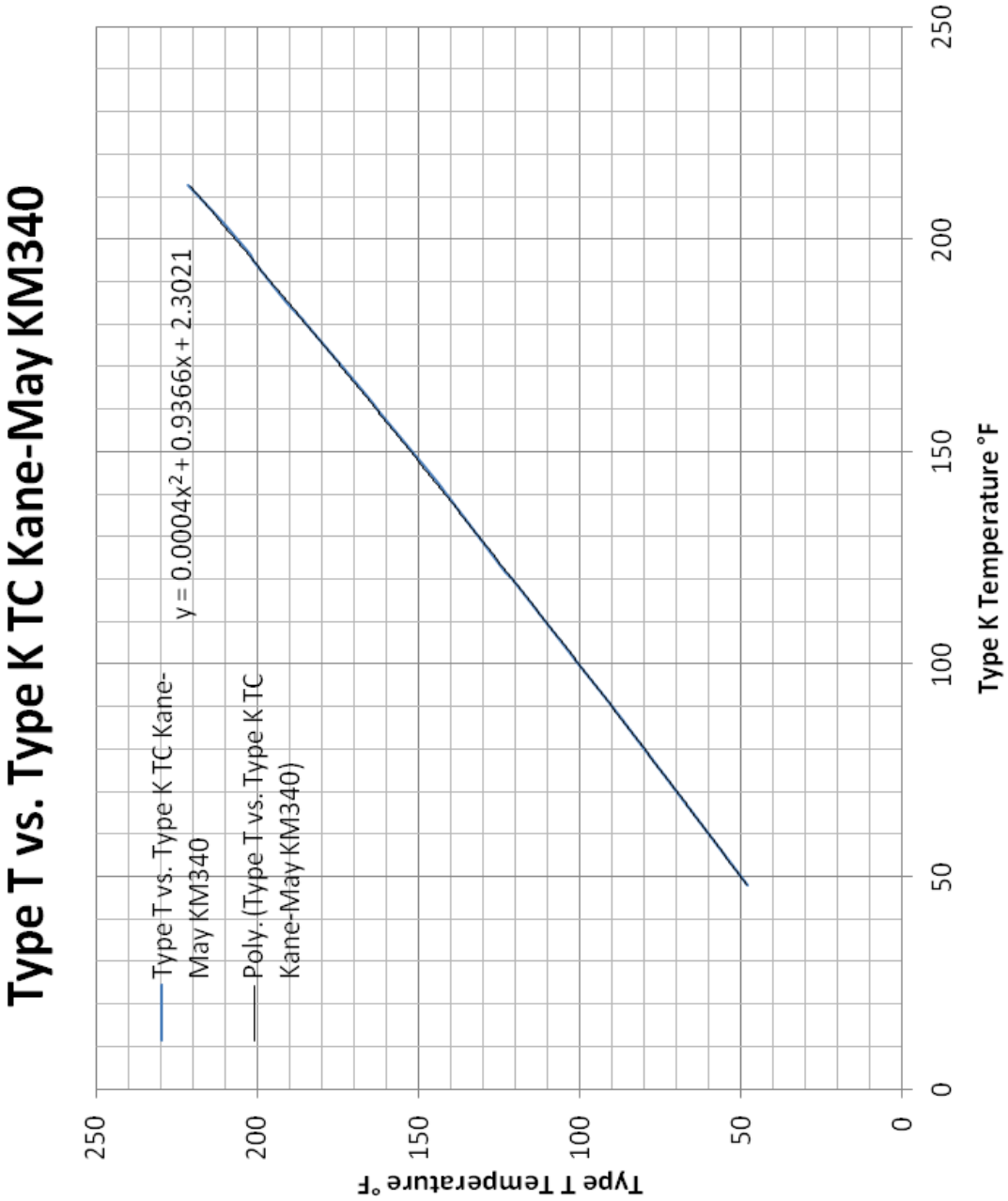

REFERENCES

[1] Private Communication from Dr. N. Schofield: Dept. of Electrical and Computer Engineering, McMaster University. Illustration and Magnetic Circuit of High Speed SRM

[2] Holman, J. P., "Heat Transfer", 6th Edition, McGraw Hill, 1986, pp. 624-627

[3]Boglietti, A., Cavagnino, A., Staton, D., Shanel, M., Mueller, M., and Mejuto, C., "Evolution and Modern Approaches for Thermal Analysis of Electrical Machines", IEEE Transactions on Industrial Electronics, Vol. 56, No. 3, March 2009, pp. 871-882

[4] Staton, D., Boglietti, A., and Cavagnino, A., "Solving the More Difficult Aspects of Electric Motor Thermal Analysis", Proc. 2003 IEEE International Conference Electric Machines and Drives, IEMDC 2003, Vol. 2, pp. 747-755

[5] Szogyen, J. R. M., "Cooling of Electric Motors", IEE J. Electric Power Applications, April 1979, Vol. 2, No. 2, 1979, pp 59-67

[6] Li, H., "Cooling of a Permanent Magnet Electric Motor with a Centrifugal Impeller", Intl. Journal of Heat and Mass Transfer, Vol. 53, 2010, pp. 797-810

[7] JMAG: "Simulation Technology for Electrical Design", www.jmag-international.com

[8] Staton, D., et al., op. cit.

[9] Ye, Z., Luo, W., "Simulative Analysis of Traction Motor Cooling System Based on CFD", IEEE, 2011

[10] Crescimbini, F., Di Napoli, A., Solero, L., and Caricchi, F., "Compact Permanent Magnet Generator for Hybrid Vehicle Applications", Proc. 2003 IEEE Industry Applications Conference, Vol. 1, pp. 576-583

[11] Hsu, J. S., Ayers, C. W., and Coomer, C., "Motor Frame Cooling with Hot Liquid Refrigerant and Internal Liquid", United States Patent Office, Patent Application No. US 2005/0235672 A1, October 27, 2005

[12] Huang, Z., Nategh, S., Lassila, V., Alakula, M., and Yuan, J., "Direct Oil Cooling of Traction Motors in Hybrid Drives", Proc. 2012 IEEE International Electric Vehicle Conference, IVEC 2012, p. 8, pp.

[13] Baggu, M. M., and Hess, H. L., "Evaluation of an Existing Thermal Model of an Induction Motor and its Further Application to an Advanced Cooling Topology", Proc. 2007 IEEE International Electric Machines and Drives Conference, IEMDC 2007, Vol. 2, pp. 1079-1083

[14] Private Communication from Dr. N. Schofield: Dept. of Electrical and Computer Engineering, McMaster University. ECE708 Coursework Notes, McMaster University, 2014

[15] Bone, C. H., "Cooling and Cooling Circuits for Electric Motors", IEE J. Electric Power Applications, Vol. 1, No. 2, 1978, pp 37-44

[16] Luke, G. E., "The Cooling of Electric Machines", AIEE Trans., vol. 45, 1923, pp. 1278-1288

[17] Ringland, G. L., "Dynamo-Electric Machine", United States Patent Office, Patent No. 1761587, June 3, 1930

[18] Yoon, M. K., Jeon, C. S., and Ken Kauh, S., "Efficiency Increase of an Induction Motor by Improving Cooling Performance", IEEE Trans. Energy Conv, vol. 17, no. 1, March 2002, pp. 1-6

[19] Pickering, S. J., Lampard, D., Hay, N., and Roylance, T. F., "Heat Transfer from the Stator End-Windings of a Low Voltage Concentric-Wound Induction Motor", Seventh International Conference on Electrical Machines and Drives, IEE Conference Publication No. 412, 1995, pp. 477-481

[20]Li, H., "Cooling of a Permanent Magnet Electric Motor with a Centrifugal Impeller", Intl. Journal of Heat and Mass Transfer, Vol. 53, 2010, pp. 797-810

[21] Kim, M-S., Lee, K-S., and Um, S., "Numerical Investigation and Optimization of the Thermal Performance of a Brushless DC Motor", Intl. Journal of Heat and Mass Transfer, Vol. 52, 2009, pp. 1589-1599

[22] Naruta, T., Akiyama, Y., and Niwa, Y., "A Study of Cooling Magnet-Wire of the Brushless DC Motor for Car Air Conditioner", Proc. Eleventh International Conference on Electrical Machines and Systems, ICEMS 2008, pp. 3514-3517

[23] Dessouky, Y. G., Williams, B. W., and Fletcher, J. E., "Cooling Enhancement of Electric Motors", IEE Proc. Electrical Power Applications, Vol. 145, No. 1, January 1998, pp. 57-60

[24] Wenjuan, Qi., Jiming, Z., Guiqing, H., and Yongxiang, X., "Thermal Analysis of Underwater Oil-filled BLDC Motor", Proc. 2011 International Conference on Electrical Machines and Systems, ICEMS 2011, p. 8, pp.

[25] Huang, Z., et al., op. cit.

[26] Ye, Z-N., Lou, W-D., Zhang, W-M, Feng, Z-X., "Simulative Analysis of Traction Motor Cooling System Based on CFD", Proc. 2011 International Conference on Electric Information and Control Engineering, ICEICE 2011, pp. 746-749

[27] Hsu, J. S., et al., op. cit.

[28] Hernden, M., and Rademacher, L., "Dynamoelectric Machine Having Fluid Cooling of Back Iron and End Turns", United States Patent Office, United States Patent No. 5363002, November 8, 1994

[29] Baggu, M. M., and Hess, H. L., op. cit.

[30] Huang et al., op. cit.

[31] Mellor, P. H., Roberts, D., and Turner, D. R., "Lumped Parameter Thermal Model for Electrical Machines of TEFC design", IEE Proceedings B, Vol. 138, No. 5, September 1991, pp. 205-218

[32] Dessouky Y. G., et al., op. cit.

[33] Festa, M., Eberhardt, H.-D., and Hofmann, W., "Inter-laminar Flux and Eddy Current Losses in a Circumferentially Cooled Stator Core", Proc. Nineteenth International Conference on Electrical Machines, ICEM 2010, Rome, p. 6, pp.

[34] Xueli, Z., Haifeng, W., Guoqiang, Z., and Guobiao, G., "Temperature Characteristics in the Stator Model of a Permanent Magnet Motor by Water Cooling and Evaporative Cooling", Proc. Eighth International Conference on Electrical Machines and Systems, ICEMS 2005, Vol. 3, pp. 2408-2010

[35] Jarczynski, E., "Stator Cooling System for Electrical Machinery", United States Patent Office, United States Patent No. 5091666, Feb 25, 1992

[36] Hamer, C., "Lamination Assembly Including an Inter-Lamination Thermal Transfer Member for an Electric Machine", United States Patent Application Publication, Publication No. US2014/0070658 A1, Mar 13, 2014

[37] Crescimbini, F., et al., op. cit.

[38] Kylander, G., "Thermal Modelling of Small Cage Induction Motors", Ph.D. Dissertation, Chalmers University of Technology, Goteborg, Sweden, Technical Report No. 265, 1995

[39] Sooriyakumar, G., Perryman, R., and Dodds, S. J., "Analytical Thermal Modelling for Permanent Magnet Synchronous Motors", Proc. Forty Second International Universities Power Engineering Conference, UPEC 2007, pp. 192-196

[40] Cezario, C. A., and Silva, H. P., "Electric Motor Winding Temperature Prediction Using a Simple Two Resistance Thermal Circuit", Intl. Journal for Computation and Mathematics in Electrical and Electronic Engineering, Vol. 29, No. 5, 2010, pp. 1325-1330

[41] Shoujun, S., Weiguo, L., and Schaefer, U., "Thermal Analysis of a 30kW Switched Reluctance Starter/Generator System Used in Aircraft", Proc. Second International Conference on Power Engineering, Energy and Electrical Drives, POWERENG 2009, pp. 331-336

[42] Duran, M. J., and Fernandez, J., "Lumped Parameter Thermal Model for Induction Machines", IEEE Transactions on Energy Conversion, Vol. 19, No. 4, December 2004, pp. 791-792

[43] Nategh, S., Wallmark, O., and Leksell, M., "Thermal Analysis of Permanent Magnet Synchronous Reluctance Machines", Proc. Fourteenth European Conference on Power Electronics and Applications, EPE 2011, p. 10

[44] Mellor, P. H., et al., op. cit.

[45] Nategh, S., et al., op. cit.

[46] Yang, B., "Development of Thermal Models for Permanent Magnet Traction Motors", M.Sc. Thesis, Royal Institute of Technology, Stockholm, Sweden, July 2009

[47] Boglietti, A., Cavagnino, A., Lazzari, M., and Pastorelli, M., "A Simplified Thermal Model for Variable Speed Self Cooled Industrial Induction Motor", Proc. 2002 IEEE Industry Applications Conference, Thirty Seventh IAS Annual Meeting, Vol. 2, pp. 723-730

[48] Mellor, P. H., et al., op. cit.

[49] Szogyen, J. R. M., op. cit.

[50] Lindstrom, J., "Thermal Model of a Permanent Magnet Motor for a Hybrid Electric Vehicle. Research Report, Dept. of Electric power Engineering, Chalmers University of Technology, Goteborg, Sweden, April 1999

[51] Kylander, G., op. cit.

[52] Nategh, S., et al., op. cit.

[53] Idoughi, L., Mininger, X., Bouillault, F., Bernard, L., and Hoang, E., "Thermal Model with Winding Homogenization and FIT Discretization for Stator Slot", IEEE Transactions on Magnetics, Vol. 47, No. 12, December 2011, pp.4822-4826

[54] Soderberg, C. R., "Steady Flow of Heat in Large Turbine Generators", AIEE Trans., Vol. 50, 1931, pp. 782-802

[55] Liwei, S., Zijian, L., Jingyi, G., Qingchu, Z., and Fuping, W., "3D Thermal Analysis of Water Cooling Induction Motor Used for HEV", 2008 IEEE Vehicle Power and Propulsion Conference, Harbin, China, VPPC 2008, p. 4, pp

[56] Cuiping, L., Yulong, P., Ronggang, N., and Shukang, C., "Analysis of 3D Static Temperature Field of Water Cooling Induction Motor in Mini Electric Vehicle", 2011 International Conference on Electric Machines and Systems, ICEMS 2011, p. 5, pp

[57] Li, L., Sun, Z., Huang, X., and Cao, J., "Thermal Analysis of High Speed Motor Based on Flow Field Calculation Considering Tooth Slots Effects", Proc. 2011 International Conference on Electrical Machines and Systems, ICEMS 2011, p. 4, pp

[58] Srinivas, K. N., and Arumugam, R., "A Novel Thermal Characterization of Switched Reluctance Motors Involving Computational Fluid Dynamics", Electric Power Components and Systems, Vol. 32, Taylor and Francis Gp., 2004, pp. 855-867

[59] Fiaz, J., Iranpour, R., and Pillay, P., "Thermal Model for a Switched Reluctance Motor of TEFC Design During Steady and Transient Operation", Electric Machines and Power Systems, Vol. 26, Taylor and Francis, 1998, pp. 77-91

[60] Mellor, P. H., et al., op. cit.

[61] Fan, J., Zhang, C., Wang, Z., and Strangas, E. G., "Thermal Analysis of Water Cooled Surface Mount Permanent Magnet Electric Motor for Electric Vehicle", Proc. 2010 International Conference on Electrical machines and Systems, ICEMS 2010, p. 5, pp

[62] Staton, D., Boglietti, A., and Cavagnino, A., "Solving the More Difficult Aspects of Electric Motor Thermal Analysis", Proc. 2003 IEEE International Conference Electric Machines and Drives, IEMDC 2003, Vol. 2, pp. 747-755

[63] Nategh, S., Wallmark, O., Leksell, M., and Zhao, S., "Thermal Analysis of a PMaSRM Using Partial FEA and Lumped Parameter Modeling", IEEE Transactions on Energy Conversion, Vol. 27, No. 2, June 2012

[64] Staton, D. A., and Cavagnino, A., "Convection Heat Transfer and Flow Calculations Suitable for Electric Machines Thermal Models", IEEE Transactions on Industrial Electronics, Vol. 55, No. 10, October 2008, pp. 3509-3516

[65] Boglietti, A., et al., op. cit.

[66] Nategh, S., et al., op. cit.

[67] Krishnan, R., "Switched Reluctance Motor Drives: Modeling, Simulation, Analysis, Design and Applications", CRC Press, 2001, pp. 30-46

[68] Ibid., pp. 109-110

[69] Ferreira, C. A., Jones, S. R., Hegland, W. S., and Jones, W. D., "Detailed Design of a 30-kW Switched Reluctance Starter/Generator System for a Gas Turbine Engine Application", IEEE Transactions on Industry Applications, Vol. 31, No. 3, May/June 1995, pp. 553-561

[70] MacMinn, S. R., and Jones, W. D., "A Very High Speed Switched-Reluctance Starter-Generator for Aircraft Engine Applications", IEEE, 1989, pp. 1758-1764.

[71] Qionghua, Z., Shuanghong, W., Zhiyuan, M., Wei, G., and Yihui, Q., "Design of a 50kW Switched Reluctance Machine for HEV Propulsion System", IEEE, 2003, pp. 3207-3211

[72] Rahman, K. M., and Schulz, S. E., "Design of High-Efficiency and High-Torque-Density Switched Reluctance Motor for Vehicle Propulsion", IEEE Transactions on Industry Applications, Vol. 38, No. 6, November/December 2002, pp. 1500-1507

[73] Uematsu, T., and Wallace, R. S., "Design of a 100kW switched reluctance motor for electric vehicle propulsion", IEEE, 1995, pp. 411-415

[74] Gallegos-Lopez, G., Reiter Jr., F., Rajashekara, K., and Krefta, R. J., "300 kW Switched Reluctance Generator for Hybrid Vehicle Applications", SAE (unknown), 2002, pp. 81-87

[75] Mueller, M. A., "Design and Performance of a 20kW, 100rpm, Switched Reluctance Generator for a Direct Drive Wind Energy Converter", IEEE (unknown), 2005, pp. 56-63

[76] Sun, T., Lee, J-Y., Hong, J-P., "Investigation on the Characteristics of a Novel Segmental Switched Reluctance Motor Driven by Asymmetric Converter and Full Bridge Inverter", Proc. 2007 International Electric Machines and Drives Conference, ICEMD 2007, pp. 815-820

[77] Lee., J-Y., Lee, B-K., Lee, J-J., and Hong, J-P., "A Comparative Study of Switched Reluctance Motors with Conventional and Toroidal Windings", IEEE, 2005, pp. 1675-1680

[78] Lindstrom, J., op. cit.

[79] Kylander, G., op. cit.

[80] Staton, D., et al., op. cit.

[81] Baggu, M. M., and Hess, H. L., op. cit.

[82] Huang et al., op. cit.

[83] Festa, M., et al., op. cit.

[84] Jarczynski, E., op. cit.

[85] Panasonic Corporation, www.panasonic.com http://na.industrial.panasonic.com/products/circuit-thermal-protection/thermal-protection/pyrolytic-graphite-sheet-pgs

[86] Holman, J. P., op. cit., pp.83-87

[87] PSIM, Power Simulation Software, http://powersimtech.com/products/psim/

[88]Holman, J. P., op. cit., pp. 545

[89] Lindstrom, J., op. cit.

[90] Sun, T., et al., op. cit.

[91] Lee, J. Y., et al., op. cit.

[92] J-Y. Lee, B-K. Lee, T. Sun, J-P. Hong, and W-T. Lee, "Dynamic Analysis of Toroidal Winding Switched Reluctance Motor Driven by a 6-Switch Converter," IEEE Trans. Magnetics, vol. 42, no. 4, pp. 1275-1278, 2006

[93] Lee, J-Y., et al., op. cit. [76]

[94] Lee, J-Y., et al., op. cit. [91]

[95] Ibid

[96] P. Desai, "The Novel Concept of Switched Reluctance Machines with Higher Number of Rotor Poles," Ph.D. dissertations, Dept. of Electrical and Computer Engineering, Illinois Institute of Technology, Chicago, pp. 82, 2009

[97] JMAG, op. cit.

[98] Desai, P., op. cit.

[99] Lee, J-Y., et al., op. cit. [76]

[100] Ibid

[101] Srinivas, K. N., and Arumugam, R., op. cit.

[102] Li, L., op. cit.

THE END